Investigating Exoplanets and Transients Using Small-Aperture Telescopes

Thesis

The Open University

Investigating Exoplanets and Transients Using Small-Aperture Telescopes

Submitted for the degree of Doctor of Philosophy

in Astronomy and Astrophysics

Richard Busuttil MPhys (Hons)

Supervisors: Dr. Ulrich Kolb, Dr. Carole Haswell

The Open University

Submitted September 2016

Abstract

This work characterises PIRATE's primary camera, the SBIG STX-16803, as well as assessing the usefulness and impact of a small-aperture semi-autonomous facility in Mallorca for exoplanet studies and studies of transient sources. Additionally, a method for exploring the Roche lobe of an exoplanet and the effects this has on the shape and density of the planet is also described.

PIRATE is a small aperture photometric facility that can be operated remotely or autonomously, is constructed from commercially available hardware and utilised by The Open University for research, education and outreach. The camera gain measurements are within the manufacturer specifications while the read noise deviates quite significantly. The camera shutter is also verified to evenly illuminate the CCD which may be suffering from a form of residual image.

Regarding exoplanets, PIRATE has helped to identify 108 false positives as well as 24 real and plausible planets. Combined, this is 67% of PIRATE's total exoplanet candidate observations. Several of these targets are explored in further detail.

Still on the subject of exoplanets, Roche calculations are applied to 207 known exoplanets and highlight that WASP-12b, WASP-19b and WASP-103b are likely to have strong distortions from a spherical shape. Look-up charts were also generated for mass ratios of 10^{-6} through to 10^{-1}. These look-up charts are intended to provide a quick reference volume correction to exoplanets (or any other system of similar mass ratios).

As part of the Gaia transient preparatory and to demonstrate the capabilities of PIRATE, SN 2014J is provided as an example. A peak B apparent magnitude, B_{max} of 11.80 ± 0.14 mag is observed at a t_{max} of 56690.79 ± 0.01 MJD and provides $\Delta m15 = 0.98 \pm 0.20$ mag. A peak $E(B-V)$ extinction of 1.24 ± 0.16 mag ($E(B-V)_{host} = 1.19 \pm 0.16$ mag) is determined.

Acknowledgements

First and foremost I wish to thank my supervisors, Ulrich Kolb and Carole Haswell for their excellent guidance and feedback over the last few years. They have provided me with the intellectual freedom to explore the subject matter as well as providing encouragement during the tough times of the PhD. I also wish to thank and acknowledge Geoff Bradshaw and his colleagues for their amazing dedication to ensuring that the Open University's CEPSAR Linux systems are kept up and running as smoothly as possible.

I am grateful to Stefan Holmes and his research on PIRATE; he was an excellent teacher and provided plenty of support during my early PIRATE days. I'm also grateful to Jakub Bochinski, Johanna Jarvis and Shripathy Hadigal; several of their PIRATE observations were of use to this thesis and they provided insightful discussions and solutions to several PIRATE solutions. The staff at the OAM are also acknowledged for their efforts behind the scenes which allowed PIRATE to function.

I wish to thank Liam Steele, Robert Farmer, Anthony Davenport, Ziad el Otell, Kieran 'Kiz' Natt, Andrew Carter, Elena Nickson and Jonathan Gregson for their help and expertise across a variety of topics, in addition to their friendship. Similarly, many thanks to Maria Duffy, Rebecca Wolsey, Alan Bradshaw, Feargus Abernethy, Peter Landsberg, Phillipa Smith and Roy Adkin for their amusing chats and entertaining anecdotes during the ritualistic 3:30pm coffee club. On the subject of coffee club, a massive thank you goes to Victoria Bending, James Holmes and Emma Fegan for keeping coffee club supplied with an abundance of Jaffa cakes, doughnuts and coffee which fuelled me through some of the long nights of writing. There are many others who have provided support and friendship that I have likely neglected to mention and to them, I offer my thanks.

I would also like to thank my parents, Paul and Pauline Busuttil, for all their support and encouraging me to follow my dreams. Finally, I wish to thank my girlfriend, Catherine Hill, for putting up with my various complaints, supporting me through the tough times and most importantly believing in me even when I had stopped believing in myself.

Contents

List of Publications **xiii**

List of Figures **xv**

List of Tables **xix**

1 Introduction **1**

1.1 PIRATE - Physics Innovations Robotic Astronomical Telescope Explorer 3

1.1.1 Other Small Aperture Facilities 4

1.2 SuperWASP 5

1.3 Exoplanets 6

1.3.1 Direct Imaging 7

1.3.2 Astrometry 7

1.3.3 Radial Velocity 8

1.3.4 Gravitational Microlensing 8

1.3.5 Pulsar Timing Variations 9

1.3.6 Transits 9

1.4 Astronomical Transient Events 12

1.4.1 Supernovae 12

1.4.1.1 Type-I SNe 12

1.4.1.2 Type-II SNe 14

1.4.2 Cataclysmic Variables (Novae, Dwarf Novae) 15

1.4.3 Tidal Disruption Events 16

1.4.4 Other Transient Events 17

2 Camera Characterisation **20**

2.1 PIRATE's Primary Camera - SBIG STX-16803 20

2.2 Photon Transfer Curves 22

2.3 Method & Results 23

2.3.1 Setup 23

2.3.2 CCD Overscan 23

2.3.3 Standard Photon Transfer Curve 28

2.3.3.1 PTC Errors 33

2.3.3.2 Flat Correction 33

2.4 Shutter Lag 35

2.5 Discussion 41

2.5.1 STX-16803 Gain and Read Noise 41

2.5.2 Residual Images 43

2.5.3 Flat Correction 45

2.6 Key Results 46

3 PIRATE Observations - Exoplanets **47**

3.1 Observational Method 48

3.1.1 Target Selection 49

3.2 PIRATE Exoplanet Pipeline 51

3.2.1 Original Exoplanet Reduction Pipeline 51

3.2.2 Modifications to the PIRATE Exoplanet pipeline 54

3.2.2.1 Correction of Bias/Dark/Flat implementation 55

3.2.2.2 Master Frame Selection 57

3.2.2.3 Auto-Frame selection 59

3.2.2.4 On-Off 61

3.3 Non-Detections and Observed Mimics 62

3.3.1 Non-Detections 62

3.3.2 Grazing 63

3.3.3 Blends 65

3.4 Observed Plausible Exoplanets 65

3.4.1 1SWASPJ065329.01+190612.1 65

3.4.2 1SWASPJ215011.04+514800.8 71
3.5 Published Planets 74
3.5.1 WASP-54b 75
3.5.2 WASP-56b 79
3.5.3 WASP-58b 80
3.5.4 WASP-59b 81
3.5.5 WASP-60b 82
3.5.6 WASP-65b 83
3.5.7 WASP-69b 84
3.5.8 WASP-86b 85
3.5.9 WASP-92b 86
3.5.10 WASP-93b 87
3.5.11 WASP-125b 88
3.6 Observation Statistics 89
3.6.1 PIRATE's Lightcurve Performance 92
3.7 Key Results 95

4 Exoplanetary Roche Lobe and Surface Geometry 97
4.1 Theory - The Roche Potential 98
4.2 Method 100
4.2.1 Roche Lobe Calculations 100
4.2.2 Mapping the Planetary Surface Roche Potential 104
4.3 Results 109
4.3.1 Planetary Lobes 109
4.3.2 Roche implications for WASP-12b 116
4.3.3 Earth-like Planets Orbiting Cool White Dwarfs 118
4.3.4 Roche Correction Look-up Chart 119
4.4 Key Results 120

5 PIRATE Observations - Gaia Transients 123
5.1 PIRATE's Previous Transient Contributions 124
5.2 Gaia Transient Alert Preparation 125
5.2.1 ACP Scheduler and The VOEvent Receiver 125

5.2.2 Gaia Data Reduction Pipeline 129
5.2.3 Cambridge Photometry Calibration Server 130
5.2.3.1 Calibrating PIRATE's Filters 133
5.2.4 PIRATE's Limiting Magnitudes 137
5.3 PIRATE Observed Transients 138
5.3.1 SN 2014J - An Initial Inspection 138
5.3.2 Other Observed Transients 143
5.4 Key Results 145

6 Conclusions and Outlook 146
6.1 Summary 146
6.1.1 SBIG STX-16803 CCD Camera 146
6.1.2 PIRATE's Exoplanet Results 148
6.1.3 Exoplanet Roche Lobes 150
6.1.4 Gaia Transient Event with PIRATE 151
6.2 Areas of Improvement and Future Work 152
6.2.1 CCD Characterisation 152
6.2.2 Improving Exoplanet Target Selection 154
6.2.3 Improving the Exoplanet and Transient Reduction Pipelines . 155
6.2.4 Exoplanet Roche Lobes 158

A Exoplanet Observation List 159

B Roche Code 174

C Known Exoplanet Roche Density Corrections 180

Bibliography 189

List of Publications

During the course of the PhD the author has directly and indirectly contributed to several publications and Astronomical Telegrams which are listed below:

- Brothwell, R. D. et al. (2014). A window on exoplanet dynamical histories: Rossiter-McLaughlin observations of WASP-13b and WASP-32b. MNRAS, 440, 3392-3401.

- Campbell, H. C. et al. (2015). Total eclipse of the heart: the AM CVn Gaia14aae / ASSASN-14cn. MNRAS, 452, 1060-1067.

- Faedi, F. et al. (2013). WASP-54b, WASP-56b, and WASP-57b: Three new sub-Jupiter mass planets from Super-WASP. A&A, 551, A73.

- Fossati, L. et al. (2012). The Habitability and Detection of Earth-like Planets Orbiting Cool White Dwarfs. ApJ, 757, L15.

- Gómez Maqueo Chew, Y. et al. (2013). Discovery of WASP-65b and WASP-75b: Two hot Jupiters without highly inflated radii. A&A, 559, A36.

- Haswell, C. A. et al. (2012). Near-ultraviolet Absorption, Chromospheric Activity, and Star-Planet Interactions in the WASP-12 system. ApJ, 760, 79.

- Hay, K. L. et al. (2016). WASP-92b, WASP-93b and WASP-118b: Three new transiting close-in giant planets. MNRAS, 463, 3276-3289.

- Henze, M. et al. (2012). New disk nova candidate in M 31. *The Astronomer's Telegram*, 3932, 1.

- Lohr, M. E. et al. (2015). The doubly eclipsing quintuple low-mass star system 1SWASP J093010.78+533859.5. A&A, 578, A103

- Maxted, P. F. L. et al. (2014). EL CVn-type binaries - discovery of 17 helium white dwarf precursors in bright eclipsing binary star systems. MNRAS, 437, 1681-1697.

- Rixon, G. et al. (2014). Gaia Alerts classified at the William Herschel Telescope. *The Astronomer's Telegram*. 6593, 1.

- Staab, D. et al. (2017). SALT observations of the Chromospheric Activity of Transiting Planet Hosts: Mass Loss and Star Planet Interactions. MNRAS, 466, 738-748.

- Wyrzykowski, L. et al. (2013). Multiband photometric follow-up of ASASSN-13aw (SN 2013dr). *The Astronomer's Telegram*, 5245, 1.

- Wyrzykowski, L. et al. (2014). Multiband photometric follow-up of supernova iPTF13ebh. *The Astronomer's Telegram*, 5926, 1.

List of Figures

1.1 Transit lightcurve diagram 10
1.2 Example Supernovae lightcurves 13
1.3 Example dwarf nova lightcurves 16
1.4 Example TDE lightcurves 17
1.5 Example microlensing lightcurve 18
1.6 Example GRB lightcurve 19

2.1 KAF 16803 quantum efficiency plot 21
2.2 Inspection of STX-16803 overscan regions 25
2.3 Closer inspection of STX-16803 overscan regions 26
2.4 KAF-16803 architecture 27
2.5 Determination of correct overscan offset level 28
2.6 STX-16803 Saturated Photon Transfer Curve 30
2.7 STX-16803 Saturated Linearity Response Curve 31
2.8 STX-16803 Unsaturated Linearity Response Curve 31
2.9 STX-16803 Unsaturated Photon Transfer Curve 32
2.10 STX-16803 Unsaturated Photon Transfer Curve - Binning 2x2 32
2.11 STX-16803 Unsaturated Photon Transfer Curve - Binning 3x3 33
2.12 STX-16803 Gain vs Signal - Binning 1x1 34
2.13 STX-16803 Shot noise vs Signal - Binning 1x1 34
2.14 STX-16803 Shot+Read noise vs Signal - Binning 1x1 35
2.15 STX-16803 Flat Corrected PTC - Binning 1x1 36

2.16 Close view of Fig. 2.15 36
2.17 Shutter lag plot 37
2.18 Shutter Correction Map 40
2.19 Baader Filter Transmissions 43

3.1 Median combined master frame FWHM comparison 58
3.2 PIRATE non-detection full lightcurve 62
3.3 PIRATE non-detection on-off lightcurve 63
3.4 PIRATE grazing full lightcurve 64
3.5 PIRATE grazing on-off lightcurve 64
3.6 PIRATE-SuperWASP Full Blend 66
3.7 PIRATE blend full lightcurve 67
3.8 PIRATE blend on-off lightcurve 68
3.9 1SWASPJ065329.01+190612.1 MCMC fits 69
3.10 1SWASPJ215011.04+514800.8 PIRATE lightcurves - plausible 73
3.11 FWHM for 1SWASPJ215011.04+514800.8 on the night of 2012-08-13 74
3.12 1SWASPJ215011.04+514800.8 MCMC fits 75
3.13 Phased PIRATE lightcurves for WASP-54b 79
3.14 Phased PIRATE lightcurves for WASP-56b 80
3.15 Phased PIRATE lightcurves for WASP-58b 81
3.16 Phased PIRATE lightcurves for WASP-59b 82
3.17 Phased PIRATE lightcurves for WASP-60b 83
3.18 Phased PIRATE lightcurves for WASP-65b 84
3.19 Phased PIRATE lightcurves for WASP-69b 85
3.20 Phased PIRATE lightcurves for WASP-86b 86
3.21 Phased PIRATE lightcurves for WASP-92b 87
3.22 Phased PIRATE lightcurves for WASP-93b 88
3.23 Phased PIRATE lightcurves for WASP-125b 89
3.24 PIRATE SuperWASP Observations 91

3.25 PIRATE lightcurve RMS scatter 92
3.26 PIRATE low RMS scatter lightcurve for the night of 30/10/2013 . . . 94

4.1 Binary system Roche potential in 3D 99
4.2 WASP-19b density profiles 106
4.3 3D Roche lobes for WASP-12b, 19b, and 103b 112
4.4 Cross sectional plots for WASP-12b, 19b, and 103b 113
4.5 Roche volume filling percentage for 207 exoplanets 114
4.6 Density correction plot for 207 exoplanets 115
4.7 WASP-12 spectra comparison 117
4.8 WASP-12b NUV lightcurves from Haswell et al. (2012) 118
4.9 Example Volume correction look-up charts 122

5.1 ACP Scheduler Console 126
5.2 Cambridge Photometry Calibration Server upload form 131
5.3 Cambridge Photometry Calibration Server example output 132
5.4 SN 2014J light curve composed of PIRATE and AAVSO data 140
5.5 Plots of observed transients 144

List of Tables

2.1 Camera shutter lag results 38

3.1 1SWASPJ065329.01+190612.1 MCMC system parameters 70
3.2 1SWASPJ215011.04+514800.8 MCMC system parameters 76
3.3 Published parameters for WASP 54b, 56b, 65b and 93b 77
3.4 PIRATE's observation log of known exoplanets 78
3.5 PIRATE's SuperWASP exoplanet candidate classification statistics . . 90
3.6 PIRATE lightcurve RMS scatter 93

4.1 Roche lobe code resolution comparison 102
4.2 Roche code comparisons to the Eggleton approximation and the Hill's sphere radius for various mass ratios 104
4.3 Roche lobe maxima percentage differences 107
4.4 Roche lobe minima percentage differences 108
4.5 Top 15 Roche filling planets and their density corrections 111

5.1 PIRATE filter calibration via CPCS 134
5.2 PIRATE Mk 1.5 limiting magnitude 137
5.3 PIRATE Mk 2 limiting magnitude 137
5.4 SN2014J fit parameters 141

A.1 PIRATE's list of observations 160

C.1 207 examined exoplanets' Roche filling fractions and density corrections 181

Chapter 1

Introduction

Large telescope facilities are expensive to construct, operate and maintain. Due to the cost there are limited facilities available, which means that researchers and astronomers are competing for these limited resources. Small aperture telescopes are a fraction of the cost and play a key role in preventing wasted observing time by providing observations to support theories and applications. In addition to this, small aperture telescopes are capable of producing high quality research, and are also used as tools for education and outreach.

This thesis focuses on the characterisation and science goals of the Physics Innovations Robotic Astronomical Telescope Explorer (PIRATE). PIRATE's primary research is that of exoplanet detection and exoplanet mimic winnowing as part of the SuperWASP consortium. While on the topic of exoplanets, Roche potential calculations of exoplanets are also explored. PIRATE is also diversifying to more routinely include transient astronomical event observations which may require rapid response observations.

The current chapter introduces the PIRATE facility as well as a few other examples of small aperture telescopes. Additionally, it covers some of the different exoplanet detection techniques, in particular the transit detection method. Finally, examples of transient events are presented.

Ch. 2 covers the characterisation of PIRATE's primary imaging camera at the time,

the SBIG STX-16803 CCD camera. Ch. 3 explores the SuperWASP exoplanet candidates that PIRATE has played a key role in observing. Remaining on the topic of exoplanets, Ch. 4 investigates an application of Roche potential calculations to exoplanets. Ch. 5 returns to PIRATE and explores the set-up and contributions PIRATE has made to the Gaia transient preparation phase. Finally, Ch. 6 summarises the conclusions from the previous chapters and suggests avenues for further development.

During the course of the PhD the author has directly and indirectly contributed to several publications and Astronomical Telegrams. Observations and data reductions have been supplied to SuperWASP for Faedi et al. (2013) (WASP-56b), Gómez Maqueo Chew et al. (2013) (WASP-65b) and Hay et al. (2016) (WASP-93b). Similarly, observations and data reductions have been supplied to the Cambridge photometry calibration server as part of the Gaia transient preparation phase which contributed to the following astronomical telegrams Wyrzykowski et al. (2013) (ASASSN-13aw) and Wyrzykowski et al. (2014) (iPTF13ebh). Observations amongst various PIRATE users (including the author) as part of a monitoring collaboration on M31 resulted in the detection of a nova candidate (Henze et al. 2012). The author aided and supervised PIRATE's use for observations in Maxted et al. (2014). PIRATE observations were also collected for Lohr et al. (2015). As recognition of PIRATE's general contributions to the SuperWASP consortium the author was included in Brothwell et al. (2014). Similarly, for the contributions to the Gaia preparation phase the author was included in Campbell et al. (2015) and Rixon et al. (2014).

The Roche lobe calculations described in this work were used in Haswell et al. (2012) and Staab et al. (2017). Similarly, the calculations and resulting Roche geometry were used to determine the ratio of illuminated area at maximum and quadrature of example exoplanets in Fossati et al. (2012).

1.1 PIRATE - Physics Innovations Robotic Astronomical Telescope Explorer

PIRATE is in the process of relocating from the island of Mallorca to the Observatorio del Teide observatory site located in Tenerife. This thesis covers PIRATE's existence in Mallorca. PIRATE was located roughly 162m above sea level at the Observatori Astronomic de Mallorca (OAM) observatory located by Costitx in Mallorca from the period of March 2008 to November 2015. The original PIRATE Mk 1 facility is detailed in Holmes et al. (2011) and consisted of a 14" Celestron Schmidt-Cassegrain reflector mounted on a Paramount ME German equatorial mount. The primary imaging camera was an SBIG STL-1001E CCD, a 1024 x 1024 pixel camera with a front illuminated CCD, producing a plate scale of 1.21" pixel^{-1}. The camera was attached to an Optec TCF microfocuser and an 8 position filter wheel containing Johnson-Cousins BVRI broadband filters and three narrow band filters; Hα, SII, and OII.

PIRATE has since undergone several revisions to both hardware and software resulting in two operating modes used in the period 2010 to 2015; PIRATE Mk 2 and a PIRATE Mk 1.5 variant. The main hardware changes making up PIRATE Mk 2 have been replacing the optical tube assembly (OTA) with a 17" Planewave Corrected Dall-Kirkham astrograph and replacing the imaging camera with a 4096 x 4096 pixel anti-blooming camera, the SBIG STX-16803, giving a plate scale of 0.63" pixel^{-1}. A 5 position filter wheel containing Baader RGB broadband filters and a Hα narrow band filter is attached. The Optec TCF microfocuser has been replaced with a Planewave focuser. PIRATE Mk 1.5 utilises the new 17" OTA with the SBIG STL-1001E camera and filter wheel, giving a plate scale of 1.68" pixel^{-1}. All variants of the PIRATE facility are constructed from commercially available equipment and software, providing a proof of concept that other institutions are able to adopt.

1.1.1 Other Small Aperture Facilities

There are a large number of small aperture facilities spread across the globe. For example, as of 02/08/2016, the Robotic Telescope List[1] contains 133 entries for various telescope facilities. The informal statistics on the list webpage indicate that 37.8% (93) of these telescopes have apertures less than 0.25m, while PIRATE's aperture group (0.25m to 0.5m) make up 35.8% (88) telescopes. A comprehensive review on each telescope is beyond the scope of this topic, however a few examples are presented in the rest of this section.

PIRATE acquired a neighbour at the OAM in 2011, the Planetary Transit Study Telescope (PTST), owned and operated by the University of Hamburg. PIRATE was used as a template for its construction and hence it has similar hardware and software to PIRATE. It has a larger 24" Planewave Corrected Dall-Kirkham and makes use of the same SBIG STX-16803 CCD. As an example, the facility has been utilised to search for transit timing variations in an exoplanet known as QATAR-1b (von Essen et al. 2013).

Another example of a small aperture facility which is utilised in a similar manner to PIRATE is the TRAnsiting Planets and PlanetesImals Small Telescope (TRAPPIST) (Jehin et al. 2011). TRAPPIST is a 60cm Ritchey Chretien telescope located at ESO's La Silla Observatory. It is equipped with a CCD camera with 15 μm pixels arranged in a square 2048^2 format; this provides a field of view of 22 by 22 arcminutes. TRAPPIST contributes to the detection and confirmation of exoplanets as part of the SuperWASP and CoRoT exoplanet surveys. In addition to this, TRAPPIST also dedicates observation time to the chemical composition of bright comets and any changes undergone by the comet during its orbit.

Several other examples of professional scientific observatories exist, such as the James Gregory Telescope (JGT - operated by the University of St. Andrews), the 1.2m EulerCam telescope, and the TUBITAK National Observatory which is the site for

[1] http://www.astro.physik.uni-goettingen.de/ hessman/MONET/links.html

five telescopes of sizes varying from 0.4m to 1.5m. Not all these facilities have well documented descriptions of their hardware and software but each telescope is contributing and advancing the knowledge around astronomy and astrophysics. However, science with small aperture telescopes is not limited to professionals only. Commercial telescopes used by the general public (often referred to as 'amateur' astronomers) are known to contribute their photometric data to databases such as the NASA Exoplanet Archive (Akeson et al. 2013) and the American Association of Variable Star Observers (Zissell 2000). These 'amateur' telescopes vary in size and brand from observer to observer but as an example, Meade Instruments, which supplies telescopes to the public, has a range of telescope options from 8" to 16".

1.2 SuperWASP

PIRATE obtains exoplanet candidate targets from the Super Wide Angle Search for Planets (SuperWASP) database. To place PIRATE's role into context, the SuperWASP instrumentation and science goals are described here.

SuperWASP (Pollacco et al. 2006) is made up of two instruments, SuperWASP North and SuperWASP South. These are located at La Palma and the South African Astronomical Observatory, respectively. Both instruments make use of an equatorial fork mount. Each instrument had eight Canon 200mm, f/1.8 telephoto lenses attached to the mount via a cradle system. The CCDs used are 2048 by 2048 pixels with each pixel being 13.5 by 13.5 μm. This combination of lens and CCD results in a field of view (FoV) of 64 degrees^2 and a plate scale of 13.7 arcseconds per pixel. For comparison, PIRATE Mk 2 has a FoV of 0.5 degrees^2 and a plate scale of 0.63 arcseconds per pixel. SuperWASP south has since been modified (Smith & WASP Consortium 2014) to make use of 85mm, f/1.2 lenses giving a FoV of 324 degrees^2.

The primary objective of SuperWASP is to survey a large area of sky for bright transiting (see Sec. 1.3.6) exoplanets with host star V magnitude ranging from 8.0 to 13.0, with data up to a V magnitude of 15 stored. Stars in this magnitude range

are bright enough for radial velocity measurements (see Sec. 1.3.3). SuperWASP focuses on high cadence observations, aiming to cover most of the visible sky and revisit a FoV within 30 minutes. The science frames are calibrated, and photometric measurements are performed on the stars. The photometry is detrended and a transit search algorithm is then performed and any potential transiting exoplanet candidates are flagged. Small aperture facilities with higher spatial resolution, such as PIRATE, as well as spectroscopic follow-up facilities are used to further investigate candidates prior to rejection or confirmation.

As of August 2016, the SuperWASP project has resulted in 132 published or conference announced exoplanets[2]. Two ground surveys have taken inspiration from the success of SuperWASP. Alsubai et al. (2013) describe the Qatar Exoplanet Survey (QES), which makes use of a similar set-up to SuperWASP. It makes use of four 400mm, f/2.8 lenses and a single 200mm, f/2.0 lens. Alsubai et al. (2013) identify an exoplanet survey gap in the V magnitude range of 13 to 15; QES is designed to fill this gap. PIRATE has observed some of the brighter QES candidates although the results of these are not described in this thesis. The second survey is the Next Generation Transient Survey (NGTS). NGTS (Wheatley et al. 2013) is made up of twelve 0.2m f/2.8 telescopes, the aim of which is to detect Neptune and super-Earth type exoplanets around stars brighter than V=13.

1.3 Exoplanets

Struve (1952) first postulated that the period around a star for a planetary companion could potentially be about 1 day and that eclipses of a 10 Jupiter mass companion with a mean density five times that of the star would result in a dip in stellar magnitude of 0.02. With the advent of the first exoplanet discoveries (Wolszczan & Frail 1992; Mayor & Queloz 1995), research efforts into the field of exoplanets have greatly increased.

[2]http://exoplanet.eu

Summarised below are several methods that are currently employed in the detection of exoplanets. For a more in depth discussion about the individual techniques the reader is directed to Haswell (2010); Seager (2010); Perryman (2011). These techniques have resulted in well over 550 exoplanets being confirmed and are of significant importance in constraining various parameters such as mass (e.g. radial velocity technique) and radius (e.g. transiting technique) as well as orbital parameters.

1.3.1 Direct Imaging

Direct imaging of exoplanets is very difficult to accomplish as exoplanets are very faint and can be hidden by the brightness of the host star. This means that in order to make detections, the exoplanets must have a large angular separation. The method is more likely to succeed if the host star is faint and the exoplanet is relatively bright. This can be accomplished by observing the system at wavelengths where the contrast ratio between the star and exoplanet is less severe, such as the infrared.

Two methods are currently employed to aid direct imaging: Coronagraphy and Angular Difference Imaging (ADI). Coronagraphy works by blocking the light from the bright star allowing fainter objects to be detected. ADI (Marois et al. 2006) takes multiple sequences of short exposure images while allowing the field-of-view to rotate with respect to the instrument. This rotation allows quasi-static PSF structures to be removed from the images which can then be rotated to align the field-of-view and are combined to reveal any faint objects.

1.3.2 Astrometry

All bodies in a planetary system orbit around a common centre of mass known as the barycentre. By detecting the change in position of a star as it orbits the barycentre, it is possible to infer the presence of exoplanets. Detecting the angular displacement, θ, is easier if the distance, d, from the observer to the system is small and the exoplanet

has a large mass, M_P, and/or has a large semi-major axis, a_P, as shown here

$$\theta = \frac{M_P}{M_*}\frac{a_P}{d} \tag{1.1}$$

where M_* is the mass of the star.

1.3.3 Radial Velocity

Similar to the astrometry method, the radial velocity method relies on detecting the reflex motion of the star. However, instead of detecting the change in position, this method detects the change in velocity which is accomplished by measuring the Doppler shift in the spectrum of the host star. The amplitude of this velocity curve can then be used to determine an upper mass limit on the planet. This method is used as both a standalone detection technique as well as a confirmation technique for the transit detection method, and there are over 500 exoplanets with measured radial velocities.

The change, $\Delta\lambda$, in wavelength, λ, due to the Doppler shift is given by

$$\frac{\Delta\lambda}{\lambda} = \frac{V}{c} \tag{1.2}$$

where V is the radial velocity and c is the speed of light. The radial velocity of a star due to a single planet has a maximum amplitude, A_{RV}, which is given by

$$A_{RV} = \frac{2\pi a M_P \sin i}{(M_P + M_*)P\sqrt{1-e^2}} \tag{1.3}$$

where M_* and M_P are the masses of the star and planet respectively, P is the orbital period, and e is the orbital eccentricity.

1.3.4 Gravitational Microlensing

When a foreground star passes across a background star, gravitational lensing will result in the foreground star appearing brighter. If there is an exoplanet orbiting the

foreground star, additional fluctuations in the brightness of the host star may occur.

Gravitational microlensing provides an insight into the approximate mass of the exoplanet as well as the semi-major axis of the planet at the time of the observation. While transiting and radial velocity methods tend to have a detection bias towards exoplanets that are close to the host star, microlensing is more sensitive to exoplanets that have a semi-major axis in the range of 1 to 10 AU. A major disadvantage to this method is that the detection is typically non-repeatable due to alignments required.

As an interesting side note, a recent two year survey by Sumi et al. (2011) detected a population of unbound or distant Jupiter-mass objects. It is noted that the objects have no host stars that can be detected within ten astronomical units through gravitational microlensing. Also, by comparing with constraints from direct imaging, it is suggested that most of these planetary-mass objects are not bound to any host star and may have formed in a protoplanetary disk and have subsequently been ejected from the system. The existence of these lone exoplanets lends support to planetary migration theories.

1.3.5 Pulsar Timing Variations

Pulsars are rapidly rotating neutron stars that emit EM radiation at highly regular intervals. In some cases this regularity can be compared with that of an atomic clock and given such a high precision in the pulses any irregularities are easily spotted. As a pulsar orbits around the barycentre of the system the pulses will undergo minute changes and by detecting and examining these irregularities it is possible to determine if the system contains an exoplanet. The first confirmed exoplanet was detected using this method by Wolszczan & Frail (1992) and there are currently 12 known exoplanets across 7 systems.

1.3.6 Transits

Examining the light curve of a star as an object transits across it will show a dip in the stellar flux due to the obstruction of light (Fig. 1.1). This light curve can inform

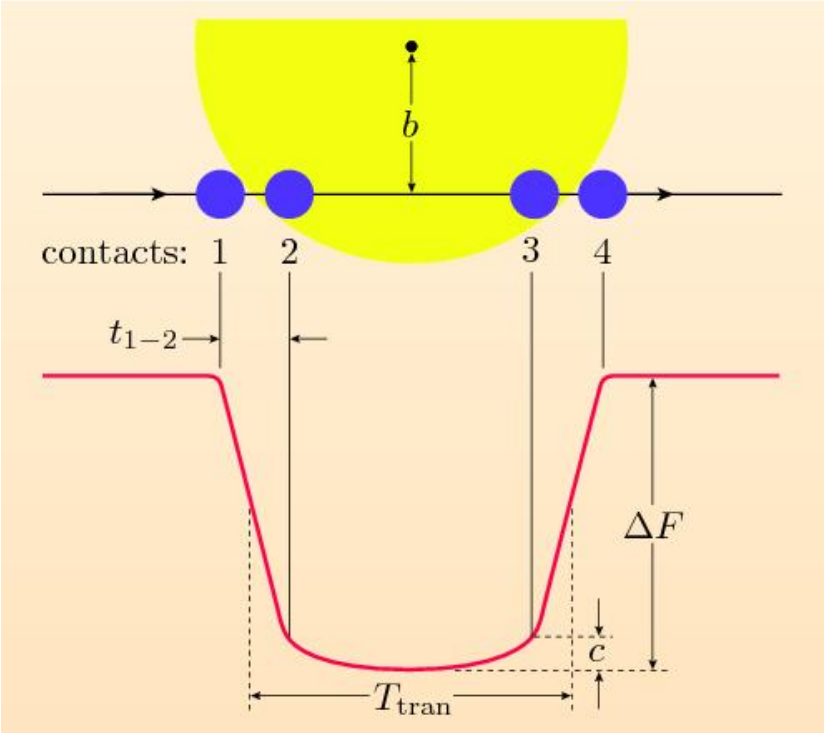

Figure 1.1: A transit light curve diagram. Contact 1 is when the limb of the planet's disk encounters the limb of the star's disk, 2 is when the planet's disk is just within the star's disk. Contact 3 is the last instant where the entire disk of the planet is within the disk of the star and contact 4 is when the planet's disk has completely left the disk of the star. t_{1-2} is the ingress duration and T_{tran} is the time between mid-ingress and mid-egress. b is the impact parameter, which indicates the distance from centre of the stellar disk to the planetary disk, and ΔF is the change in flux between out of transit level and mid-transit level. c is the curvature height which is due to stellar limb darkening. (Haswell 2010)

the observer about the size of the exoplanet through the transit depth as well as the orbital period from the time interval between transits. As an example, a Jupiter-sized exoplanet transiting across a Sun-like star gives a transit depth of $\sim$1% in the optical compared to $\sim 10^{-2}$% for an Earth-sized planet. The planetary radius is given by

$$\frac{\Delta F}{F} = \frac{R_P^2}{R_*^2} \tag{1.4}$$

where F and ΔF are the observed stellar flux and change in flux at mid-transit respectively while R_P and R_* are the respective radii of the planet and star. The equation describing the transit duration, T_{dur}, of an exoplanet is given by

$$T_{dur} = \frac{P}{\pi} \sin^{-1} \left(\frac{\sqrt{(R_* + R_P)^2 - a^2 \cos^2 i}}{a} \right) \tag{1.5}$$

where P is the orbital period, a is the orbital separation and i is the inclination.

The transit method is one of the most efficient methods for detecting exoplanets where a wide area of sky is surveyed simultaneously. However, it has a drawback in the form of astrophysical mimics. Astrophysical mimics produce dips in the observed flux of a star that mimic a planetary transit. This can occur under the following circumstances:

1. blended eclipsing binaries where a deeply eclipsing binary star is blended with a brighter star;

2. grazing eclipsing binaries where the nearer star in a binary system only just passes across the limb of the farther star;

3. transits of very small stars across very large stars, resulting in a transit depth comparable to that of an exoplanet.

Mimic 1 can be eliminated by using a higher spatial resolution instrument in order to separate the blended stars while mimic 2 can be removed with improved signal-to-noise photometry, as the exact shape of the transit lightcurve will differ from that of an exoplanet. Typically, an exoplanet transit lightcurve has a 'U' shape while a grazing eclipse has a 'V' shape. Mimic 3 requires follow up measurements using a different technique. The method used to differentiate between exoplanets and small stars (e.g. brown dwarfs) is to conduct dynamical measurements to estimate masses. This is typically done using the radial velocity technique. With these mimics in mind, a positive exoplanet-sized transit detection does not necessarily mean that the object is an exoplanet and remains a candidate until follow up observations are made.

1.4 Astronomical Transient Events

Astronomical transient events are phenomena that are ephemeral. The duration of such events vary depending on the type of event and the underlying physics. In some cases these transient events can last a few seconds while in others they can last months or years. This section covers a few examples of known types of astronomical transient events.

1.4.1 Supernovae

Supernovae (SNe) are currently divided into two separate types, type-I and type-II, each of which contains a subset of types. Observed SNe are classified into these two types and further subsets depending on their spectra and lightcurve features. One of the primary features that seperate type-I and II SNe is that type-II spectra contain H lines while type-I lack any H features. Further classfication details are described in Filippenko (1988); da Silva (1993); Pastorello (2012) and summarised below. Fig. 1.2 shows a selection of example light curves for various supernovae.

1.4.1.1 Type-I SNe

Type-I SNe are subdivided into Ia, Ib and Ic catagories. These catagories are defined by the observed spectra with type-Ia exhibiting Si II and S II lines with no presence of H and He I. Type-Ib spectra have strong He I lines while type-Ic contain Ca II and O I lines and a lack of H, He I and S II.

The exact mechanisms for a type-Ia SNe are still under debate but are widely accepted as being caused by white dwarfs accreting mass, such as from a binary companion. The white dwarf will accrete mass until the Chandrasekhar limit for a white dwarf is reached, $\sim$1.4 $M_{\odot}$ (Mazzali et al. 2007), the gravitational pressure then overpowers the competing electron degeneracy pressure and results in the inward collapse of the white dwarf. The increased pressure on the core of the star then results in run-away C and O fusion reactions which increase the temperature within the star. These high

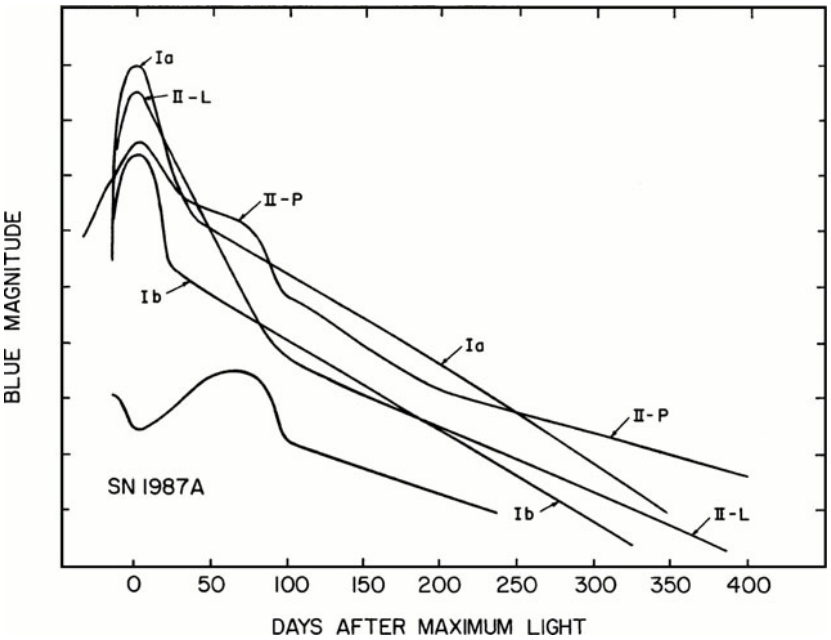

Figure 1.2: Example light curves in blue filter for Supernovae of Types Ia, Ib, II-L, II-P, and SN 1987A. The curve labeled Ib is an average which includes Type Ib and Type Ic. SNe 1979C and 1980K are used to create Type-IIL. Image taken from https://ned.ipac.caltech.edu/level5/March03/Filippenko/Filippenko2_2.html.

temperatures drive highly kinetic particles, increasing the internal pressure, and a thermonuclear explosion occurs. As the process for type-Ia SNe is typically the same it can be used as a standard candle to estimate distances and red shifts on cosmological scales as well as extinction along the line of sight due to dust. Carrol & Ostlie (2007, pg. 686) state that the absolute magnitudes in B (M_B) and V (M_V) bands at peak brightness are approximately the same (Eq. 1.6).

$$M_B \approx M_V \approx -19.3 \pm 0.03 \tag{1.6}$$

Unlike type-Ia SNe, type-Ib and Ic SNe occur due to the core collapse of massive stars. The mechanisms involved are expected to be similar to that of type-II SNe, although they occur from massive stars stripped of their hydrogen (both) and helium (Ic) shells and hence are rarer. Typically, the maximum absolute B magnitude of Ib and Ic are 1.0 to 1.5 magnitudes fainter than type-Ia.

1.4.1.2 Type-II SNe

Type II SNe occur due to the core collapse of massive stars (M > 8 $M_{\odot}$). These are mainly subdivided into IIP, IIL, IIn and IIb catagories although other minor categories also exist.

Following the initial luminosity rise and a short post-maximum decline, type-IIP SNe exhibit a long-duration phase of constant luminosity, known as the plateau. The plateau occurs due to the shock wave caused by the core-collapse depositing energy into the hydrogen envelopes. The hydrogen, ionised by the shock wave, then begins to cool and recombine resulting in a steady release of energy in the form of photons. In addition to this, internal radioactive decay can prolong the plateau by supplying extra energy to the outer envelopes.

On the other hand, Type-IIL exhibit a steady, almost linear, post-maximum decline rate. There is no plateau present and these transients occur less frequently than Type-IIP.

Type-IIn spectra show narrow H emission lines compared to other Type-II SNe. These lines are often superimposed on broader components. These features are best explained by the SN interacting with dense material surrounding the progenitor star. The narrow H emission lines arise from the ionised (due to the shock wave) circumstellar gas. The broader lines are produced by supernova ejecta. Typically, the photometric development of these SNe is slower than other types.

Likely due to tidal interaction with a companion star, the hydrogen atmosphere of the type-IIb progenitor is severely depleted. The weak H emission lines eventually become undetectable and interestingly, type-IIb define a transition between type-II and type-Ib SNe. The evolution of the photometric light curves is fast and very similar to other type-I SNe.

1.4.2 Cataclysmic Variables (Novae, Dwarf Novae)

In cataclysmic variables (CVs) a white dwarf accretes mass from a nearby low-mass binary companion through Roche lobe overflow. In the absence of a strong magnetic field an accretion disk is formed around the white dwarf which transports the material onto the white dwarf. CVs are primarily divided into novae and dwarf novae but other subdivisions also exist.

Novae, also known as classical novae, are characterised by a sudden increase in luminosity. As material rich in hydrogen is accreted onto the white dwarf, it forms a layer on the surface. With more material flowing onto the surface, the bottom of the layer increases in temperature and density. An outburst occurs when the conditions are right for thermonuclear burning of this hydrogen layer. The process is uncontrolled and the resulting luminosity rise typically increases by $\sim$10-12 magnitudes and occurs very rapidly over a matter of days. Subsequently, the luminosity decline rate in the visual wavelengths is relatively slow, taking weeks to months to drop by 2 magnitudes. Unlike the supernova process, the white dwarf will typically survive the outburst and some novae are known to repeat the process every few decades.

Like novae, dwarf novae also undergo luminosity outbursts, although the underlying mechanics are quite different. A typical dwarf nova will display a luminosity increase of between 2 and 6 magnitudes. The luminosity increase, however, is due to an increase in brightness of the accretion disk surrounding the white dwarf rather than coming from the white dwarf itself. This makes dwarf novae very important to the accretion disk community as they provide unique opportunities to study the accretion disk itself. Under nominal conditions, matter is transferred through the accretion disk at a slow rate. An outburst occurs when the mass transfer rate is suddenly increased, forcing more material through the accretion. The causes for this increase in mass transfer rate are still heavily debated but two possible scenarios are accretion disk instability or mass transfer instability from the companion star to the white dwarf. This process will typically re-occur every 30 to 300 days. An example lightcurve of SS Cygni, a

dwarf nova, is shown in Fig. 1.3.

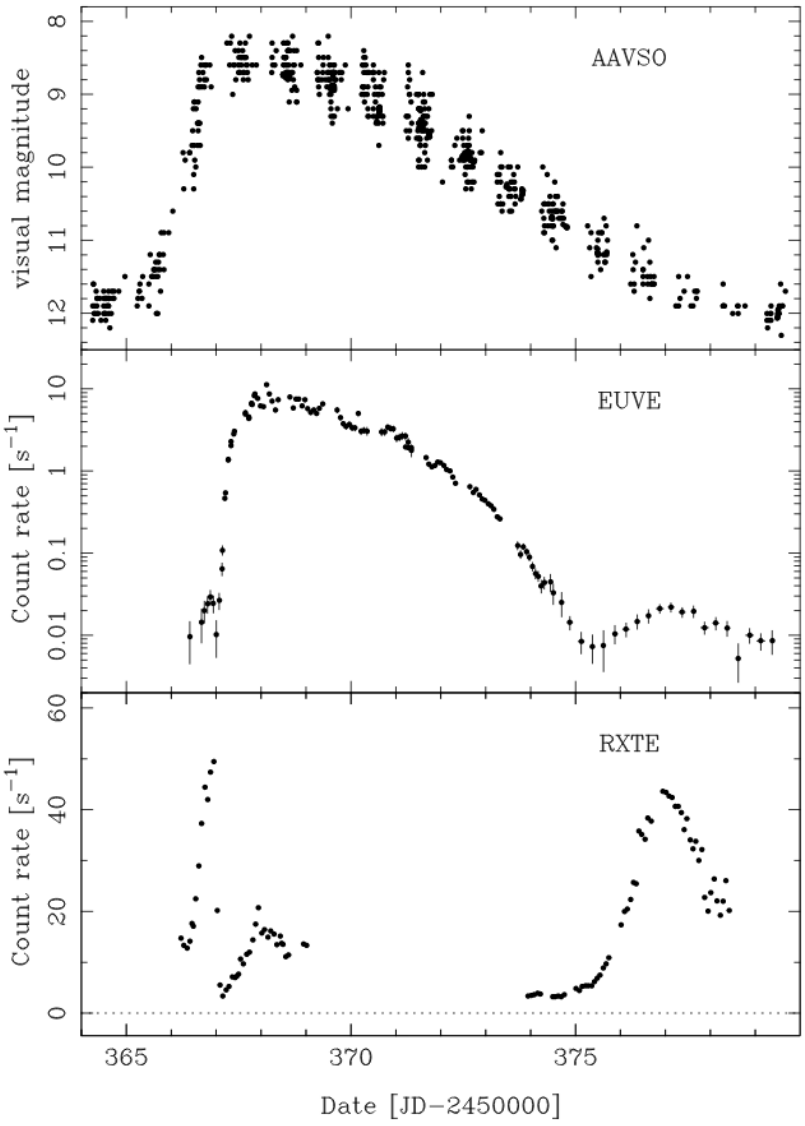

Figure 1.3: Example lightcurves of SS Cygni, a dwarf nova. The lightcurves are from three separate instruments (AAVSO, EUVE and RXTE. Image taken from Wheatley et al. (2003)

1.4.3 Tidal Disruption Events

The tidal shear forces from a supermassive black hole are capable of overpowering a star's self-gravity. If a star's orbit brings it into the tidal disruption radius of the black hole, the star will break apart. Some of the stellar mass will be accreted onto the black hole while the rest will be ejected. An accretion flare is formed from this tidal disruption event (TDE).

Emissions from a TDE are likely to be a combination of a photosphere forming in the debris and hot accretion disk emission. Depending on the angle to the line of sight, it is expected that the photosphere will dominate the early phases with the disk emission becoming more prominent at a later phase as the debris spreads out and becomes less opaque. The detection and study of TDEs provides a useful tool for studying supermassive black holes. Fig. 1.4 shows an example lightcurve for a TDE candidate.

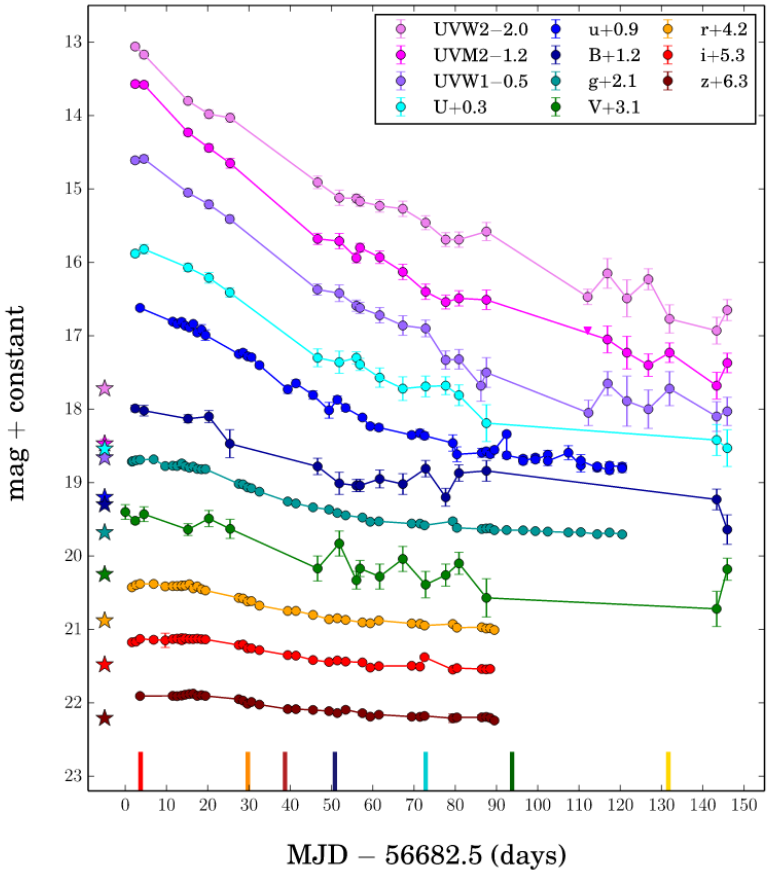

Figure 1.4: Example lightcurves of ASASSN-14ae, a TDE candidate. Image taken from Holoien et al. (2014)

1.4.4 Other Transient Events

Besides the transients mentioned above, other transient events also exist such as microlensing events and gamma ray bursts. Microlensing events follow the same principles as gravitational lensing, when a high mass object and a source object form a very

precise line of sight with the observer, light is bent around the massive object which acts as a lens. The "lens" in gravitational lensing is typically a galaxy or a galaxy cluster and the effect is strong enough as to be resolved by high resolution telescopes. Microlensing occurs on a much smaller scale with a "lens" such as a star or planet. This relatively low mass object produces a very weak effect and isn't resolvable. Evidence that a microlensing effect is occuring is by monitoring the source object's luminosity. A luminosity increase will occur as the "lens" object aligns with the observer's line of sight. Unlike the gravitational lensing events, which are known to last millions of years, microlensing events can occur over a matter of seconds to years. Fig. 1.5 is an example microlensing event for OGLE-2005-BLG-390Lb.

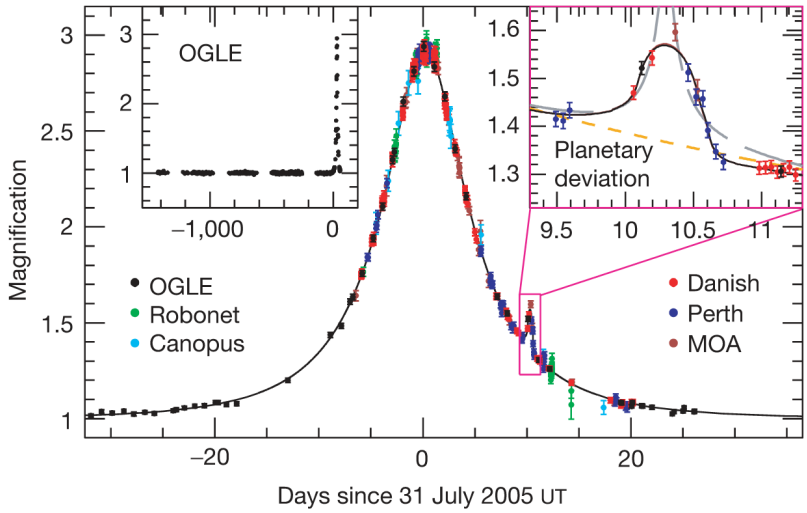

Figure 1.5: Example microlensing event with the upper right box showing a deviation, due a planetary body, at around 10 days after the peak of magnification. The upper left shows the relatively constant brightness prior to the lensing event. Image taken from Beaulieu et al. (2006)

Gamma ray bursts (GRBs), so called due to the sudden emission of gamma rays, are one of the most energetic events known to occur, easily comparable in energy release to SNe. The event durations typically range from several milliseconds to minutes and are commonly divided into two separate groups, short and long bursts. GRBs shorter than 2 seconds are classified as short bursts and are associated with neutron star mergers with either another neutron star or a black hole. The long burst classification is for any GRB over 2 seconds. Some of these bursts have been observed to occur at similar

times to core-collapse SNe, hinting at a highly probable link between the two. Fig. 1.6 is an example lightcurve of a GRB afterglow.

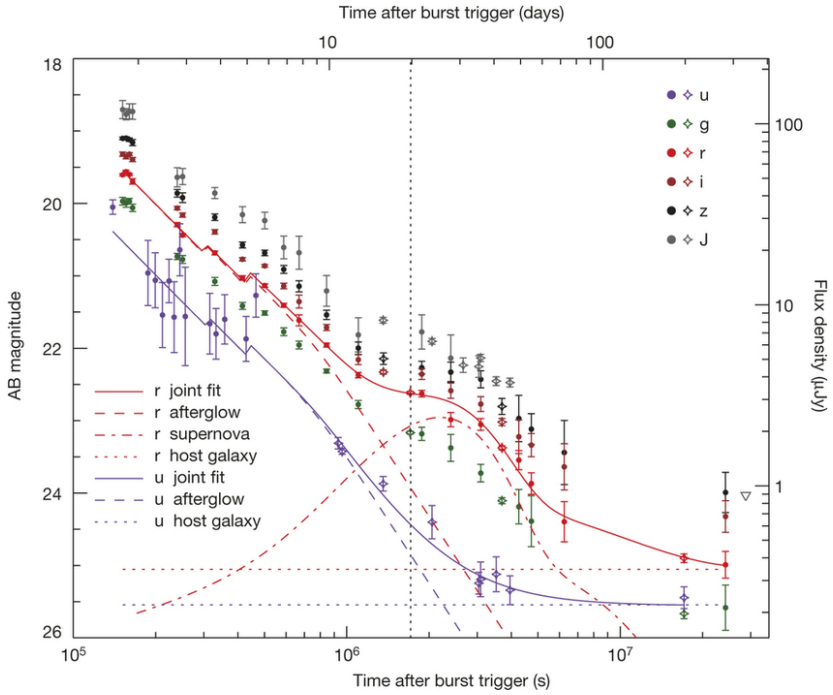

Figure 1.6: Example GRB afterglow lightcurve for GRB 111209A modelled by a broken power law (dashed red line). The associated supernova is SN 2011kl. Image taken from Greiner et al. (2015)

Chapter 2

Camera Characterisation

In order to obtain reliable photometric measurements it is important to understand the performance of the CCD camera in use. This section details the methods used to characterise PIRATE's primary science camera, the SBIG STX-16803. The investigation makes use of photon transfer curves to identify the gain and read noise. Additionally, the number of flats required to properly calibrate the resultant science frames is found and recommendations made based upon the results and practicality. The camera shutter is also examined and to ensure that the CCD is evenly illuminated. In order to clarify the role of the author in this chapter it is important to note that all the measurements and analysis were performed by the author.

2.1 PIRATE's Primary Camera - SBIG STX-16803

PIRATE's current primary imaging camera is manufactured by the Santa Barbara Instrument Group (SBIG[1]). The SBIG STX-16803 camera uses a Kodak KAF-16803 CCD which has a square 4096 by 4096 pixel array with 9 μm pixels and features an anti-blooming gate (SBIG specification sheet[2]). The anti-blooming gate allows saturated pixels to bleed in a controlled manner by siphoning off the excess charge rather than allowing electrons to spill over into neighbouring pixels and potentially interfer-

[1] http://www.sbig.com

[2] http://www.sbig.com/products/cameras/stx/stx-16803/

ing with the target (Howell 2011, pg. 19-20). The trade off for this feature is that a CCD with an anti-blooming gate has a reduced quantum efficiency as each pixel has a significant portion of its volume dedicated to this gate. The STX-16803 has a peak quantum efficiency of 60% at a wavelength of 550 nm (Fig. 2.1) as specified by the manufacturer. In contrast a typical CCD can achieve peak efficiencies of around 90% (Howell 2011, pg. 6).

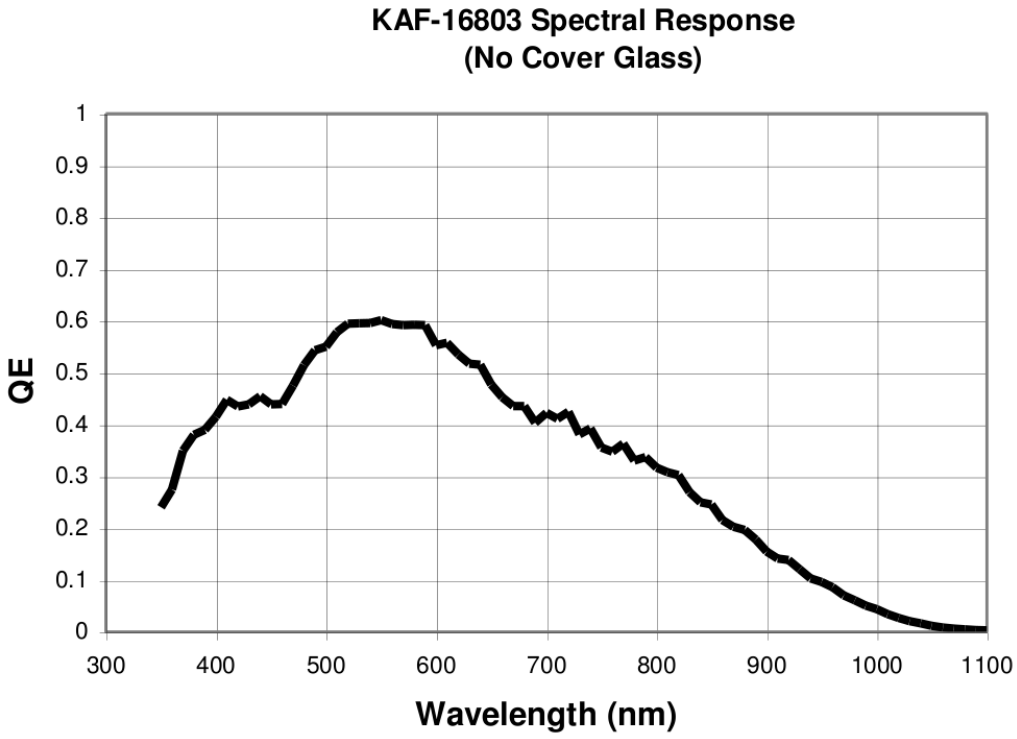

Figure 2.1: The Kodak KAF 16803 CCD quantum efficiency plot showing a peak quantum efficiency of 60% at 550 nm. *Source: Kodak KAF-16803 Image Sensor Device Performance Specification document*

The read noise of the CCD, which as the name implies is the noise associated with the transfer and digitisation of electrons, is specified (by the manufacturer) to be 9 electrons per pixel. The dark current at -20°C is 0.02 electrons per pixel per second with a doubling temperature of 6.3 K. The gain is 1.27 electrons per ADU.

2.2 Photon Transfer Curves

Photon Transfer Curves (PTCs) are a powerful tool for understanding the performance of CCD cameras. The following section describes the theory behind PTCs. The primary methodology and notation used in this chapter is taken from Janesick (2007) unless stated otherwise. A simple way to look at PTCs is using the following concept. Consider the camera as a black box that takes collected light and outputs it as digital data. The noise inherent to a non variable light source is shot noise, hence any additional noise in the digital data is due to the black box. The PTC compares the expected photon shot noise with the measured output.

The total noise measured is a combination of the read, shot and fixed pattern (FPN) noise. FPN is a noise source that arises from the fact that pixels on a CCD aren't exactly the same and have minute variations. These pixels may have slightly different sizes, quantum efficiencies, and other potential defects. This gives rise to noise that has a fixed pattern and can typically be reduced through the use of flat field frames. The total noise can hence be expressed as

$$\sigma_{total} = \left[\sigma_{read}^2 + \sigma_{shot}^2 + \sigma_{fpn}^2\right]^{0.5} \tag{2.1}$$

where σ_{total} is the total noise, while σ_{read}, σ_{shot} and σ_{fpn} are the read, shot and FPN noise respectively. The shot noise, σ_{shot}, is given by

$$\sigma_{shot} = \left[\frac{S}{K_{adc}}\right]^{0.5} \tag{2.2}$$

where S is the signal in ADU and K_{adc} is the gain. Likewise the FPN, σ_{fpn}, is given by

$$\sigma_{fpn} = P_n S \tag{2.3}$$

where P_n is the FPN quality factor calculated by the ratio of the rms noise of a uniform light source to the mean signal, S. P_n is typically expected to be a minimum of $\sim$1%

for CCD sensors (Janesick 2007, pg. 30). Substituting these back into Eq. 2.1 gives

$$\sigma_{total} = \left[\sigma_{read}^2 + \frac{S}{K_{adc}} + (P_n S)^2\right]^{0.5} \tag{2.4}$$

2.3 Method & Results

This section employs the PTC theory and describes the considerations required for the application to the STX-16803.

2.3.1 Setup

As PIRATE is located in Mallorca and operated remotely, there are practical limitations as to what equipment can be used to accomplish the task of characterising the CCD. In order to generate the flat field frames of the data, the in dome lights were switched on and the mount pointed at a dome surface which had a near-uniform surface brightness. Ideally, the surface would be flat and evenly illuminated, although in this case the surface brightness was variable. The surface brightness variability was mimimised by an initial visual inspection using two high resolution web cameras located within the dome, and was later confirmed through the use of contour plots on sample light frames.

2.3.2 CCD Overscan

Prior to generating the PTCs it is necessary to remove the pedestal level, also known as a bias offset, of the CCD. This offset represents the output from the CCD when there are no signal sources. This could be accomplished by calibrating the data frames by taking a series of bias and/or minimum exposure dark frames. However, this is not ideal, as dark current may be present as well as light leaks. Additionally, the bias offset can vary from frame to frame.

Typically, the extended horizontal register on the CCD is used to determine the offset. This has the advantage of providing an accurate value for the bias offset on a

frame by frame basis. As an added bonus the read noise can be measured from the overscan by determining the standard deviation in this region.

Physically the SBIG STX-16803 has several shielded rows and columns of pixels beyond the 4096^2 photoactive pixel region. The SBIG driver has the option to readout this region, but is disabled by default. The overscan can be set from a range of 0 (i.e. Off) to 200 using 'Configure Driver' within the SBIGDriverChecker. The SBIG STX is only capable of 128 overscan lines and columns and is made up of a mixture of active and dummy pixels[3]. The dummy pixels are generated by overclocking the CCD, i.e. reading out the same shielded pixels repeatedly.

Examining the lines and columns along a flat frame shows the overscan region for the STX-16803. Figs. 2.2 & 2.3 shows the output from an example Baader R filter flat frame taken with the 128 pixel overscan region enabled. The left and right columns show line 2176 and column 2176 respectively, which cross at the centre of the photoactive region. The middle panels show that within the 128 pixel overscan region there is a sharp peak. This peak increases relative to the collected photons in the image (ie. a longer exposure duration results in an increased peak) and occurs along line 118 and column 120. It is attributed to an unusable photoactive column and line on the CCD as demonstrated by Fig. 2.4. The key point to highlight in Fig. 2.4 is that any pixels which are white are photoactive. The photoactive pixels surrounding the primary 4096x4096 photoactive region are a photoactive buffer, and the remaining line/column pixels are test rows. Interestingly the test pixels for line 118 match up as being the 11th pixel away from the imaging border, while the measured column peak is along the 9th pixel. This could simply be a fault with the manufacturing process but may also highlight another unknown effect occurring within the CCD. Additionally, adjacent pixels to these 'peak' pixels also exhibit higher values. Bearing this in mind it is important to determine a usable overscan which isn't influenced by this photoactive test region. As a safety point the overscan is arbitrarily selected as being a few pixels away from the 'peak' pixels. Pixel 1 through to 110 works for both overscan sections

[3]Private communication with David Morrow - SBIG technical support

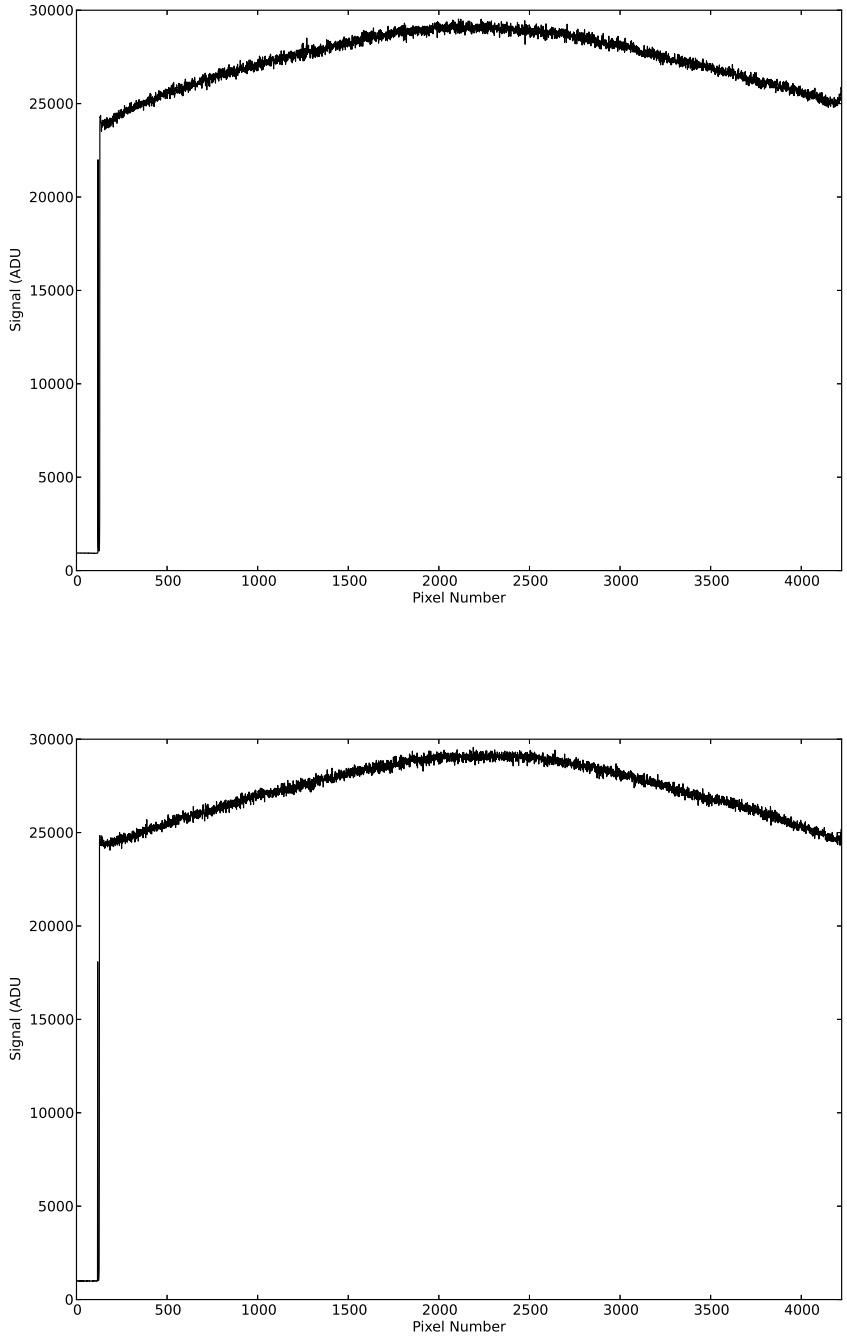

Figure 2.2: Inspection of line 2176 (Top) and column 2176 (Bottom) showing an entire row of a dome flat using the SBIG STX-16803 with the 128 pixel overscan region enabled. The y-axis provides the counts in ADU and the x-axis has the respective column and line pixel number.

and gives a comparable mean in pixels 1 through to 50 for the respective regions.

Fig. 2.5 shows a comparison between differently calibrated bias frames. The mean

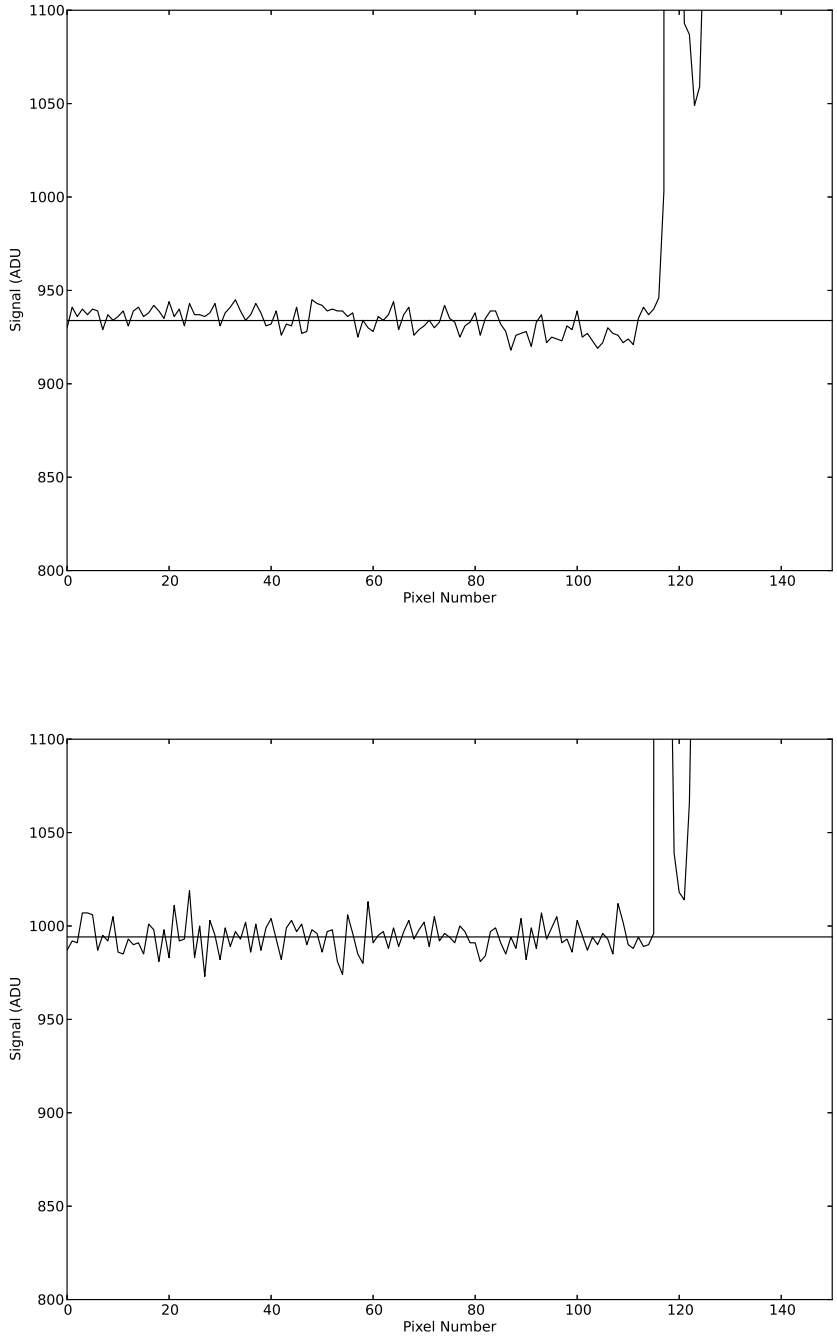

Figure 2.3: Closer inspection of Fig. 2.2 looking at the low count overscan region for line 2176 (Top) and column 2176 (Bottom). Once again, the y-axis provides the counts in ADU and the x-axis has the respective column and line pixel number. Pixels 1 through to 128 are in excess to the photoactive part of the CCD.

ADU values of the 4096^2 photoactive area are 987.2, 3.3, 49.9 and -6.3 respectively for uncalibrated, master bias, line overscan and column overscan corrected bias frames.

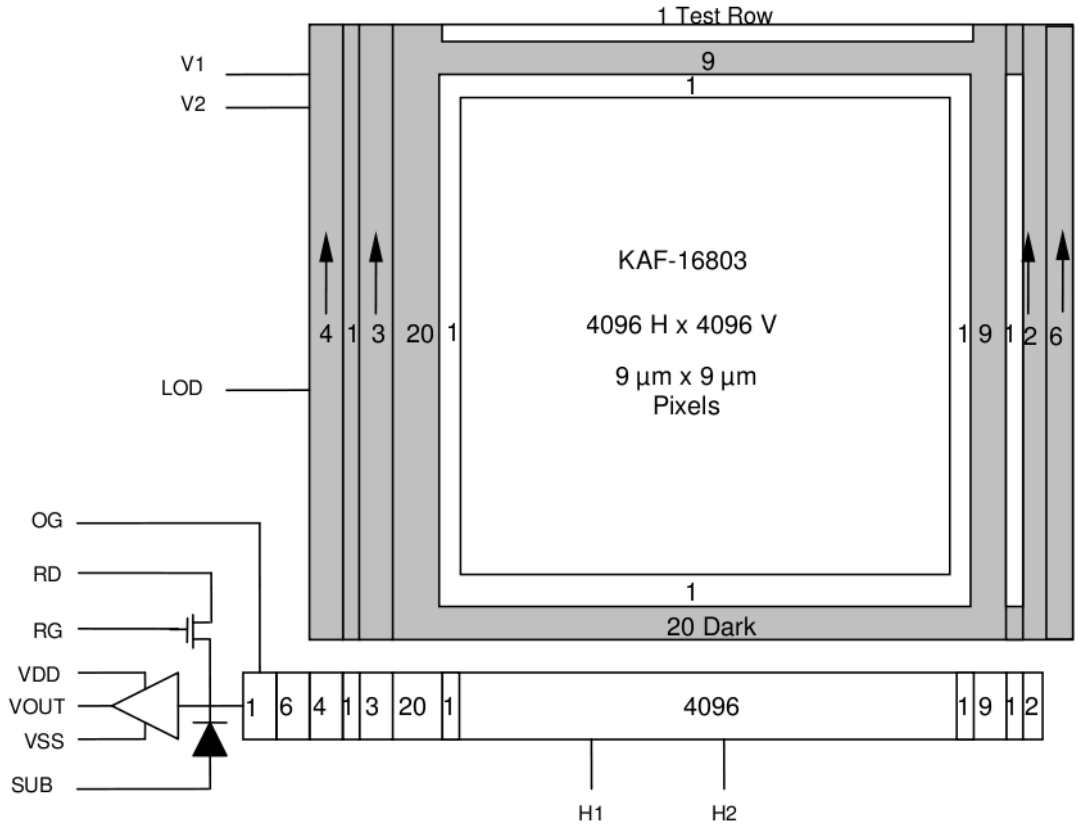

Figure 2.4: KAF-16803 architecture. *Source: Kodak KAF-16803 Image Sensor Device Performance Specification document*

These mean values have a standard deviation of 15.1 ADU for uncalibrated and overscan corrected images, but 12.4 ADU for the master bias corrected version. As the overscan corrected image is a simple subtraction of constant value, the standard deviation is expected to be the same in the uncalibrated and overscan corrected images as the features remain the same. As expected, the master bias calibrated image impacts the noise in the image; additionally, it also corrects for large scale two dimensional patterns. The PTCs examined later require a simple offset subtraction which doesn't effect the noise in the image. As mentioned previously the overscan is a representation of the actual offset within each frame. The mean column overscan corrected bias frame (-6.3 ADU) is at a similar offset correction to the mean from the master bias corrected frame (3.3 ADU) making it the most suitable selection for PTC curves.

Although it hasn't been tested, it would be interesting to see how the PTCs would be affected by the removal of the notable curve seen in the bias frames in Fig. 2.5. This

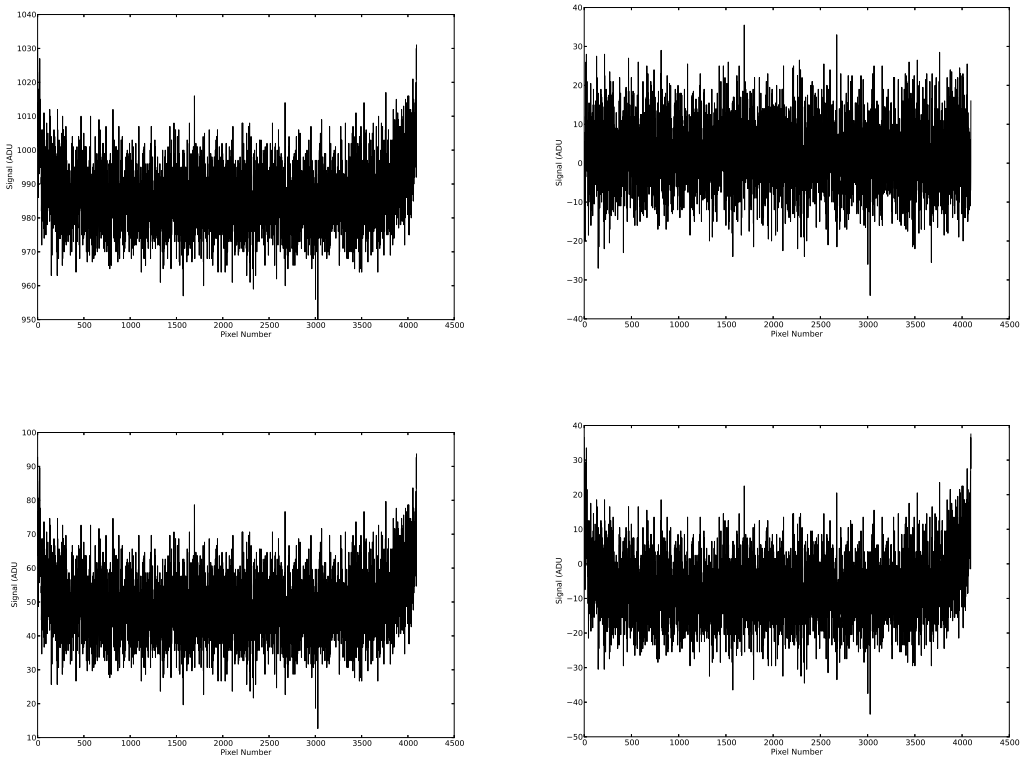

Figure 2.5: Plots of a bias frame column. Upper left is the uncalibrated bias frame, upper right is a bias frame with a master bias frame consisting of 50 bias frames subtracted. Lower left and right images show the bias frames after respective mean line and column overscan subtraction.

shape could potentially be removed by taking the mean overscan value and scaling the bias frame features by the value. If this feature is removed, it can potentially push down the noise within the PTCs themselves, improving the accuracy of the results.

2.3.3 Standard Photon Transfer Curve

Several series of light frames were taken using the method described in Section 2.3.1 at a CCD temperature of -20°C. These light frames have exposure intervals ranging from a minimum of 0.1s up to saturation exposures for on chip binnings of 1x1, 2x2 and 3x3, hereafter referred to as binnings 1, 2 and 3 respectively. In this experiment six series were collected for binnings 1, 2 and 3. The images are overscan corrected using the column section, as determined in Section 2.3.2, and trimmed using the Image

Reduction and Analysis Facility[4] (IRAF is a general purpose software system for the reduction and analysis of astronomical data) down to 31^2, 17^2 and 11^2 pixels around the centre of the light collecting area (i.e. ignoring the overscan regions) of the CCD for binnings 1, 2 and 3 respectively. The overscan correction is applied in order to remove the pedestal counts from the data leaving a corrected signal. The mean corrected signal, S, and standard deviation, σ_{total}, of each trimmed image section is then found using IRAF's imstat command.

The difference between two frames with the same exposure and hence similar counts is taken, effectively removing the FPN from the total noise. The noise in the difference image is given by

$$\sigma_{shot+read} = \frac{\sigma_\Delta}{2^{0.5}} = \left[\sigma_{total}^2 - \sigma_{fpn}^2\right]^{0.5} \tag{2.5}$$

where σ_Δ is the standard deviation of the difference image. The FPN is

$$\sigma_{fpn} = \left[\sigma_{total}^2 - \sigma_{shot+read}^2\right]^{0.5} \tag{2.6}$$

Plotting the total noise on a logarithmic scale of noise vs signal in ADU (blue line in Fig. 2.6) and extrapolating back to a signal of 0 ADU gives the read noise (yellow line) for the CCD. With both the FPN and read noise in hand it is now possible to calculate the shot noise from Eq. 2.1. The shot noise can then be used to determine the CCD gain, K_{adc}. The gain is measured from the plot by extrapolating the shot noise best fit (red line) to $\sigma_{shot} = 1$. Similarly, the intercept along the signal axis for FPN (green line) is equal to P_n^{-1}.

It is apparent that the signal from exposures of the same time duration has increased in Fig. 2.6. This is verified by plotting a signal vs exposure time plot (Fig. 2.7) which also shows the region over which the CCD behaves linearly.

The data set collection was repeated in a four series set and another linearity plot was generated (Fig. 2.8). These were collected by grouping exposure intervals, starting

[4]http://iraf.noao.edu/

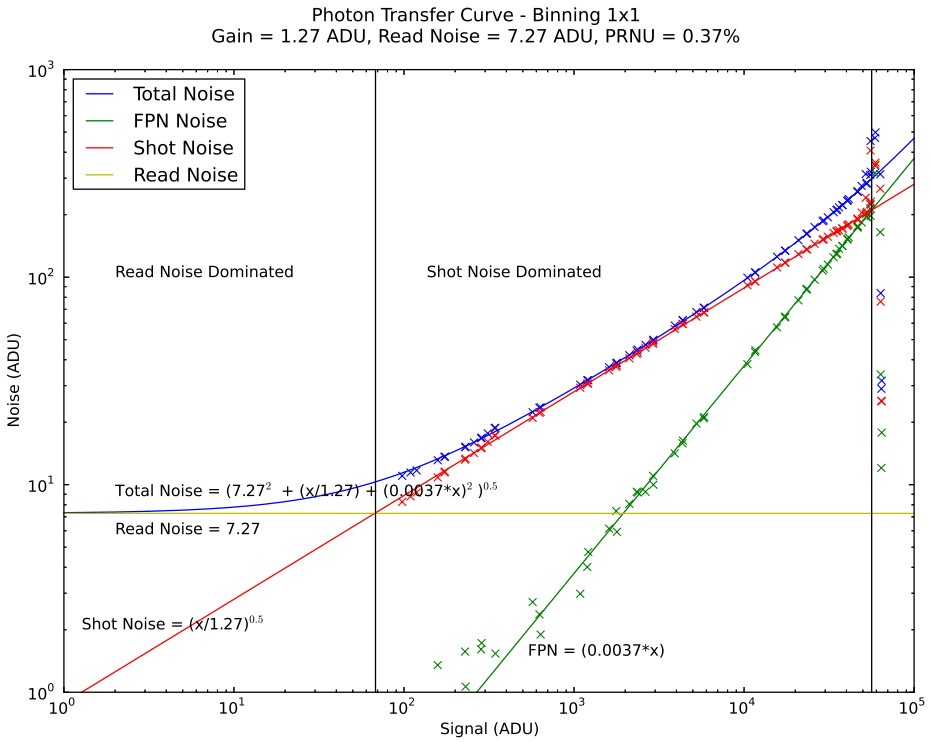

Figure 2.6: Photon transfer curve (PTC) of the SBIG STX-16803 at 1x1 pixel binning. The blue, green, red and yellow lines represent the total, fixed pattern, shot and read noise respectively. The vertical black line at the read and shot noise intersection denotes the region where the noise switches from read noise dominated to shot noise dominated. Similarly, the intersection between the shot and the fixed pattern noise (FPN) indicates the region where FPN begins to dominate.

at the short intervals, rather than completing a series at a time. This confirms that this method generates a stable signal across the exposure intervals up to saturation where at 220s the separation effect can be seen to occur once again. New PTCs for binning 1 data, as well as binnings 2 and 3, were generated using this data collection method and are shown in Figs. 2.9, 2.10, & 2.11 respectively. These PTCs provide the gain, read noise and fixed pattern noise (or Photo Response Non-Uniformity, PRNU). For binnings 1, 2 and 3 respectively, the gain is 1.25 ± 0.01, 1.26 ± 0.01 and 1.28 ± 0.01 e^-/ADU, the read noise is 9.17 ± 0.12, 15.85 ± 0.61 and 21.76 ± 0.96 ADU, and the PRNU is 0.34 ± 0.02, 0.15 ± 0.01 and 0.14 ± 0.01 %. The read noise can be converted into electron units by multiplying it by the appropriate gain values giving 11.46 ± 0.15, 19.97 ± 0.78 and 27.85 ± 1.25 e^-.

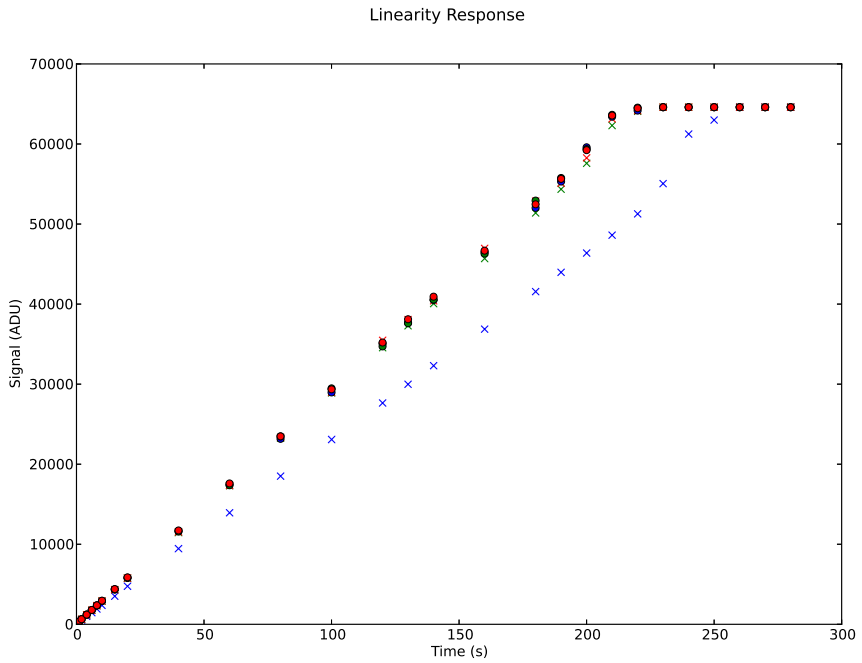

Figure 2.7: Linearity response curve for SBIG STX-16803. Note that blue crosses are the first series going up to saturation, after saturation, counts in subsequent series are elevated.

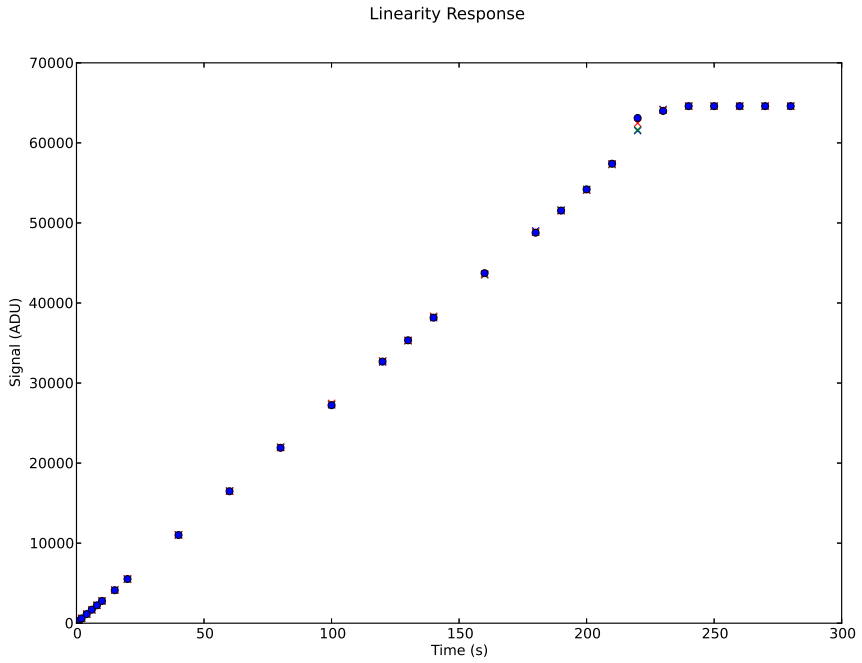

Figure 2.8: Similar to Fig. 2.7, data collection was repeated with four series. These were collected by grouping exposure intervals rather than completing a series at a time, negating the effects of saturation on the shorter exposure times as seen in the previous figure.

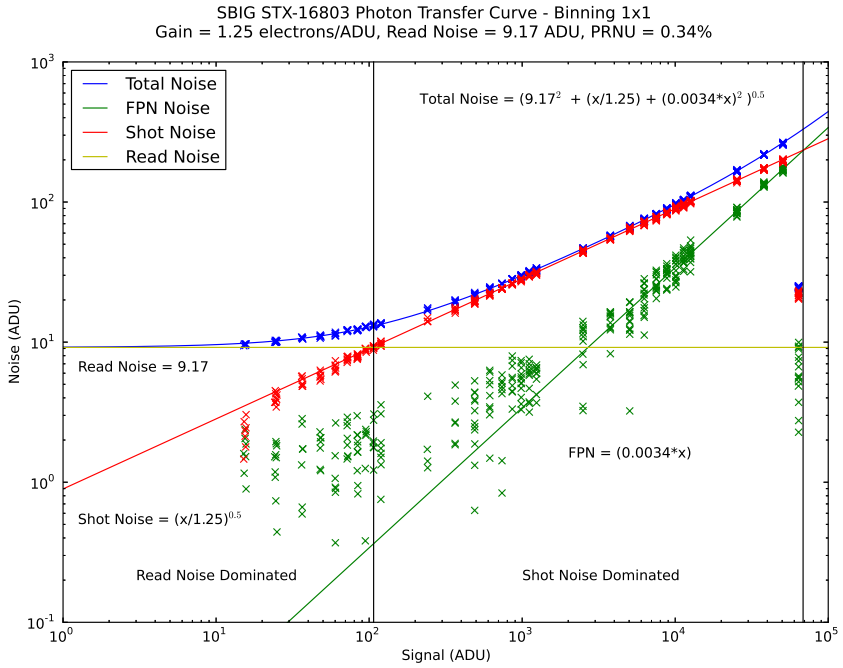

Figure 2.9: Similar to Fig. 2.6, using the data collection method described in Fig. 2.8

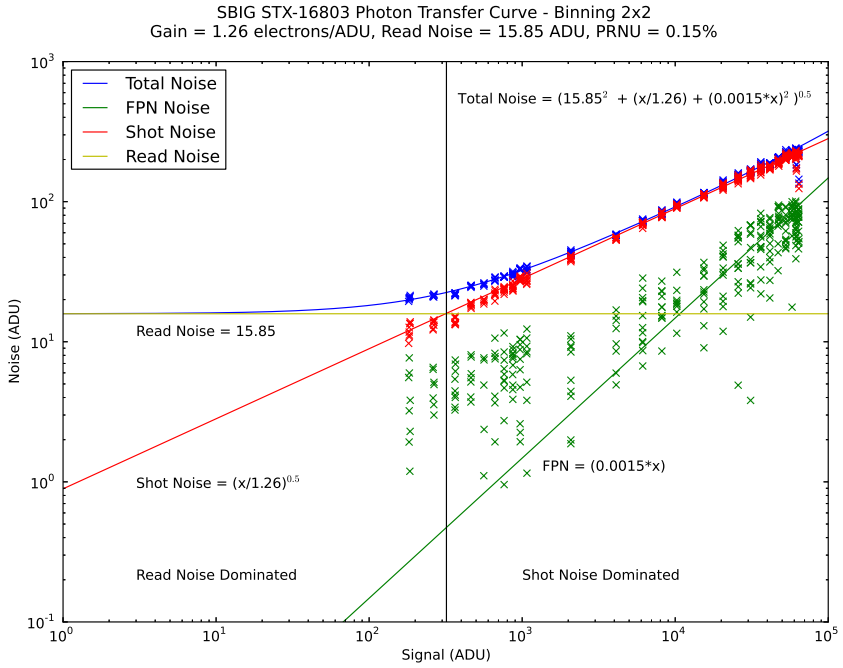

Figure 2.10: Similar to Fig. 2.9 but for binning 2x2, using the data collection method described in Fig. 2.8

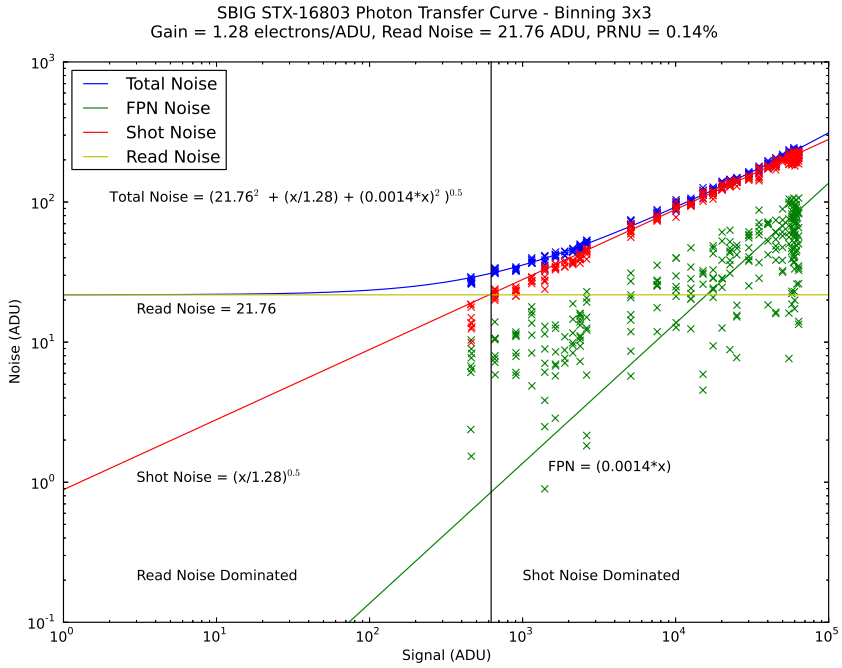

Figure 2.11: Similar to Fig. 2.9 but for binning 3x3, using the data collection method described in Fig. 2.8

2.3.3.1 PTC Errors

Inaccuracies in generating and processing the data, such as when removing the pedestal offset can be explored through the plots of gain, K_{adc}, shot noise, σ_{shot}, and the combined read shot noise, $\sigma_{shot+read}$, vs signal, S (Figs. 2.12, 2.13, 2.14). These binning 1 plots show that there is a deviation from the lines of best fit at low signal in all three plots, with Fig. 2.14 being a very subtle deviation in noise of $\sim$ -1 ADU at the lowest signal counts. Generating the same plots for binnings 2 and 3 show similar deviations.

2.3.3.2 Flat Correction

In addition to determining the characteristics of the CCD another powerful feature of generating photon transfer curves is that an ideal number of flat field calibration frames can be determined. This is achieved by flat field correcting the PTC data frames which results in a reduction in the fixed pattern noise. In a best case scenario the flat field correction will reduce the total noise to a shot noise limited state.

50 dome flat frames were collected and calibrated using a 50 frame master bias

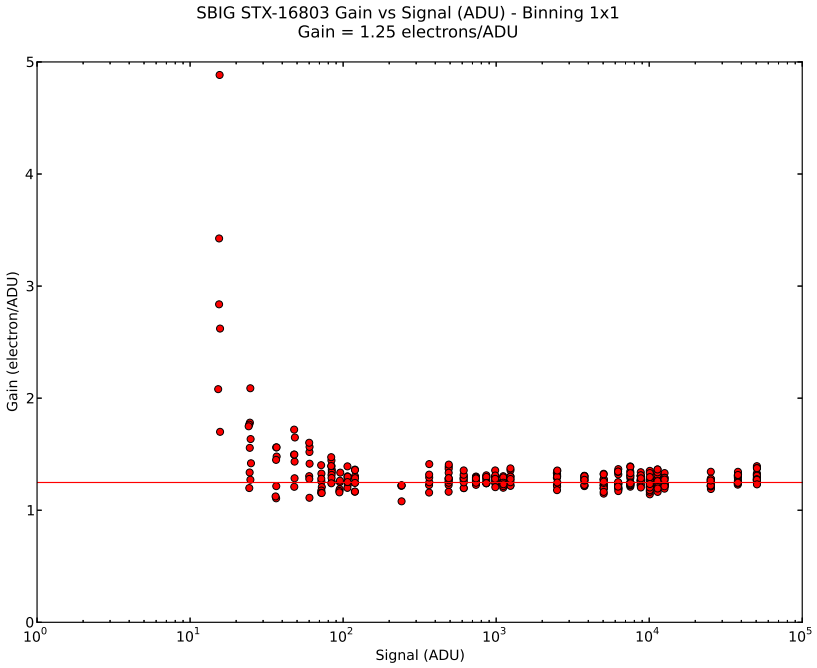

Figure 2.12: STX-16803 gain vs signal for binning 1x1 based on the data from Fig. 2.9 showing a gain offset for the lowest signal measurements. The gain points for saturated signal have been omitted.

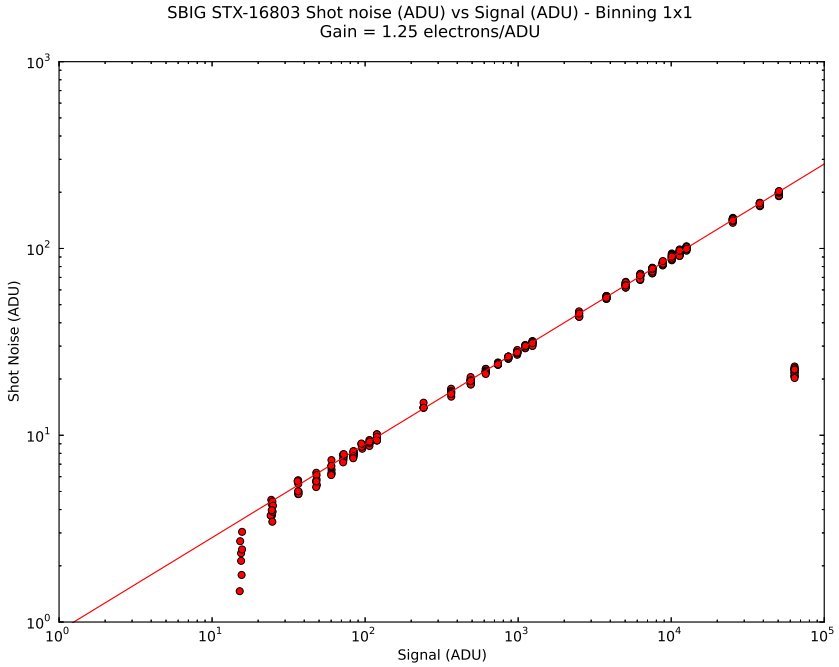

Figure 2.13: STX-16803 shot noise vs signal for binning 1x1 based on the data from Fig. 2.9 showing a noise offset from the line of best fit at the lowest signal measurements. The outliers at the highest signal are due to the saturated signal.

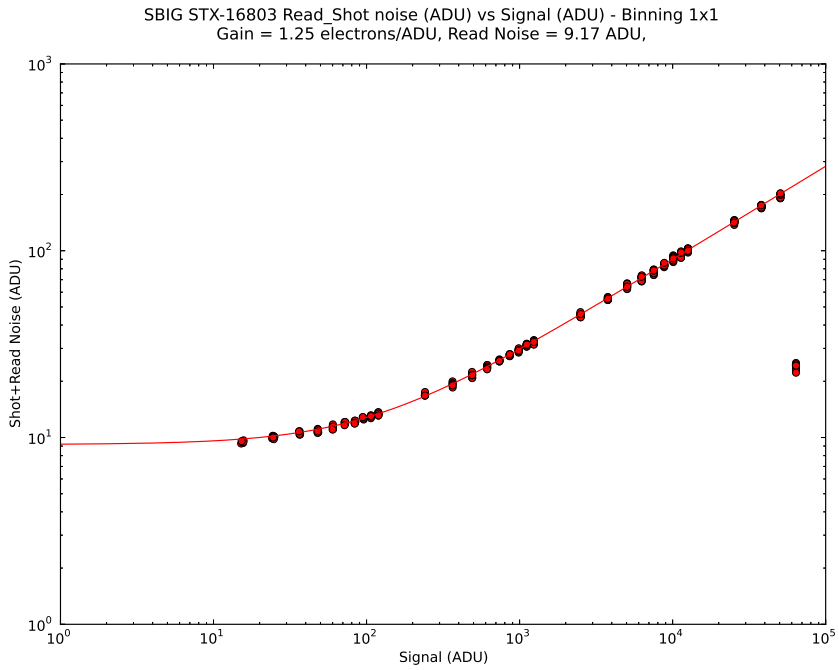

Figure 2.14: STX-16803 shot+read noise vs signal for binning 1x1 based on the data from Fig. 2.9 showing a noise slight offset from the line of best fit at the lowest signal measurements. The outliers at the highest signal are due to the saturated signal.

and master dark. The corrected flats are then combined into several master flat frames containing 5, 10, 15, 25 and 50 flats. The master flats have mean counts of 31000 ADU equating to a total of 193750, 387500, 581250, 968750 and 1937500 electrons in each master flat respectively. The data frames are then calibrated using the master flat calibration frames and the reduction to the total noise can be seen in Fig. 2.15. Closer examination of the higher signal, and hence higher FPN contribution in Fig. 2.16 shows that increasing the number of individual flats in the master frame improves the correction. The results are discussed in detail in Sec. 2.5.3.

2.4 Shutter Lag

The SBIG STX-16803 is advertised as having a mechanical, evenly illuminated shutter. A mechanical shutter typically works by covering and uncovering the aperture using a screen. Ideally the CCD surface should be uniformly exposed for the complete exposure duration. The real world performance is compared with the ideal using the

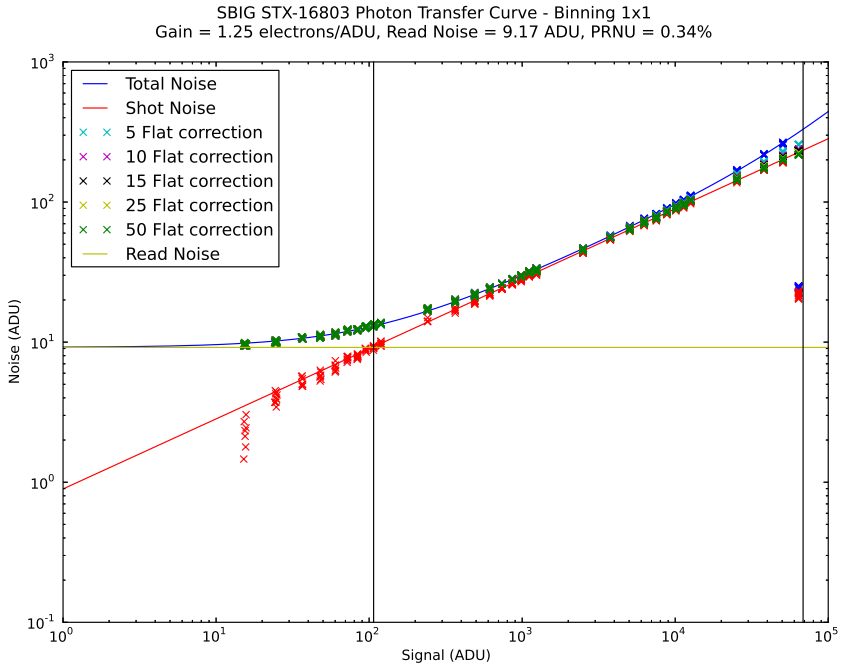

Figure 2.15: Fig. 2.9 with flat correction applied, showing a decrease in total noise with increasing master flat size.

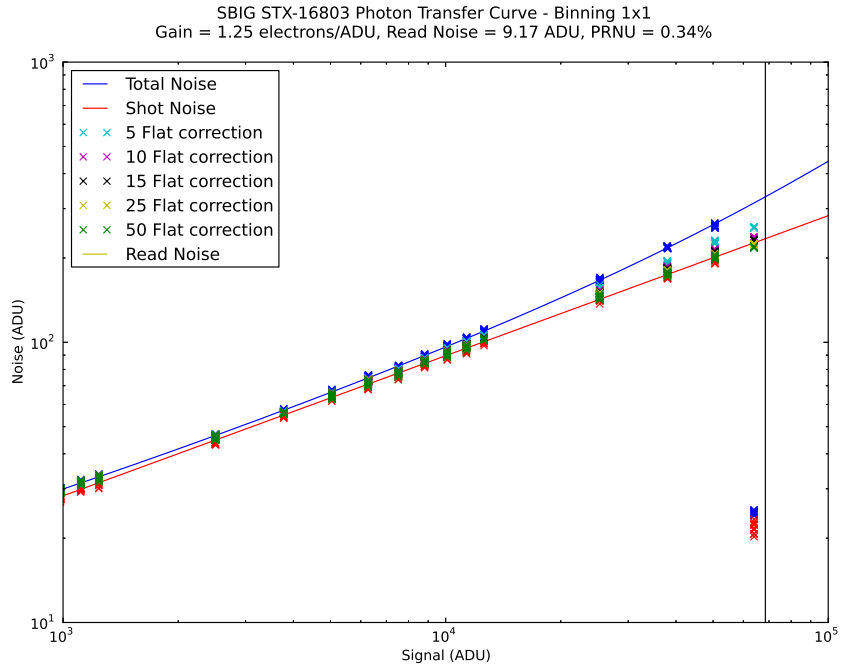

Figure 2.16: Fig. 2.15 PTC zoomed into the higher signal area.

method described by Zissell (2000).

The first step to determine if a shutter correction map is required is to examine the linearity plot of a series of short exposures. This is best accomplished by taking

several series of flats with an unchanging light source. For this test the PIRATE dome was illuminated with the in-dome lights. The lights were allowed to warm up for approximately 20 minutes and then alternating long and short exposures taken in order to minimise the effects of minute changes in the lights. The dome flats were bias corrected using a total of 50 bias frames. Frames of the same exposures are average combined together using IRAF's 'imcombine' function.

Several areas on the CCD are sampled with a 50^2 pixel box. The photon counts are then plotted against the exposure time (Fig. 2.17). The exposure duration offset can now be determined graphically by plotting a linear fit through the points back to the x axis intersection. In an ideal scenario this will intersect at 0. However, for the STX-16803 it is found that exposures are longer than expected.

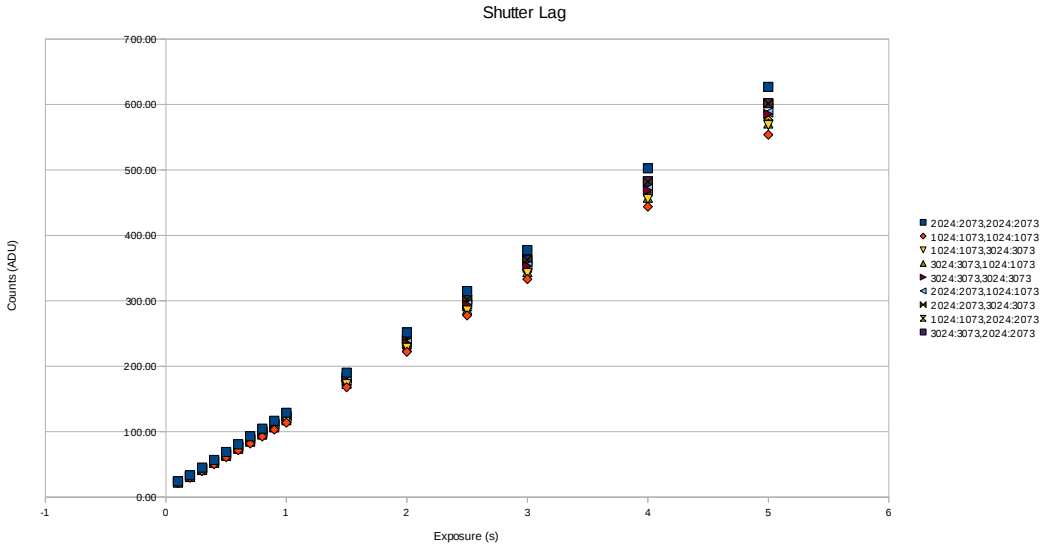

Figure 2.17: This plot shows the exposure and count data from Table 2.1. Fitting these points with a line of best fit and determining the x-axis intersect provides a shutter lag value for the various sections of the CCD.

The values show that the shutter lag is fairly uniform across the STX CCD with an average of -0.060 $\pm$ 0.002s. This translates to a counts value of 6.87 $\pm$ 0.03 ADU for this data set under these particular lighting conditions (dome lights). The uniformity

Table 2.1: Table showing shutter lag results for various sections on the SBIG STX 16803 camera. This shows a roughly uniform exposure across the CCD with an average lag of -0.0595 $\pm$ 0.0023s

Area	2024 : 2073, 2024 : 2073	1024 : 1073, 1024 : 1073	1024 : 1073, 3024 : 3073	3024 : 3073, 1024 : 1073	3024 : 3073, 3024 : 3073	2024 : 2073, 1024 : 1073	2024 : 2073, 3024 : 3073	1024 : 1073, 2024 : 2073	3024 : 3073, 2024 : 2073
Exposure (s)	Counts (ADU)								
0.1	24.40	21.43	22.60	22.27	23.21	22.80	23.86	22.64	23.28
0.2	33.47	29.76	31.15	30.84	31.95	31.48	33.07	31.32	32.30
0.3	45.18	39.97	41.49	41.48	42.79	42.51	43.90	42.13	43.65
0.4	56.95	50.38	52.12	52.19	53.89	53.55	55.01	52.80	54.71
0.5	69.01	61.08	62.85	63.15	64.73	64.71	66.68	64.29	66.21
0.6	80.90	71.77	73.90	73.91	76.21	76.02	78.20	75.52	77.83
0.7	92.99	81.96	84.64	84.76	86.92	87.08	89.34	86.33	89.11
0.8	104.70	92.70	95.38	95.63	98.31	98.41	101.00	97.52	100.60
0.9	116.80	103.20	106.50	106.70	109.80	109.60	112.50	108.50	112.10
1	129.00	113.80	117.30	117.50	120.70	120.80	124.20	119.60	123.60
1.5	190.30	168.00	172.60	173.30	178.20	178.20	182.90	176.90	182.80
2	251.70	222.10	228.20	229.30	235.30	236.10	241.60	233.80	241.70
2.5	314.80	277.70	285.10	286.20	293.90	294.60	301.70	291.90	301.90
3	377.50	333.20	342.30	344.00	353.00	353.80	362.50	350.90	362.80
4	502.50	443.90	455.60	457.50	468.90	471.00	482.10	467.10	482.60
5	626.90	553.80	568.50	570.90	585.50	587.80	601.40	583.20	602.00
Shutter Lag	-0.0576	-0.0579	-0.0621	-0.0598	-0.0626	-0.0580	-0.0623	-0.0574	-0.0575

can be further confirmed by generating a shutter correction map, S_m, which is given by

$$S_m = \frac{S_{os}t_l - S_{ol}t_s}{S_{os} - S_{ol}} \tag{2.7}$$

where S_{os} and S_{ol} are the mean photon counts for flats of equal short and long exposure respectively, with bias and dark calibration. Similarly, t_s and t_l are the respective exposure times for the short and long flats. Applying this to 25 frames of both 0.1s and 5s exposures results in the evenly illuminated output seen in Fig. 2.18. The values for each pixel in S_m are now of unit time and taking a 3-sigma clipped mean of S_m gives a mean of -0.10 $\pm$ 0.02s. Eq. 2.8 describes how to apply the correction to any light frames.

$$S_c = \frac{S_o}{1 - \frac{S_m}{t_o}} \tag{2.8}$$

where S_c is the corrected image, S_o is the original image of exposure duration, t_o.

This exercise has proven that the shutter is evenly illuminated apart from one hot corner in the upper right of the CCD. PTCs aren't time dependent meaning that irrespective of the exposure time the plots aren't effected by shutter lag. Similarly, the implications for differential photometry are negligible as the CCD is confirmed to be evenly illuminated.

The hot corner is attributed to an issue between ACP (observatory control software), MaximDL (camera control software) and the SBIG STX-16803 driver which results in the CCD amplifier being active during exposures, resulting in it heating up and giving off infrared radiation or increasing thermally-induced electrons which the corner pixels pick up and measure. Enabling the 'Disable slew during image download' option in ACP's general preferences was found to reduce the hot corner effect although it is still minutely present. Additionally, during routine maintenance the shutter was found to be badly damaged. The damaged shutter shouldn't impact the PTC results (as stated previously, PTCs aren't time dependent) as long as there was even

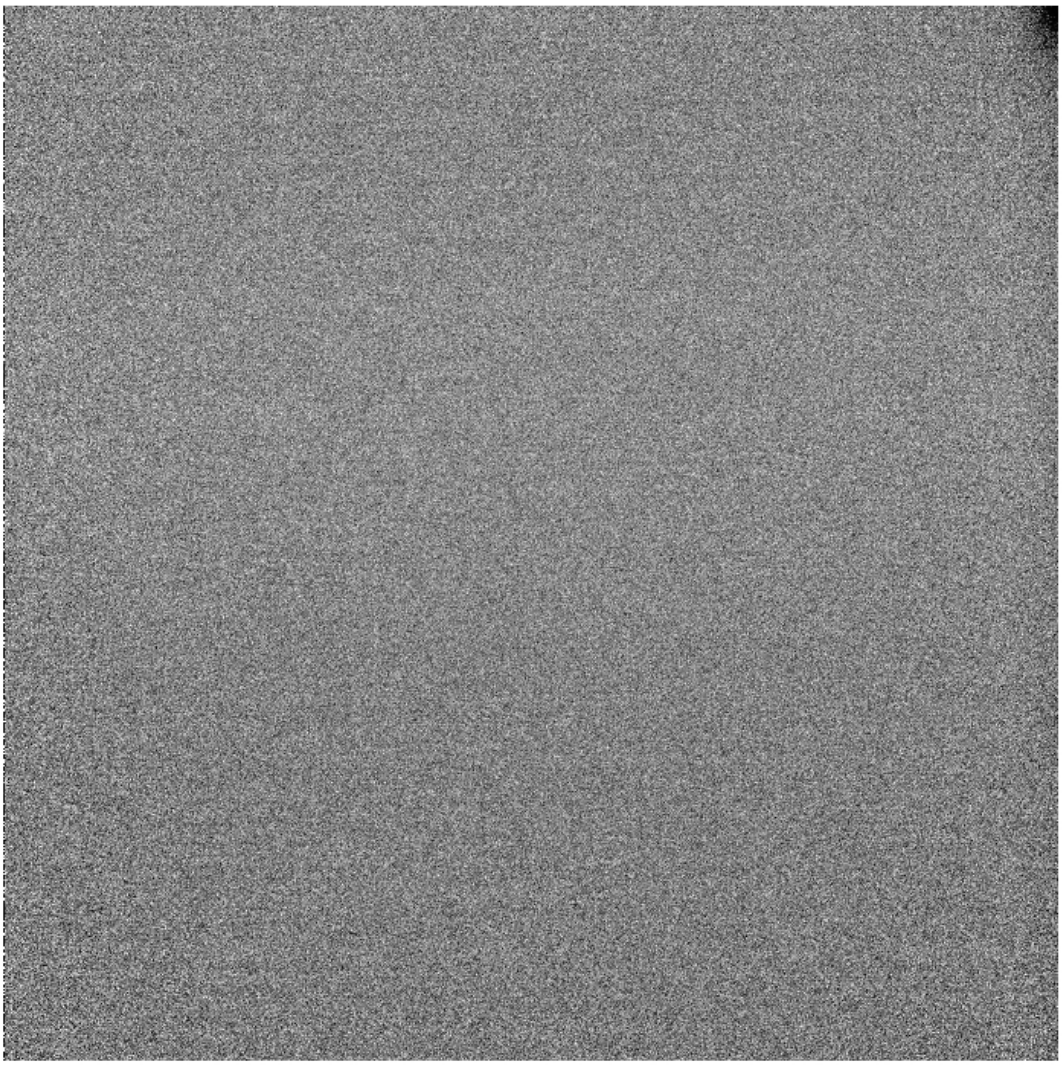

Figure 2.18: The shutter map produced using 25 calibrated frames of both 0.1 and 5s exposures. Note that the image appears fairly uniform except for the hot corner in the upper right corner. The hot corner is black due to the fact that it is variable in intensity and appears in the dark and bias calibration frames, this resulted in an over compensation of the hot corner.

illumination of the measured CCD pixels. However, it could influence the shutter lag measurements. At the time of writing, the shutter has been repaired but the CCD is yet to be re-mounted on PIRATE for additional testing.

2.5 Discussion

2.5.1 STX-16803 Gain and Read Noise

As stated previously, the SBIG STX-16803 CCD has an advertised gain and read noise of 1.27 e^-/ADU and 9 e^- respectively. The generation and analysis of the photon transfer curve provides a respective gain and read noise at binning 1 of 1.25 $\pm$ 0.01 e^-/ADU and 11.46 $\pm$ 0.15 e^-. In addition to this, PTC's for binning 2 and 3 were also generated giving respective gain and read noise values of 1.26 $\pm$ 0.01, 1.28 $\pm$ 0.01 e^-/ADU and 19.97 $\pm$ 0.78 and 27.85 $\pm$ 1.25 e^-. The specified gain value is a close match to the measured gain varying by at most 1.6% in binning 1. Conversely, the read noise in binning 1 has a specification difference of 27.3%. The read noise difference is either a designed feature or could potentially be due to the aging of the apparatus.

An unusual feature is the fact that the read noise increases with binning. It is expected that with on-chip binning the read noise will remain roughly constant (Howell 2011, pg. 50). Taking binning 2 as an example, the charges from four pixels are co-added and then converted into a single super pixel by the analog-to-digital (A/D) converter. The final conversion to a digital number is the main source of read noise (Janesick 2001, pg. 101) so this method effectively increases the signal-to-noise ratio as compared to binning 1 where each pixel read out will have its own read noise source. In order to confirm if the binned read noises are real, the standard deviation of the overscan can be taken and the results compared. Taking an average of the overscan from the first series for binnings 1, 2 and 3 gives read noises of 11.35 $\pm$ 0.15, 19.49 $\pm$ 0.47 and 27.82 $\pm$ 1.18 e^- respectively. There is less than an electron of difference between these values and the ones previously determined. These differences are well within the errors confirming that these values are real.

While the read noise does increase with binning it is noted that there is still a reduction of read noise across all the binned pixels. There is roughly a doubling and tripling of read noise in binnings 2 and 3 respectively suggesting that the A/D converter has been used multiple times during the reading out of each binned pixel. Upon

examining the STX-16803 specification sheet it can be seen that the CCD is capable of on-chip binnings of 1x1, 2x2, 3x3, 9x9 and 1xn. Based on this, it is suspected that the 1xn binning method is used for the other on-chip binnings and is then binned into the larger super pixel post conversion either on chip or via software communicating with the SBIG driver.

Figs. 2.12, 2.13 and 2.14 for binning 1 highlight an issue with the noise and gain response at low signals which is also seen in binning 2 and 3. Two potential causes for this are inaccuracies in the removal of the pedestal level or in the read noise measurement (Janesick 2007, pg. 60) where even a single count can cause variations, especially at low signals. The read noise measurement has already been confirmed to be accurate to within an electron and hence to well within a single digital count. This leaves the overscan subtraction as a potential cause. It was previously mentioned that the column overscan correction results in a mean offset of -6.27 across an entire photoactive region. Adding 6.27 ADU back into the signal, and recalculating the PTCs causes a severe increase in the deviations, suggesting that the offset isn't the cause.

Similarly, the photon transfer curves (Figs. 2.9, 2.10 and 2.11) highlight an issue with the FPN at low signal counts which do not intersect with the line of best fit and show a large scatter. The fixed pattern noise term, like the shot noise, is dependant on the signal which is in turn being measured from an illuminated dome and through the optics. Figs. 2.2 & 2.3 shows that the CCD is far from evenly illuminated and while best efforts have been made to select a low gradient area of the CCD, minor non-uniformities still exist. Initial PTC tests of binning 1 using a larger 201^2 pixel area demonstrated that this uneven illumination significantly impacts the plots in Figs. 2.12, 2.13 and 2.14 as well as the FPN. The 31^2 pixel area used in Fig. 2.9 provided a signifcant improvement while allowing a large enough sample for all three binnings.

2.5.2 Residual Images

Fig. 2.7 also highlights an issue which occurs at signals which are, or are close to, saturating the pixels. Following saturation, CCD exposures demonstrate an increase in photon counts compared to previous exposures with the same duration. This is considered to be a form of residual image. Residual images come in two main forms, Residual Surface Image (RSI) and Residual Bulk Image (RBI) (Janesick 2001, pg. 657, 659). In both cases the residual image is formed by a trapping of charge, in the case of RSI this is on the Si-SiO_2 interface, while RBI is caused by the trapping of charge between the two charged layers of the CCD known as the epitaxial/substrate interface.

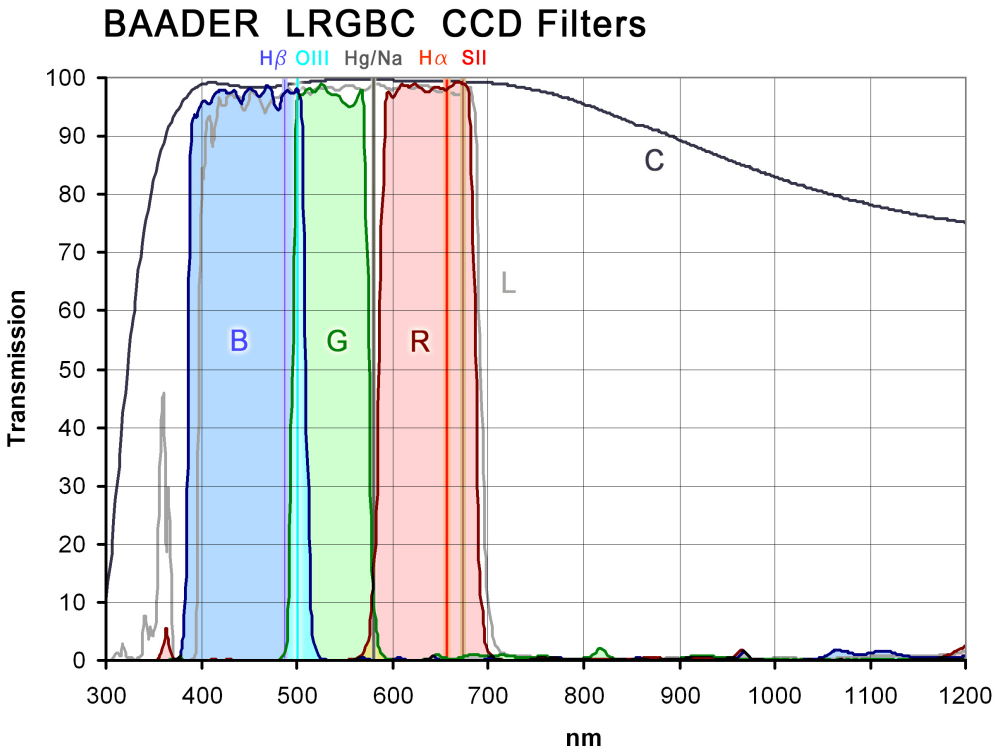

Figure 2.19: Baader filter transmission showing the wavelength range for various Baader Filters. The SBIG STX-16803 is operated with Clear, R, G, B and H-alpha

During RSI, charge trapped on the surface is released into the pixel wells and results in a deferred charge during readout which visually appears as a streaking across pixels on the image. It is eliminated by setting the CCD clocking voltage to inversion which allows electron hole recombination to occur in the Si-SiO_2 interface preventing

any spurious charge leaking into the pixel well. This is a common feature on modern CCDs and as no streaking occurs on saturated stellar images on the STX-16803 this is unlikely to be the cause for the residual counts seen in Fig. 2.7.

RBI on the other hand is a design flaw inherent to front-side illuminated CCDs and is predominantly seen at wavelengths greater than 700 nm (Janesick 2001, pg. 660). At these longer wavelengths the photons are able to reach the epitaxial/substrate interface, where the charge is trapped and then leaked into the pixel wells. The exposures used to generate Fig. 2.7 were taken in a Baader clear filter which allows wavelengths greater than 700 nm (see Fig. 2.19). This has also been seen, although not thoroughly explored, in the Baader R filter. A simple experiment to check for the effects of RBI to the STX-16803 would be to generate a similar plot to Fig. 2.7 using a shorter wavelength filter such as the Baader B filter. A significant problem with RBI is that it can influence the quantum efficiency of the CCD, increasing with increasing trapped charge. Additionally, RBI doesn't require saturation to collect charge and hence can influence lower signal images as well as saturated ones.

One method of dealing with RBI is to build a light source (typically a long wavelength LED) into the camera itself and flash the CCD, exposing the pixels to signal levels several times the required full well depth of the CCD. The pixels are then flushed and the science image taken. This results in the traps being filled prior to the image exposure and a stable and higher quantum efficiency photometric system at the expense of some time resolution. The STX-16803 does not have this feature but it is one worth exploring for the future and as PIRATE primarily operates in the R filter for exoplanet observations, which Fig. 2.19 shows to overlap with 700 nm this may be a useful future investment. In the interim, it is recommended to explore the other filters available to PIRATE such as the Baader G and B. As an aside, in backside-illuminated CCDs, the epitaxial/substrate interface is removed via a thinning process during manufacturing and hence these CCDs do not suffer from RBI.

2.5.3 Flat Correction

The effect of flat correcting the PTC can be examined in Fig. 2.15. Graphically it can be seen that increasing the number of flats in the master flat frame provides a significant reduction in total noise. This is due to the removal, or suppresion, of the FPN. Examining the total noise for the data points scattered around 38,000 counts shows an average noise reduction of 12.2, 16.1, 17.2, 18.4 and 19.5% for the master flats containing 5, 10, 15, 25 and 50 frames respectively. In comparison, the total and shot noise difference is 21.0%.

This highlights the importance of flat correction in improving the signal-to-noise performance of the CCD and also shows diminishing returns to the improvement when adding larger number of flat frames. PIRATE is capable of collecting up to 15 dusk sky flats per R,G,B filter or 25+ in a single filter and the same is true for dawn flats. This number limitation is imposed by the changing brightness of the sky as the Sun is setting. Hence PIRATE is more than capable of achieving very good flat calibration. Based on these results and the practicality of obtaining flats, it is recommended that PIRATE should aim to collect a minimum of 15 flats, or roughly 581,250 e^- (465,000 ADU). One approach, which PIRATE should explore, is to generate a master frame with a larger number of flats (and electrons) with a weighted combination of frames taken over several nights with a higher weighting being placed on the flats taken closest to the night in question. This would allow for a significantly larger catalogue of flats to be used while the weighting would allow any relevant CCD noise features to still be present.

An interesting point to note in Fig. 2.15 is that at saturation, the flat corrected total noise doesn't drop but rather increases compared to the uncalibrated total noise. Fig. 2.16 shows this more clearly. This is likely due to the fact that the noise structure is contained within the master flat and is re-introduced into the saturated image. Also, although it is beginning to approach the regime at high signal in binning 1, at no point does the CCD enter a FPN dominated state (ie. FPN becomes a larger noise

contribution than shot noise) in any of the three tested binnings.

2.6 Key Results

The key results from this chapter are as follows:

- PIRATE's SBIG STX-16803 CCD is found to have a read noise and gain in 1x1 pixel binning of 11.46 $\pm$ 0.15 e^- and 1.25 $\pm$ 0.002 e^-/ADU, respectively. Pixel binnings of 2x2 and 3x3 resulted in read noises of 19.97 $\pm$ 0.78 e^- and 27.85 $\pm$ 1.25 e^-, as well as gains of 1.26 $\pm$ 0.006 e^-/ADU and 1.28 $\pm$ 0.010 e^-/ADU, respectively. The CCD gain results show a slight discrepancy from the manufacturer specifications of $\sim$1.6% while the read noise varied by 14.6% in binning 1x1 and increased with the larger binnings.

- The increase in read noise with increased binning size suggests that A/D converter is being used multiple times, possibly in a 1xn pixel configuration.

- The SBIG STX-16803 camera is found to have an evenly illuminated shutter.

- The CCD is potentially suffering from residual bulk images.

- A large number of flat-field frames is found to be ideal for reducing noise, with practicality in mind it is recommended that a minimum of 15 flat-field frames are acquired.

Chapter 3

PIRATE Observations - Exoplanets

Struve (1952) first postulated that the period around a star for a planetary companion could potentially be about 1 day and that eclipses of a 10 Jupiter mass companion with a mean density five times that of the star would result in a dip in stellar magnitude of 0.02. With the advent of the first exoplanet discoveries (Wolszczan & Frail 1992; Mayor & Queloz 1995), research efforts into the field of exoplanets have increased. The SuperWASP project is one such endeavour with the main goal being to detect and identify transiting exoplanets.

SuperWASP is a wide-angle exoplanet transit survey which relies on surveying a large portion of the sky throughout the night. To accomplish this it makes use of a wide field-of-view, but this means that it has a low angular resolution. Intermediate aperture telescopes which have better resolving power than SWASP are necessary to refine and confirm exoplanet transit detections. There are a significant number of plausible signals within SuperWASP that turn out to be false positives, therefore these intermediate telescopes primary objective is to locate the target star and separate its lightcurve from other stars that would be blended together on SuperWASP. With a positive transit-like signal, or for isolated stars, radial velocity measurements can also be taken to measure the mass of the elements within the stellar system. Intermediate telescopes are capable of producing scientifically publishable results but it is better to use the data in combination with significantly larger telescopes. These telescopes are expensive to run and

oversubscribed, so a scientific case can be presented with the use of the intermediate telescope data.

PIRATE falls into the intermediate aperture telescope position and this chapter details the methodology and results of PIRATE's SuperWASP related exoplanet observations. SuperWASP exoplanet candidate target selection and data collection are described along with the PIRATE exoplanet reduction pipeline which has been modified and improved upon. This methodology has meant that PIRATE has helped to identify a large number of false positives as well as real and plausible planets. Several of the false positives, plausible and known exoplanets are examined in detail in this chapter. Finally, two example targets are used to explore the lightcurve performance of PIRATE which is dependent on sky conditions.

In order to clarify the role of the author in this chapter it is important to note that some parts of this chapter report and describe other people's work. Sec. 3.2.1 describes the pipeline created by Stefan Holmes, while Sec. 3.2.2 describes the author's modifications to the pipeline. Sec. 3.3 provides a selection of lightcurves for non-detection and exoplanet mimics observed and analysed by the author. The plausible planets described in Sec. 3.4 made use of SuperWASP data and commentary, in addition to PIRATE data, to allow the author to form a discussion on the planets. Within this section a report on the published planets is also provided with the relevant PIRATE observers shown in Tab. 3.5. Sec. 3.6 makes use of PIRATE observation data from a variety of PIRATE users with the majority being collected by the author; the analysis of this data is that of the author.

3.1 Observational Method

A typical observation session with PIRATE tends to strike a balance between practicality as well as equipment safety and longevity. The observation method summarised here tends to be performed by submission of ACP plans from start to finish but can be performed manually if required.

A session begins with the powering on of PIRATE and cooling of the CCD to $-20°$C or $-10°$C depending on the amount of power required by the CCD cooling fan, this usually falls into a winter and summer operating mode respectively. The SBIG STX-16803 CCD camera is rated to cool down to $-50°$C below ambient temperature. Roughly 20 minutes prior to sunset, weather permitting, the dome is opened to minimise any temperature gradients between the local atmospheric temperatures and the equipment. It is noted that in the summer months, the inside of the dome can get quite warm. Hence, opening the dome also allows the CCD cooler to reach the desired temperature with lower power requirements, potentially increasing the longevity of the camera. Just after sunset, dithered sky flats in the required filters are acquired. The dome is then closed to prevent any potential light leaks affecting bias and dark calibration frame acquisition. Once completed, the dome is re-opened to allow for further equipment-atmospheric temperature equilibrium.

At nautical dusk (when the Sun is at $12°$ below the horizon) test frames are taken to establish a suitable exposure time for any current visible targets; other non-visible target exposure times will be extrapolated from this if using ACP plans. The target observations are then submitted and PIRATE will begin data acquisition. Each frame is automatically plate solved by ACP and re-aligned if any drift greater than a few arcseconds is detected. At the end of the observing session, dawn sky flats are acquired followed by a second round of bias and dark calibration frames. The CCD is then warmed and PIRATE is powered down.

3.1.1 Target Selection

The SuperWASP Hunter pages, a database of SuperWASP analysis results, provide a convenient tool to aid in target selection. This tool supplies the user with a list of targets that will be undergoing a partial to full transit during a specified night for an observing site at a given longitude and latitude. The list of potential targets for PIRATE generated this way then needs to be winnowed further to select optimal targets for the

night.

An ideal target for a full lightcurve observation will not be too faint ($M_V \gtrsim 13$) and have a transit depth detectable by PIRATE in a single observation session (see Sec. 3.6.1). Also, a target that is too bright ($M_V \lesssim 9$) will prevent the observation of suitable comparison stars. In either case the target must not cross the meridian during its transit period, as a pier flip will occur and rotate the field of view by 180°. This would result in the flux from off-centre stars landing on pixels significantly offset from the original location which are likely to have a different response. Flat field calibration will reduce this effect but, as was pointed out in Sec. 2.5.3, a large number of high signal-to-noise flat frames are required and will minimise rather than remove the effect altogether. Additionally, the target must have an altitude greater than 30° (ie. airmass less than 2) throughout the observation.

In the event that such a target isn't available, on-off observation techniques can be employed to check for variability in nearby stars that would be unresolvable by SuperWASP and hence be included in the SuperWASP aperture measurements. The on-off method employed by PIRATE is to acquire a few minutes of science frames for target 1, move onto target 2 and acquire, move onto target 3 and acquire, etc. This is continued until the sequence has a duration which is ideally less than the shortest transit duration of the targets. The sequence is then repeated throughout the night with targets being added or removed as necessary. On-off targets should still have the same meridian-crossing and altitude restrictions as a full transit lightcurve.

Other considerations to bear in mind are the potential for the expected ephemeris to have drifted. Several years may have passed since the last observation resulting in the ephemeris uncertainties compounding as time moves on. The on-off methodology can potentially be used to refine the transit ephemeris if the signal to noise ratio is high enough. Additionally, some blended stars may be difficult or impossible to resolve using PIRATE making them unsuitable as targets for PIRATE. Finally, a check on whether PIRATE has observed the target previously and the outcomes of those observations should also be considered.

With all these criteria a level of flexibility and compromise may be required in order to obtain any targets for a given night. Although astronomical dusk (Sun is at 18° below the horizon) is an ideal start time for observations, nautical dusk, providing more background noise, could be used to cover transits within this time frame. Similarly, a target with a large ephemeris drift may be the only suitable choice, and at the very least a null detection could help to reduce the drift.

3.2 PIRATE Exoplanet Pipeline

The original PIRATE pipeline used for exoplanet photometric reduction and lightcurve generation, described in Holmes et al. (2011), has undergone several revisions. Documented here is a summary of this pipeline followed by the various revisions and modifications that have taken place.

3.2.1 Original Exoplanet Reduction Pipeline

The original pipeline makes use of a custom Interactive Data Language[1] (IDL) script which reads in a user generated list of science frames or, alternatively, displays each science frame individually and asks the user to accept or reject each frame. Separate lists are also generated in the background for each type of calibration frame. The IDL script generates an appropriate IRAF script for the CCDPROC task with the previously mentioned lists. This task is executed by the user from within IRAF and is responsible for combining the calibration frames and using them to calibrate the science frames. Finally, the task performs a post-calibration rotation on the science frames taken prior to a pier flip. This rotation is to simplify the identification of stars for which photometry will be measured.

With calibration completed, the IDL script then measures the mean of each calibrated science frame. The frames with the lowest mean imply that there is a low sky background noise. From the quartile of the lowest mean frames, the frame with

[1] http://www.harrisgeospatial.com/ProductsandTechnology/Software/IDL.aspx

the highest standard deviation is suggested as a master frame and is displayed to the user for a visual check. Typically, the highest standard deviation frame is assumed to contain a large number of detectable point sources. The user can reject this frame if desired and will be asked to input the name of a replacement frame.

Following the designation of the master frame, the user is asked to determine a representative FWHM for the master frame which can be accomplished using the IRAF imexamine task. This value is input into the IDL script which generates an IRAF script to locate all sources with a 6σ detection or higher using the DAOFIND task and perform initial photometry using the PHOT task. All sources that do not fail the PHOT task have their co-ordinates recorded. A star is then selected by the user and the big box and small box search radii defined. The search radii are used to determine the centre of the star in other frames and hence a linear transformation of the co-ordinates can be applied to all point sources. Photometry is then performed at the pixel co-ordinates of all point sources known in all images, typically with the aperture set at 3 times FWHM, although this is also user configurable.

A data cube containing the entire night's photometry for the target is then generated. This data cube then undergoes two separate filtering steps. The first filter applied is that any science frames that have a fraction of the total point sources which fail photometry are removed. This removes any bad science frames that have passed initial screenings. The fraction applied to this filter is user definable but by default is set at a quarter (ie. 25%). A second filter is then applied that removes any point sources which suffer a photometry failure in one or more of the retained frames.

The filtered data cube is then sorted by instrumental magnitude and differential photometry is applied to the light curves of all point sources using an ensemble technique similar to that of Burke et al. (2006). In order to determine which point sources to include in the ensemble, each point source light curve is divided by a comparison point source lightcurve; this is then normalised. A 3σ clipped mean and associated standard deviation is then determined for each normalised comparison curve. This list is ordered by standard deviation and starting with the comparison point source with

the lowest standard deviation, each comparison source is added to the ensemble in incrementing standard deviation. Each comparison light curve is added to the ensemble using an inverse variance weight.

So, for a single target point source with a range of comparison stars, $1 \leq i \leq N$, within a given science frame, j, the ensemble is computed as

$$E_j = \frac{\sum_{i=1}^{N} \omega_{ij} F_{ij}}{\sum_{i=1}^{N} \omega_{ij}} \tag{3.1}$$

Here, F_{ij} are the comparison stars' individual fluxes and the weights, ω_{ij}, are given by the inverse square of the comparison flux uncertainty, σ_{ij},

$$\omega_{ij} = \frac{1}{\sigma_{ij}^2} \tag{3.2}$$

The uncertainty in the ensemble being given by

$$\sigma_{E_j} = \left[\sum_{i=1}^{N} \omega_{ij} \right]^{-0.5} \tag{3.3}$$

The ensemble flux, E_j, can then be applied to the target point source flux, F_{*j} to generate a differential target flux, d_{*j}, using the form

$$d_{*j} = \frac{F_{*j}}{E_j} \tag{3.4}$$

This is applied to every frame to create a differential lightcurve for the target point source. The differential lightcurve is normalised by taking the median value of the light curve and dividing by it and then the rms scatter is computed. The accepted differential lightcurve is the one with lowest rms scatter and comparison point sources are no longer added to the ensemble once they begin to increase the rms scatter. This method is applied to all detected point sources and results in each target having a unique comparison ensemble.

In the final steps, the pipeline generates plots of all the normalised target point

source light curves. This is followed by asking the user to specify the primary target in the field of view, which is then used to collate all the light curves of all the point sources within the equivalent of the SuperWASP aperture (4.5 times the SuperWASP plate scale of 13.7 arcseconds) around the target star. These collated data are output and allow for a quick look of the target and the surrounding stars.

3.2.2 Modifications to the PIRATE Exoplanet pipeline

The pipeline has undergone several changes, some minor and some major. The most major in terms of software development has been the switch from the IDL/IRAF to a converted version making use of Python and pyraf. Pyraf is a python binding for calling IRAF commands within Python, allowing simpler programming and interactions within the pipeline. Python has a growing user base within the astronomical community and in addition to a plethora of new developments, many common astronomical tools (originally developed in other code languages) have been adapted to work within Python. In addition to these benefits, Python removes certain limitations imposed by the IDL language which requires user licenses in order to operate. Python is a free and open source programming language which doesn't require any paid for licenses. The free and open source nature of Python has resulted in a large global user base outside of the astronomical community which means programming aid is easily accessible and readily available.

As part of this change a few new options have been implemented into the pipeline. It is now capable of being split into separate calibration and reduction sections or being used as a whole. This allows the user to calibrate data for use with other software or reduction techniques and also allows the user to take already calibrated data, skip the calibration process and start at data analysis.

In addition to this, a parameter file has been introduced. The IDL/IRAF version often required the user to dig into the code to find and adjust certain settings, which isn't user friendly and can result in the user forgetting to revert certain settings. The

Python code aims to minimise this by adding a parameter file which a user can edit without requiring intimate knowledge of the code. These parameters include but are not limited to the point source detection threshold, the photometric aperture size and the saturation limit of the CCD.

The ensemble method used to generate lightcurves has also been altered. In some situations the ensemble selected for a point source would contain a single star rather than an ensemble of stars. This has been modified to enforce an arbitrary minimum of 10 stars so as to suppress any features that a single star comparison ensemble might introduce. Ideally, this would be a user definable value but at present it is hardcoded into the pipeline. This methodology still requires proper analysis in order to confirm that this improves performance, or at the very least, determine an ideal minimum number of stars to include in an ensemble.

3.2.2.1 Correction of Bias/Dark/Flat implementation

As part of the conversion process from the IDL pipeline to the Python version it was identified that the calibration process was implemented incorrectly for PIRATE's typical observations. The IDL pipeline performed calibration using the following steps

1. Combine Bias into master Bias
2. Combine Dark into master Dark
3. Combine Flat into master Flat
4. Correct science frame with the above master frames

This is incorrect as flat frames taken by PIRATE are typically not of the same exposure and hence have to be bias and dark corrected prior to applying the combination routine. Similarly, dark frames contain bias pedestal counts which need to be removed prior to scaling them to the correct duration to apply to the flat frames. Two options were identified as listed below

1. Option A

    (a) Combine Bias into master Bias

    (b) Correct individual darks by master Bias

    (c) Combine corrected Darks into master Dark

    (d) Correct individual flats by master Bias and master Dark

    (e) Combine correct Flats into master Flat

    (f) Correct science frame with the above master frames

2. Option B

    (a) Combine Bias into master Bias

    (b) Combine Same exposure duration Darks into master Dark

    (c) Correct master dark by master Bias

    (d) Correct individual flats by master Bias and corrected master Dark

    (e) Combine correct Flats into master Flat

    (f) Correct science frame with the above masters frames

Option A subtracts the master bias from individual dark frames prior to combining into a master dark whereas option B is less computationally expensive as it subtracts the master bias in a single operation from the master dark. The downside to option B is that the dark frames must all be of the same exposure duration prior to combining in order to avoid scaling the bias counts. In both cases, the final result should be the same. To allow for flexibility of the pipeline, option A was implemented although it is worth noting that in typical PIRATE observing sessions dark frames with exposure durations equal to the science frames are usually acquired.

Applying both the IDL and Python methods to a single test case science frame showed that the corrected calibration lowered the mean count and standard deviation by 1.6 and 0.4 ADU respectively These differences are negligible to PIRATE's end

results prior to the detection of this error but nonetheless this has removed a small source of error.

While on the topic of calibration it is worth noting that CCD overscan, as described in Section 2.3.2, has also been implemented into the calibration process and the user can apply the respective settings via the parameter file. If the overscan function is switched on in the parameter file then the calibration process, option A, is adjusted to remove the pedestal in dark and flat calibration frames and the science frames as part of the calibration process.

3.2.2.2 Master Frame Selection

As stated in Section 3.2.1, the master frame used for point source identification is selected to be the science frame with the highest standard deviation from the quartile of science frames with the lowest average counts. For general use this has been acceptable but in some cases false detections have been made due to cosmic ray events and hot pixels. If stringent settings are applied to the pipeline frame rejection settings it is possible to lose an acceptable frame. In addition to this, extra computational power will be required for attempts to locate and measure these false point sources until they are rejected further on due to incomplete lightcurves.

To overcome this, all science frames are aligned with the original master frame and five science frames are median combined into a new combined master frame. The five science frames are selected using the same logic as the previous old master frame method, they are selected to have highest standard deviation from the quartile of science frames with the lowest average counts (ie. they are the best 5 frames). The use of the median removes the cosmic ray detections and, if the science frames have been dithered on acquisition, hot pixel false detections can also be minimised. The alignment process applied to all science frames also has the added benefit of simplifying the placement of photometric apertures, as all point sources are now aligned to the same image pixels co-ordinates.

This method adds two constraints to the data fed into the pipeline, the first being

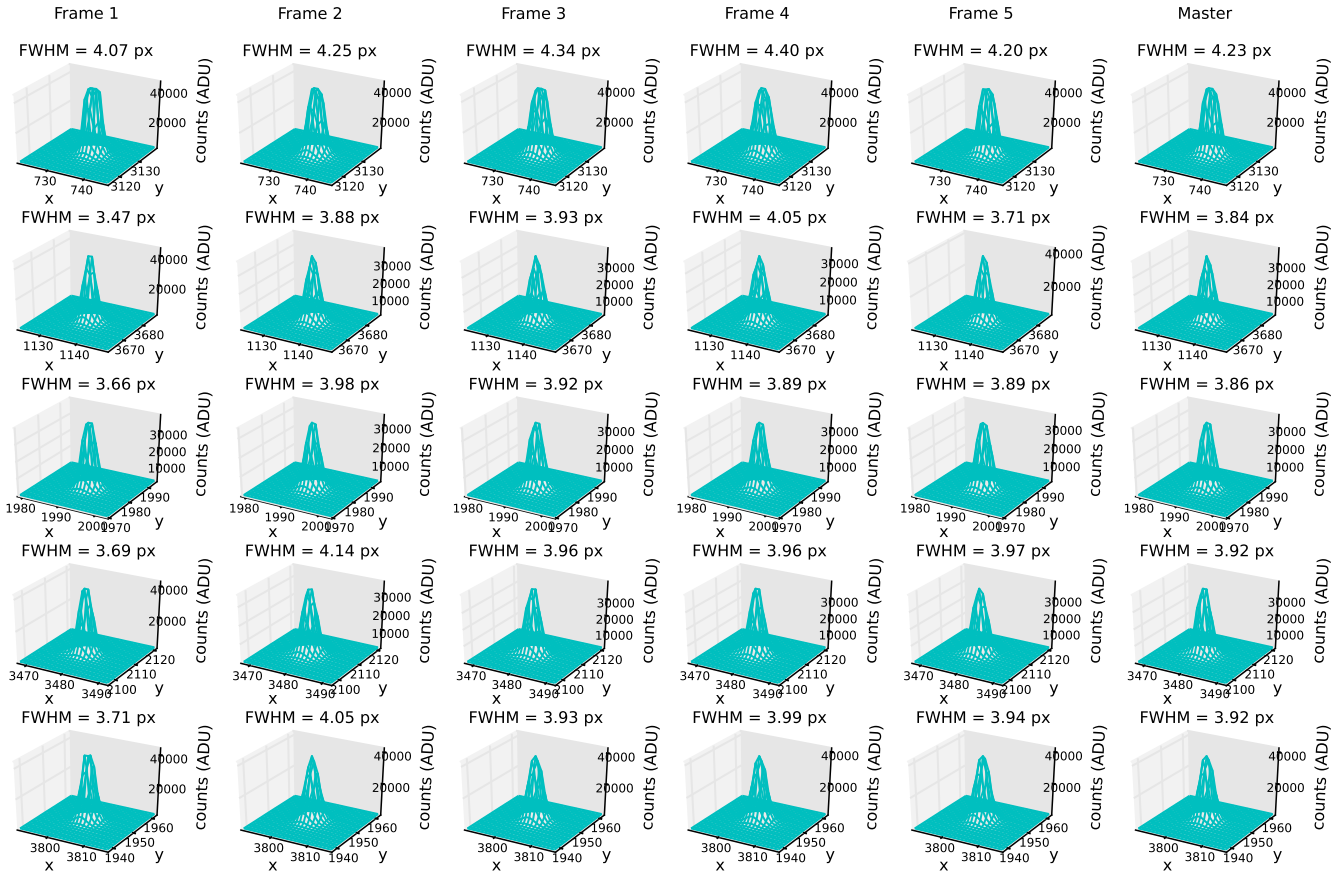

Figure 3.1: Comparison of point source FWHM for the combined master frame and the individual frames used in the median combine for a single field of view using the SBIG STX-16803 CCD camera. Under the old single master frame selection method frame 1 would be selected as the master frame. The amplitude is in counts (ADU) and the other axes are in image pixel co-ordinates. The FWHM is measured in pixels, with each pixel representing 0.63 arcseconds.

that a minimum of 20 usable science frames are required to meet the master science frame selection criteria. Ideally, more frames are collected and used in order to make use of the highest standard deviation constraint, which is effectively ignored at 20 frames. Under the old master frame method, the constraint was set at 4 usable frames. The second constraint is that all the science frames are required to be plate solved in order to align them.

As part of the combination process, the FWHM of the stars in the combined master frame are altered. Fig. 3.1 shows the PSF of a selection of five point sources from a single field of view for the combined master frame and the individual frames used to create it. Under the old single master frame selection method frame 1 would be selected as the master frame. This figure shows that, in all examined cases, the FWHM of the combined master frame is larger than that of frame 1, although due to the nature of the median combine method, it is also never the largest of the 5. This increase in the FWHM can result in faint stars going undetected in the initial point source identification setting if the user-definable detection threshold parameter, which has a default of 6σ, is set too high. The benefit to this is that it reduces computation time as the faint stars on the edge of detectability are likely to fail a photometric measurement in at least one science frame and be removed from the final data set due to an incomplete light curve. Another benefit is that this is a more representative measurement of the FWHM as the pipeline utilises the same FWHM setting to perform photometry on all frames.

3.2.2.3 Auto-Frame selection

An automatic "good" science frame selection method has been implemented into the pipeline. The purpose of this is to bring the pipeline a step closer to being fully automated so that the pipeline could be scripted to perform an initial run once it detects new data. This routine works by checking that each uncalibrated science frame is plate solved and rejecting or adding the frame to a list of approved frames. As plate solving occurs as part of the image acquisition, each science frame should already contain this

information. If a science frame does lack the plate solving then it is an indication that there is an issue with the frame and it should not be included in the list of "good" science frames. As the master frame selection (see Section 3.2.2.2) also requires plate solving in order to operate correctly, this also ensures that all frames used are plate solved, alerting the user to any potential issues at the start of the pipeline rather than several steps in.

This is a simple implementation and the user should ensure that the frames selected are acceptable, as in some instances science frames which are unsuitable for photometry or unsuitable for the pipeline may still be accepted. Photometric issues can range from science frames with saturated stars to unusual features due to overhead aircraft, internal reflection or cloud coverage. These are situations where a robust software may still be able to plate solve the science frames even with sparse or poor data. Other examples of pipeline issues are several frames taken at different CCD binnings, filters or even cameras, which should be reduced separately. A science frame may also be pointing at a different target and will be rejected further along in the pipeline process as long as it hasn't been selected as the primary master frame.

The pipeline issues can be tackled by having the user identify a single suitable science frame that meets the criteria placed upon, e.g. correct target, filter, binning, exposure, etc. The FITS header for this selected frame can be read and all science frame headers can be compared against it to ensure that the values in each constraint are identical. This can save time compared to manual identification of "good" frames, but this solution creates a separate issue in that the "automatic" frame selection still requires human input, negating some of the benefits of being automated. Photometric issues could similarly be reduced by user intervention, such as manually identifying stars in the selected frame and ensuring that they are present and unsaturated throughout the frames, but this would be impractical for large data sets and negates some of the benefits of being automated.

Science frames that have an aircraft or dense clouds moving across the frame may be automatically removed from the pipeline data cube, as any science frames that have

a user-defined fraction of photometry failures are removed. Setting a stringent value on the fraction of photometry failures improves the effectiveness of the removal process but the applicability will be variable as photometrically suitable science frames may be discarded if too many stars on the frame edges are missing due to pointing errors on the telescope mount.

3.2.2.4 On-Off

The on-off observations described in Sec. 3.1.1 result in small groupings of data points with large gaps between each group. These groups are intended, in the case of exoplanets, to help locate a transit event for the refinement of an ephemeris which has drifted due to its uncertainties. In practice, however, detecting small changes of the order of 1% is difficult. The data tends to be noisy, and the movement of the telescope mount between targets can result in stellar flux not landing on the same pixels as the previous grouping, potentially burying a small change in signal within the noise.

In order to aid the user in discerning any potential patterns in the lightcurve, the pipeline calibrates a single average point for each grouping which is overplot onto the data. The user is able to turn this function on or off using the parameter file and in order to identify groupings. This feature uses a user-supplied time gap parameter to determine the cut-off point between groupings. The time difference between each subsequent data point is determined and if it is smaller than the time gap, then the data is included in the grouping. If the time difference is larger, then a new grouping is initiated and the process continues until all data points are accounted for.

An issue encountered with calculating the mean of the groupings is that any anomalous flux data points can severely impact the calculation and shift the mean data point away from the rest of the grouped data points. This can be further improved by calculating a sigma-clipped mean to prevent particularly noisy data from interfering with the resulting output. The sigma-clipped mean has been applied to the on-off data presented in this thesis but has yet to be implemented into the pipeline due to the author's time constraints.

3.3 Non-Detections and Observed Mimics

The previously described observation and reduction methodology has resulted in a large number of results. Shown below is a small sample of lightcurves for non-detections and exoplanet mimics observed with PIRATE. Examples of full and on-off observations are provided.

3.3.1 Non-Detections

Fig. 3.2 shows a lightcurve for a SuperWASP candidate target observed on 2011-10-10. There are no obvious changes in flux greater than the scatter of the data points, roughly 2%.

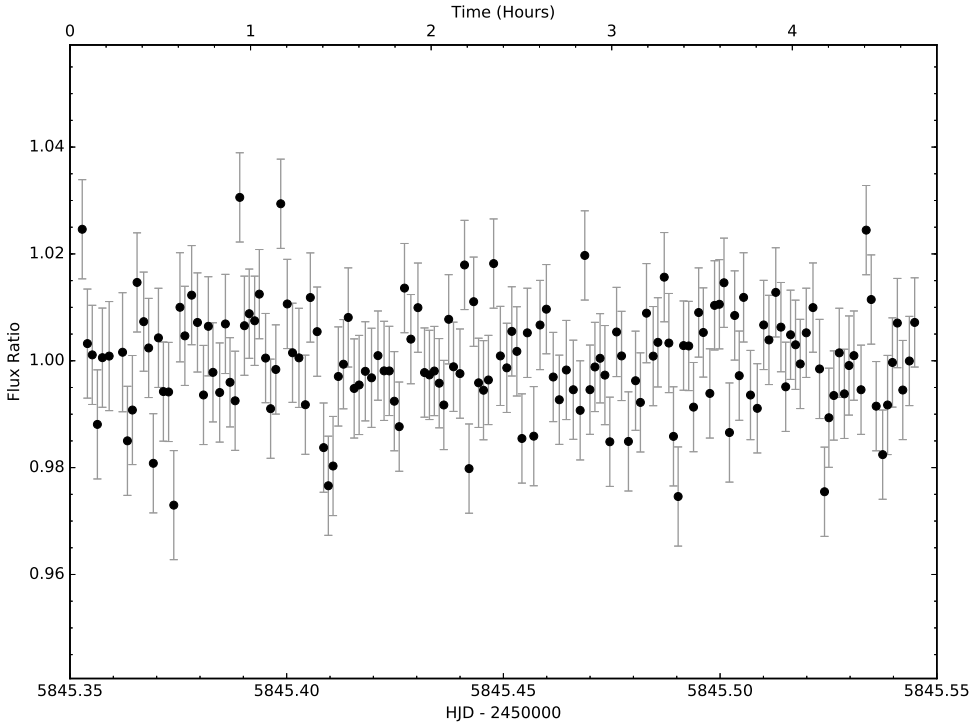

Figure 3.2: Example of a full PIRATE lightcurve for the night of 2011-10-10 with no obvious detections.

Similarly Fig. 3.3 shows a lightcurve for a SuperWASP candidate target observed on 2013-07-16. This target was observed using the on-off method described in Sec. 3.1.1. The scatter here is below 1% with no obvious flux change.

Although these observations are classified as non-detections, there could still be an

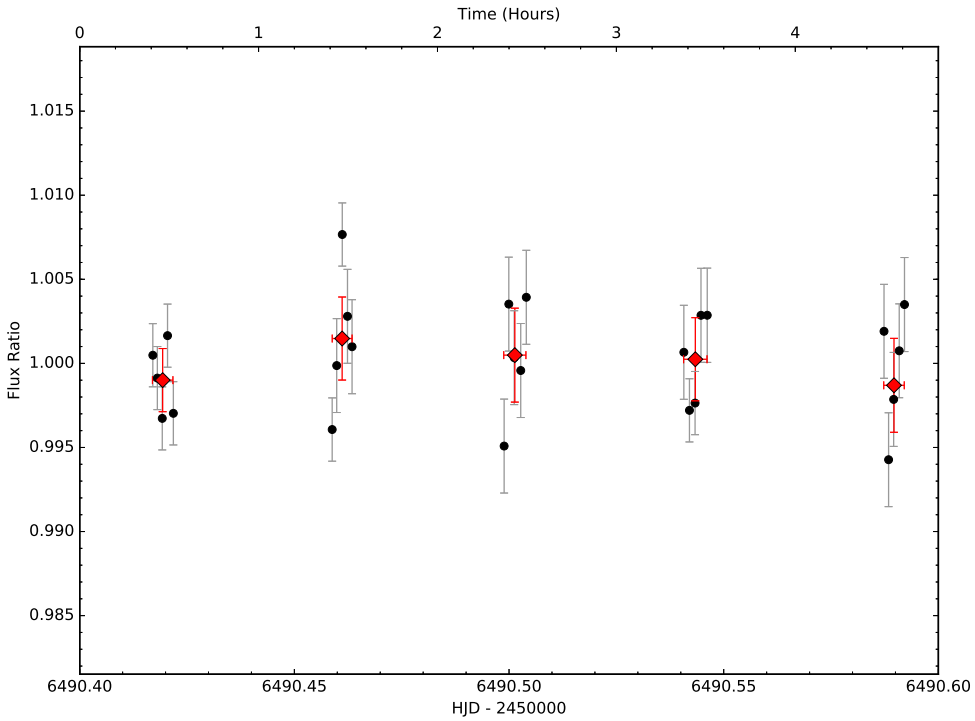

Figure 3.3: Example of an on-off PIRATE lightcurve for the night of 2013-07-16 with no obvious detections. The black circles are individual PIRATE measurements while the red circles are sigma-clipped means for each grouping of measurements.

exoplanet around the targets. An exoplanet transit, smaller than the data noise, could be buried within the scatter. Alternatively, there may be a large ephemeris drift on the predicted transit time due to errors in the originally derived orbital parameters from the SuperWASP measurements.

3.3.2 Grazing

A grazing eclipsing binary, as mentioned in Sec. 1.3.6, occurs when the nearer star in a binary system only just passes across the limb of the farther star which results in a V-shaped lightcurve. Figs. 3.4 and 3.5 are examples of grazing eclipsing binaries observed with PIRATE on 2012-02-29 and 2013-07-15, respectively. Fig. 3.4 shows a full lightcurve with an eclipse depth of $\sim$2 to 3%, a depth comparable to an exoplanet transit while Fig. 3.5 is an on-off lightcurve that has a feature depth greater than 6%, far too large for an exoplanet transit. In both cases the shape of the lightcurves show long duration ingress and egress but no transit floor, typical of a grazing eclipse.

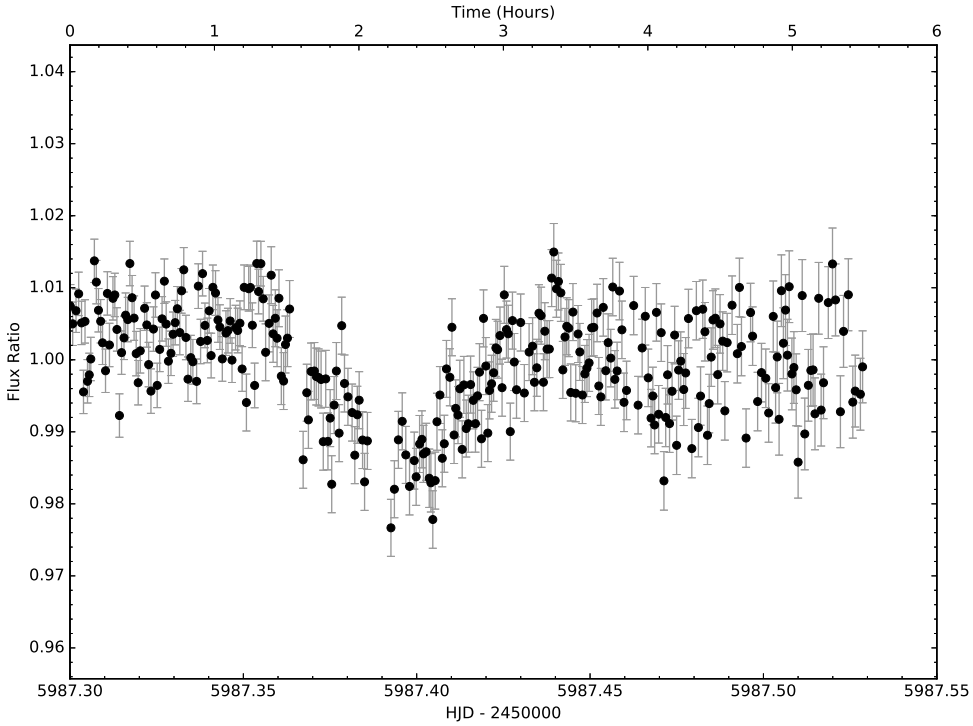

Figure 3.4: Example of a full PIRATE lightcurve of a grazing eclipse for the night of 2012-02-29.

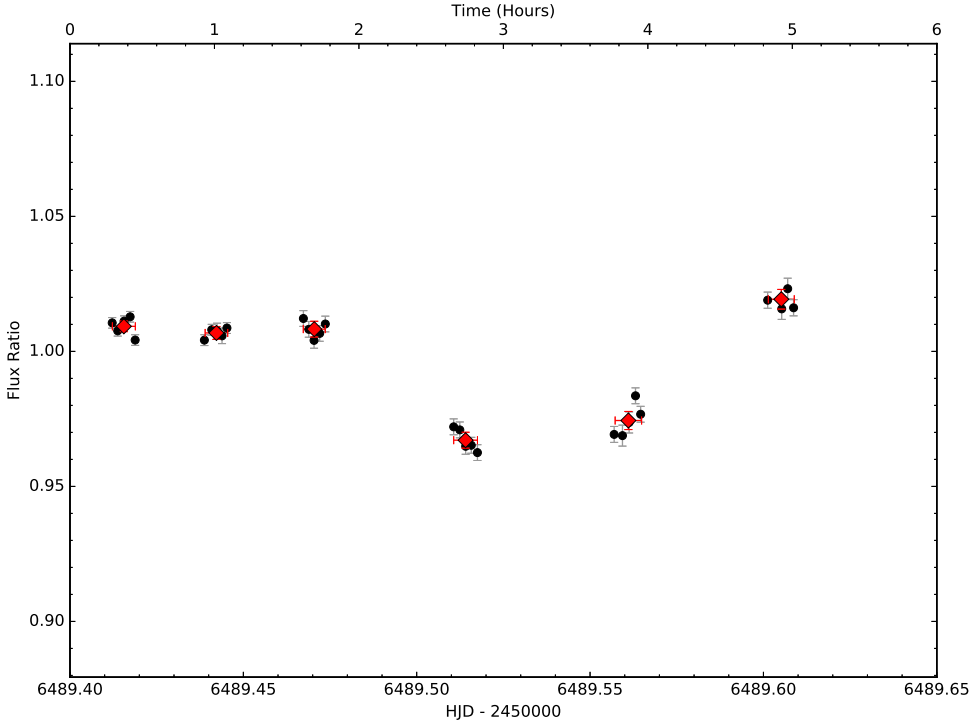

Figure 3.5: Example of an on-off PIRATE lightcurve of a grazing eclipse for the night of 2013-07-15. The black circles are individual PIRATE measurements while the red circles are sigma-clipped means for each grouping of measurements.

3.3.3 Blends

The SuperWASP aperture can include more than one star within the measuring aperture as shown in Fig. 3.6. This can result in deeply eclipsing binaries being blended with a brighter star and a total combined flux change mimicing that of an exoplanet.

Fig. 3.7 is a light curve example of a blended eclipse with the target, star 1156, showing no signal above the 1% scatter. Within the same SuperWASP aperture, star 1166 shows a deep eclipse of ∼60%. Similarly, Fig. 3.8 provides an on-off example of a blend with the target, star 3319, once again not showing any appreciable transit signal while star 3266 shows a drop in flux of ∼15-20%.

3.4 Observed Plausible Exoplanets

Having provided a selection of false positive examples, the topic will now shift to exploring plausible exoplanets. The plausibles presented here provide initial hints of potentially being exoplanets and merit further discussion.

3.4.1 1SWASPJ065329.01+190612.1

This target was observed on the night of 2011-10-06 and 2012-01-17 using the PIRATE Mk 2 set-up. Images in both instances were obtained using 60s 2x2 binned exposures in the R filter. The SuperWASP Markov chain Monte Carlo (MCMC) code (version 3.14), originally detailed in Collier Cameron et al. (2007) and further developed in Pollacco et al. (2008); Enoch et al. (2010), is used on the SuperWASP and both the PIRATE photometry data sets. Two runs have been performed, with the first imposing a stellar main sequence mass-radius relationship of the form $\frac{M_*}{M_\odot} \approx (\frac{R_*}{R_\odot})^{1.25}$, and the second MCMC run without this constraint. Henceforth, the MCMC stellar main sequence mass-radius relationship shall be referred to as 'MCMC MS'. These separate runs provide the fits shown in Fig. 3.9 as well as the system parameters shown in Tab. 3.4.1.

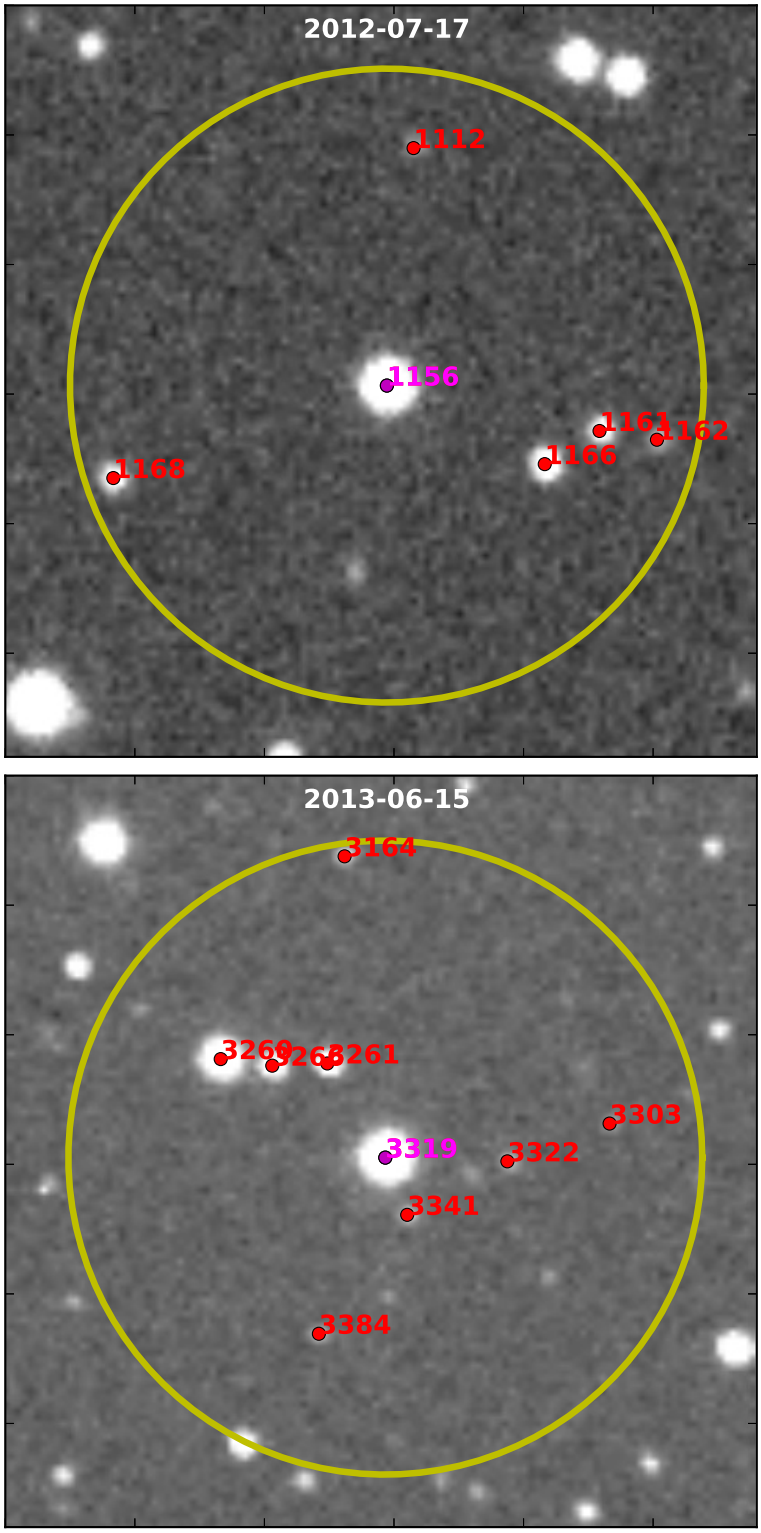

Figure 3.6: Example of the SuperWASP aperture (yellow circle) placed directly over the target stars, 1156 (top) and 3319 (bottom), for the nights of 2012-07-17 and 2013-06-15, respectively. Star 1166 (top) contains the signal seen in Fig. 3.7 while star 3266 (bottom) contains the signal seen in Fig. 3.8.

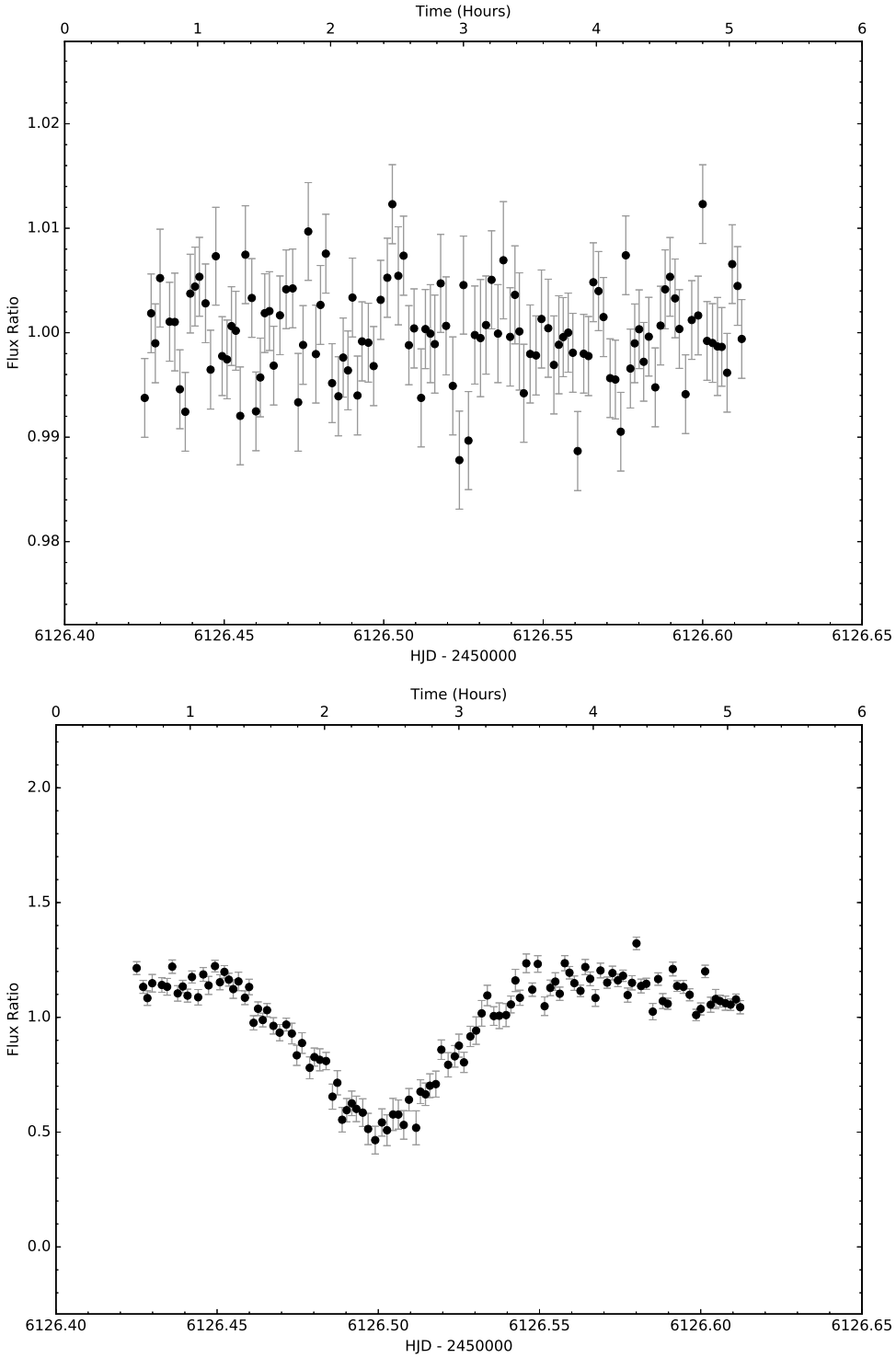

Figure 3.7: Example of a full PIRATE lightcurve for the night of 2012-07-17 with no obvious detection in the target star (top), but a deep signal in the nearby star (bottom). These stars are labeled as 1156 and 1166 respectively in Fig. 3.6

The separate PIRATE lightcurves show an ingress (2011-10-06) and a full transit (2012-01-17). A pier flip occurred mid-transit on 2012-01-17 although this hasn't

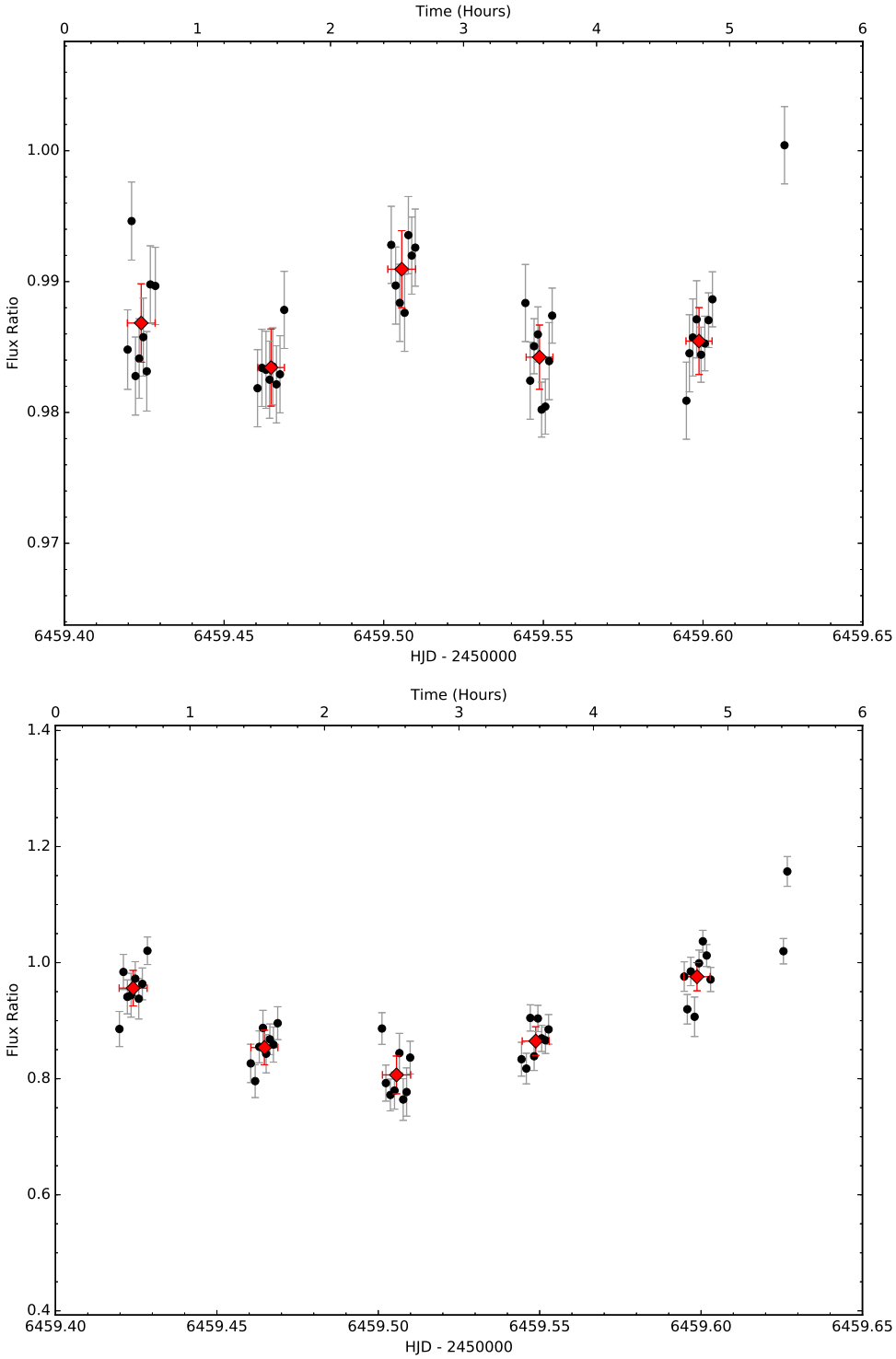

Figure 3.8: Example of an on-off PIRATE lightcurve for the night of 2013-06-15 with no obvious detection in the target star (top), but a deep signal in the nearby star (bottom). These stars are labeled as 3319 and 3266 respectively in Fig. 3.6. The black circles are individual PIRATE measurements while the red circles are sigma-clipped means for each grouping of measurements.

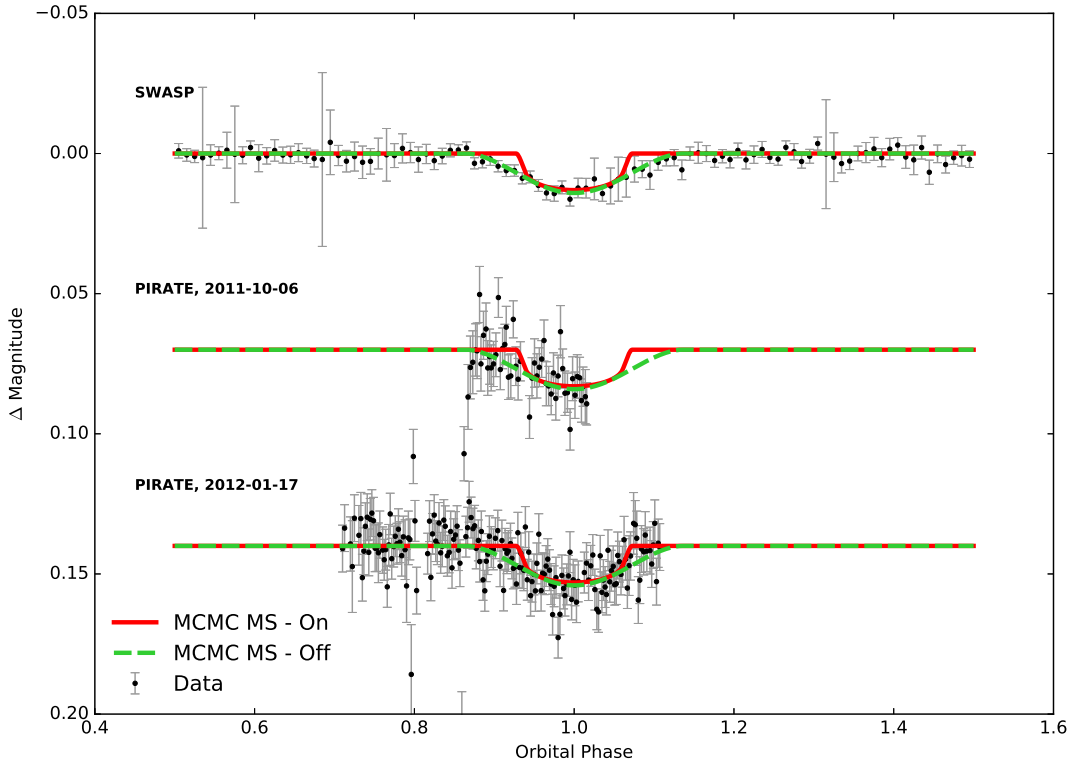

Figure 3.9: SuperWASP folded and binned lightcurve as well as PIRATE lightcurves for the nights of 2011-10-06 and 2012-01-17. The modelled lines are MCMC generated with a stellar main sequence mass-radius relationship setting switched on (red solid line) and off (green dashed line).

caused any visible data offsets; separate reductions of pre and post pier flip have shown the transit shape to be real. It is debatable as to whether there is a transit floor within these and the SuperWASP lightcurves, although it is noted that the ingress and egress clearly dominate the transit duration. However, based on these data sets alone it is difficult to completely reject the target and categorize it as a grazing eclipse, as even a short transit floor could imply a highly inclined planet.

The MCMC runs performed on the combined photometry shows that a better fit to the data is achieved when the MCMC MS is switched off. This results in the planet fit taking on a 'V' shape, similar to that expected from a grazing eclipse. On the SuperWASP hunter pages, collaborators report that two SOPHIE radial velocity measurements have shown no significant variations with a limiting mass of $<0.1\ M_J$ (dated 2012-02-22). Additionally, the SuperWASP hunter pages list the target as a K3 effective temperature star and the giant flag has been set to 'true'. Taking these at face

Table 3.1: System parameters and 1σ error limits derived from the MCMC analysis for 1SWASPJ065329.01+190612.1. 'MS On' and 'MS Off' refer to the MCMC stellar main sequence mass-radius switch setting being either on or off.

Parameter	Symbol	MS On	MS Off	Units
Stellar Parameters				
Stellar mass	M_*	$0.954^{+0.025}_{-0.026}$	1.121 ± 0.032	$M_\odot$
Stellar radius	R_*	$1.169^{+0.040}_{-0.042}$	$2.319^{+0.079}_{-0.091}$	$R_\odot$
Stellar surface gravity	$\log g_*$	$4.281^{+0.025}_{-0.023}$	$3.757^{+0.028}_{-0.023}$	cgs
Stellar density	ρ_*	$0.595^{+0.058}_{-0.048}$	$0.0899^{+0.0099}_{-0.0074}$	$\rho_\odot$
Planet Parameters				
Planet mass	M_p	-	-	M_J
Planet radius	R_p	1.111 ± 0.042	$4.64^{+1.19}_{-1.07}$	R_J
Planet equilibrium temperature	T_{eq}	2338^{+63}_{-65}	3091^{+77}_{-76}	K
Orbital Parameters				
Epoch (BJD - 2450000.0)	T_0	$5379.4456^{+0.0014}_{-0.0015}$	5379.4470 ± 0.0015	days
Orbital period	P	$0.5910224^{+0.0000011}_{-0.0000012}$	0.5910217 ± 0.0000017	days
Transit duration	t_T	$0.0825^{+0.0023}_{-0.0025}$	$0.0884^{+0.0059}_{-0.0052}$	days
Planet/star area ratio	$(R_p/R_*)^2$	0.00954 ± 0.00038	$0.0177^{+0.0031}_{-0.0023}$	
Impact parameter	b	$0.077^{+0.060}_{-0.051}$	$1.031^{+0.082}_{-0.078}$	R_*
Orbital inclination	i	$88.2^{+1.2}_{-1.4}$	$38.7^{+3.9}_{-3.0}$	$^\circ$
Orbital eccentricity	e	0 (fixed)	0 (fixed)	
Orbital separation	a	$0.01357^{+0.00012}_{-0.00013}$	0.01432 ± 0.00014	AU

value, this suggests that the MCMC MS switch should appropriately be set to off. At this setting, the planet has a radius of $4.64^{+1.19}_{-1.07} R_J$ and an inclination of $38.7^{+3.9}_{-3.0}{}^\circ$, for comparison, the largest currently known planets are at $\sim 2\ R_J$ or less while the highest inclination for a transiting exoplanet is 77.6°(http://exoplanets.org, Wright et al. 2011).

It is clear that both PIRATE and SuperWASP have detected a periodic signal; however, the lack of radial velocity detections as well as the results from the MCMC cast serious doubts as to whether this is a planet. It has since been flagged as rejected on the SuperWASP database.

Yet, this is an interesting target because if this is a grazing eclipse, a companion star would have a higher-amplitude radial velocity signal than an exoplanet due to its larger mass. The lack of such a radial velocity signal is puzzling because even taking the orbital inclination of $38.7^{+3.9}_{-3.0}{}^\circ$ and $m \sin i < 0.1$ into account, results in an object with a mass of $0.160^{+0.011}_{-0.012} M_J$. This suggests a companion object with a radius significantly larger than a planet but with a mass lower than that of Saturn which doesn't seem to be

feasible.

It can be argued that the lack of radial velocity detections is due to a blended star that is unresolvable by SuperWASP, SOPHIE and PIRATE. SOPHIE has a minimum resolving power of 3 arcseconds due to the optical fiber aperture used in the spectograph, while PIRATE has observed the target down to a resolution of 1.26 arcseconds per pixel. Images taken with PIRATE show no sign of a closely blended star which can often take a 'snowman' or figure of 8 like appearence. If a blend is present, it is beyond PIRATE's ability to detect it and hence would also be blended in both SuperWASP and SOPHIE. This would not only impact the radial velocity measurements but photometry measurements too. Several star catalogues (USNO-B1.0, GSC 2.3.2, UCAC4, APASS DR9 and Gaia DR1) have been checked with no evidence for a blend being found within 12 arcseconds of the target star.

With the evidence currently available this target produces a conundrum as there is certainly a periodic signal. Potentially, the radial velocity measurements could have been taken at the wrong times, although no observation timings are supplied to confirm or reject this conjecture. Proceeding forward, up to date photometry should be collected to further refine and correct the ephemeris. Furthermore, the radial velocity measurements should be revisited and confirmed to be on target. The blend scenario case should also be investigated further using equipment with significantly higher resolution than that of PIRATE.

3.4.2 1SWASPJ215011.04+514800.8

This target was observed by PIRATE on the night of 2012-08-13 using the PIRATE Mk 2 set-up. Images were obtained using 45 s unbinned exposures in the R filter. Due to issues tracking the target past the meridian, the observing run was aborted at an orbital phase of $\sim$1.08 and promptly restarted. As part of the resubmission a pier flip and focusing run occur that results in a significant data offset if reduced as a single run (see Fig. 3.10). The entire data set is affected by large FWHM stars (see Fig. 3.11) which

start at ∼2.5” and gradually decay to ∼4.5”. The re-focusing temporarily relieves this issue but it can be seen to worsen as the observations continue.

As a fixed aperture size is used in the reduction pipeline, and as the master frame selection process typically results in the best focused images being selected, a small aperture will typically be used. In this instance a FWHM of 3.8 pixels (2.4”) is defined, this large amplitude change in FWHM results in flux being missed outside of the measuring aperture. There is also the potential that this will contaminate the sky background measuring aperture, which in this instance has an inner radius starting at 11.8 pixels (7.4”) from the centre of the star measuring aperture. For this particular case, the sky background contamination, if present, will be minor.

Within the SuperWASP aperture of the target star there is another star that also shows a large flux drop (see lower image in Fig. 3.10) of at least ∼15%. This star is strongly blended with a brighter star in PIRATE’s images and the shape of the lightcurve suspiciously mirrors the change in FWHM. As such, this casts serious doubt that the signal seen in this star is real, although the timing of the event does correspond to the expected transit timing of 6153.507 HJD according to the SuperWASP Hunter pages. The observations for the night presented here have had both sides of the pier flip separately re-reduced and it is noted that the pipeline is unable to locate and identify the nearby blended star, adding further weight to the conclusion that this signal is unlikely to be real.

Once again, the SuperWASP MCMC code (version 3.14) is used on the SuperWASP and both the PIRATE photometry data sets for the target star with the MCMC MS switch set to on as the SuperWASP hunter pages list the target as a G2 effective temperature star and the giant flag has been set to ‘False’. This provides the fits shown in Fig. 3.12 as well as the system parameters shown in Tab. 3.4.2. The PIRATE lightcurve shows a roughly 3% transit which the MCMC has issues fitting through the data points, likely due to the large errors associated with the measurements, and models a $1.84^{+0.23}_{-0.19}$% change. The shape of the curve is also quite ‘V’ shaped with a large impact parameter of $0.795^{+0.04}_{-0.05}R_*$.

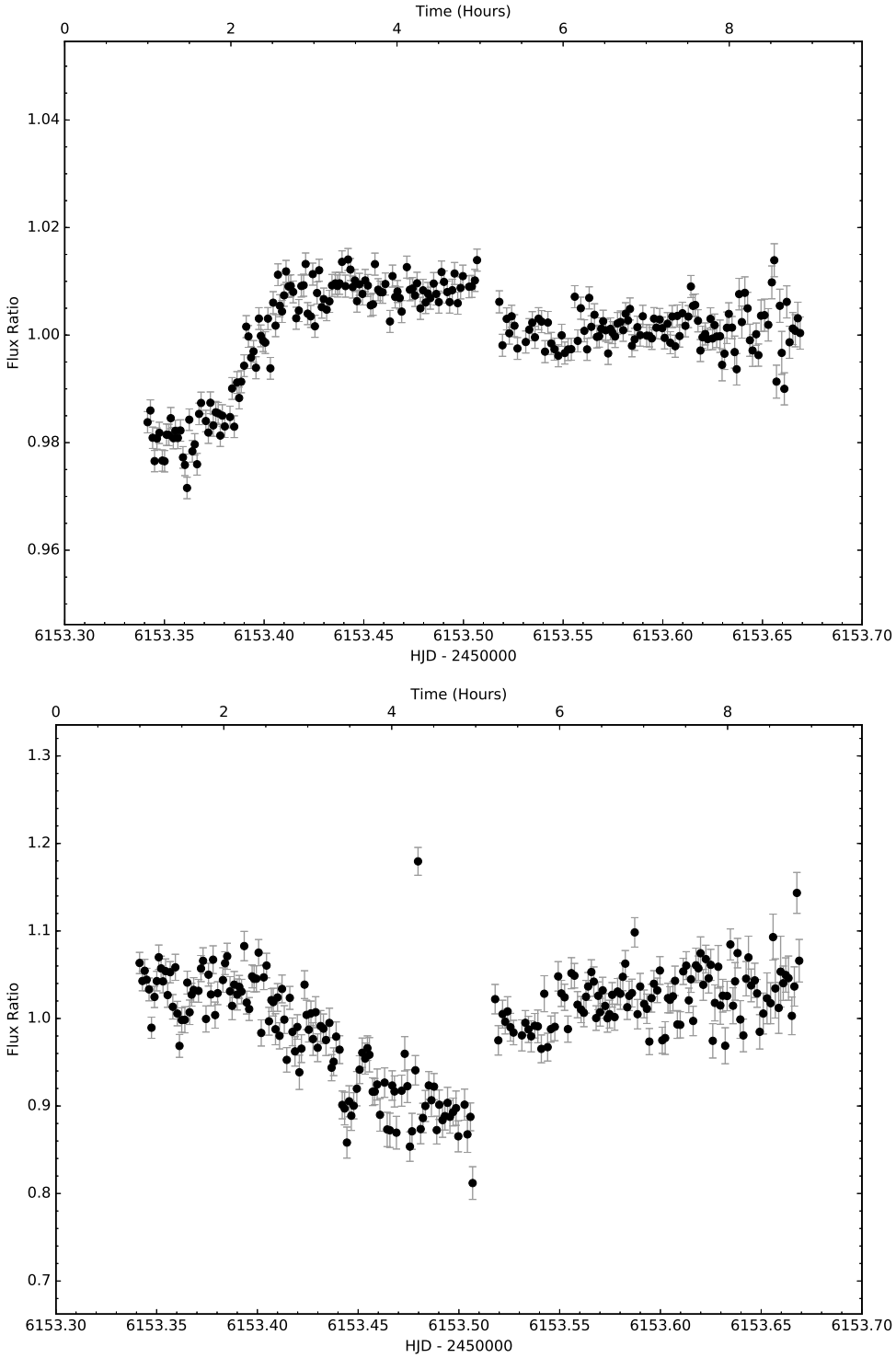

Figure 3.10: PIRATE lightcurves for the night of 2012-08-13. The target (top) is showing a recovery from a drop in flux of ∼3% between 6153.33 HJD and 6153.42 HJD while a nearby blended star has a change in flux of at least 16% between 6153.40 HJD and 6153.51 HJD. The gap in the data at 6153.51 HJD is due to a pier flip and refocusing event which also causes the data offset following 6153.51 HJD.

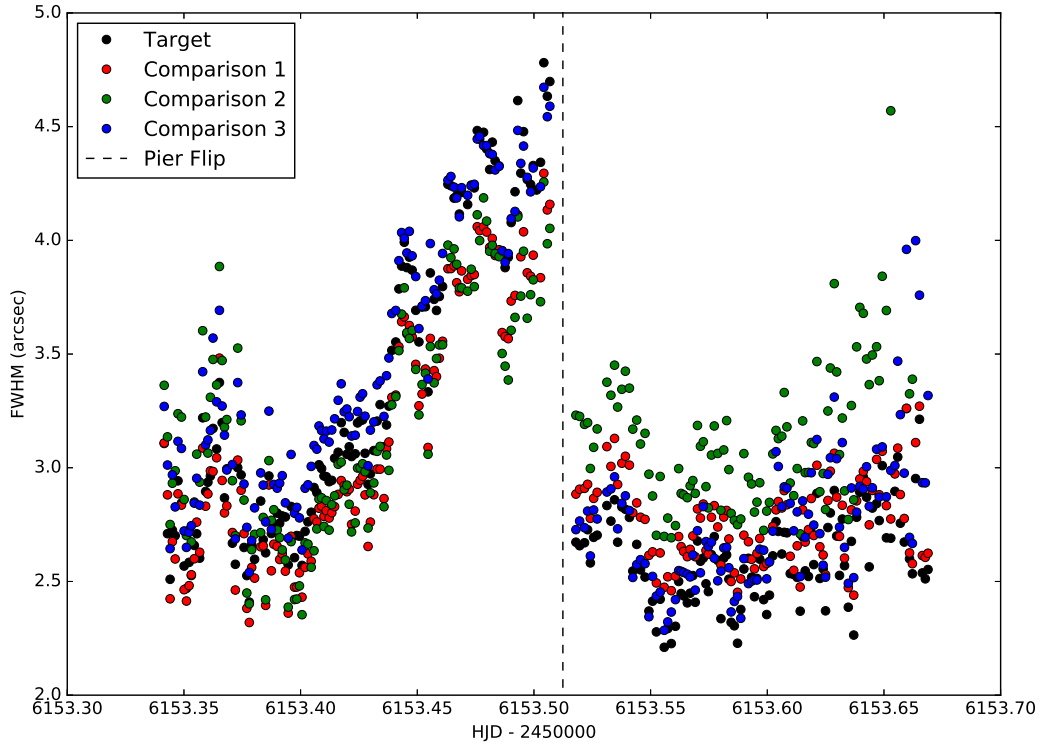

Figure 3.11: The FWHM in arcseconds for the target and three comparison stars. A pier flip and re-focusing, denoted by the vertical dashed line, occurs partway through the data.

The MCMC output provides an ingress duration of $0.01912^{+0.0040}_{-0.0006}$ days which, given the entire transit duration, implies that the transit floor makes up $\sim$50.5% of the transit. However, the PIRATE data is rather noisy due to the poor seeing conditions as well as the focus drift and is poorly fit by the MCMC code. Based on these data sets alone it is difficult to completely rely on the MCMC output for the transit shape, but it does aid in refining the ephemeris which had drifted (or been altered by the tentatively blended star event) by $\sim$3.48 hours. Further observations are required to both refine the transit parameters and identify if the blended star is a real periodic event.

3.5 Published Planets

Throughout the course of this work, several planets have been identified which have made use of PIRATE photometry for the discovery papers. Here, WASP-54b and

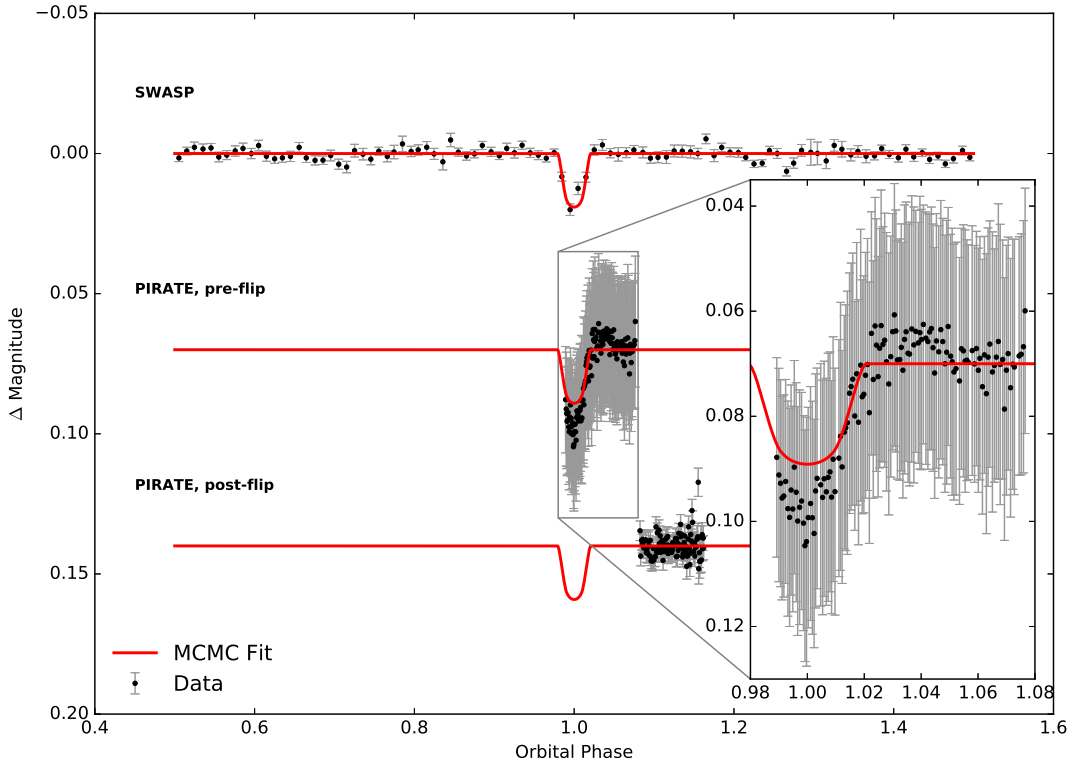

Figure 3.12: SWASP folded and binned lightcurve as well as PIRATE lightcurves for the night of 2012-08-13. The PIRATE data has pre and post flip data reduced separately. The modelled red line is MCMC generated with a stellar main sequence mass-radius relationship enforced.

WASP-56b (Faedi et al. 2013), WASP-65b (Gómez Maqueo Chew et al. 2013), and recently submitted WASP-93b (Hay et al. 2016) are mentioned along with PIRATE's observational details. The published parameters for these planets are shown in Table 3.5.

In addition to the previously mentioned exoplanets, PIRATE has also attempted observations of several other planets. For some targets, PIRATE has not been included in the publications due to a lack of usable data while some other targets are still awaiting publication. Table 3.5 lists all of PIRATE observations of known exoplanets.

3.5.1 WASP-54b

WASP-54b (Faedi et al. 2013) was found to be a highly bloated planet with a radius and mass of $1.653^{+0.090}_{-0.083} R_J$ and $0.636^{+0.025}_{-0.024} M_J$ respectively, orbiting its host star every $3.6936411^{+0.0000043}_{-0.0000074}$ days. The host star is a F9 star with a V magnitude of 10.42.

Table 3.2: System parameters and 1σ error limits derived from the MCMC analysis of 1SWASPJ215011.04+514800.8.

Parameter	Symbol	Value	Units
Stellar Parameters			
Stellar mass	M_*	$1.021^{+0.027}_{-0.025}$	$M_\odot$
Stellar radius	R_*	$1.026^{+0.054}_{-0.049}$	$R_\odot$
Stellar surface gravity	$\log g_*$	$4.424^{+0.037}_{-0.038}$	cgs
Stellar density	ρ_*	$0.94^{+0.14}_{-0.12}$	$\rho_\odot$
Planet Parameters			
Planet mass	M_p	-	M_J
Planet radius	R_p	$1.35^{+0.14}_{-0.11}$	R_J
Planet equilibrium temperature	T_{eq}	1594^{+53}_{-49}	K
Orbital Parameters			
Epoch (BJD - 2450000.0)	T_0	$5592.8839^{+0.0035}_{-0.0040}$	days
Orbital period	P	$1.8935066^{+0.0000054}_{-0.0000063}$	days
Transit duration	t_T	$0.0773^{+0.0025}_{-0.0026}$	days
Planet/star area ratio	$(R_p/R_*)^2$	$0.0184^{+0.0023}_{-0.0019}$	
Impact parameter	b	$0.795^{+0.043}_{-0.045}$	R_*
Orbital inclination	i	$82.77^{+0.67}_{-0.69}$	$\circ$
Orbital eccentricity	e	0 (fixed)	
Orbital separation	a	$0.03016^{+0.00027}_{-0.00025}$	AU

The planet has a transit depth and duration of 0.86 ± 0.02 % and $0.1863^{+0.0015}_{-0.0018}$ days respectively. There are indications of an eccentric orbit ($0.067^{+0.033}_{-0.025}$), although further observations are recommended to refine the orbital parameters.

PIRATE observed WASP-54b twice on the nights of 2012-03-22 and 2012-04-17 (see Fig. 3.13) using the PIRATE Mk2 configuration, with both data sets being used for the discovery paper Faedi et al. (2013). The 2012-03-22 observation acquired 152 usable R band frames with 60s exposures while the 2012-04-17 observation acquired 165 usable R band frames with 25s exposures. In both instances, only partial coverage was obtained, which included the ingress and transit floor, with the second observation not acquiring any out of transit data.

Table 3.3: Published system parameters for WASP-54b and WASP-56b (Faedi et al. 2013), WASP-65b (Gómez Maqueo Chew et al. 2013) and WASP-93b (Hay et al. 2016)). Notes: $^{(a)}$ Faedi et al. (2013) provide circular and eccentric orbital parameter solutions for WASP-54b, the eccentric results are shown here. $^{(b)}$ WASP-93b parameters are currently submitted for peer review and subject to change. $^{(c)}$ Epoch is in HJD rather than BJD.

Parameter	Symbol	WASP-54b$^{(a)}$	WASP-56b	WASP-65b	WASP-93b$^{(b)}$	Units
Stellar Parameters						
Stellar mass	M_*	1.213 ± 0.032	1.017 ± 0.024	0.93 ± 0.14	1.334 ± 0.033	$M_\odot$
Stellar radius	R_*	$1.828^{+0.091}_{-0.081}$	$1.112^{+0.026}_{-0.022}$	1.01 ± 0.05	1.524 ± 0.040	$R_\odot$
Stellar surface gravity	$\log g_*$	$3.997^{+0.032}_{-0.035}$	4.35 ± 0.02	4.40 ± 0.02	4.197 ± 0.019	cgs
Stellar density	ρ_*	$0.198^{+0.025}_{0.024}$	0.74 ± 0.04	$0.91^{+0.03}_{-0.04}$	0.376 ± 0.028	$\rho_\odot$
Planet Parameters						
Planet mass	M_p	$0.636^{+0.025}_{-0.024}$	$0.571^{+0.034}_{-0.035}$	1.55 ± 0.16	1.47 ± 0.29	M_J
Planet radius	R_p	$1.653^{+0.090}_{-0.083}$	$1.092^{+0.035}_{-0.033}$	1.112 ± 0.059	1.597 ± 0.077	R_J
Planet surgace gravity	$\log g_p$	2.726 ± 0.042	$3.039^{+0.035}_{-0.038}$	$3.458^{+0.014}_{-0.018}$	3.120 ± 0.093	cgs
Planet density	ρ_p	$0.141^{+0.022}_{-0.019}$	$0.438^{+0.048}_{-0.046}$	$1.13^{+0.07}_{-0.08}$	0.360 ± 0.084	ρ_J
Planet equilibrium temperature	T_{eq}	1759 ± 46	1216^{+25}_{-24}	1480 ± 10	1942 ± 38	K
Orbital Parameters						
Epoch (BJD - 2450000.0)	T_0	$5518.35087^{+0.00049}_{-0.00056}$	5730.799 ± 0.001	6110.68772 ± 0.00015	$6079.56420 \pm 0.00045^{(c)}$	days
Orbital period	P	$3.6936411^{+0.0000043}_{-0.0000074}$	$4.617101^{+0.000004}_{0.000002}$	2.3114243 ± 0.0000015	2.7325321 ± 0.0000020	days
Transit duration	t_T	$0.1863^{+0.0015}_{-0.0018}$	0.1484 ± 0.0025	0.11396 ± 0.00045	0.0931 ± 0.0010	days
Planet/star area ratio	$(R_p/R_*)^2$	0.0086 ± 0.0002	0.01019 ± 0.00041	0.01280 ± 0.00015	0.01097 ± 0.00013	
Impact parameter	b	$0.490^{+0.026}_{-0.044}$	$0.272^{+0.029}_{-0.018}$	$0.149^{+0.082}_{-0.095}$	0.9036 ± 0.009	R_*
Orbital inclination	i	$84.97^{+0.63}_{-0.59}$	$88.5^{+0.1}_{-0.2}$	$88.8^{+0.8}_{-0.7}$	81.18 ± 0.29	$^\circ$
Orbital eccentricity	e	$0.067^{+0.033}_{-0.025}$	0 (fixed)	0 (fixed)	0 (fixed)	
Orbital separation	a	0.04987 ± 0.00044	0.05458 ± 0.00041	$0.0334^{+0.0016}_{-0.0017}$	2.685 ± 0.245	AU

Table 3.4: PIRATE observation details of known exoplanets. The Observers are R. Busuttil (RB), S. Holmes (SH), J.J Bochinski (JJB), J.F. Jarvis and S. Hadigal (SH2). The '?' represent missing reductions while the 'Unknown' represents poor data and/or ephemerides making the transit coverage, if any, difficult to determine.

Exoplanet	Observer	Date (Y/M/D)	PIRATE	Filter	Exposure (s)	N_{points}	Transit Coverage?	Used in Publication?
WASP-54b	JJB	2012-03-22	Mk 2	R	60	152	Partial	Y
	JJB	2012-04-17	Mk 2	R	20	165	Partial	Y
WASP-56b	RB	2011-12-05	Mk 2	R	60	109	Partial	Y
	RB	2011-12-06	Mk 2	R	60	94	OOT	Y
WASP-58b	RB	2012-02-18	Mk 2	R	120	56	Partial	N
WASP-59b	RB	2011-12-06	Mk 2	R	60	102	Partial	N
	RB	2012-08-23	Mk 2	R	120	111	Partial	N
WASP-60b	SH	2010-10-27	Mk 1.5	R	45	?	?	N
	SH2	2012-07-25	Mk 2	R	60	?	?	N
	RB	2012-08-24	Mk 2	R	120	111	Partial	N
	RB	2012-09-06	Mk 2	R	75	203	Full	N
WASP-65b	RB	2012-01-19	Mk 2	R	60	197	Full	Y
	RB	2012-02-18	Mk 2	R	120	105	Partial	Y
	RB	2012-03-02	Mk 2	R	150	46	OOT	Y
	RB	2012-03-03	Mk 2	R	180	100	Full	Y
WASP-69b	RB & SH2	2012-06-29	Mk 2	R	40	72	Partial	N
WASP-70b	JJB	2012-10-03	Mk 2	R	60	?	?	N
WASP-85b	RB	2013-02-21	Mk 2	R	120	?	?	N
WASP-86b	RB	2012-07-23	Mk 2	R	90	146	Partial	N (in prep)
WASP-92b	RB	2012-07-24	Mk 2	R	150	77	Partial	N
	RB	2012-08-19	Mk 2	R	120	102	Partial	N
WASP-93b	SH	2010-12-29	Mk 1.5	R	30	104	Partial	N
	SH	2010-12-29	Mk 1.5	B	60	104	Partial	N
	RB	2011-10-31	Mk 2	R	45	155	Full	Y
	RB	2012-07-22	Mk 2	R	120	87	Partial	N
	RB	2012-09-09	Mk 2	R	90	114	OOT	N
	RB	2013-09-02	Mk 2	R	90	34	Full	Y
	RB	2013-09-05	Mk 2	R	70	145	Partial	N
	RB	2013-10-16	Mk 2	R	210	58	Full	N
WASP-125b	RB	2013-03-02	Mk 2	R	60	75	Unknown	Not Published
	JFJ	2014-03-27	Mk 1.5	R	60	34	Unknown	Not Published
	JFJ	2014-04-16	Mk 1.5	R	60	35	Unknown	Not Published

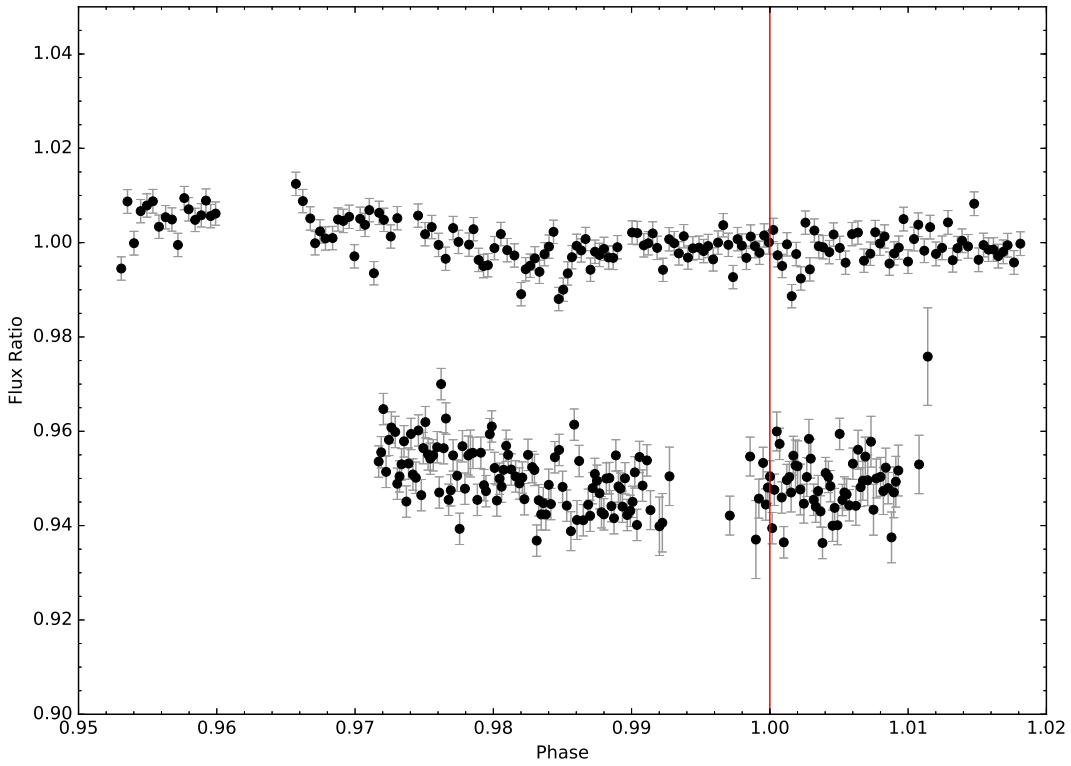

Figure 3.13: PIRATE lightcurves for WASP-54b plotted against the orbital phase. The top plot is for the night of 2012-03-22 and the bottom (offset) is for 2012-04-17. The vertical red line is were the transit is expected to occur.

3.5.2 WASP-56b

WASP-56b (Faedi et al. 2013) was found to have a radius and mass of $1.092^{+0.035}_{-0.033}$ R_J and $0.571^{+0.034}_{-0.035}$ M_J respectively, orbiting its host star every $4.617101^{+0.000004}_{0.000002}$ days. The host star is a G6 star with a V magnitude of 11.484. The planet has a transit depth and duration of 1.019 ± 0.041 % and 0.1484 ± 0.0025 days respectively.

WASP-56b was observed twice, using PIRATE Mk 2, on the nights of 2011-12-05 and 2011-12-06 (see Fig. 3.14). Once again, both data sets were used in the discovery paper with the first night acquiring 109 usable R band frames and the second acquiring 94 usable R band frames. Both nights used 60s exposures and the first night captured mid transit and egress, while the second night consisted soley of out of transit data. Despite the lack of transit data in the second night, the out of transit data can still be useful for refining ephemerides.

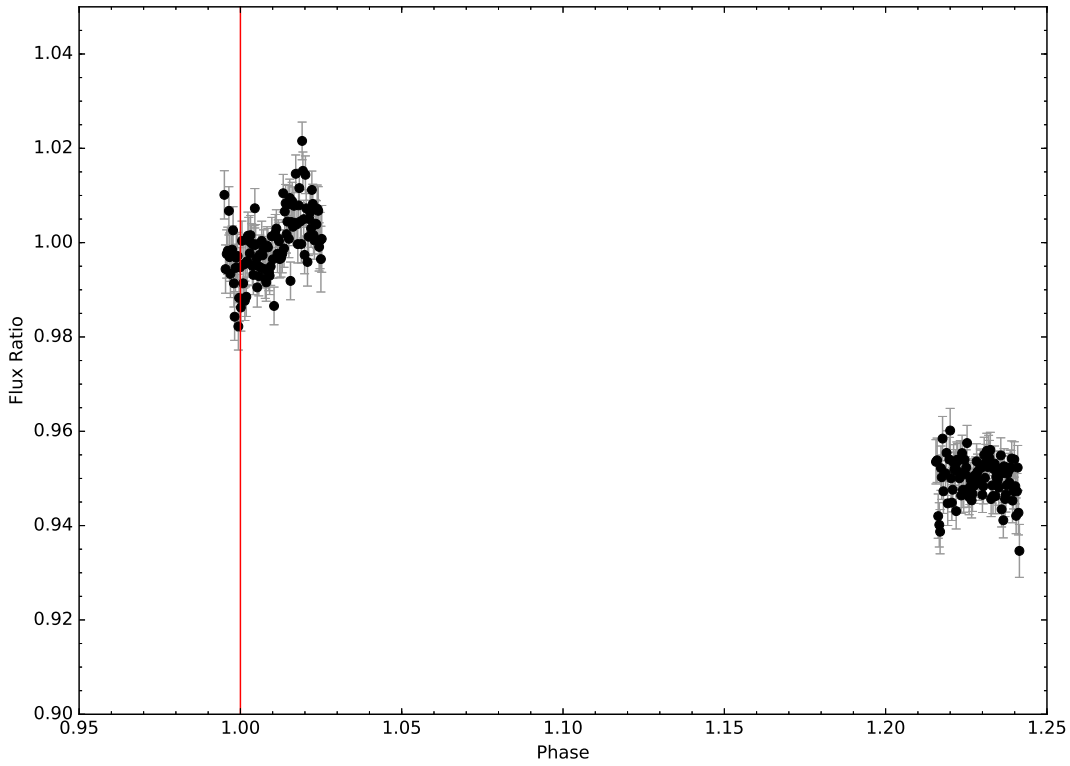

Figure 3.14: PIRATE lightcurves for WASP-56b plotted against the orbital phase. The top plot is for the night of 2011-12-05 and the bottom (offset) is for 2011-12-06. The vertical red line is were the transit is expected to occur.

3.5.3 WASP-58b

WASP-58b (Hébrard et al. 2013) was found to have a radius and mass of 1.27 ± 0.2 R_J and 0.89 ± 0.07 M_J respectively, orbiting its host star every 5.017180 ± 0.000011 days. The host star is a G2V star with a V magnitude of 11.66. The planet has a transit depth and duration of 1.45 ± 0.10 % and 0.1582 ± 0.0043 days respectively.

WASP-58b was observed using PIRATE Mk 2 on 2012-02-18 (see Fig. 3.15). The data is of low quality and didn't show any planet like transits. Hence, it was not uploaded to the SuperWASP hunter pages and in turn was not used in the discovery paper. Exposures of 120s in the R filter were taken and a potentially partial transit can now be seen. Although there is no obvious planetary transit there is an increase in flux after the mid-transit of $\sim$2%. Potentially, this could have been the egress, and in retrospect the data should have been uploaded.

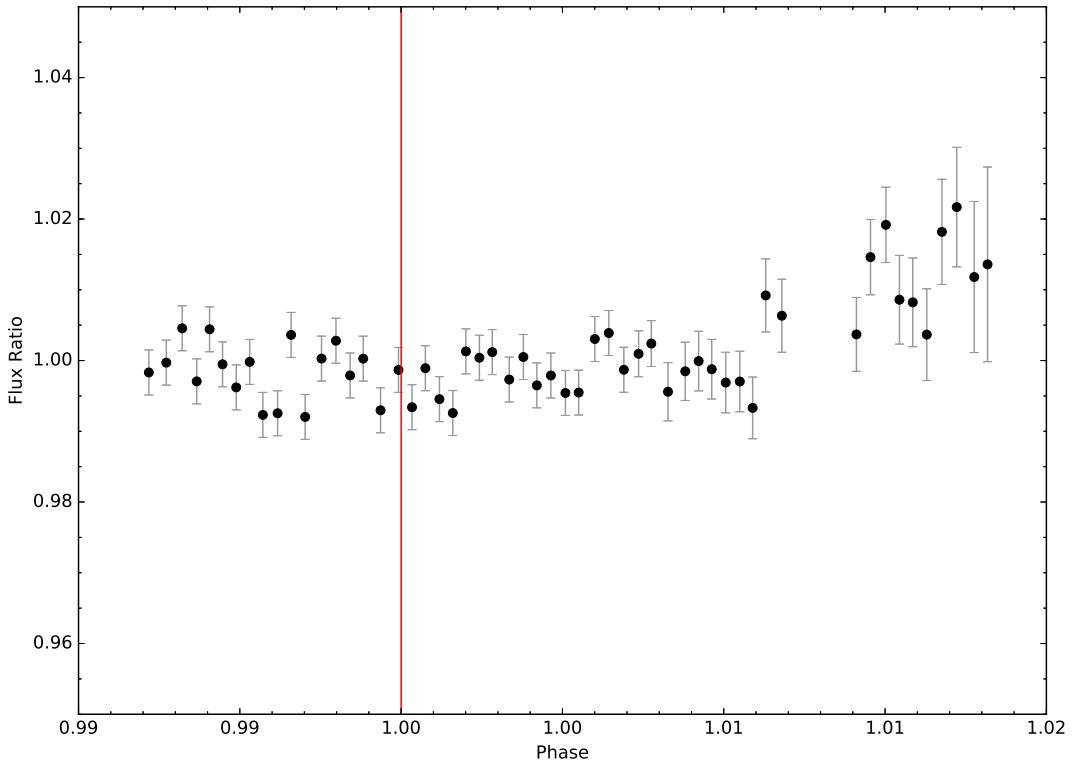

Figure 3.15: PIRATE lightcurves for WASP-58b plotted against the orbital phase. The plot shows data from the night of 2012-02-18. The vertical red line is were the transit is expected to occur.

3.5.4 WASP-59b

WASP-59b (Hébrard et al. 2013) was found to have a radius and mass of 0.775 ± 0.068 R_J and 0.863 ± 0.045 M_J respectively, orbiting its host star every 7.919585 ± 0.000010 days. The host star is a K5V star with a V magnitude of 13.00. The planet has a transit depth and duration of 1.69 ± 0.08 % and 0.102 ± 0.002 days respectively.

WASP-59b was observed twice using PIRATE Mk 2 on the nights of 2011-12-06 and 2012-08-23 (see Fig. 3.16). Exposures of 60s and 120s in the R filter were taken respectively. The data for 2011-12-06, is very noisy making it difficult to discern any notable pattern however the observation does coincide with the expected mid-transit point. The second data set shows an ingress-like shape at the end but coincided with detrimental conditions and was believed to be a false signal.

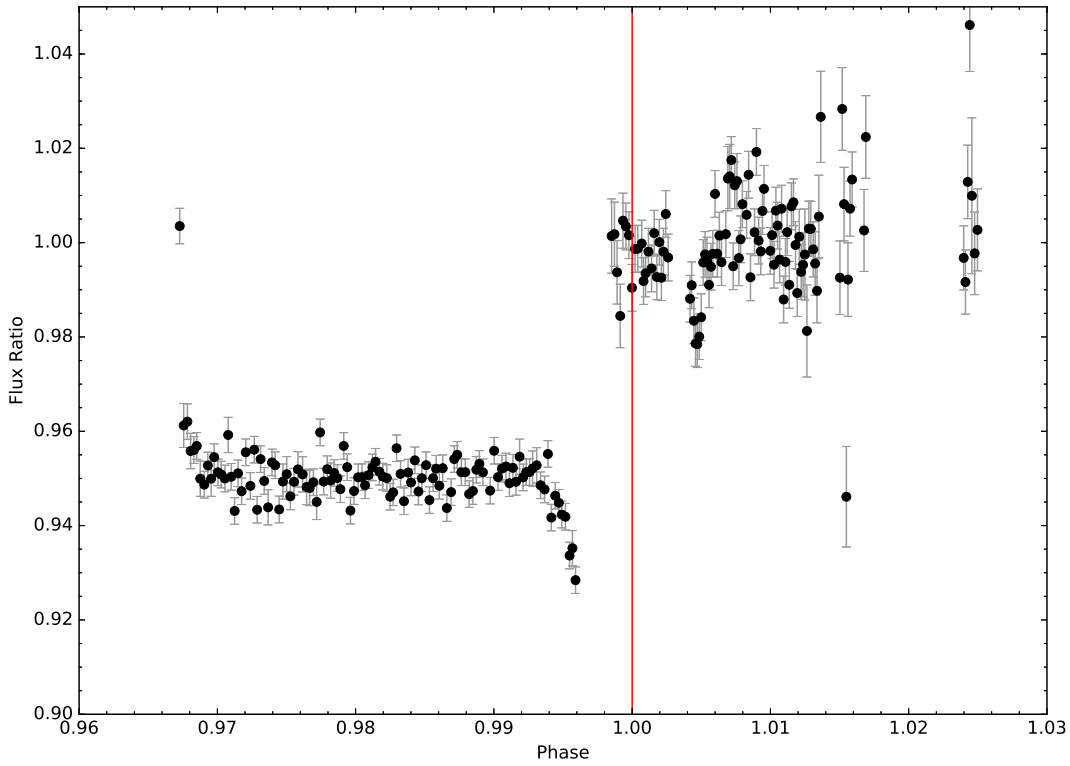

Figure 3.16: PIRATE Lightcurves for WASP-59b plotted against the orbital phase. The top plot is for the night of 2011-12-06 and the bottom (offset) is for 2012-08-23. The vertical red line is were the transit is expected to occur.

3.5.5 WASP-60b

WASP-60b (Hébrard et al. 2013) was found to have a radius and mass of $0.86 \pm 0.12\ R_J$ and $0.514 \pm 0.034\ M_J$ respectively, orbiting its host star every 4.3050011 ± 0.0000062 days. The host star is a G1V star with a V magnitude of 12.18. The planet has a transit depth and duration of 0.60 ± 0.06 % and 0.139 ± 0.005 days respectively.

WASP-60b was observed four times, once with PIRATE Mk 1.5 on the night of 2010-10-27, and the remainder using PIRATE Mk 2 on the nights of 2012-07-25, 2012-08-24 and 2012-09-06 (see Fig. 3.17). All observations were in the R filter with exposures of 45s, 60s, 120s an 75s respectively. For the nights of 2010-10-27 and 2012-07-25, the data was unusable. On 2012-08-24 there is a potential transit, however the data is plagued by noise at this point preventing any meaningful interpretation of the data. For the night of 2012-09-05, there is no obvious sign of a transit, although there is an increase in noise where the transit is expected to occur.

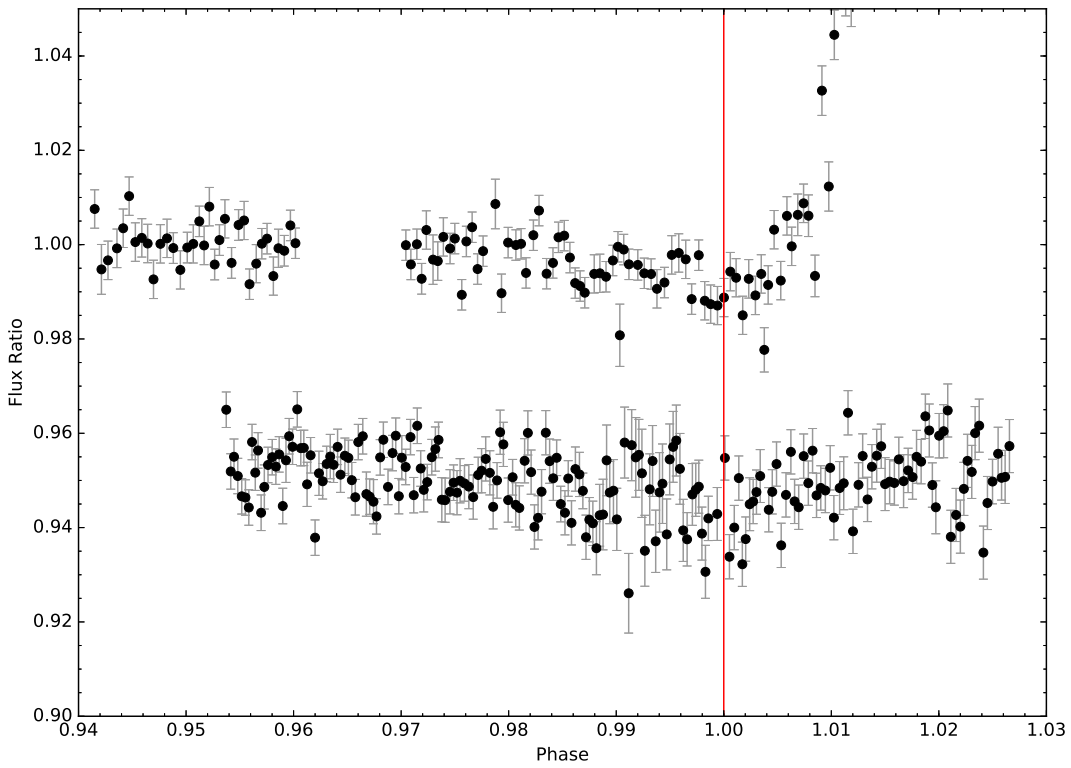

Figure 3.17: PIRATE Lightcurves for WASP-60b plotted against the orbital phase. The top plot is for the night of 2012-08-24 and the bottom (offset) is for 2012-09-06. The vertical red line is were the transit is expected to occur.

3.5.6 WASP-65b

WASP-65b (Gómez Maqueo Chew et al. 2013) was found to have a radius and mass of $1.112 \pm 0.059\, R_J$ and $1.55 \pm 0.16\, M_J$ respectively, orbiting its host star every 2.3114243 ± 0.0000015 days. It is one of the densest discovered planets in the 0.1 to 2.0 M_J mass range with a density of $1.13^{+0.07}_{-0.08}\rho_J$. The host is a G6 star with a V magnitude of 11.90. The planet has a transit depth and duration of 1.280 ± 0.015 % and 0.11396 ± 0.00045 days respectively.

Four observations of WASP-65b were collected using PIRATE Mk 2 on the nights of 2012-01-19, 2012-02-18, 2012-03-02 and 2012-03-03 (see Fig. 3.18). The observations were all acquired in the R band with the following number of respective usable frames: 197, 105, 46 and 100. Exposure durations for these frames were 60s, 120s, 150s and 180s. The 2012-02-18 observation captured the ingress along with pre-ingress out of transit data and contributed to the MCMC modelling of WASP-65b. The

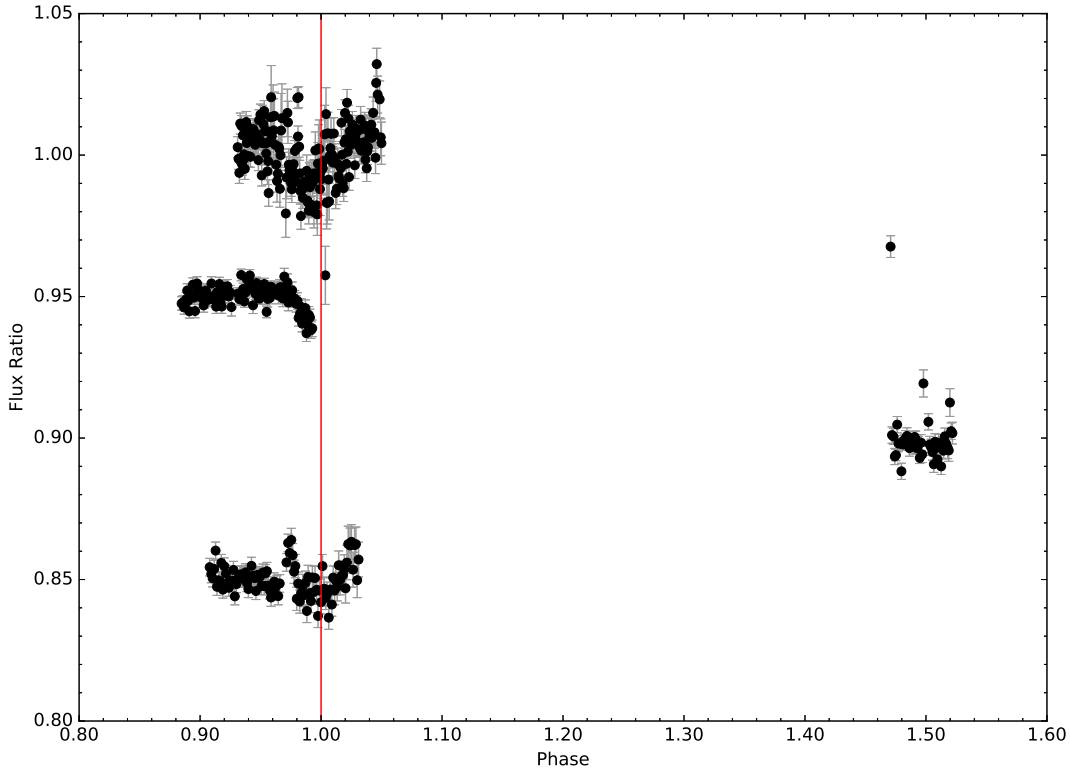

Figure 3.18: PIRATE lightcurves for WASP-65b plotted against the orbital phase. From the top, the plots are for the nights of 2012-01-19, 2012-02-18, 2012-03-02 and 2012-03-03. The vertical red line is were the transit is expected to occur.

other observations covered both out of transit and in transit data under poor weather conditions and were only used to refine the ephemeris of the transit.

3.5.7 WASP-69b

WASP-69b (Anderson et al. 2014) was found to have a radius and mass of $1.057 \pm 0.047\ R_J$ and $0.260 \pm 0.017\ M_J$ respectively, orbiting its host star every 3.8681382 ± 0.0000017 days. The host star is a K5 star with a V magnitude of 9.87 ± 0.02. The planet has a transit depth and duration of 1.786 ± 0.042 % and 0.0929 ± 0.0012 days respectively.

WASP-69b was observed using PIRATE Mk 2 on the night of 2012-06-29 (see Fig. 3.19).. The observation consisted of 40s exposures using the R filter. Due to poor weather conditions the data is of low quality and there are no obvious signs of a transit.

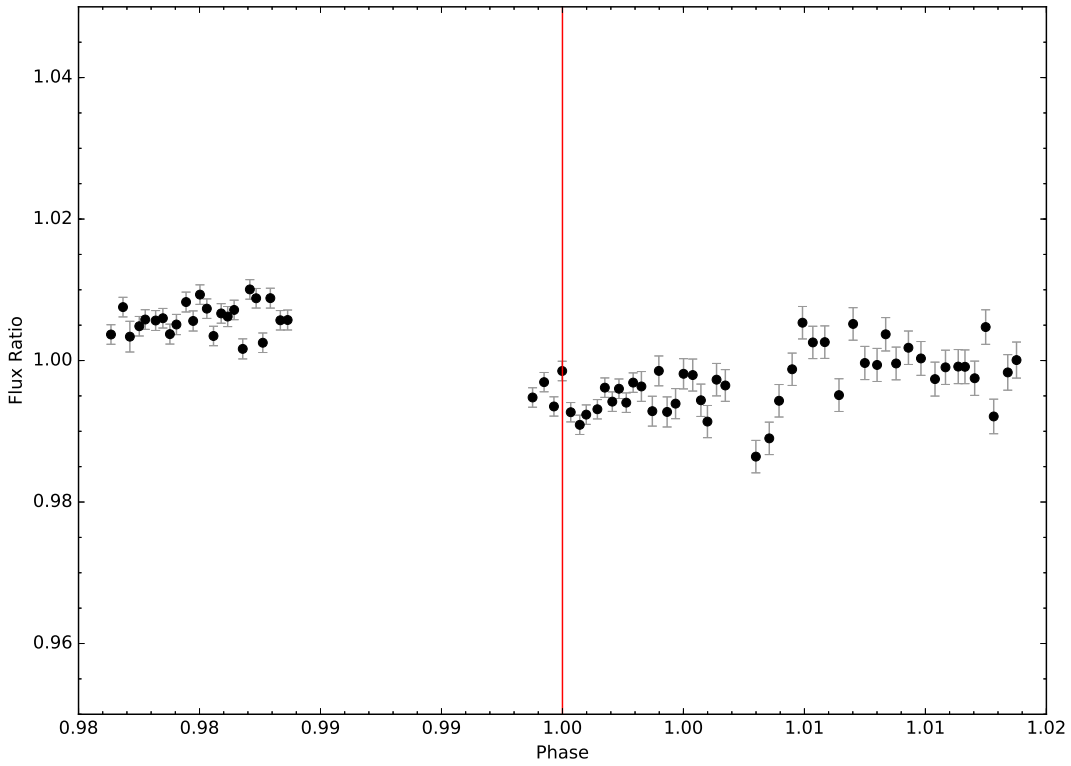

Figure 3.19: PIRATE Lightcurve for WASP-69b plotted against the orbital phase. The plot shows data from the night of 2012-06-29. The vertical red line is were the transit is expected to occur.

3.5.8 WASP-86b

WASP-86b Faedi et al. (2016) was found to have a radius and mass of $0.632^{+0.014}_{-0.013}$ R_J and 0.821 ± 0.056 M_J respectively, orbiting its host star every 5.031555 ± 0.000002 days. The host star is a F7 star with a V magnitude of 10.66 ± 0.05. The planet has a transit depth and duration of 0.25 ± 0.008 % and $0.1674^{+0.0015}_{-0.0010}$ days respectively.

WASP-86b was observed on the night of 2012-07-23 using PIRATE Mk 2 (see Fig. 3.20).. It was observed using 90s exposures in the R filter. The lightcurve and showed a 0.5% ingress which coincided with deteriorating weather conditions. The slope of the ingress also looks 'V' shaped rather than 'U' shaped emphasised by the sharp egress. If this is the transit, it appears to be too deep and is not in phase with expected transit time.

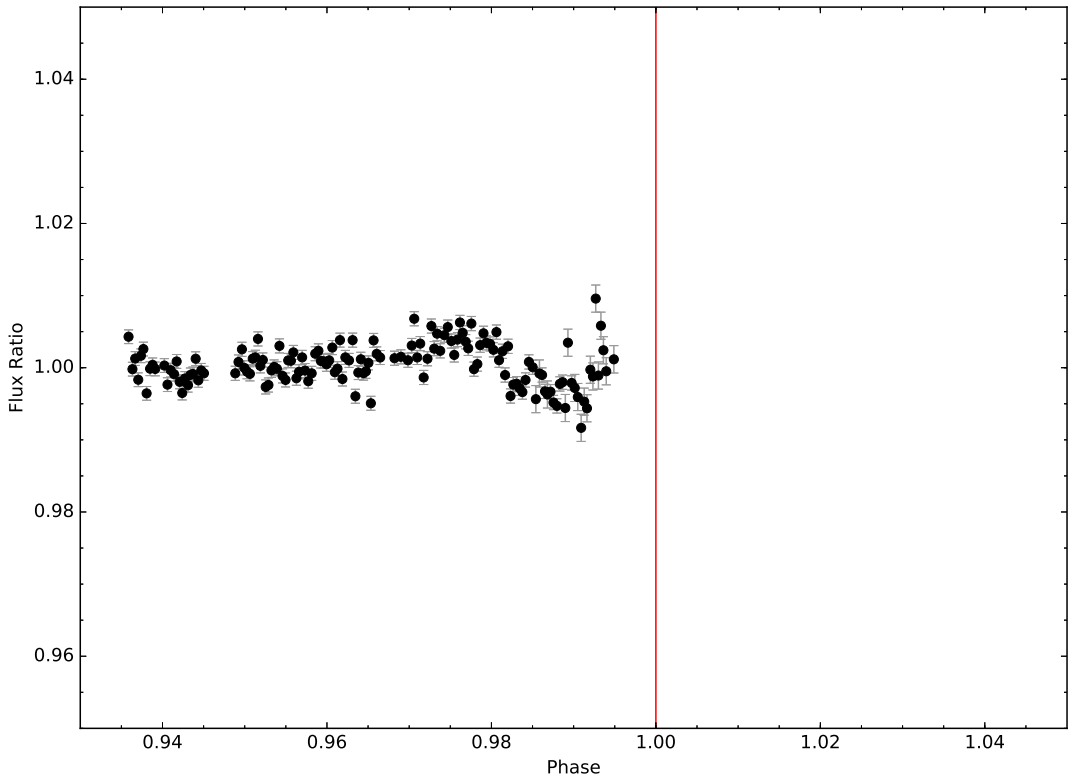

Figure 3.20: PIRATE Lightcurves for WASP-86b plotted against the orbital phase. The plot shows data from the night of 2012-07-23. The vertical red line is were the transit is expected to occur.

3.5.9 WASP-92b

WASP-92b (Hay et al. 2016) was found to have a radius and mass of 1.461 ± 0.077 R_J and 0.805 ± 0.68 M_J respectively, orbiting its host star every 2.1746742 ± 0000016 days. The host is a F7 star with a V magnitude of 13.18. The planet has a transit depth and duration of 1.254 ± 0.029 % and 0.1153 ± 0.0012 days respectively.

WASP-92b was observed twice using PIRATE Mk 2 on the nights of 2012-07-24 and 2012-08-19 (see Fig. 3.21). Both observations made use of the R filter with the first observation using 150s exposures and the second using 120s exposures. Despite both nights covering the expected transit time there is no sign of an exoplanet transit. This is attributed to too much data scatter and noise.

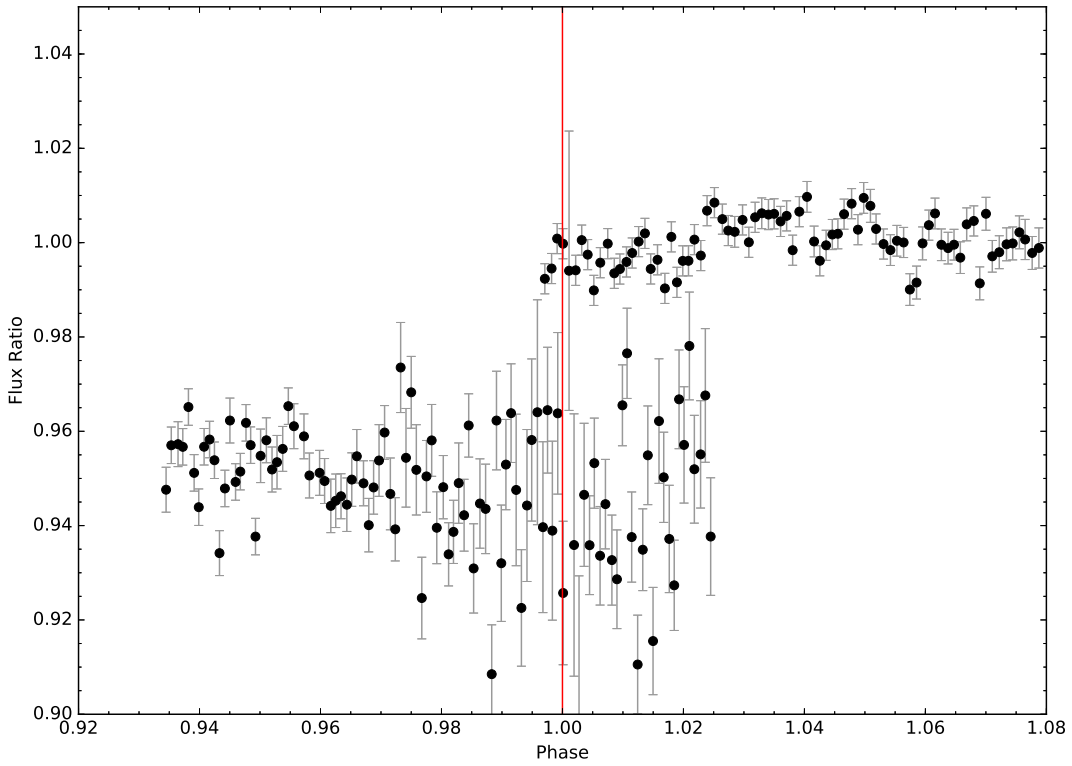

Figure 3.21: PIRATE Lightcurves for WASP-92b plotted against the orbital phase. The top plot is for the night of 2012-07-24 and the bottom (offset) is for 2012-08-19. The vertical red line is were the transit is expected to occur.

3.5.10 WASP-93b

WASP-93b (Hay et al. 2016) was found to have a radius and mass of $1.597 \pm 0.077\ R_J$ and $1.47 \pm 0.29\ M_J$ respectively, orbiting its host star every 2.7325321 ± 0.0000020 days. The host is a F4 star with a V magnitude of 10.97. The planet has a transit depth and duration of 1.097 ± 0.013 % and 0.0931 ± 0.0010 days respectively.

Eight observations of WASP-93b have been acquired by PIRATE. Two filters, R and B band, were used on the night of 2010-12-29 using the PIRATE Mk 1.5 set-up resulting in 104 usable frames per filter with exposures of 30s and 60s respectively. These two observations were of variable quality and unreliable resulting in two transit like signals occuring earlier than expected. These were re-analysed and it was decided to exclude from the WASP-93b paper due to their poor quality. The rest of observations made use of PIRATE Mk 2 and the R band filter on the nights of 2011-10-31, 2012-07-22, 2012-09-09, 2013-09-02, 2013-09-05 and 2013-10-16. This resulted in 155,

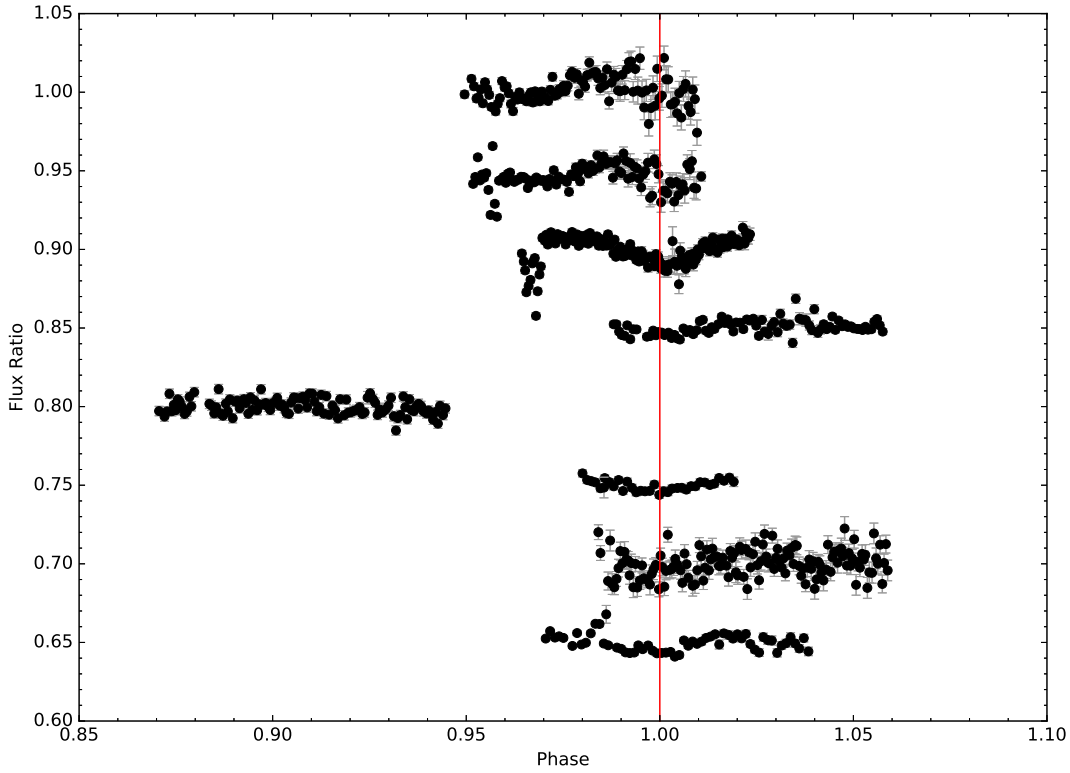

Figure 3.22: PIRATE lightcurves for WASP-93b plotted against the orbital phase. From the top, the plots are for the nights of 2010-12-29 (Mk 1.5 R Filter), 2010-12-29 (Mk 1.5 B Filter), 2011-10-31, 2012-07-22, 2012-09-09, 2013-09-02, 2013-09-05 and 2013-10-16. The vertical red line is were the transit is expected to occur.

87, 114, 34, 145 and 58 usable frames respectively with exposures of 45s, 120s, 90s, 90s, 70s and 210s respectively. The 2012-09-09 observation covered only out of transit data while 2012-07-22 and 2013-09-05 covered partial transits. The remaining three observations covered full transit events, although only the 2011-10-31 and 2012-07-22 observations were used in the publication as the 2013-10-16 observation was of a very poor quality.

3.5.11 WASP-125b

WASP-125b is yet to be published but was observed by PIRATE three times. Once was using PIRATE Mk 2 on the night of 2013-03-02 using 60s exposures in the R filter. The other two were observed using the on-off method with PIRATE Mk 1.5 on the nights of 2014-03-27 and 2014-04-16. Both observations used 60s exposures in the R

filter. The night of 2013-03-02 doesn't show any obvious signs of a transit. 2014-03-27 shows a ∼10% increase in flux from the initial observation set (seen on the left of the vertical red line in Fig. 3.23) which is too deep to be a planet. On the right of the vertical red line is the data from 2014-04-16 has data which is of too poor quality to make any inference from.

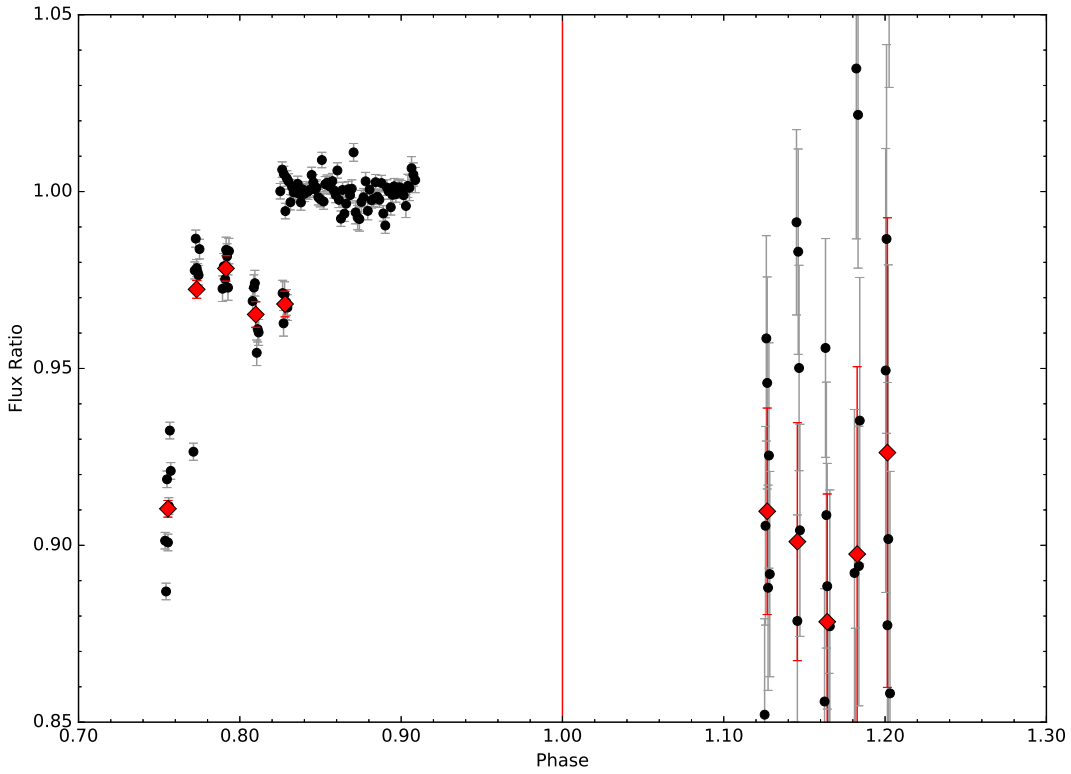

Figure 3.23: PIRATE Lightcurves for WASP-125b plotted against the orbital phase. The top continuous data set is from the night of 2013-03-02. The data set below that is from 2014-03-27 and is offset for clarity. To the right of the vertical red line is the data set from 2014-04-16. The vertical red line is were the transit is expected to occur.

3.6 Observation Statistics

Throughout PIRATE's operation in Mallorca (2009-2015, including PIRATE Mk 1), it has logged 411 observation sessions across 201 SuperWASP exoplanet candidates (see Tab. A.1). Of these 411 observations the author has observed 223 (54.3%). 92 of these observations are unreduceable due to poor weather conditions, insufficient number of science frames (less than 20) or hardware/software issues (eg. poor tracking).

Additionally, 55 other observations are lacking any records of their reductions and the observers have since left the Open University. The remaining 264 observations have resulted in a few candidates being classified as exoplanets and a significantly larger portion being rejected, with several instances being in conjunction with other observatories.

Table 3.5 shows a breakdown of the 201 exoplanet candidate classifications. SuperWASP hunter pages classification, where present, supersede the PIRATE internal classification in this table. Of the 201 candidates, 26 (12.9%) are planets or plausible exoplanets showing transit-like signals. 118 (58.7%) candidates have been rejected for various reasons (41, 20.4%) or due to blending (43, 21.4%), variability and non-planetary grazing eclipses (34, 16.9%). 23 (11.4%) are unclassified due to a lack of data (19, 9.5%) or have a signal which is noisy and leads to an unknown classification (4, 2.0%). The 33 (16.4%) non-detections can be caused by ephemeris drift of the target (and possible blends) or could have a signal below PIRATE's noise limits. The final classification to touch upon is the single 'Other', which in this case is a target which displays both a blended and plausible signal.

Table 3.5: PIRATE's SuperWASP exoplanet candidate classification statistics while located in Mallorca from 2009 to 2015.

Classification	Number of Candidates	Percentage (%)
Planets and plausible planetary candidates	26	12.9
Eclipsing binaries, low mass eclipsing binaries and variable stars	34	16.9
Blend	43	21.4
Non detection	33	16.4
Rejected	41	20.4
Unknown	4	2.0
Unclassified	19	9.5
Other	1	0.5
Total	201	-

These results show that PIRATE's greatest contributions to the SuperWASP project come primarily from the identification of false positives, in particular, blends. PI-

RATE's higher resolution of 0.63 arcsec/pix (PIRATE Mk 2) and 1.69 arcsec/pix (PIRATE Mk 1.5) as compared to SuperWASP's 13.7 arcsec/pix allows for such blends to be easily separated from the target star. PIRATE is capable of observing and contributing to bright SuperWASP exoplanet candidates, although these are typically on the limits of what PIRATE can achieve (see Sec. 3.6.1). Non-detections are also very useful to the SuperWASP project as they allow for refinement of the ephemeris if ephemeris drift is suspected.

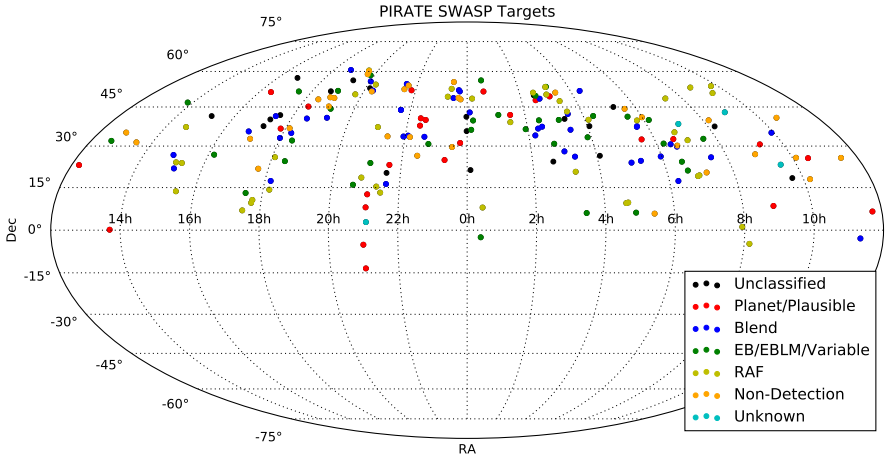

Figure 3.24: PIRATE SuperWASP observations

Fig. 3.24 shows the location of candidates on the sky and the coverage that PIRATE has achieved. Despite the inability to observe during poor weather seasons which can last a month or two, as well as the use of PIRATE for undergraduate teaching commitments, the sky coverage is fairly robust. The figure shows that the bulk of PIRATE's observations lie in the declination range of $\sim 0^\circ$ to $\sim 60^\circ$. Some observations do drop below 0°, although these are typically observed at low altitude (i.e. high airmass) and for short durations, making them less than ideal targets. Overall, PIRATE is able to observe and monitor targets across the entire range of right ascensions and a range of 0 to 60° declinations.

3.6.1 PIRATE's Lightcurve Performance

By examining the RMS scatter of each stellar lightcurve for a given field, it is possible to provide an indication of PIRATE's performance in regards to lightcurve measurements. Fig. 3.25 provides an example of PIRATE's performance for a full lightcurve on the night of 30/10/2013 (blue circles) and an 'on-off' target on the night of 29/06/2013 (red circles). These were generated by taking the instrumental magnitude for all stars on a given night and determining the zero-point by cross-referencing the star position with that from a catalogue. This is then used to scale the instrumental magnitude of the target to the appropriate apparent magnitude for the catalogue used. In this case the UCAC4 catalogue is used as it contains the APASS/r measurements, which are a good match to PIRATE's filter response (see Sec. 5.2.3.1).

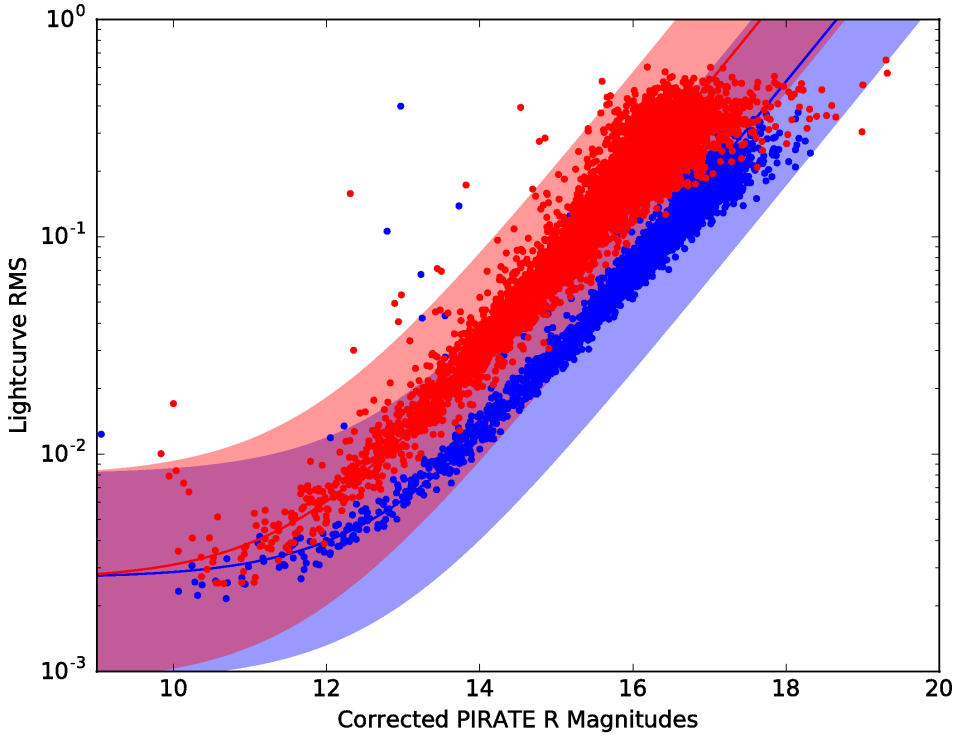

Figure 3.25: Examples of PIRATE's lightcurve RMS scatter for varying magnitudes, calibrated to the UCAC4 catalogue r mag scale. Blue and red points are from the nights of 30/10/2013 and 29/06/2013 and represent a full and on-off data set respectively, taken with the SBIG STX-16803 camera. The lines of associated colour are best fits to the form of $y = a + be^x$ with the transparent colours representing a ± 3 times the RMS scatter range

The results from these two nights indicate that a 1% flux change would be smaller than the RMS scatter for magnitudes fainter than 13.74 and 12.76 mags for 30/10/2013 and 29/06/2013 respectively. In order to acquire a more reliable 3σ detection of a 1% flux change, the target would need to be 11.30 and 10.40 mags on the respective nights. The difference between the RMS scatter on the two nights is not necessarily indicative of a scatter difference between full and on-off methods as they are also influenced, to varying degrees, by weather and sky conditions.

Another factor to consider is the exposure time as increasing the time will increase the signal to noise ratio. PIRATE's mount is capable of tracking a target up to $\sim$15 minutes, but for exoplanets this is likely to saturate bright targets an it comes at a cost of time resolution. In practice, typical PIRATE exposures range from 30s to the occasional 180s. The ideal exposure is one that maximises the signal-to-noise ratio without saturating the pixels of the target and possible blend stars.

Table 3.6: The transit depth required to detect a 1 and 3σ transit for varying magnitudes.

Corrected	Transit depths (%)			
PIRATE	30/10/2013		29/06/2013	
R Magnitude	1σ	3σ	1σ	3σ
10.0	0.29	0.86	0.31	0.93
10.5	0.30	0.89	0.34	1.02
11.0	0.32	0.95	0.39	1.17
11.5	0.34	1.04	0.47	1.42
12.0	0.40	1.19	0.61	1.82
12.5	0.48	1.44	0.83	2.49
13.0	0.62	1.85	1.20	3.60
13.5	0.84	2.53	1.80	5.42
14.0	1.21	3.64	2.81	8.43
14.5	1.83	5.48	4.46	13.38

A range of values determined from Fig. 3.25 are given in Tab. 3.6. This provides an insight on how to effectively make use of a Mallorca-based facility like PIRATE for future exoplanet-related targets, as well as aiding in the analysis of the current targets. Given a known target magnitude and potential transit depth a decision can be made on whether to perform a full or on-off lightcurve measurement. For example, on the

night of 30/10/2013, the target had a PIRATE corrected R magnitude of 10.07 with the SuperWASP archive suggesting a 0.32% transit. Comparing this with Tab. 3.6 it can be seen that such a transit, if real, would likely be on par with the lightcurve RMS scatter making it difficult to detect. Fig. 3.26 shows the target lightcurve for the night of 30/10/2013. The sigma clipped RMS scatter of the target lightcurve is 0.22%, indicating that a 0.32% transit may be barely detectable ($\sim$1.45σ). There is no obvious transit signal in the lightcurve, but as the transit depth is below 3σ it cannot be confirmed with certainty.

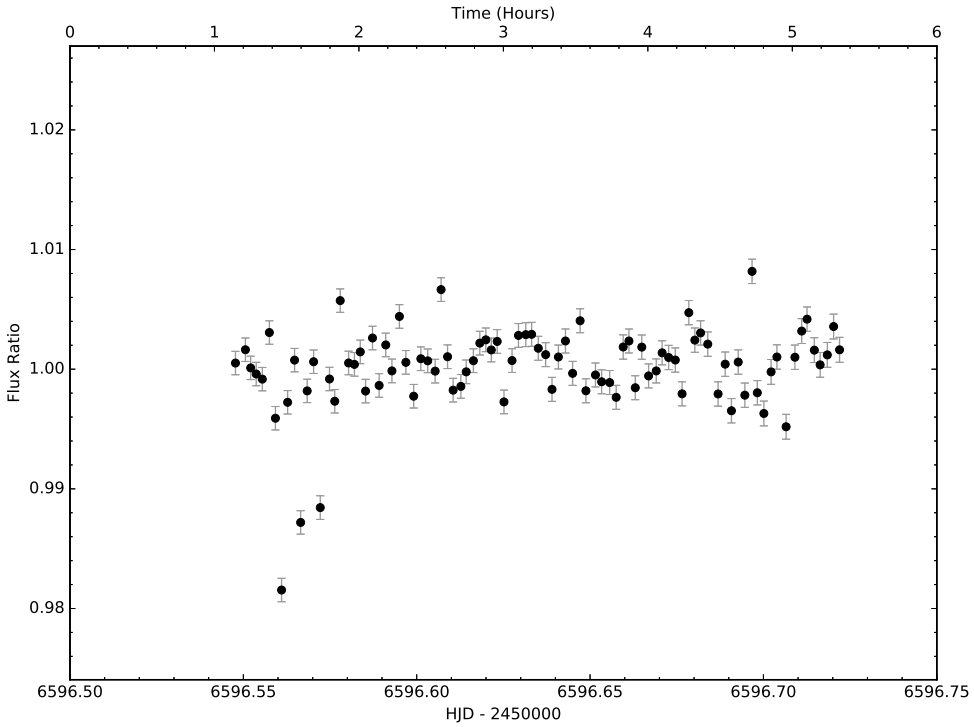

Figure 3.26: Target lightcurve for the night of 30/10/2013. The target has a sigma clipped RMS scatter of 0.22%.

Instead of searching for an exoplanet transit, a search for blends can be examined instead. The target has several other stars that fall within the SuperWASP aperture, with PIRATE detecting a total of seven other stars. Two of these stars are faint and have incomplete lightcurves which are automatically removed from the analysis by the pipeline. The remaining five, have corrected R magnitudes of 12.17, 12.22, 14.58, 17.02 and 17.35. Treating the target plus these five potential blends as a single star, it is possible to determine the percentage flux change required on a star by star basis

to mimic a 0.32% transit. The two stars fainter than 17 magnitudes are unable to dim sufficiently to provide a large enough percentage change, hence these can be ignored as potential blend sources along with the two fainter stars removed by the pipeline. The remaining 12.17, 12.22 and 14.58 magnitude stars require flux changes of 2.71%, 2.80% and 31.8% respectively. These values should all be easily detectable against the RMS scatter. However, no such blend signal was detected in any of these stars, strongly supporting the conclusion that no blend signal occured during the observing window. This leaves a few scenarios that could be occuring, the first of which is that the transit window has been missed due to a significant ephemeris drift or it could also be a false positive. Another possibility is that the target is real but requires more sensitive observations to detect, or a number of repeat PIRATE observations to suppress the noise.

This isn't an exhaustive analysis of all the targets observed but does provide an indication that PIRATE is capable of searching for exoplanets that produce a $\sim$1% transit around a star of $\sim$11.5 magnitudes or brighter, although it is dependent on the sky conditions. In the event that there aren't any suitable targets that match these criteria, then PIRATE can be used to look for mimics instead. As an aside, it is noted that stars which have a RMS scatter that is greater than the 3σ value for their magnitude are strong indicators that the star is undergoing detectable variations which may be of scientific interest.

3.7 Key Results

The key results from this chapter are as follows:

- The PIRATE exoplanet pipeline has been converted from IDL and IRAF to Python and Pyraf.
- A flaw in the calibration method used on the old pipeline was found and corrected. The errors arising from the flaw are negligible to PIRATE's end results

prior to the detection of this error but nonetheless this has removed a small source of error.

- A new master frame selection method was implemented into the pipeline that uses multiple frames to create a robust master frame that is able to remove cosmic ray detections and potentially minimise false star detections due to hot pixels. The new master frame also provides a truer representation of the stellar FWHM across multiple science frames.

- A simple auto-frame selection method for the pipeline is presented that can automatically identify 'good' science frames through the use of plate solving.

- Examples of PIRATE's lightcurve performance are presented that indicate that PIRATE is capable of at least identifying $\sim$1% transits around $\sim$11.5 magnitude stars.

- In terms of volume, PIRATE's greatest contribution to the SuperWASP project has been in identifying false positives, in particular blends, with the bulk of PIRATE's observations in the declination range of $\sim 0^{\circ}$to $\sim 60^{\circ}$.

- Examples of PIRATE's SuperWASP observations are presented and discussed.

Chapter 4

Exoplanetary Roche Lobe and Surface Geometry

Remaining on the topic of exoplanets, this chapter investigates the application of Roche potential calculations to exoplanets. The Roche potential is typically used to describe equipotential surfaces within close binary stars. Here, the same method is applied to a sample of exoplanets and their host stars. The purpose of this study is to explore the distortion that the exoplanets are undergoing due to the gravitational effects of the host star. Furthermore, computations over a range of mass ratios and planetary radii are performed in order to generate volume correction look-up charts.

Parts of this work have been used to explore the habitability and detection of Earth-like planets around cool white dwarfs (Fossati et al. 2012) as well as exploring whether an extended gas envelope around WASP-12 is beyond the critical Roche equipotential (Haswell et al. 2012). The code described in this chapter has also been used in Staab et al. (2017), a discussion of which is beyond the scope of this thesis. Some conclusions in this chapter have been published by an independent study, Burton et al. (2014). The unique contributions of this work compared to that of Burton et al. (2014), in addition to the previously stated papers, are the generation of volume correction look-up charts as well as the inclusion of the inclination effects in the study.

4.1 Theory - The Roche Potential

The discussion begins with an explanation of the Roche Potential. The Roche potential in a co-rotating frame is given by

$$\Phi = -\frac{GM_*}{r_*} - \frac{GM_P}{r_P} - \frac{G(M_* + M_p)r^2}{2a^3} \tag{4.1}$$

where G is the gravitational constant, a is the orbital separation, M_* and M_P are the masses of the star and planet respectively. The distance of a particle to the axis of rotation is $r = \sqrt{\left(x - \frac{M_*}{M_* + M_P}\right)^2 + y^2}$, while $r_* = \sqrt{(x-a)^2 + y^2 + z^2}$ and $r_P = \sqrt{x^2 + y^2 + z^2}$ are the particle distance from the star and planet respectively with the origin at the centre of mass of the planet; x and y are in the orbital plane and z is orthogonal to the plane. In Eq. 4.1 the first and second terms on the right hand side represent the gravitational potential due to the star and planet respectively while the last term is due to the centrifugal force of the rotating system. Fig. 4.1 demonstrates the lines of Roche equipotential for a binary system.

Each body is surrounded by a series of closed equipotentials, defined by Eq. 4.1, which a fluid body will fill exactly. The critical equipotential surrounding a single object is known as the Roche lobe and the enclosed region defines the region of gravitational dominance by the enclosed body. The lobes of the planet and star are centrifugally stretched and meet at a point and this is known as the inner Lagrangian point, L_1. Material within the planet's Roche lobe will be bound to the planet. However, if the planet's Roche lobe is over-filled then mass transfer is expected to occur via the L_1 point. In the absence of significant other forces, this material will form an accretion disk around the other object.

By normalising Eq. 4.1 and defining the ratio of masses in the system as $q = \frac{M_p}{M_*}$, a normalised Roche potential is produced:

$$\Phi_N = -\frac{1}{r_*} - \frac{q}{r_P} - \frac{1+q}{2}\left[\left(x - \frac{1}{1+q}\right)^2 + y^2\right] \tag{4.2}$$

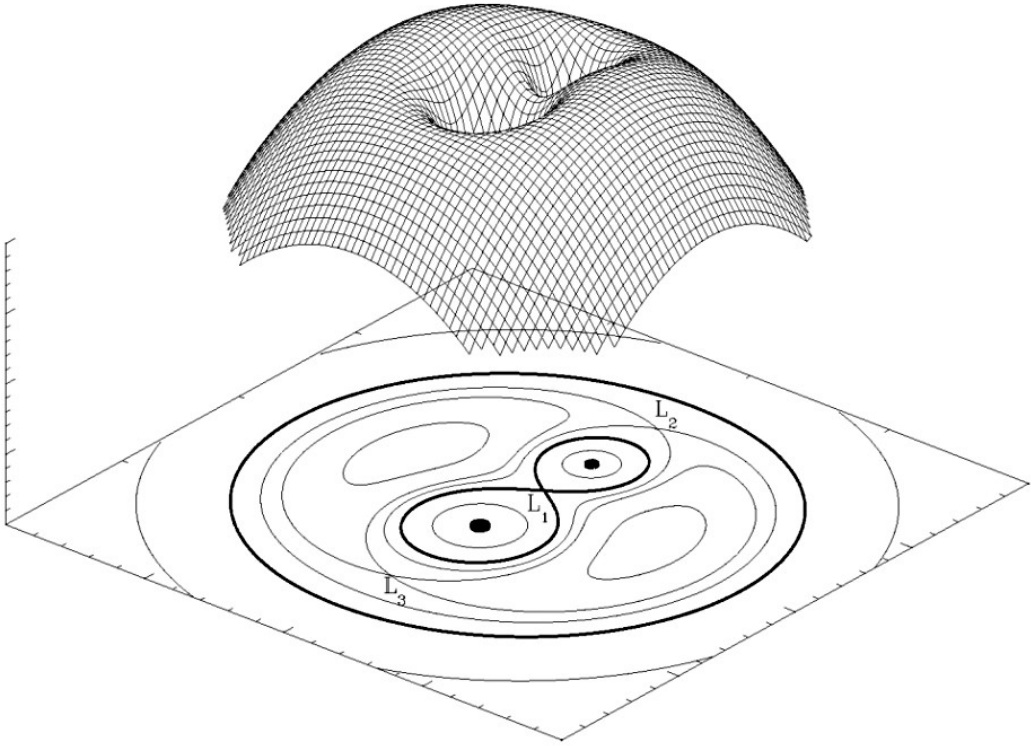

Figure 4.1: A three-dimensional representation of the Roche potential in a binary system. The equipotential plot at the bottom of the figure shows the Roche lobes of each object (tear-drop shapes). The Lagrangian points (L_1, L_2 and L_3) are where the forces cancel out. If one object fills its Roche lobe, mass is expected to transfer to the companion object via the saddle point, L_1. (Figure from http://hemel.waarnemen.com/Informatie/Sterren/hoofdstuk6.html#mtr)

This normalised Roche potential is more convenient as it is scale-free and hence allows for easier analysis of the shapes of the Roche lobe around the exoplanets than Eq. 4.1. The volume equivalent radius of a Roche lobe and the distance to the inner Lagrangian point are often approximated by the Eggleton (Eq. 4.3, Eggleton 1983) and Hill Radius (Eq. 4.4) approximations respectively. These are given by

$$R_{Egg} = a\frac{0.49q^{\frac{2}{3}}}{0.6q^{\frac{2}{3}} + \ln\left(1+q^{\frac{1}{3}}\right)}, \text{ where } 0 < q < \infty \tag{4.3}$$

$$R_{Hill} = a\sqrt[3]{\frac{q}{3}} \tag{4.4}$$

The Eggleton approximation (Eq. 4.3) is applicable to a whole range of q values from the very small to the infinite, with Eggleton claiming a better than 1% accuracy

across the entire range.

4.2 Method

Having described the Roche potential, the discussion will now proceed to describe how the Roche potential is used to calculate and map the critical equipotential surface (the Roche lobe) as well as the shape of exoplanets.

4.2.1 Roche Lobe Calculations

A C++ code (see Appendix B) was created that is capable of mapping the Roche equipotentials, as defined by Eq. 4.2, of an exoplanet and the Roche lobe around it. Several assumptions are made in order to make use of the Roche potential and will need to be kept in mind. Firstly, the masses of the exoplanets and their host stars are treated as centrally condensed objects or point masses. Another assumption is that the planetary orbital and rotational periods are equal, signifying that tidal locking has occurred. Finally, the orbits are also assumed to have an eccentricity of 0 and hence have circular orbits.

The assumptions may not be applicable to all exoplanets, but aren't unrealistic. The Love number, k_{2p}, describes the concentration of the planet's interior mass (Ragozzine & Wolf 2009) with smaller numbers indicating a larger central concentration. For WASP-12b, k_{2p} is expected to be 0.15 ± 0.08 at eccentricities close to zero (Campo et al. 2011). For perspective, a main sequence solar-like star, Jupiter and Saturn values of k_{2p} are $\sim$0.03, $\sim$0.49 and $\sim$0.32 (Ragozzine & Wolf 2009). Additionally WASP-12b is observed to have a near-circular orbit with an eccentricity of $0.017^{+0.015}_{-0.010}$ (Husnoo et al. 2011), which is comparable to that of Earth's eccentricity of 0.016. Tidal locking is also expected to occur in short-period hot Jupiters (Nagasawa et al. 2008) due to the strong gravitational forces acting upon them.

The code uses spherical coordinates and steps through the polar, θ, and azimuthal, ϕ, angles while adjusting the radial distance, ρ, to determine the Roche lobe and plan-

etary potential surfaces. For reference, the conversion from spherical to cartesian coordinates is as shown in Eq. 4.5.

$$\begin{aligned} x &= \rho \sin(\theta)\cos(\phi) \\ y &= \rho \sin(\theta)\sin(\phi) \\ z &= \rho \cos(\theta) \end{aligned} \tag{4.5}$$

To map the Roche potential, the potential at a single point needs to be known allowing for all other equipotentials to be located by varying ρ. For the Roche lobe the potential at the inner Lagrangian point, L_1, is taken as it is an easily identifiable Roche potential turning point between the planet and the host star (see Fig. 4.1). With the Roche potential identified, the code then steps through values of ρ at varying angles until an equipotential value is found to be matching the inner Lagrangian potential.

Once ρ is determined the value is used to determine the volume of the segment, δV, being looked at.

$$\delta V = \frac{\rho^3 \sin(\theta)\delta\theta\delta\phi}{3} \tag{4.6}$$

Employing this method gives results accurate to 4 significant figures or better (see Tab. 4.1) but Eq. 4.6 can be simplified by setting $\delta U = \sin(\theta)\delta\theta$ and sampling from $U = 0$ to $U = 1$. As the sample is being taken over 0 to 1, this doesn't cover the entire azimuthal range of 0°to 180°. Two possible resolutions are to step through from -1 to 1, or multiply δU by 2. Both take advantage of the symmetry of the Roche equipotentials but the doubling in the latter suggestion is less computationally expensive and is the preferred choice which results in Eq 4.7. Table 4.1 shows the outcomes of both the above methods (Eqs. 4.6 & 4.7) when applied to calculating the volume of a sphere and comparing the percentage difference, $\Delta\%$, to the volume of perfect sphere, $V = \frac{4\pi\rho^3}{3}$. The smaller the percentage difference the more precise is the answer.

$$\delta V = \frac{2\rho^3 \delta U \delta\phi}{3} \tag{4.7}$$

Table 4.1: Comparison of various resolutions used in the code. It should be noted that Eq. 4.7 performs fewer calculations as the grid in the δU is sampling over 0 to 1 and doubled whereas Eq. 4.6 uses 0 to 180. The final column is a numerically stable version of Eq. 4.7 using the Kahan summation algorithm (Kahan 1965)

ρ	$\delta\phi$,$\delta\theta$	δU	Eq. 4.6 Δ%	Eq. 4.7 Δ%	Eq. 4.7 Δ% (Stable)
10	0.1	0.001	0.000025384664346	-0.000000000052067	0.000000000000000
	0.01	0.0001	0.000000278712447	-0.000000159115654	-0.000000000000022
	0.001	0.00001	0.000000167700529	-0.000009355618219	0.000000000000000
	0.0001	0.000001	-0.000049572620040	0.002715919712005	-0.000000000000022
1	0.1	0.001	0.000025384835000	-0.000000002237909	-0.000000000000021
	0.01	0.0001	0.000000250743312	0.000000069380683	-0.000000000000021
	0.001	0.00001	-0.000000267915995	-0.000031428685290	-0.000000000000021
	0.0001	0.000001	0.000105968464323	0.002439093912975	-0.000000000000021
0.1	0.1	0.001	0.000025384908343	0.000000001176702	-0.000000000000021
	0.01	0.0001	0.000000251539655	0.000000198384531	-0.000000000000021
	0.001	0.00001	0.000000360866439	0.000005811211592	-0.000000000000021
	0.0001	0.000001	0.000032751553233	-0.001044147351016	-0.000000000000021

It should be noted that Eq. 4.7 performs fewer calculations as the grid in the δU is sampling over 0 to 1 whereas Eq. 4.6 uses 0°to 180°. This means that there is a lower sampling resolution using Eq. 4.7 but it operates faster and is less susceptible to rounding errors. The variables $\delta\phi$, $\delta\theta$ and δU are intended to be infinitesimal so the precision is expected to improve with finer sampling of these values. However, rounding errors in the calculations are shown to play a significantly larger role at finer resolutions. The rounding errors, caused by many repeated additions within the calculation, can clearly be seen coming into effect in both circumstances at settings of $\delta\phi = \delta\theta = 0.0001$, $\delta U = 0.000001$. With Eq. 4.6 the rounding errors follow a decreasing trend until this point where the precision has decreased beyond that of the lowest sample resolution examined. Eq. 4.7 follows a different trend, steadily reducing in precision as the sampling resolution increases.

Examining the effects that the radius, ρ, has on the different methods shows that the magnitudes of the percentage differences remains roughly similar for Eq. 4.6 at $\delta\phi = \delta\theta = 0.1$ & 0.01, decreases with increasing ρ for $\delta\phi = \delta\theta = 0.001$, and gives varied results at $\delta\phi = \delta\theta = 0.0001$. Eq. 4.7 provides percentage difference magnitudes that vary across all ρ with no obvious pattern.

As mentioned previously, the deviations in both the described methods are due to rounding errors within the code. The significant variations in these rounding errors show that the code is numerically unstable. This is attributed to the large number of summations taking place. By employing the Kahan summation algorithm (Kahan 1965), the code is brought into numerical stability as shown in the final column of Table 4.1. Code 4.1 shows a code snippet of how the algorithm is applied to the program. Rather than directly adding δV onto volume a correction value is calculated and incorporated into the next iteration of δV prior to adding the value to the volume. The errors remain fairly consistent despite the changes in the radii as well as the $\delta\phi$ & δU steps. The two outliers in $\rho = 10$ with results of 0 are unaccounted for but do give an exact match to the expected volume for a sphere of that radius.

```
correction = 0.0;
volume = 0.0;
// start loop
   // calculate delta_v then perform Kahan summation algorithm
   delta_v = delta_v - correction;
   volume2 = volume + delta_v;
   correction = (volume2 - volume) - delta_v;
   volume = volume2;
// end loop
```

Code 4.1: Example application of the Kahan algoritm

The distance units used through this chapter are normalised to the orbital separation, a, as this is the natural distance scale. The majority of the exoplanets examined in this work have normalised radii ranging between $10^{-3}a$ to $10^{-6}a$. The numerical stability of the code demonstrated above suggests that this should not impact the accuracy of the calculations and is verified by applying the code down to radii of 10^{-7}. As such, Eq. 4.7 with the Kahan summation algorithm is used with $\delta\phi = 0.005$ and $\delta U = 0.00005$ throughout the rest of this work unless stated otherwise. This offers a low enough number of calculations to allow computations to complete in hours rather than days but also provides a fine sampling resolution, necessary for any extreme non-spherical Roche lobes and planetary shapes. At this setting there are 72000 and 20000 steps in ϕ and U respectively, giving a total of 1440 million points across the equipotential surface.

The next step is to verify that the code functions correctly when applied to determining the normalised volume equivalent radii of a Roche lobe, R_2, which is the radius of a sphere with a volume equivalent to that of the Roche lobe. Eggleton (1983) performed accurate and precise integrations, valid to "5 or more significant figures", over a range of q values from 10^3 down to 10^{-3}. Eggleton (1983) then used these values to verify, to better than 1%, the validity of the analytic approximation in Eq. 4.3. Table 4.2 explores the output from the calculations presented in this thesis and the analytic approximation in Eq. 4.3 as well as Eq. 4.4. The output shows that the Eggleton approximation, Eq. 4.3, is still valid to within 1% down to more extreme mass ratios, q, of 10^{-6}. The Hill radius approximation shows better approximations at more extreme mass ratios. It is also noted that at mass ratio values of 10^{-2} & 10^{-3}, the R_2 results were found to be identical to the precise integrated values (0.1012 & 0.0482 respectively) that Eggleton (1983) published.

Table 4.2: Comparisons for various mass ratios, q, between the volume equivalent radius, R_2, and the Eggleton approximation, R_{Egg}, as well as the distance of the inner Lagrangian point from the centre of mass of the lower mass object, R_{L1}, and the Hill's sphere radius, R_{Hill}. (Note: All distance values are normalised to the orbital separation)

q	R_2	R_{Egg}	$\frac{R_{Egg}}{R_2}$	R_{L1}	R_{Hill}	$\frac{R_{Hill}}{R_{L1}}$
10^{-6}	0.004921	0.004895	0.9947	0.006918	0.006934	1.0023
10^{-5}	0.010573	0.010532	0.9961	0.014863	0.014938	1.0050
10^{-4}	0.022649	0.022623	0.9989	0.031834	0.032183	1.0110
10^{-3}	0.048218	0.048366	1.0031	0.067691	0.069336	1.0243
10^{-2}	0.101243	0.102009	1.0076	0.141475	0.149380	1.0559

4.2.2 Mapping the Planetary Surface Roche Potential

In the $y-z$ plane (the plane that is observed during a transit at an inclination, i, of 90°) the dimensions of the Roche lobe differ, with the y radius being larger than the z radius due to the centrifugal stretching. Depending on the degree of the Roche lobe filling, a planet will also suffer this distortion to varying degrees. A planet seated well within

the lobe will be closer to a spherical shape than a planet that is nearly filling the Roche lobe.

The occulting area of a planet (recall Eq. 1.4) in the $y-z$ plane (when $x=0$) is calculated and reduced until it matches an area with a radius equivalent to the observed occulting disk. The potential at this point is then used to map the planetary surface.

To map the Roche potential, the potential at a single point needs to be known allowing for all other matching equipotentials to be located. As stated previously, for the Roche lobe, the single point is taken to be the inner Lagrangian point as it is simple to identify. For the planetary surface within the critical equipotential one might use the mean planetary radius determined from a transit event. However, this estimate will give varying results depending on which point in the x,y,z axes is taken, especially for gas planets, because the planet will be distorted to match the shape of the equipotential. To overcome this problem, the occulting area of the planet in the $y-z$ plane (when $x=0$) is calculated and reduced until it matches an area equivalent to the mean planetary radius.

The currently known (2nd October, 2014) best estimate inclinations for transiting exoplanets range from 77.6°to 90°(http://exoplanets.org, Wright et al. 2011). To calculate the area of the planet being observed at an inclination, i, a simple rotation matrix around the y-axis with the origin at the planet's centre is applied,

$$\begin{bmatrix} x' \\ y' \\ z' \end{bmatrix} = \begin{bmatrix} \sin i & 0 & \cos i \\ 0 & 1 & 0 \\ -\cos i & 0 & \sin i \end{bmatrix} \begin{bmatrix} x \\ y \\ z \end{bmatrix} \tag{4.8}$$

where x', y', z' are the translated co-ordinates in the observer's reference frame with an inclination, i. The occulting area is now calculated in the $y'-z'$ plane when $x'=0$, however, it should be noted that for large difference from 90° this method will not be as accurate due to the maximum & minimum z' moving away from $x'=0$. Tables 4.3 & 4.4 show how far the maximum and minimum points deviate from the centre point of calculations. There is less than half a percent difference over the range of

the previously mentioned known transiting exoplanet inclinations. Even then, only OGLE-TR-56b (Torres et al. 2008) has the highest inclination of 77.6°while the rest are at 79°or above, implying a deviation of 0.29% or better for the majority of the exoplanets examined in this work.

Burton et al. (2014) examined the change in bulk density as a function of the orbital period for WASP-19b in order to verify the internal consistency of their calculations. In addition to this, at a 10 day period it was found that the difference between the calculated planet volume and a sphere with the observed radius was 0.001%. In both of the above cases the orbital inclination is not taken into account. The bulk density experiment is replicated here, assuming an orbital inclination of 90°, with the methodology described throughout this chapter. The values of WASP-19b are from Hellier et al. (2011), the same as those used in Burton et al. (2014). A smooth curve similar to Burton et al. (2014) is seen in Fig. 4.2 but the values arrived at appear different. Closer examination at a 10 day period show that the distortion from spherical is found to be 0.0608%, taking this a step further, at 100 days the distortion is 0.0006%. Comparing this work and that of Burton et al. (2014) shows there is a difference between the 10 day results for WASP-19b. This could be partially attributed to conversion errors, such as using constants to differing accuracies.

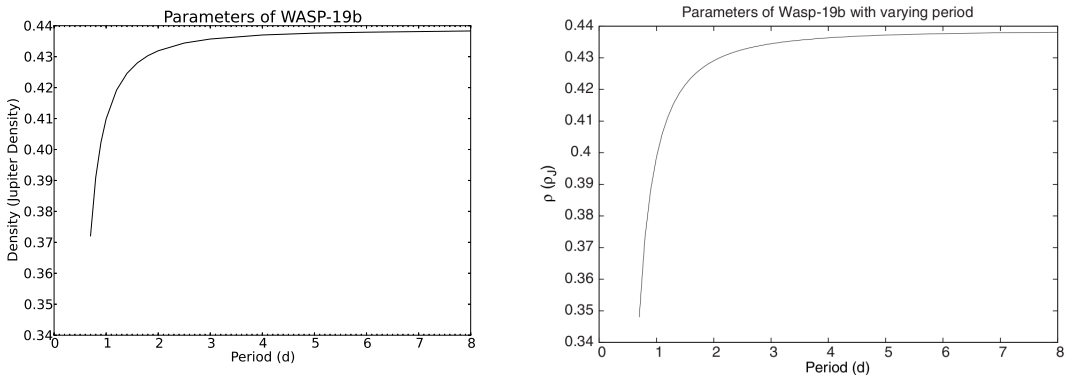

Figure 4.2: Plots of WASP-19b density at various periods. The left figure is from this work and the right is from Burton et al. (2014).

Alternatively, it is also noted that the code in this work operates on small numbers that may require precision greater than 64-bit double precision floating numbers.

Table 4.3: Roche Lobe Maxima - Showing the percentage difference between z-axis values from the centre and the true maximum point along the z-axis for varying values of q at different inclinations, i. Centre denotes the z' value when $x' = y' = 0$. Deviation is the maximum z' value along the x'-axis when $y' = 0$.

Inclination, i (°)	Mass Ratio, q								
	0.001			0.0001			0.00001		
	Centre	Deviation	%	Centre	Deviation	%	Centre	Deviation	%
89	0.043616	0.043619	0.01	0.020399	0.020400	0.00	0.009501	0.009501	0.00
88	0.043625	0.043633	0.02	0.020402	0.020405	0.01	0.009502	0.009503	0.01
87	0.043639	0.043653	0.03	0.020408	0.020413	0.02	0.009505	0.009507	0.02
86	0.043657	0.043679	0.05	0.020416	0.020424	0.04	0.009508	0.009512	0.04
85	0.043679	0.043711	0.07	0.020425	0.020438	0.06	0.009512	0.009518	0.06
84	0.043706	0.043748	0.10	0.020437	0.020455	0.09	0.009518	0.009526	0.08
83	0.043736	0.043791	0.13	0.020450	0.020475	0.12	0.009524	0.009535	0.12
82	0.043770	0.043840	0.16	0.020466	0.020497	0.15	0.009531	0.009545	0.15
81	0.043808	0.043895	0.20	0.020483	0.020523	0.20	0.009539	0.009557	0.19
80	0.043851	0.043956	0.24	0.020503	0.020551	0.23	0.009548	0.009570	0.23
79	0.043897	0.044023	0.29	0.020524	0.020582	0.28	0.009557	0.009584	0.28
78	0.043947	0.044095	0.34	0.020547	0.020616	0.34	0.009568	0.009600	0.33
77	0.044002	0.044174	0.39	0.020573	0.020653	0.39	0.009580	0.009617	0.39
76	0.044061	0.044258	0.45	0.020600	0.020693	0.45	0.009593	0.009636	0.45
75	0.044124	0.044348	0.51	0.020629	0.020736	0.52	0.009606	0.009656	0.52

Table 4.4: Minima - Showing the percentage difference between z'-axis values from the centre and the true minimum point along the z'-axis for varying values of q at different inclinations, i. Centre denotes the minimum z' value when $x' = y' = 0$. Deviation is the minimum z' value along the x'-axis when $y' = 0$

.

Inclination, i (°)	Mass Ratio, q								
	0.001			0.0001			0.00001		
	Centre	Deviation	%	Centre	Deviation	%	Centre	Deviation	%
89	-0.043608	-0.043608	0.00	-0.020397	-0.020397	0.00	-0.009500	-0.009500	0.00
88	-0.043610	-0.043611	0.00	-0.020399	-0.020400	0.00	-0.009501	-0.009502	0.01
87	-0.043617	-0.043620	0.01	-0.020403	-0.020406	0.01	-0.009504	-0.009505	0.01
86	-0.043627	-0.043636	0.02	-0.020409	-0.020415	0.03	-0.009507	-0.009510	0.03
85	-0.043642	-0.043657	0.03	-0.020417	-0.020426	0.04	-0.009511	-0.009515	0.04
84	-0.043660	-0.043684	0.05	-0.020427	-0.020441	0.07	-0.009515	-0.009523	0.08
83	-0.043683	-0.043717	0.08	-0.020439	-0.020458	0.09	-0.009521	-0.009531	0.11
82	-0.043710	-0.043756	0.11	-0.020452	-0.020478	0.13	-0.009528	-0.009541	0.14
81	-0.043741	-0.043801	0.14	-0.020468	-0.020501	0.16	-0.009535	-0.009552	0.18
80	-0.043776	-0.043852	0.17	-0.020486	-0.020527	0.20	-0.009544	-0.009565	0.22
79	-0.043816	-0.043910	0.21	-0.020506	-0.020557	0.25	-0.009554	-0.009579	0.26
78	-0.043859	-0.043974	0.26	-0.020528	-0.020589	0.30	-0.009564	-0.009594	0.31
77	-0.043907	-0.044044	0.31	-0.020551	-0.020624	0.36	-0.009575	-0.009611	0.38
76	-0.043960	-0.044121	0.37	-0.020577	-0.020662	0.41	-0.009588	-0.009629	0.43
75	-0.044016	-0.044205	0.43	-0.020605	-0.020704	0.48	-0.009601	-0.009649	0.50

This is due to the fact that double-precision floating points are stored in the fashion of $\pm s.15d \times 10^y$, where s ranges from 0 to 9, $15d$ are the 15 decimal places to which double is accurate to and y ranges from -1024 to 1024. Typically there are two more decimal places available but these are used as rounding values to allow up to 15 decimal places of accuracy. This provides a roughly 16 significant figure result. As such, supplying the normalised observed radius of WASP-19b at a 10 day period translates from 0.007363410633283 to $7.363410633283 \times 10^{-3}$, effectively losing 3 decimal places of accuracy. Compensating for this by converting all values to 'long double' precision which effectively operates at 80-bit on the processor and outputs a rounded 64-bit result doesn't have an effect, suggesting that the value determined by the code is not a propagation of error issue. A more thorough analysis may be needed to say with certainty that the extra decimal places are or are not required, but for this specific situation this does not appear to be the case.

4.3 Results

The Roche code has been used to explore multiple exoplanet geometries and volume correction look-up charts have been generated, the results of which are presented here.

4.3.1 Planetary Lobes

The Roche code was applied to 207 exoplanets with their associated parameters taken from the Exoplanet Orbit Database (http://exoplanets.org, Wright et al. 2011). The code was set to iterate with the following values, $\delta\phi = 0.005$ and $\delta U = 0.000025$. The full table of results is shown in Appendix C while a top 15 selection of the exoplanets that are close to filling their lobe are shown in Table 4.5. The table shows volume filling and bulk density change results with the orbital inclination ignored and with an inclination correction applied (as described in Sec. 4.2.2). In order for the inclination to have a significant effect and show an appreciable difference to the uncorrected values, a planet must fill the Roche lobe to a degree that will allow distortion

of the planet's surface to occur. An undistorted planet will remain spherical and hence have the same shape at any inclination. In addition to the above requirement, a larger inclination allows for smaller distortions to have a bigger impact on the results. It is noted that typical measurement uncertainties on exoplanet system parameters lead to errors on the derived bulk densities in the order of $\sim$5% (Burton et al. 2014)

WASP-19b, WASP-12b and WASP-103b are the most heavily distorted exoplanets with inclination-corrected volume filling percentages of 59.11%, 54.35% and 41.72% and inclination corrected bulk density changes of 12.71%, 11.84% and 8.89% while the rest of the sample are at $\sim$20% or lower lobe filling and $\sim$4% or lower bulk density change. Fig. 4.3 provides a 3D visual representation of these systems while Fig. 4.4 shows the effect and magnitude of the distortion for these three planets. The *x* and *y* are in the orbital plane and the *z* is perpendicular to them. The *y*-*z* plane along the bottom row in Fig. 4.4 is a minimum cross-section and shows that the total calculated area of this plane is the same as that presented to an observer during transit (at inclination = 90°) but deviating from circular. There is a slight increase in the *y* axis and a similar decrease in the *z* axis. Conversely, a strong distortion from circular is present in the *x*-*y* and *x*-*z* cross sections for all three cases.

These exoplanet distortions are similar to ellipsoidal variables in binary star systems, where at least one of the stars is distorted from spherical. Due to the shape of the star, the total flux seen by an observer will vary depending on the phase of the orbit. Indeed, Li et al. (2010) state that the light curve from a tidally distorted exoplanet will be different from a spherical counterpart. This is because the exoplanet will present its larger cross-section (i.e. *x*-*z* plane) at orbital phases of 0.25 and 0.75 and alter the amount of reflected stellar flux. At these phases WASP-19b, WASP-12b and WASP-103b have a total area increase of 11.78%, 10.82% and 7.97%. This won't be the total area of reflecting light as the planet will have a day and night side. Due to the planetary distortions, the increase in reflective area presented to the observer is 12.04%, 11.02% and 8.08%. The reflectivity values are larger than the total area increase due to the fact this effect is occuring on the more heavily distorted side of the planet, i.e. the inner

Table 4.5: Roche lobe filling fractions and density change fractions for the top 15 biggest lobe filling exoplanets. q, i and P are the mass ratio, inclination and periods, respectively. R_2 is the Roche lobe volume equivalent radius. R_ϕ and $R_{i\phi}$ are the volume equivalent radii of the planet at inclinations of 90°and i, respectively. The larger sample of 207 exoplanets can be seen in Appendix C. (Note: All distance values are normalised to the orbital separation)

Planet	q	i (°)	P (d)	R_2	R_ϕ	$R_{i\phi}$	Fill Fraction (90°)	Fill Fraction (i)	Δ Density (90°)	Δ Density (i)
WASP-19b	0.00114340	79.40	0.79	0.050348	0.042345	0.042254	0.5949	0.5911	0.8657	0.8729
WASP-12b	0.00100595	82.50	1.09	0.048291	0.039449	0.039410	0.5452	0.5435	0.8783	0.8816
WASP-103b	0.00116168	86.30	0.93	0.050609	0.037823	0.037816	0.4174	0.4172	0.9105	0.9111
WASP-52b	0.00049992	85.35	1.75	0.038427	0.022684	0.022680	0.2057	0.2056	0.9574	0.9579
HAT-P-32b	0.00070876	88.90	2.15	0.043075	0.025297	0.025297	0.2025	0.2025	0.9584	0.9584
CoRoT-1b	0.00103089	85.10	1.51	0.048678	0.028505	0.028500	0.2008	0.2007	0.9591	0.9596
OGLE-TR-56b	0.00105281	77.60	1.21	0.049013	0.027664	0.027639	0.1798	0.1793	0.9636	0.9664
WASP-78b	0.00062996	83.20	2.17	0.041447	0.022732	0.022727	0.1650	0.1649	0.9663	0.9671
WASP-4b	0.00128287	89.47	1.34	0.052270	0.028103	0.028103	0.1554	0.1554	0.9688	0.9689
WASP-48b	0.00077768	80.09	2.14	0.044401	0.023369	0.023358	0.1458	0.1456	0.9705	0.9720
WASP-17b	0.00040720	86.63	3.73	0.035929	0.018667	0.018666	0.1402	0.1402	0.9713	0.9715
HAT-P-23b	0.00176405	85.10	1.21	0.057969	0.028402	0.028399	0.1176	0.1176	0.9768	0.9771
HAT-P-41b	0.00053824	87.70	2.69	0.039368	0.019058	0.019058	0.1135	0.1135	0.9770	0.9771
TrES-3b	0.00195385	81.85	1.31	0.059923	0.028300	0.028293	0.1053	0.1053	0.9794	0.9801
Qatar-1b	0.00121583	83.47	1.42	0.051365	0.023901	0.023897	0.1007	0.1007	0.9800	0.9805

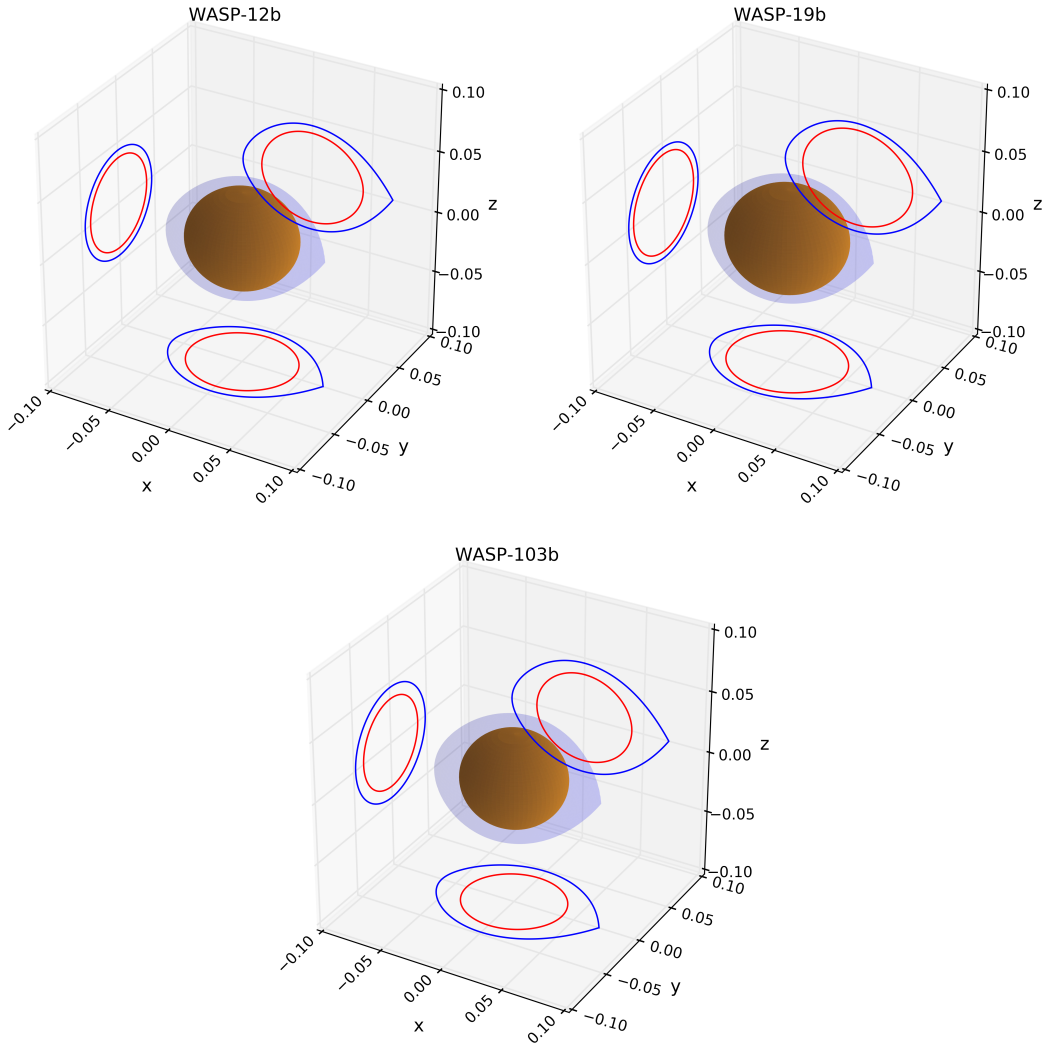

Figure 4.3: 3D and cross sectional plots of WASP-12b, WASP-19b & WASP-103b showing the volume of the Roche lobe occupied. The blue sphere and lines represent the Roche lobe while the orange sphere and red lines represent the mapped planetary surface.

Langrangian point, L_1, is on the day side of the planet.

In addition to the significant planetary distortion of WASP-19b and WASP-12b, both planets have orbital inclinations of 79.4°and 82.5°, respectively. This results in a change to the bulk density correction between the 90°inclination and their respective inclinations of -0.72% and -0.33% respectively. OGLE-TR-56b is not as distorted but also undergoes a change to the bulk density correction of -0.28% which demonstrates that even with a significantly lower distortion, the high inclination of 77.6% can produce relatively strong changes. The rest of the sample, excluding WASP-48b, have

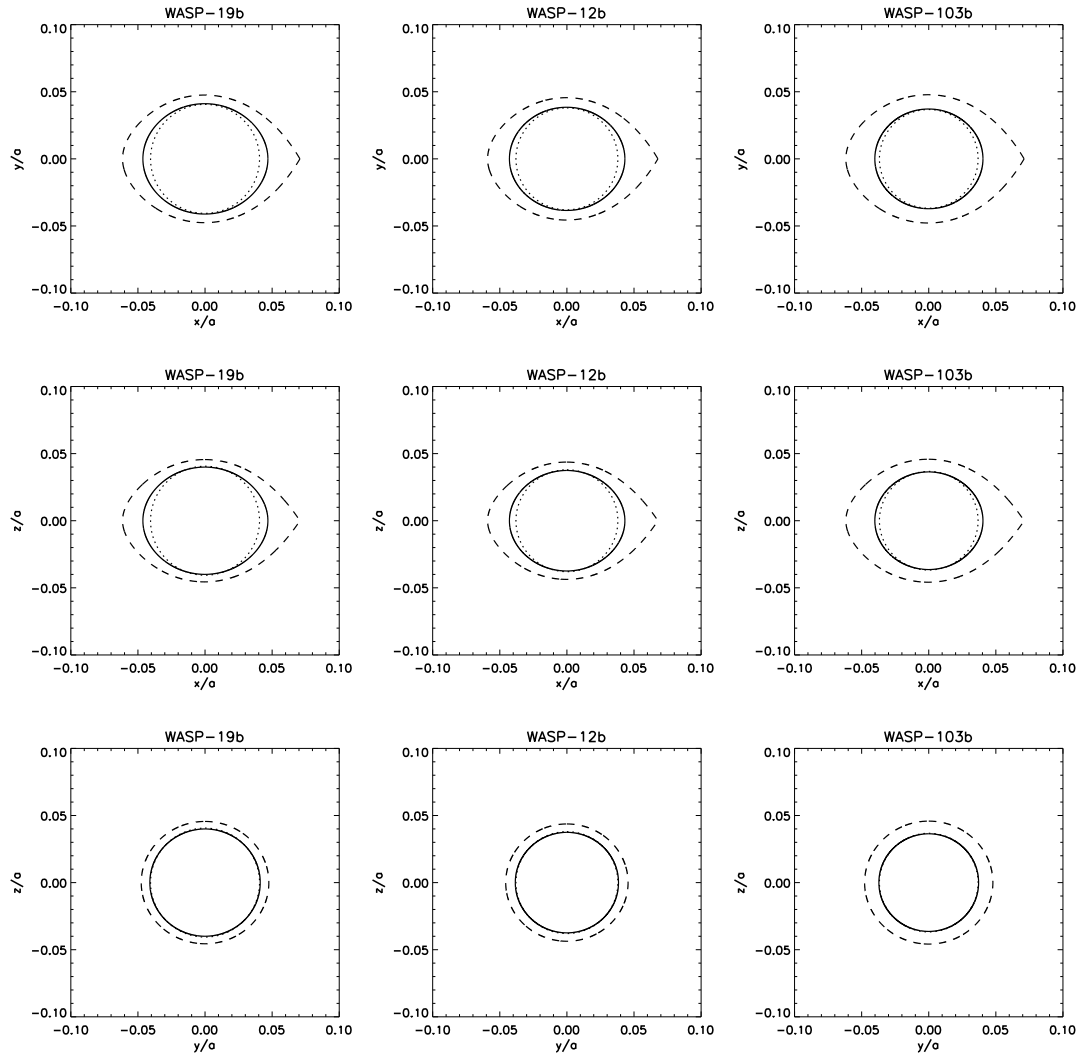

Figure 4.4: Cross sectional plots of WASP-19b, WASP-12b & WASP-103b in different planes showing how the planetary surface deviates from spherical. The top, middle and bottom rows are in the *x*-*y*, *x*-*z* and *y*-*z* planes. The dashed, solid and dotted lines are the Roche lobe, mapped planetary surface and circle with observed radius (i.e. assuming a perfectly spherical planet) respectively.

changes of $\sim$ -0.08% or less from the 90°inclination case with WASP-48b being an exception at -0.15%. Bearing in mind that errors in derived exoplanet bulk densities are in the order of $\sim$5%, it is clear that with current limitations the inclination of an exoplanet has a negligible impact on the final bulk density correction values for all but the most heavily distorted and highly inclined exoplanets. Despite this, it should be included for both completeness and accuracy as measurements will improve over time.

Figs. 4.5 & 4.6 show how deeply the exoplanets fill their Roche lobes and the

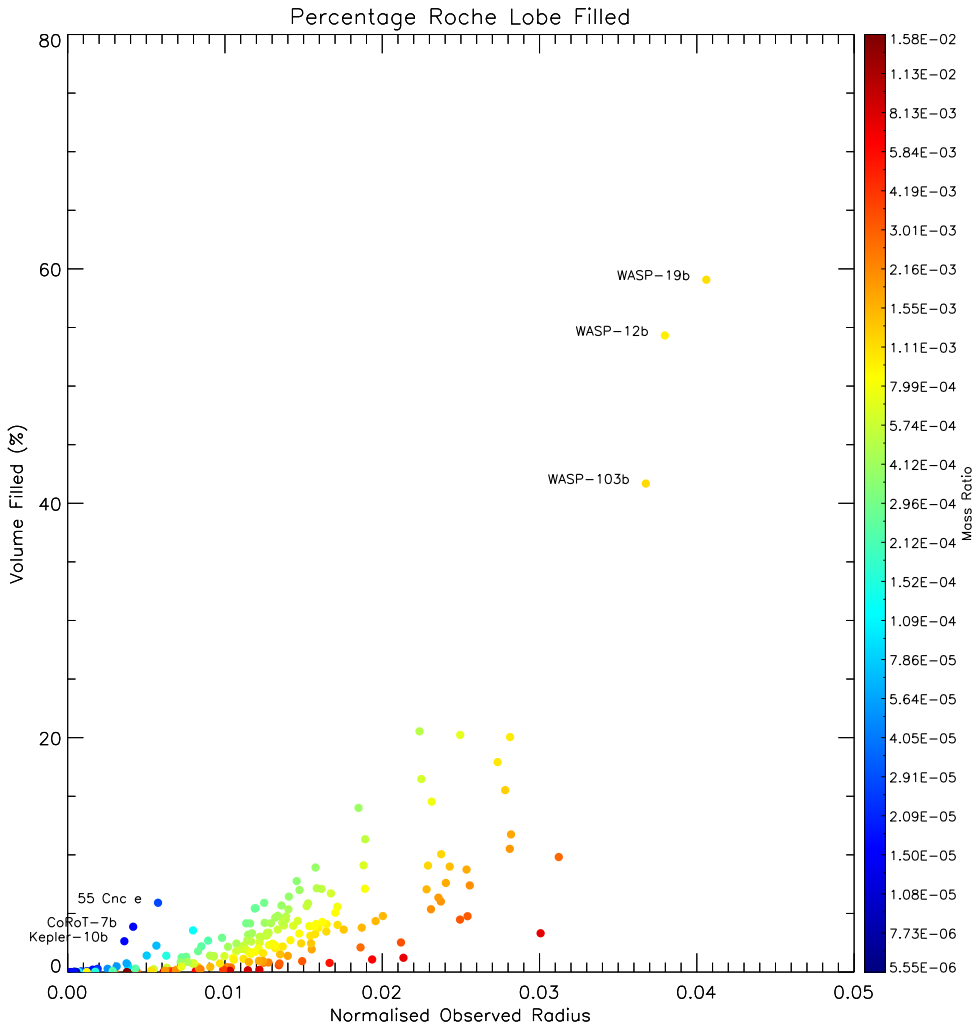

Figure 4.5: The Roche lobe filling percentage as a function of the normalised radius. The color gradient represents the mass ratio of the planets. The sample contains 207 known exoplanets with WASP-19b, WASP-12b and WASP-103b being the closest to filling their Roche lobes. 55 Cnc e, CoRoT-7b and Kepler-10b are also highlighted (blue dots). See Appendix C for full list of planets.

calculated density corrections, respectively. Both plots have the inclination taken into account. Both figures show a pattern influenced by the mass ratio. As the mass ratio becomes smaller (more extreme), i.e. the host star becomes more gravitationally dominant, the radius required to fill in the Roche lobe becomes smaller. This is to be expected as at larger mass ratios, systems have larger planetary Roche lobes to fill. However, this highlights a clear pattern in Fig. 4.5; as the radius increases smaller changes in the radius are required to influence the volume filling percentage. The impact of this is that small errors on the observed radius can have profound effects on the

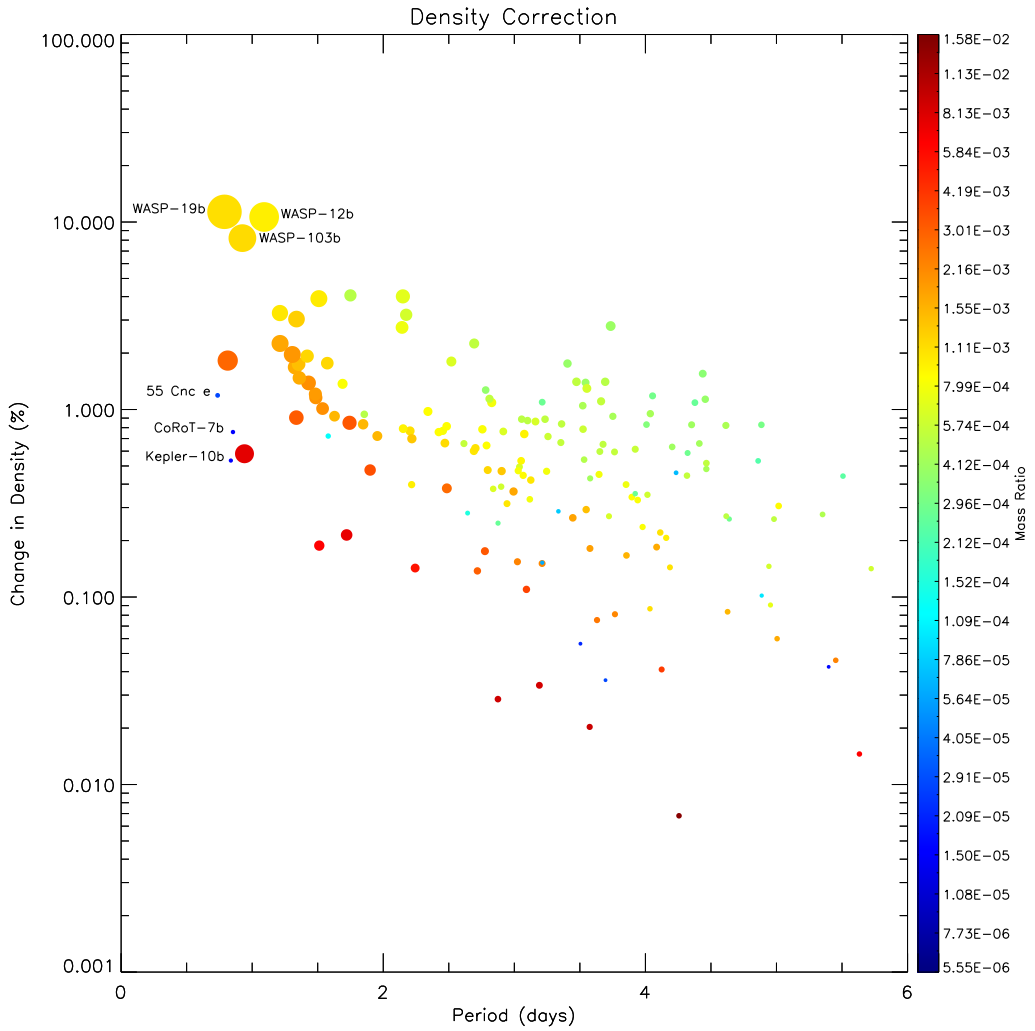

Figure 4.6: Period of 207 exoplanets plotted against the change in density. The color gradient represents the mass ratio of the planets while the circle size provides an indication of the normalised observed radius. The sample contains 207 known exoplanets with WASP-19b, WASP-12b and WASP-103b having very strong density corrections. 55 Cnc e, CoRoT-7b and Kepler-10b are also highlighted (blue dots). See Appendix C for full list of planets.

volume filling percentage and hence the density correction.

An interesting point is raised when looking at the three small normalised radii, small mass ratio systems at a period of less than a day (see Fig.4.6). In order of decreasing density correction, these planets are 55 Cnc e, CoRoT-7b and Kepler-10b. All three are classified as Super-Earth objects with densities equivalent to that of Earth.

Models of 55 Cnc e initially suggested a rock-iron composition supplemented by a significant mass of water, gas, or other light elements (Winn et al. 2011). Further

models, based on the planet having material similar to that of the host star composition, suggest a more solid carbon-rich planet (Madhusudhan et al. 2012). In order for the Roche model to be valid the planet needs to be centrally condensed. Of course, the centrally condensed mass isn't properly satisfied by the models in Winn et al. (2011) and Madhusudhan et al. (2012), but there will be strong gravitational effects from the host star making it likely that 55 Cnc e will require a density correction even if not to the full 1.18% as predicted by the Roche calculations.

CoRoT-7b provides a challenge in respect to determining its mass, due to stellar activity influencing the radial velocity measurements. Queloz et al. (2009), Hatzes et al. (2010), Pont et al. (2011) and Boisse et al. (2011) arrive at varying masses of 4.8, 6.9, 1-4 & 5.7 $M_{\oplus}$ respectively. The wide range of values suggested by Pont et al. (2011) allow for the planet to lie within both an Earth-like rocky regime, or a mini-Neptune gaseous water regime. Hatzes et al. (2011) and Ferraz-Mello et al. (2011) improve upon the measurement by reducing the uncertainties due to the stellar activity, achieving masses of 7.42 & 8.0 $M_{\oplus}$. These improved results are achieved by taking multiple measurements on the same observation nights, effectively beating down the stellar 'jitter'. This final result points to an Earth-like rocky composition.

Kepler-10b had a less controversial discovery and parameter determination than COROT-7b. It is the first definitive rocky planet discovered by KEPLER (Batalha et al. 2011). All three planets are clearly quite interesting scientific candidates for the effects of the Roche potential distortions on rocky planets. 55 Cnc e provides the best candidate for some minor differences to be detected by ellipsoidal variations due to having the largest calculated density correction.

4.3.2 Roche implications for WASP-12b

At the time of its detection, WASP-12b was the most heavily irradiated, shortest period, and largest radius exoplanet discovered (Hebb et al. 2009). This made it an ideal candidate for UV spectroscopy to look for absorption due to atmospheric/exospheric

gas. WASP-12b was expected to be undergoing atmospheric escape similar to that observed in HD 209458b. It was found that WASP-12b has an expanded exosphere that over-fills the Roche lobe (Fossati et al. 2010a; Haswell et al. 2012). The NUV wavelength ranges covered various metal lines and found that NaI, MgI, MgII, AlI, ScII, MnII, FeI, and CoI are present in the exosphere.

Further analysis of the host star was presented in Fossati et al. (2010b) with one of the aims being to search for pollution in the photosphere due to accreted material from the exoplanet. It was concluded that hints of pollution may exist although further work was required to provide firm evidence. In combination with the NUV data from Haswell et al. (2012) it is noted that WASP-12 shows a lack of MgII emission cores when compared to similar stars (Fig. 4.7). This is attributed to one of several possibilities: the star is passing through a low level of activity; it is significantly older than reported; the MgII resonance lines are being absorbed by planetary material overflowing through inner Lagrangian of its Roche lobe and surrounding the star.

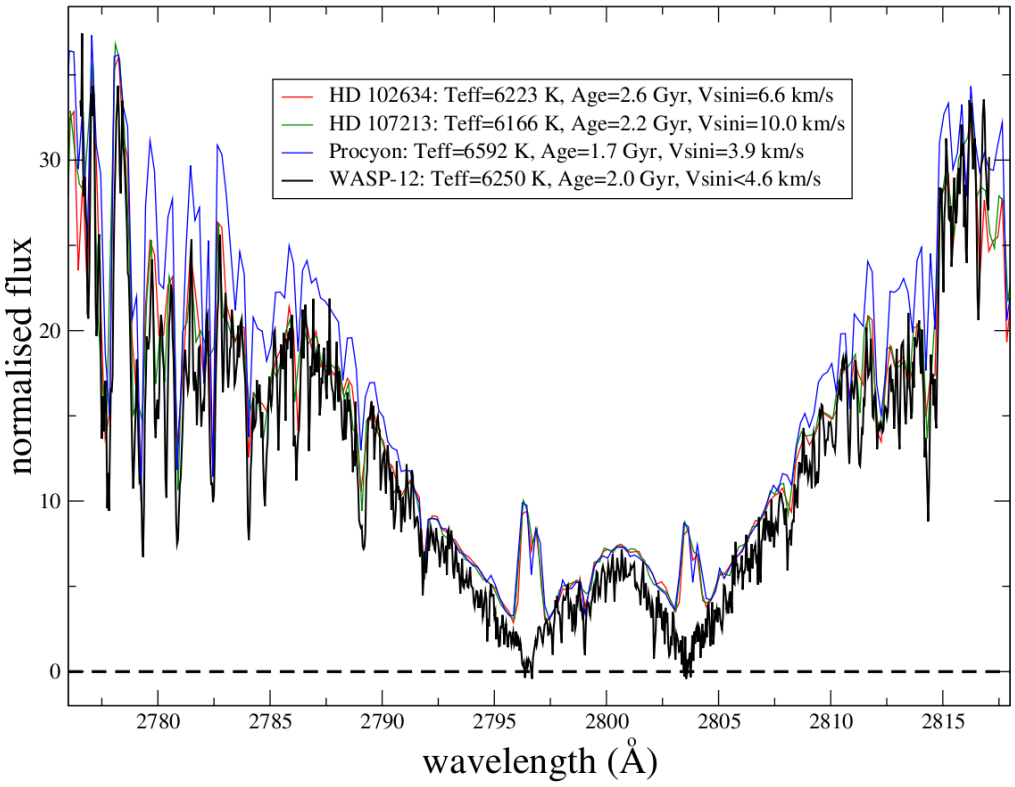

Figure 4.7: Comparison of spectra for WASP-12 and three similar stars. Notice the MgII double peaks for the similar stars while WASP-12's spectrum shows no flux at the wavelengths between 2795 and 2805 Å. (Figure from Haswell et al. (2012))

Haswell et al. (2012) further developed the results and conclusions in Fossati et al. (2010a) with added observations (Fig. 4.8). Transit depths in the NUVA and NUVC spectral regions were detected which were up to a factor of three deeper than the optical transit. These observations in conjunction with the Roche lobe work presented both here and in Haswell et al. (2012) show that the absorbing gas far overfills the planet's Roche lobe. This adds further support to the planet being surrounded by an envelope of planetary material.

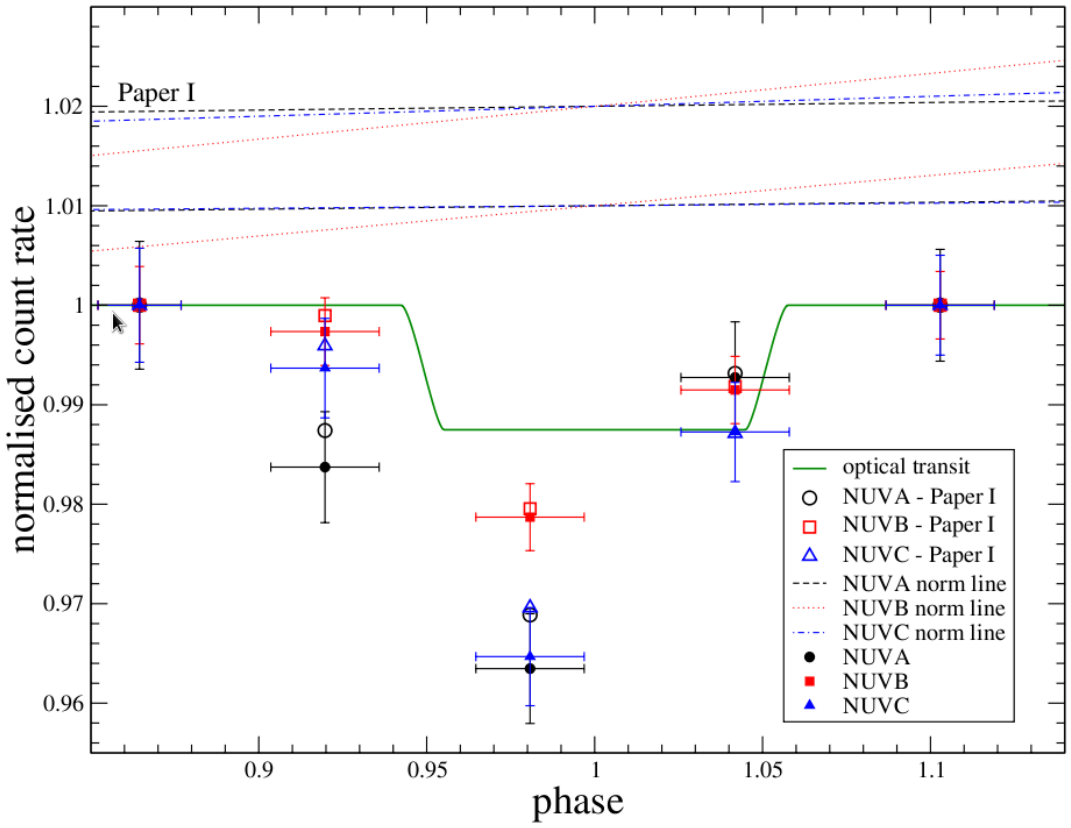

Figure 4.8: WASP-12b light curve obtained for transits at different wavelengths (NUVA: 2539-2580 Å, NUVB: 2655-2696 Å, NUVC: 2770-2811 Å) taken from Haswell et al. (2012). 'Paper I' refers to data from Fossati et al. (2010a). The normalization lines indicate the tilt which has been removed from the data in setting the first and last point to unity. The upper set of normalization lines corresponds to the Fossati et al. (2010a) reduction. The green line shows the model transit of the optically opaque planet across a uniform brightness stellar disk.

4.3.3 Earth-like Planets Orbiting Cool White Dwarfs

Salaris et al. (2010) present white dwarf cooling models and suggest that white dwarfs

initially cool down rapidly, with temperature decreasing by thousands of degrees in $\sim$3 Gyr. Once an effective temperature of $\sim$6000 K is reached, crystallization slows the cooling process creating a cool white dwarf (CWD). The outcome of this is a habitable zone that can survive for up to 8 Gyr (Agol 2011). At nearly double the age of the Earth this amount of time is more than adequate for life to form and evolve. This makes CWDs very interesting observational targets both in terms of the prospect of life and the relative ease of transit detection compared with similar sized planets around a Sun-like star.

The Roche geometric distortions for planets orbiting at 0.01 AU from 0.6 $M_{\odot}$ white dwarfs, the CWD habitable zone (Agol 2011), was calculated and presented in Fossati et al. (2012). It was found that planets with masses and radii similar to Earth, CoRoT-7b, Kepler-10b, and Kepler-11b were all noticeably distorted from spherical. This resulted in ratios of illuminated areas at superior-conjunction and at quadrature of 1.95, 1.95, 1.97, and 1.90, respectively. A spherical planet would have a ratio of exactly 2.0 as such a planet would have symmetrical hemispheres at both quadrature and superior-conjunction.

Kepler-11d was also placed into this scenario and was found to overfill its Roche lobe. A planet such as this would lose its outer layers until it exactly fills the critical equipotential surface. At quadrature, it would be heavily distorted and an enlarged teardrop-shaped cross-section would be presented. The illuminated area at photometric maximum being only 1.52 times that at quadrature. These illuminated area ratios would impact the photometric light curve of such planets, introducing a variability which will be synchronised with the orbital phase of the planet.

4.3.4 Roche Correction Look-up Chart

As systems are studied further and their parameters further refined, so too are the volume and density corrections presented in this work. The benefits from using a normalised and unitless equation is that look-up charts can be calculated such as those

shown in Fig. 4.9. This allows for volume (and density) corrections to be determined without the need to calculate an individual system every time the parameters are refined and improved. This Roche code is applied with settings of $\delta\phi = 0.1$ and $\delta U = 0.001$, which allows the generation and collection of a large sample of data points relatively quickly.

Fig. 4.9 once again highlights that the inclination of a planet will have minimal impact at low volume corrections. There is a notable impact on the corrections at larger radii (i.e. substantially filled Roche lobes), adding to the argument for including it in calculations. A full set of figures with mass ratios from 10^{-6} through to 10^{-1} at inclinations of 75°to 90°have been generated.

WASP-19b has a $\sim$2% transit depth with a mass ratio of $\sim$0.00114, inclination of 79.40° and a normalised observed radius of $\sim$0.0406. Inspecting the appropriate look-up chart with these values shows that this planet will require a volume correction of $\sim$12%. For comparison, the calculated value volume correction is 11.28% which shows that there is an inaccuracy to this method. A potential solution would be to generate a data cube of results which a user can then use to find a more accurate value.

4.4 Key Results

The key results from this chapter are as follows:

- A Roche potential surface mapping code was generated in order to explore the effects that the Roche potential has on exoplanets. The code has been rigorously tested and found to be valid and consistent.

- The effect of an exoplanet's orbital inclination is found to only have a minor impact on distortion results. The effects are more readily seen in planets that heavily fill their Roche lobes along with those that have high inclinations.

- The code was applied to 207 exoplanets and highlighted that WASP-19b, WASP-12b and WASP-103b have significantly filled lobes which leads to strong distor-

tions from a spherical shape resulting in density corrections of 12.71%, 11.84% and 8.89% for these three planets.

- The calculated values for WASP-19b and WASP-12b differ from those of Burton et al. (2014) but the qualitative results are the same; both planets are undergoing severe distortion effects.

- The Roche calculations were applied to WASP-12b in Haswell et al. (2012) and it was found that the the opaque material surrounding the planet far overfills its Roche lobe.

- Fossati et al. (2012) also demonstrated the application of this work to habitable planets around cool white dwarfs. It was found that planets with masses and radii similar to Earth, CoRoT-7b, Kepler-10b, Kepler-11b and Kepler-11d orbiting at 0.01 AU from a 0.6 $M_{\odot}$ cool white dwarf were all noticeably distorted from spherical. The Kepler-11d facsimile was also found to overfill its Roche lobe and would be expected to be losing mass.

- Look-up contour plots were generated for mass ratios of 10^{-6} through to 10^{-1}.

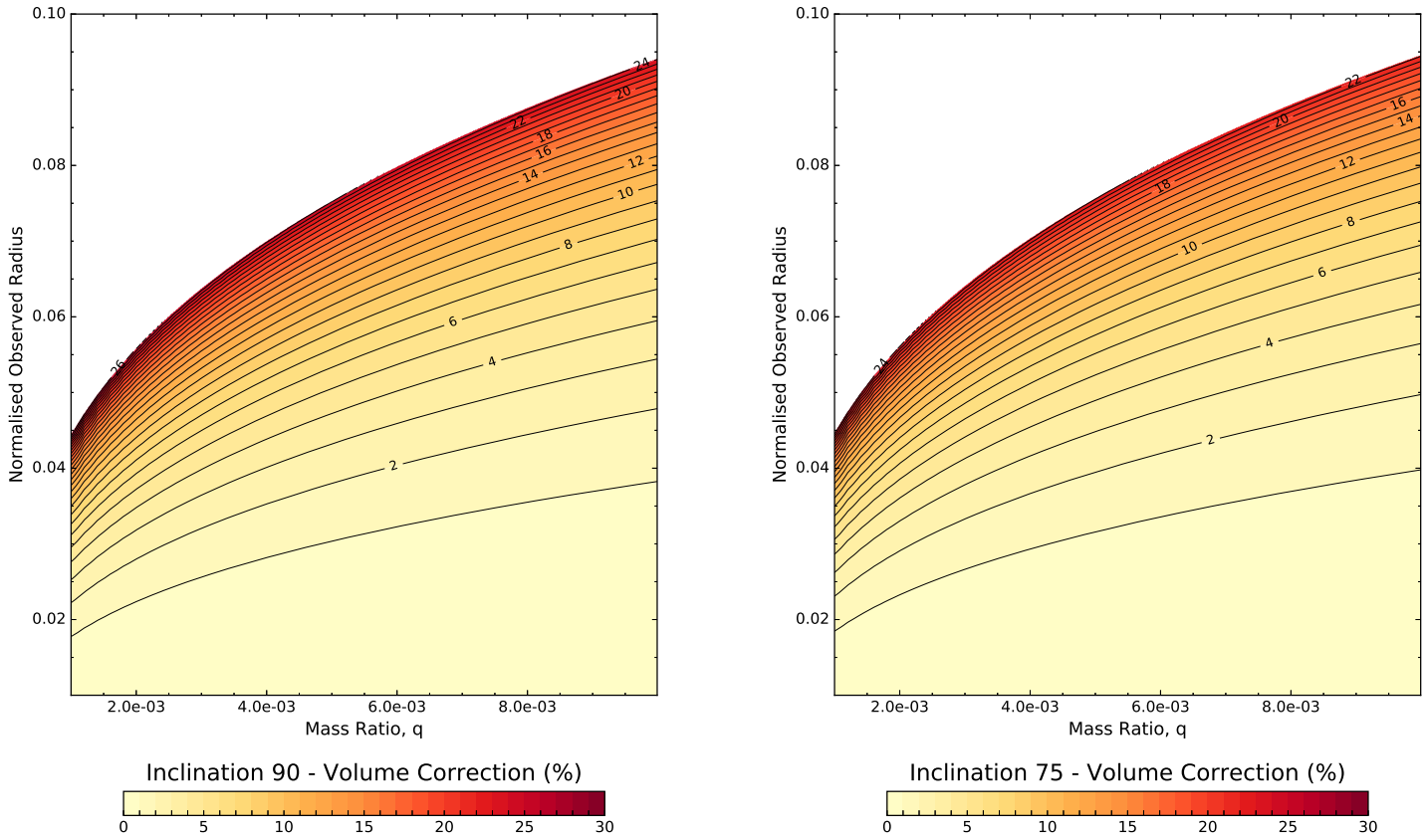

Figure 4.9: Comparison of the volume corrections required at inclinations of 90°(left) and 75°(right). Note the subtle differences at the higher normalised observed radii

Chapter 5

PIRATE Observations - Gaia Transients

The topic now returns to PIRATE and the contributions it has made to the Gaia transient verification phase. The European Space Agency launched the Gaia satellite in December 2013 with one aspect of the science output being an all-sky multi-epoch photometric survey covering approximately one billion stars ($\sim$1% of stars in the Milky Way). Over the course of 5 years it will monitor and detect variability with millimag precision down to V = 15 mag and about 0.01 mag precision down to V = 20mag (Wyrzykowski et al. 2012). Gaia is also capable of detecting new objects appearing in its field-of-view, thus detecting most classes of transient phenomena such as supernovae, novae and microlensing events. The Gaia Science Alerts system will detect and provisionally classify these photometric transients but a network of followup instruments is needed to undertake further study and eventually classify all of these objects. The following sections will look at how PIRATE has contributed to this effort pre-launch and during the verification stages of Gaia.

In order to clarify the role of the author in this chapter it is important to note that some parts of this chapter report on previous work by other observers as well as describe the commercial software in use. The author has heavily modified Stefan Holmes' exoplanet pipeline described in Sec. 3.2.1 to create a transient photometry

pipeline. Through the use of the Cambridge photometry calibration service (CPCS), the author has matched PIRATE's filters to known catalogue filters. Using a similar methodology to the CPCS, the author was able to examine a selection of frames to identify PIRATE's limiting magnitude. The majority of observations and reduction of transients data have been carried out by the author. As an example, SN 2014J is analysed by the author to showcase PIRATE's abilities but makes use of some AAVSO data to fill in the gaps in PIRATE observations. Sec. 5.3.2 reports on other transients for which the author has collected observational data.

5.1 PIRATE's Previous Transient Contributions

Bloom et al. (2012) demonstrates that PIRATE can and has already played a key role in observational transient science. A serendipitous pre-discovery observation of SN 2011fe in M101 (the Pinwheel Galaxy) allowed for an upper limit constraint on the radius of the primary-star progenitor, R_p. Nugent et al. (2011) observed SN 2011fe with the Palomar Transient Factory and placed an initial radius constraint of $R_p \lesssim 0.1R_\odot$. This constraint excludes red giants and main sequence stars as the progenitor. Using PIRATE's data point along with those of Nugent et al. (2011), Bloom et al. (2012) placed an improved constraint of $R_p \lesssim 0.02R_\odot$. The constrained radius along with a non-detection of a quiescent X-Ray counterpart and an inferred synthesized ^{56}Ni mass allowed a limit on the average density of the primary star to be estimated as well as the effective temperature. By process of elimination it was suggested that the progenitor primary star could only be a compact degenerate object such as a white dwarf or neutron star. Additionally, a further inference was also made about the suspected Roche lobe overflowing companion star, with an estimated radius constraint of $R_c \lesssim 0.1R_\odot$. This also excludes overflowing red giant and main-sequence stars as the secondary star.

At the time of publication, PIRATE's observation was the earliest SN Ia detection with an estimated observation time of $\sim$4 hours post first light. Since then Zheng et al. (2013) has beaten this record with an estimated observation time of $\sim$2.4 hours. Zheng

et al. (2013) also point out that the power law used to fit the rising light curve is not sufficient for every SNe Ia as a varying power law is apparent within the early rising light curve and proposes using a broken power law as used to fit gamma-ray burst afterglows (Zheng et al. 2012).

Holmes et al. (2011) briefly mentions some of PIRATE's contributions to the detection of several novae candidates in M31 as part of a collaboration with the Max Planck Institute for Extraterrestial Physics (MPE). For this research work, PIRATE routinely observed M31 and the data would then be collected and analysed by colleagues at the MPE. This collaborative effort has resulted in four seperate novae candidate detections (Burwitz et al. 2009, 2010a,b; Henze et al. 2012). This collaboration has now run its course, although the PIRATE team is always willing to explore new avenues of collaboration as well as renew previous ones.

5.2 Gaia Transient Alert Preparation

The previous section highlights that PIRATE is capable of detecting and contributing to transient event science and has already made significant contributions. Additionally, early observations of transients provide key factors in our understanding of these events (Bloom et al. 2012; Zheng et al. 2013). PIRATE is now embarking on a new phase of transient observations, the long term photometry of Gaia transients. In preperation for this, the PIRATE observation team has observed several targets to test the effectiveness of PIRATE's stability, procedures and limitations as well as that of the Cambridge Photometry Calibration Server.

5.2.1 ACP Scheduler and The VOEvent Receiver

During the Gaia transient alert & follow-up development and exploratory phase, observations were carried out by manually planning and submitting follow-up photometry runs which is less than ideal for time critical observations. In an effort to resolve this, ACP Scheduler (ACPS), described in Denny (2004), was added to the PIRATE con-

trol PC. ACPS (see Fig. 5.1) is an add-on software for ACP designed to allow full automation of ACP and hence fully automate PIRATE.

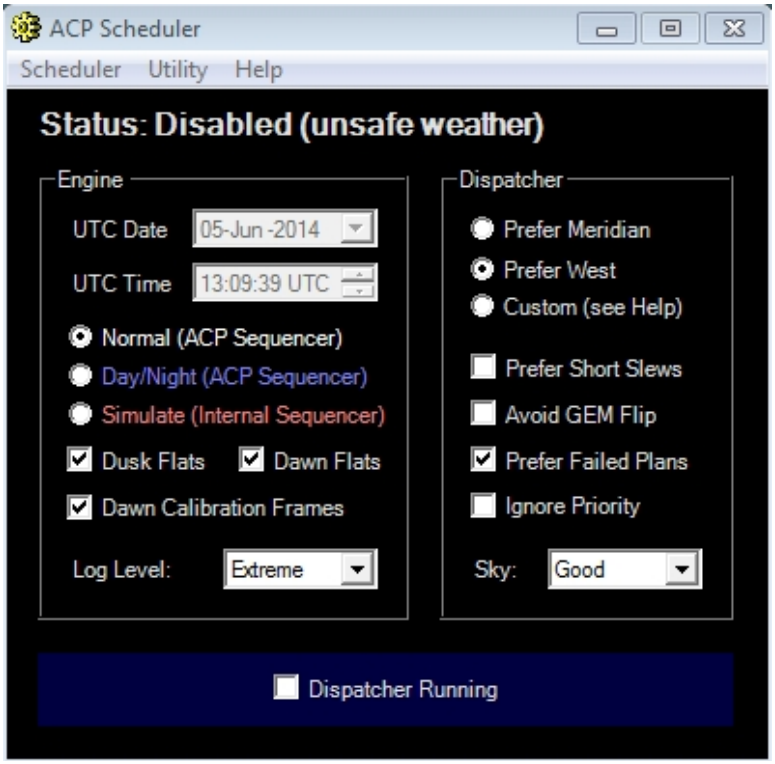

Figure 5.1: ACP Scheduler Console

A typical observation session with ACPS runs through an automated start-up script which initiates all of the relevant software and connects the equipment to ACP before cooling the CCD to its operating temperature; typically -20°C in the winter months and -10°C in the summer. ACPS then opens the dome and takes dusk flats if requested by the user and allowed by the weather monitoring software (Weather Watcher). This is followed by waiting in a dew avoidance position for the sky to get dark enough to commence observations, this is either nautical or astronomical twilight depending on the scientific goals of the imminent run. As dawn approaches, dawn flats are taken and then the dome is closed for dark and bias calibration frame acquisition. Once completed the ACPS warms the CCD, disconnects the equipment and shuts down all software with the exception of Weather Watcher, ACP and ACPS. ACPS can be left running and will repeat the entire cycle of start up, observations and shutdown until user intervention and/or an error occurs at which point ACPS will stop dispatching

observations and make the operator aware via email that assistance is required.

Observations for ACPS are dictated by the user ahead of time and input into a database which ACPS then automatically and appropriately dispatches targets from. The conditions for selection are based on a built in efficiency weighting (including but not limited to transit altitude and slew distance) that selects the optimum target for the current time and conditions. These weightings can be altered by the user to better suit the needs of the observation. In addition to this ACPS also has user constraints which can be set to include a maximum air-mass, an air-mass range, a minimum altitude, hour angle range, moon distance avoidance, moon-set, sky condition and a time range. When an observation has been completed the dispatcher then selects the next optimum target for the updated time and conditions. In the event of an interruption due to the weather the plan is set as failed and upon weather clearance, with the appropriate setting selected, the observation resumes if possible.

A VOEvent receiver is packaged along with ACPS. VOEvent is an International Virtual Observatory Alliance (IVOA) standard (Seaman et al. 2011) using the XML language. The purpose of the VOEvent standard is to report astronomical events in a descriptive yet concise format that can be created, communicated and parsed quickly by the receivers. This facilitates time-critical observations of transient events and is very suitable for automated robotic telescopes.

The PIRATE VOEvent receiver is connected to a broker in order to identify and filter alerts of transient events. When an observable alert is received, the VOEvent receiver adds the observation request to the ACPS database and sets it as a high priority target. For PIRATE, the input into the database is handled by customised RTML code, based upon the template supplied with ACPS, which is specific to the observation target. From January 2013 to November 2015, PIRATE was linked up to the Caltech Realtime Transient Survey (CRTS), CBAT Transient Object Confirmation (TOC) and Swift GRB (S-GRB) alerts. There are also options for user-defined surveys, one of which will be dedicated to Gaia transient alerts when they become available as VOEvents.

The alert filter is defined in a java script with the pre-defined filters for CRTS, TOC and S-GRB located in the file. The filter was set up to accept alerts of 20th magnitude or brighter for CRTS and TOC and an intensity ratio (burst/background) of 0 for the S-GRB. The CRTS and TOC values were beyond the limit of what PIRATE could reasonably detect (see Sec. 5.2.4) but allowed PIRATE to attempt observations of targets that may still have been increasing in brightness (such as supernovae) since creation of the alert. An additional benefit was that more alerts came through, facilitating system testing and further fine tuning. Similarly, the S-GRB intensity ratio setting allowed for GRB alerts to be observed even if the optical magnitude was outside of PIRATE's abilities. The primary reason for this being that the intensity ratio is not a good indicator of magnitude as GRB afterglows may be affected by extinction and high redshift as well as being intrinsically faint in the optical. These are commonly referred to as 'dark' GRBs. In theory, if PIRATE observed but didn't detect a GRB afterglow it could still contribute by placing a limit on the magnitude for the area of sky surveyed. This same logic was also applied to the CRTS and TOC observations and will be applied to future Gaia VOEvent alerts.

Once a valid alert is filtered the VOEvent receiver runs the relevant RTML script, pre-edited by the user, for the target, which inputs the relevant fields into the ACPS database. These fields include the exposure times, filters, CCD binnings and coordinates as well as other attributes. At present the event filter is set up to link to a single RTML script per survey. This has a problem that there is no flexibility in PIRATE's observation strategy for differing magnitude targets. Two potential solutions exist, the "quick and dirty" method is to program a range of exposure times into the RTML script. Unfortunately this results in all the observations taking place even if the exposure time is less than ideal for the target. If a suitable range of exposures is applied in the RTML then at least one of the exposures should contain a detectable source which doesn't saturate. This is a suitable option for targets where the magnitude is unknown, such as GRB afterglows. The alternaive option is to edit the java script to call a different RTML for each magnitude with exposures set to the optimum

times. The rigidity of this solution has pitfalls of its own. In particular, if conditions require a differing exposure time, such as shorter exposure times when winds are high, then there is no flexibility for this situation. The ideal solution appears to lie between the two options with multiple filters being set up in the event filter file along with an RTML containing optimum, shorter and longer exposure times.

5.2.2 Gaia Data Reduction Pipeline

Described here is the reduction pipeline used to calibrate, measure and upload the resulting magnitude data to the Cambridge Photometry Calibration Server (CPCS, see Sec. 5.2.3). The pipeline is a heavily modified version of the reduction methods described in Holmes et al. (2011) and relies on IRAF to calibrate and perform photometry on the science frames. IDL makes up the bulk of the code and is used to generate the commands for use in IRAF, analyse the IRAF output and refine/restructure the output into the CPCS required format as well as a succinct summary for user verification of data.

The pipeline is run on a target by target basis per filter and typically on separate nights so as to use relevant calibration frames. A parameter file containing the settings for the pipeline is generated in the working folder or, if a user-modified parameter file is already present, it will be read. Science frames are also required to be plate solved in order to convert from pixel $x-y$ co-ordinates to a CPCS required right ascension (RA) and declination (Dec).

Holmes et al. (2011) describe how the science and calibration frame lists are generated and calibrated by the pipeline in combination with IRAF's CCDPROC utility. The user is then required to determine an appropriate full-width half-max (FWHM), typically taken to be the average of several stars, for each individual science frame. The FWHM is used to locate the star pixel positions on each frame using IRAF's DAOFIND along with a detection threshold defined in the parameter settings file (4σ by default). A maximum pixel count setting is also present in the settings file and used

by the DAOFIND package, providing the ability to ignore saturated or near saturated stars. Photometry is performed on the stars located with the IRAF PHOT package using three different aperture annuli representing multiples of the FWHM as defined in the parameter setting file. Stars that aren't detected in all three apertures are removed from the sample; this is a requirement to bypass a limitation of the pipeline but has the added advantage of ignoring low signal-to-noise stars, defective pixels and cosmic rays depending on the aperture sizes used. For example, a large-aperture annulus of three times the FWHM placed over a low signal-to-noise star ($\sim 2\sigma$) is unlikely to be detected due to the background noise within the aperture.

To convert $x-y$ pixel co-ordinates to RA and Dec the XY2SKY function, contained in the IRAF WCSTOOL package, is used. A file is then output for each science frame containing a list of all the stars, and their associated headers, in a Sextractor[1] (a source extraction software frequently used in astronomy) format. This includes an individual identification number for each star, flux, magnitudes and associated errors per aperture as well as the $x-y$ and RA & Dec co-ordinates.

The pipeline requests user input for the International Virtual Observatory Resource Name (IVORN), a unique target identifier, and performs a dry-run of the CPCS upload procedure with appropriate settings applied. This allows the user to verify the results for upload prior to running the full CPCS submission. In the event that the results are acceptable, the user allows the pipeline to generate and run the final upload bash script. If the results require parameter adjustment, the script generates the final upload scripts and exits without upload. The user can edit the settings in the dry-run or final upload scripts and manually execute them when required.

5.2.3 Cambridge Photometry Calibration Server

The Cambridge Photometry Calibration Server[2] (CPCS) is used to calibrate submitted photometry in instrumental magnitudes against catalogued measurements. Calibrating

[1] https://www.astromatic.net/software/sextractor
[2] http://gsaweb.ast.cam.ac.uk/followup

photometric data to a standardised format allows multiple observatories to contribute to a single target in a larger collaborative effort. This collaboration provides a significant advantage for small to medium sized observatories as it provides the ability to generate a more complete long-term photometric light curve, which may not have been possible at a solo observatory due to technical and environmental down time as well as competing observational commitments.

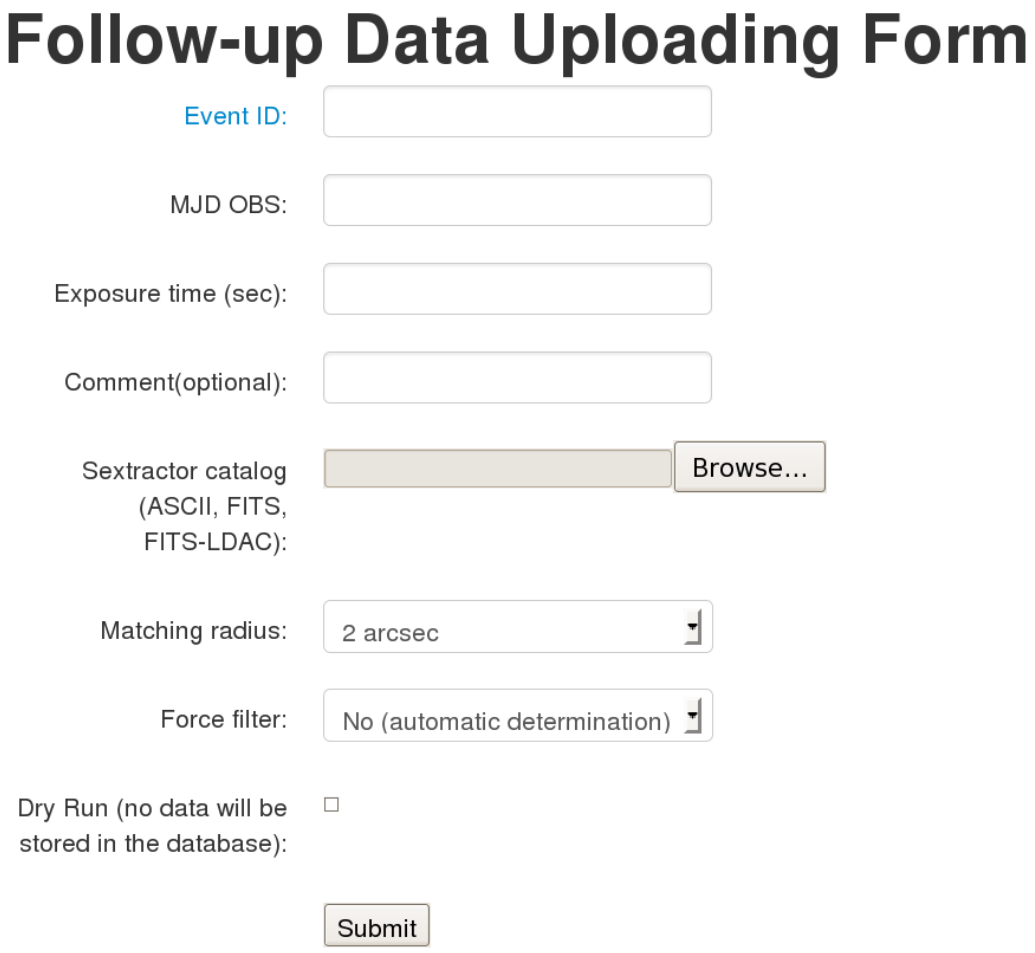

Figure 5.2: The Cambridge Photometry Calibration Server upload form.

Prior to uploading the photometry, the event being measured needs to be included in the CPCS database if not already present. This is accomplished by registering the target's unique IVORN code. Uploading photometry can take place manually via a website form (Fig. 5.2) or a command line/script submission method; the latter also allows for automatic submission. The photometry file needs to include the RA and Dec of the measured stars and target as well as the associated magnitudes and mea-

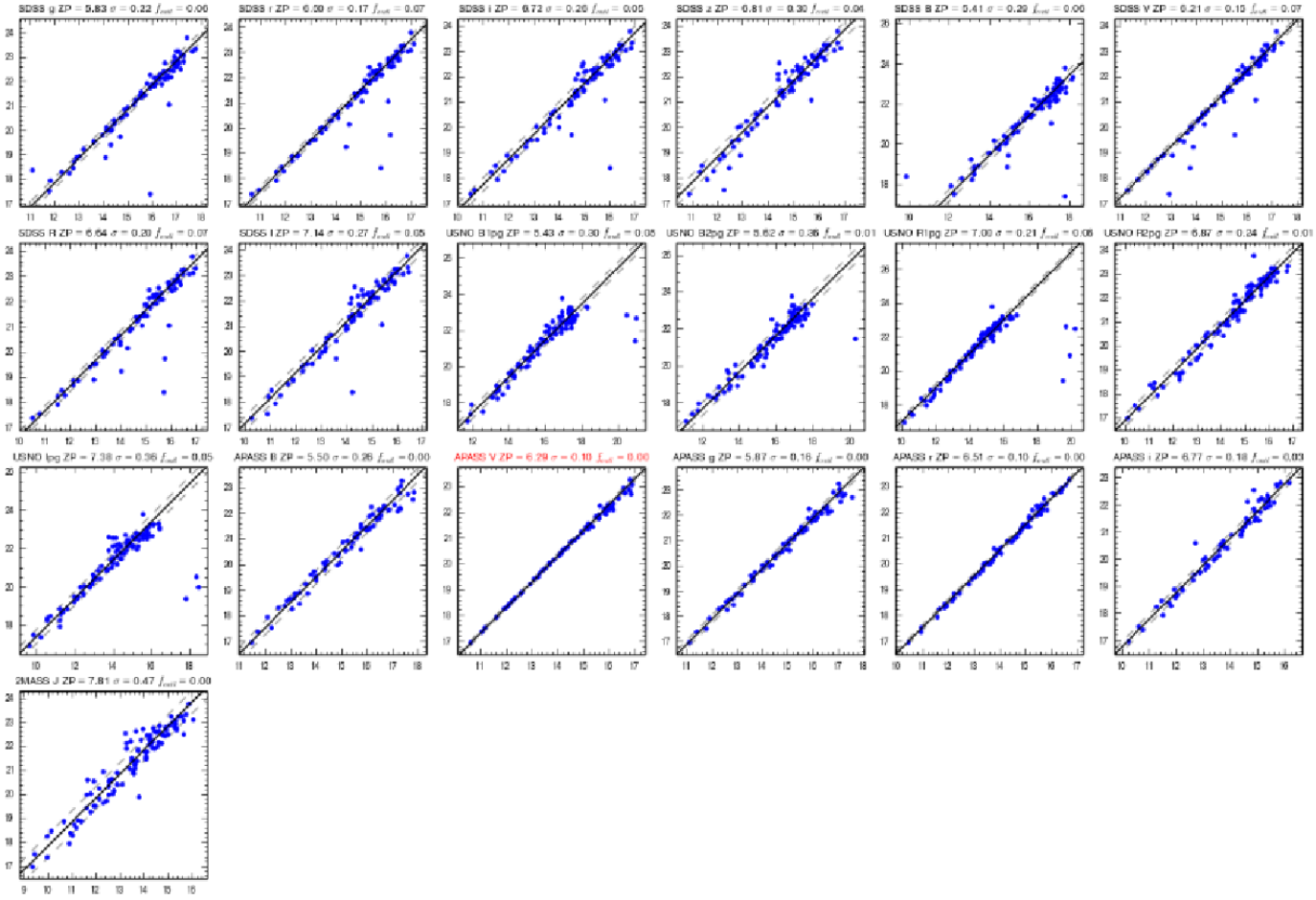

Figure 5.3: An example output from the Cambridge Photometry Calibration Server. The uploaded data file was based on observations using PIRATE in the Mk 1.5 configuration with the V filter. The matching radius was set to 2 arcseconds. The highlighted red plot shows that the calibration server has chosen the APASS catalogue's V filter as the best fit for PIRATE's data.

surement errors. Both the form and the command line submission methods need to be supplied with the target event IVORN code, the modified Julian date (MJD) of the observation, the exposure duration in seconds (there is also an optional comments field for remarks about the data point). An appropriate matching radius and filter selection for the CPCS catalogue point-source matching routine are also applied. The user also has the opportunity to test upload settings without registering the data, via a 'dry run' setting.

The CPCS calibration takes the instrumental magnitude of the catalogued stars and determines the zero point magnitude for a given catalogue filter. This is then used to scale the instrumental magnitude of the target to the appropriate apparent magnitude for the catalogue filter used. Fig. 5.3 shows an example output from the CPCS web form for a PIRATE Mk 1.5 data set taken in the V filter. It has been statistically determined by the CPCS to have a best match with the APASS catalogue's V filter with a rms scatter of 0.10 mag and an outlier fraction of less than 0.05 (which is rounded to 0.0 in this figure). The APASS/r filter (two plots to the right of the APASS/V filter) is also a very close match to the data set displaying similar scatter and outlier fraction. Supplying the same data using a command line submission provides a higher significant figure output, confirming the APASS/V filter as the dominant filter. This hints at an issue with the CPCS automatic filter selection which can potentially result in an inappropriate selection for the given filter and is discussed further in Section 5.2.3.1.

5.2.3.1 Calibrating PIRATE's Filters

PIRATE has two CCD cameras available, the SBIG STX-16803 and the STL-1001E. These cameras define two different operating modes, referred to as PIRATE Mk 1.5 (STL-1001E) and PIRATE Mk 2 (STX-16803). PIRATE Mk 1.5 made use of Baader Johnson-Cousins BVRI photometric filters while PIRATE Mk 2 used Baader LRGB filters which have a "top hat" spectral response (Fig. 2.19).

The CPCS doesn't always select the most appropriate filter when set to automatic filter selection. Observations made using PIRATE's filters are passed through the

CPCS in order to identify which catalogues provide best matches. This in turn allows the user to specify the optimum filter choice. Table 5.1 shows the results from the CPCS when allowed to automatically set the filter.

Table 5.1: Comparison of PIRATE filters passed through the CPCS with the filter selection set to 'automatic' and a matching radius set to 2 arcseconds. The first column is the PIRATE Mk 1.5 and 2 filter. The second and third columns in between show the dominating catalogue filters as matched by the CPCS with the percentage number of occurrences shown in brackets. The fourth column shows percentage occurrences of other filters. The last column, sample size, refers to the number of frames uploaded to the CPCS.

PIRATE	CPCS Catalogue Filters (%)			Sample
Filter	Primary	Secondary	Other	Size
I - Mk 1.5	APASS/i (93.1%)	USNO/Ipg (2.5%)	Other (4.4%)	204
R - Mk 1.5	APASS/r (78.3%)	APASS/i (16.8%)	Other (4.9%)	203
V - Mk 1.5	APASS/V (86.2%)	APASS/r (10.5%)	Other (3.3%)	181
B - Mk 1.5	APASS/g (52.8%)	APASS/B (44.9%)	Other (2.3%)	178
R - Mk 2	APASS/r (100%)	-	-	113
G - Mk 2	APASS/V (100%)	-	-	112
B - Mk 2	APASS/g (68.9%)	APASS/B (30.2%)	SDSS/g (0.9%)	106

For PIRATE Mk 1.5, the filters for V, R and I are dominated by the APASS/V, APASS/r and APASS/i catalogues respectively. The average RMS scatter for these matches are 0.066 ± 0.035, 0.045 ± 0.018 and 0.066 ± 0.023 respectively. The corresponding average outlier fractions are 0.021 ± 0.029, 0.014 ± 0.019 and 0.019 ± 0.022 respectively. The B filter on the other hand is nearly evenly divided with APASS/g just slightly more dominant than APASS/B. Examination of the average RMS scatter for the APASS/g and APASS/B catalogue matches where APASS/g was dominant, gives 0.044 ± 0.035 and 0.078 ± 0.031 respectively, with outlier fractions of 0.025 ± 0.024 and 0.010 ± 0.017. A similar treatment for when the APASS/B was dominant, gives 0.096 ± 0.034 and 0.074 ± 0.030 respectively, with outlier fractions of 0.007 ± 0.018 and 0.013 ± 0.023.

Remarkably, for PIRATE Mk 2 the filters R and G are constantly resolved as APASS/r and APASS/V catalogue matches respectively. The average RMS scatter

for these matches are 0.055 $\pm$ 0.018 and 0.065 $\pm$ 0.016 respectively. The corresponding average outlier fractions are 0.011 $\pm$ 0.008 and 0.007 $\pm$ 0.007 respectively. The B filter is once again split between APASS/g and APASS/B although even more dominantly towards APASS/g. Like the Mk 1.5 treatment, examining the Mk 2 APASS/g and APASS/B catalogue matches where APASS/g was dominant, gives average RMS scatters of 0.076 $\pm$ 0.024 and 0.100 $\pm$ 0.020 respectively, with outlier fractions of 0.014 $\pm$ 0.016 and 0.014 $\pm$ 0.012. A similar treatment for when the APASS/B was dominant gives 0.116 $\pm$ 0.015 and 0.104 $\pm$ 0.012 respectively, with outlier fractions of 0.005 $\pm$ 0.007 and 0.028 $\pm$ 0.008. For both PIRATE Mk 1.5 and Mk 2, the matches for the catalogues listed as 'Other' are as follows:

I - Mk 1.5 gave three SDSS/I, two SDSS/z, and one each of SDSS/i, USNO/R1pg, USNO/R2pg and USNO/B2pg.

R - Mk 1.5 gave two each of USNO/R1pg, USNO/R2pg, SDSS/r and APASS/V along with a single SDSS/R and SDSS/u.

V - Mk 1.5 gave two each of SDSS/i and APASS/B, and one each of APASS/i and USNO/B2pg.

B - Mk 1.5 gave two USNO/B2pg as well as a single USNO/B1pg and SDSS/u.

B - Mk 2 gave a single SDSS/g result.

These 'Other' filters can be ignored as all occurrences are explained by one or more of the following issues. Having a low number of matched catalogue stars, typically less than 20 for the current data sets, causes high inaccuracies in the plots (ie. the RMS scatter is an order of magnitude greater than the average values listed earlier) and in some cases the CPCS cannot resolve for the prefered filter. This could initially be attributed to the prefered catalogue not containing sufficient data for the field in question, either due to a sparse field being imaged or the catalogue not covering the target area of the sky. Both are ruled out in the above scenario as other calibrations of

the same sky have calibrated successfuly. The primary reasoning for a lack of detected stars in the target field is that the data is of low quality, which has been confirmed in this case.

Another issue, which was highlighted earlier, is that the CPCS will select the catalogue with the lowest RMS scatter. This is a major issue with the automation of filter selection as it ignores the outlier fraction. In the case of the 'Other' catalogues the scatter is averaged to be 0.01 less than the prefered catalogue but has an average outlier fraction difference of 0.12. This highlights that examination of the outlier fraction should definitely take place via a dry run prior to uploading the data. In addition to this there are also instances of the inappropriate filter selection taking place for targets with large scatter. The single SDSS/g occurence in the PIRATE Mk 2 B filter is an example of this, where the scatter is 0.157. Bearing in mind that the CPCS selects the lowest scatter as the best catalogue this means that in both APASS/g and APASS/B this value is even higher at 0.163 and 0.177 respectively. This is another indication that this particular data point is of low quality despite having over 200 detected stars. In this instance the lack of quality is due to low signal to noise on a significant number of the stars in the field of view.

With the exception of both the PIRATE B filters, it is clear that the dominant catalogues should be used for the relevant filters. The average RMS scatter for Mk 1.5 and Mk 2 B filter matches shows that the APASS/B catalogue provides a fairly consistent value whether it is dominant or not while the APASS/g catalogue is less reliable and can vary quite considerably. Both of the PIRATE B filters have a spectral response curve that lies somewhere between the APASS/g and APASS/B catalogues. The recommendation for both cases is to use the APASS/B catalogue for reliability; however, using the alternative catalogue to contribute to existing collaborator data can be justified.

5.2.4 PIRATE's Limiting Magnitudes

The limiting magnitude of an observatory site on a given night is dependent on a large number of factors, including but not limited to the weather, seeing, Moon phase and exposure time. Tables 5.2 & 5.3 show the varying limiting magnitudes and associated stellar FWHM of a small selection of images in different filters for PIRATE Mk 1.5 and 2 respectively.

Table 5.2: The FWHM and associated limiting magnitudes for PIRATE Mk 1.5

Date	Filter	Frame	Bin	Exposure (s)	Airmass	FWHM (")	Limiting Mag
22/02/14	I	9	1x1	300	1.12	2.28	16.37
22/02/14	R	9	1x1	300	1.13	2.28	16.82
22/02/14	V	9	1x1	300	1.14	2.28	16.74
22/02/14	B	9	1x1	300	1.16	2.65	16.14
26/02/14	I	2	1x1	300	1.01	3.46	17.27
26/02/14	R	2	1x1	300	1.01	3.21	17.95
26/02/14	V	2	1x1	300	1.00	3.30	17.68
26/02/14	B	2	1x1	300	1.00	3.89	16.76

Table 5.3: The FWHM and associated limiting magnitudes for PIRATE Mk 2

Date	Filter	Frame	Bin	Exposure (s)	Airmass	FWHM (")	Limiting Mag
30/07/13	R	2	2x2	600	1.07	2.39	18.21
30/07/13	G	2	2x2	600	1.08	2.08	18.30
30/07/13	B	2	2x2	600	1.10	2.33	18.31
06/07/13	R	1	2x2	150	1.09	2.33	17.29
06/07/13	G	1	2x2	150	1.09	2.39	17.38
06/07/13	B	1	2x2	150	1.09	2.52	17.43

The data for these tables are generated using a similar methodology to the CPCS calibration server. The point sources are matched to the UCAC4 catalogue (which includes the APASS measurements). The B filters for both Mk 1.5 and Mk 2 are calibrated to the APASS/g filter while the rest of the filters are matched to the best filter as described in Sec. 5.2.3.1. It is worth noting that the APASS catalogue covers a range of magnitudes from $\sim$10 to $\sim$16 mags so direct star matching won't provide the user with the faintest detected stars. This is overcome by calculating the magnitude

zero point and correcting the instrumental magnitudes by this value. The faintest point source with a 6σ detection is used as the limiting magnitude value.

From this selection it is possible to see that that the stellar FWHM on site varied considerably between 2.08 and 3.89 arc seconds depending on the filter and night. Examining a larger data set for July 2013 in R, G, and B shows that the site had a stellar FWHM of 2.82 $\pm$ 0.54, 2.80 $\pm$ 0.54, 2.82 $\pm$ 0.60 arc seconds respectively. Similarly, the faintest magnitude limits determined are around 18 mags with typical limits being around 17.5 mags.

5.3 PIRATE Observed Transients

As part of the Gaia verification phase, PIRATE has observed and monitored a number of transient events. The type Ia supernova, SN 2014J, is explored in depth and provided as an example of what a small aperture telescope like PIRATE is capable of accomplishing.

5.3.1 SN 2014J - An Initial Inspection

One target to which PIRATE has made a significant contribution via CPCS is SN 2014J. Fossey et al. (2014) announced the discovery of supernova SN 2014J in the Cigar Galaxy (M82) which, at 3500 Kpc, was the closest type-Ia since SN 1972E (3680 Kpc) and provided a rare opportunity for detailed observations to test current SN models and theories. The supernova's bright apparent magnitude allowed PIRATE to observe SN 2014J over a period of 3 months from 27th January 2014 till 28th April 2014 with a break in between 3rd March and 27th March due to PIRATE's teaching commitments.

The following discussion illustrates the capabilities of calibrated photometric monitoring using a small-aperture telescope such as PIRATE, located at the Mallorca site. Eq. 5.1 is an empirical model for fitting SNe lightcurves (Contardo et al. 2000). The measured values in this fit are the magnitude, m, and time, t. The initial magnitude

rise of the supernova is described by denominator with a rise time of Θ at a phase τ. A linear decay, representing the gradual drop in the magnitude, is described by the first two terms in the numerator, with f_0 and γ being the respective intercept and gradient at phase $t - t_0$. Two gaussian terms are also included to represent the primary and secondary peaks, g_0 and g_1 are the respective amplitudes while σ_0 and σ_1 define the widths.

$$m = \frac{f_0 + \gamma(t - t_0) + g_0 \exp\left[\frac{-(t-t_0)^2}{2\sigma_0^2}\right] + g_1 \exp\left[\frac{-(t-t_1)^2}{2\sigma_1^2}\right]}{1 - \exp\left[\frac{\tau - t}{\Theta}\right]} \tag{5.1}$$

SN 2014J was observed with PIRATE Mk 1.5 using the Johnson-Cousins BVRI broadband filter set. A fit was determined for the light curve in each filter using Eq. 5.1 and a Python package, LMFIT (v0.8.3). The PIRATE data is calibrated to APASS BVri using the CPCS. There is a lack of data (due to PIRATE's teaching commitments) between MJD 56720 and 56747 preventing accurate fits due to a lack of constraints on the secondary Gaussian term ($g_1 \exp\left[\frac{-(t-t_1)^2}{2\sigma_1^2}\right]$) in Eq. 5.1. The secondary maximum is expected to be easily visible in the redder part of the spectrum and dwindling towards the blue end. Despite the lack of a peak for the secondary maximum, enough observations have been gathered to at least imply its existence. In particular the observations at 56720 and just prior have been crucial in determining the start of the secondary maximum.

AAVSO data, obtained from the AAVSO International Database, is used to fill in the missing data ranges. AAVSO data points with no uncertainty values are removed, and the dates are converted from JD to MJD. The PIRATE and AAVSO data are fit separately and the peak magnitudes in each filter are obtained. Based on these fits, offsets are applied to AAVSO data to match PIRATE filter apparent magnitudes. AAVSO data between MJD 56715 and 56755 is used to fill in the gaps in the PIRATE data. Additionally AAVSO data prior to MJD 56685 is used to more accurately constrain the initial rise of SN 2014J. The resulting combined PIRATE and AAVSO data are shown in Fig. 5.4.

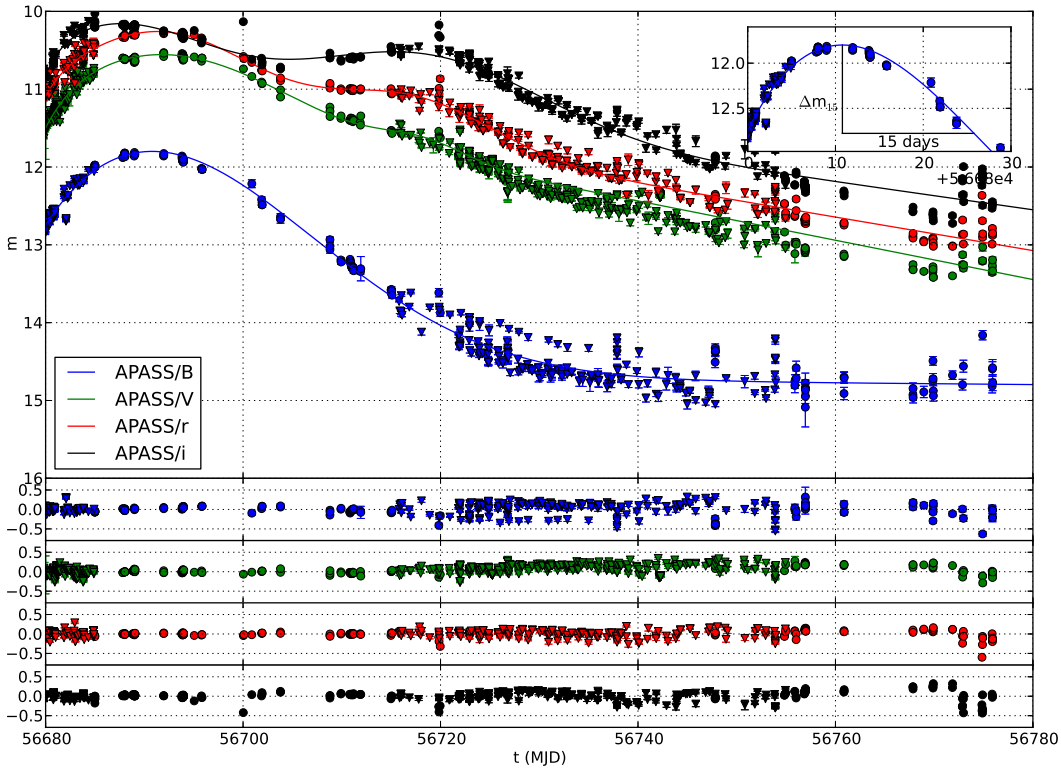

Figure 5.4: SN 2014J light curves in APASS BVri with lines of best fit. The solid circles are PIRATE data while the triangles are AAVSO data with apparent magnitude offsets applied to match the PIRATE data. The bottom four plots show the residuals for each of the filters while the box in the upper right corner shows the B filter $\Delta m15$. The parameters for the fits are shown in Table 5.4. The gap in the PIRATE data between MJD 56720 and 56747 is due to an interruption in observations for teaching commitments.

Ideally the following analysis would be performed on K-corrected data. A K-correction is a correction to magnitude of the object which accounts and corrects for redshift when the target is observed through a filter. In effect this corrects the redshifted data to an equivalent measurement at the rest frame of the target. Sadly, this requires currently unavailable filter transmission details for both PIRATE and the AAVSO observing telescopes and is beyond the scope of this work. Additionally, for accurate measurements, difference imaging photometry would also be employed in order to remove the host galaxy flux from that of SN 2014J. The fitting parameters were constrained to the final ranges as seen in Table 4.1 in Contardo (2001). The parameters determined for SN 2014J from this empirical approach for each filter are shown in Table 5.4.

Table 5.4: SN2014J fit parameters. Bounds indicate the range each variable was allowed to explore. The Init columns under each filter denote the initial parameters used to generate the fits. The Fit columns are the final output parameters for the associated filter.

	Bounds		B		V		R		I	
	Lower	Upper	Init	Fit	Init	Fit	Init	Fit	Init	Fit
f_0	-10	30	13.2	14.70 ± 21.77	10	11.28 ± 0.02	13.2	11.20 ± 0.05	13.2	10.89 ± 0.12
γ	0.001	1	0.5	0.001 ± 0.18	0.4	0.03 ± 0.00	0.5	0.02 ± 0.001	0.5	0.02 ± 0.00
g_0	-8	-0.001	-1.5	-3.21 ± 8.14	-1.5	-0.73 ± 0.02	-1.5	-0.92 ± 0.05	-1.5	-0.71 ± 0.11
t_0	56675	56700	56689	56687 ± 19.1	56689	56694 ± 0.6	56689	56692 ± 0.4	56689	56688 ± 1.4
σ_0	0.5	80	13	18.70 ± 12.25	24	11.20 ± 0.76	13	8.76 ± 0.66	13	8.79 ± 1.72
g_1	-8	-0.001	-0.001	-0.01 ± 11.90	-0.001	-0.20 ± 0.02	-1.5	-0.63 ± 0.03	-1.5	-0.89 ± 0.07
t_1	56695	56750	56719	56696 ± 23200	56714	56718 ± 0.5	56719	56717 ± 0.6	56719	56718 ± 0.7
σ_1	0.5	50	50	50.0 ± 3200.0	50	4.35 ± 0.48	5.0	8.28 ± 0.56	5.0	11.88 ± 0.86
τ	56600	56700	56673	56658 ± 17.7	56673	56669 ± 0.6	56673	56672 ± 1.3	56673	56673 ± 2.4
Θ	1	20	3	8.35 ± 15.85	3	4.15 ± 0.31	3	2.54 ± 0.50	3	2.13 ± 0.97

These fits provide the opportunity to determine the peak B magnitude, B_{max} and date t_{max}. The supernova decline rate from peak magnitude to 15 days later, $\Delta m15$, which describes the light curve shape, can also be determined. From the B filter fit a B_{max} of 11.80 $\pm$ 0.14 is observed at a t_{max} of 56690.79 $\pm$ 0.005 and provides $\Delta m15 =$ 0.98 $\pm$ 0.20. In comparison, Marion et al. (2015) obtain a B_{max} of 11.68 $\pm$ 0.01 at a t_{max} of 56689.74 $\pm$ 0.13 and a fitted/calculated $\Delta m15$ of 1.12 $\pm$ 0.02. It is recognised that the Marion et al. (2015) methods differ from the fitting methods described above. Of particular note, in Marion et al. (2015) the photometry is K-corrected by the fitting package, SNooPy, which simultaneously fits all filters with each fit having an effect on the other. Attempts to apply SNooPy to the PIRATE data have been unsuccessful due to the lack of PIRATE filter transmission response curves. The results above show that the Python LMFIT method is comparable to the SNooPy method for B_{max} and t_{max} The $\Delta m15$ result from the LMFIT analysis has a relatively large uncertainty range that encompasses the $\Delta m15$ determined by Marion et al. (2015).

The absolute peak magnitudes in B and V filters are expected to be about 19.3 $\pm$ 0.03 (e.g. Carrol & Ostlie 2007, pg. 686), differences in these values are indicative of extinction, $E(B-V)$, along the line of sight. A peak $E(B-V)$ extinction of 1.24 $\pm$ 0.16 is determined, based on the measured apparent magnitudes, which includes extinction due to both the Milky Way and the supernova host galaxy, M82. Taking the extinction due to the Milky Way, $E(B-V)_{MW}$, of 0.05 (Marion et al. 2015), this leaves an extinction due to the host galaxy, $E(B-V)_{host}$, of 1.19 $\pm$ 0.16. This is within the errors of the $E(B-V)_{host}$ of 1.22 $\pm$ 0.05 and 1.23 $\pm$ 0.06 as determined by Goobar et al. (2014) and Marion et al. (2015) respectively, both of which have employed SNooPy.

Phillips et al. (1999) describe a method of determining a reddening-free decline rate, $\Delta m15_{true}$, using Eqs. 5.2 & 5.3. This method is intended for use on the "tail" ($\sim$ 30+ days past the B-band maximum) of SNe Ia. As this section is only intended as a quick look at the SN 2014J the values at maximum determined previously are used in both Eqs. 5.2 & 5.3.

$$E(B-V)_{true} = 1.018\left[\frac{1}{E(B-V)_{obs}} - 0.072\right] \tag{5.2}$$

$$\Delta m15_{true} \simeq \Delta m15_{obs} + 0.1E(B-V)_{true} \tag{5.3}$$

Setting $E(B-V)_{obs} = 1.24 \pm 0.16$, Eq. 5.2 provides a $E(B-V)_{true} = 1.39 \pm 0.19$ Taking this value and setting $\Delta m15_{obs} = 0.98 \pm 0.20$ in Eq. 5.3, provides a $\Delta m15_{true} \simeq 1.12 \pm 0.28$. The dereddened $\Delta m15_{true}$ matches that of Marion et al. (2015) but has the issue of having a 25% uncertainty. The method developed for the SNe "tail" works because it was developed to cover epochs where all SNe show the same $(B-V)$ colour. As stated previously, at peak magnitude SNe Ia are expected to have equal absolute magnitudes. Hence, in both cases, the extinction observed is due to reddening of the SNe and is equally applicable in this particular scenario.

5.3.2 Other Observed Transients

During this reporting period PIRATE has also contributed data to several other transient events. The events observed are iptf13ebh, ASASSN-13aw, ASASSN-13ax, ASASSN-13dl and ASASSN-14ae; for which plots are shown in Fig. 5.5. Of these targets, iptf13ebh and ASASSN-13aw are type-Ia and have resulted in astronomers telegrams (ATEL).

PIRATE contributed to ASASSN-13aw data collection by supplying the only post-maximum measurements on the CPCS. A peak magnitude, found at 56491 $\pm$ 3 MJD, was determined for ASASSN-13aw by using a parobolic fit on the collective APASS/r band data (Wyrzykowski et al. 2013). Additionally, the co-ordinates of the SN were improved giving an RA,Dec(J2000.0)= 17:19:30.10, 47:42:03.40.

In contrast, PIRATE had a minimal contribution to iptf13ebh in terms of data volume, supplying only two nights of data. These two nights however contain important APASS/g and APASS/V measurements near the maximum. The lightcurves for iptf13ebh were fitted with the SALT2 fitter (Guy et al. 2007). The parameters used for

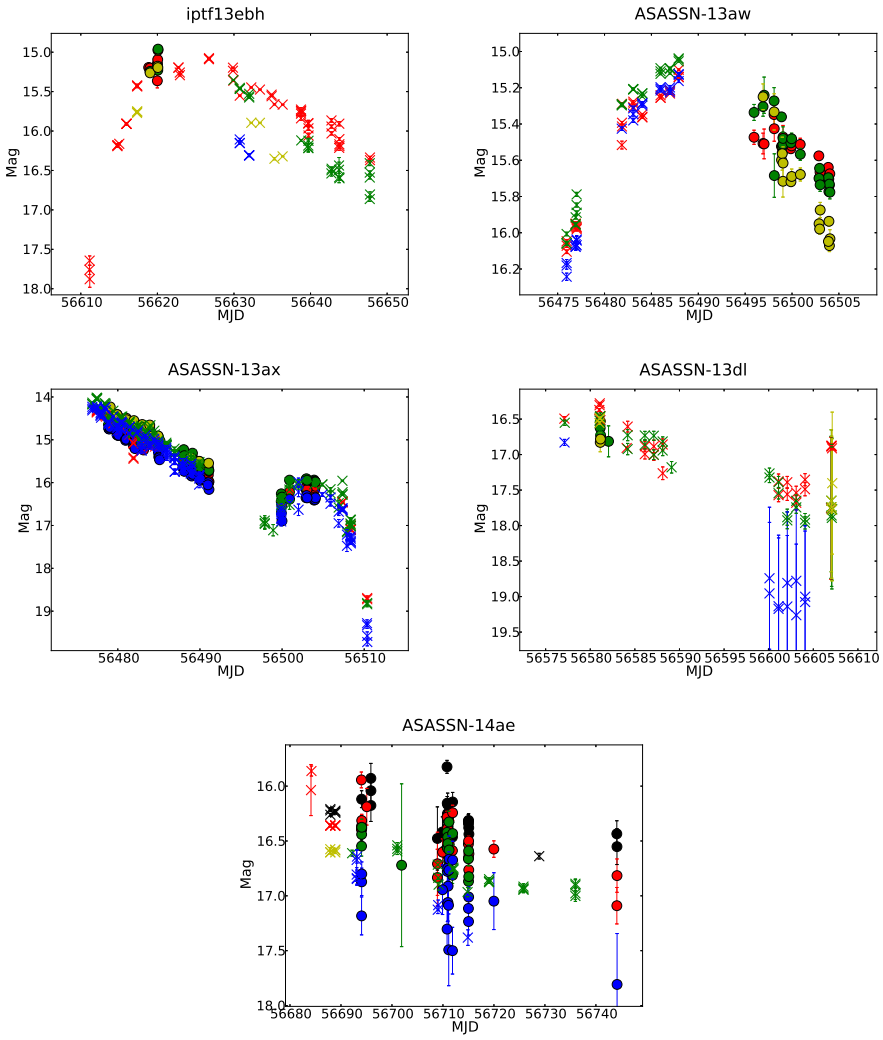

Figure 5.5: Plots showing observed data for iptf13ebh, ASASSN-13aw, ASASSN-13ax, ASASSN-13dl and ASASSN-14ae. Solid circles are PIRATE data while the crosses are CPCS collaborator data. All filters shown are calibrated to the APASS catalogue with each colour representing a filter. Filters g, B, V, r and i are yellow, blue, green, red and black respectively

the fit can be found in Wyrzykowski et al. (2014) but a peak magnitude was determined at 56623.6 $\pm$ 4.5 MJD.

The remaining transients, ASASSN-13ax, ASASSN-13dl and ASASN-14ae are still awaiting scientific exploitation of the data. ASASSN-13ax (Copperwheat et al. 2013; Kato et al. 2014) is a dwarf nova , ASASSN-13dl (Prieto et al. 2013) is a suspected SN of type-Ia and ASASSN-14ae (Holoien et al. 2014) is most likely a tidal disruption event (see Sec. 1.4.3). Of the three, ASASSN-13ax has a lot of high quality data from multiple observers, including PIRATE, covering a period of $\sim$35 days.

ASASSN-14ae has been independently investigated in detail by Holoien et al. (2014). Finally, ASASSN-13dl was a faint target which resulted in large uncertainties from all contributors. PIRATE provided a minimal amount of data for this target but it appears that this data could potentially be close to the maximum.

5.4 Key Results

The key results from this chapter are as follows:

- The Cambridge Photometry Calibration Server is used to compare the PIRATE filters with known catalogues. It is found that for PIRATE Mk 1.5, the filters for VRI are clearly dominated by the APASS/V, APASS/r and APASS/i respectively. For PIRATE Mk 2 the filters RG are constantly resolved as APASS/r and APASS/V catalogue matches respectively. In both PIRATE configurations the B filter is split between APASS/g and APASS/B with a dominance towards APASS/g. Despite the dominance of APASS/g, the recommendation based on this work is to prefer APASS/B as it tends to provide a more consistent RMS scatter across observations.

- The limiting magnitude for PIRATE Mk 1.5 and 2 is presented and found on average to be $\sim$17.5 mags.

- An analysis of SN 2014J has been provided as an example of the capabilities of PIRATE during the Gaia transient verification phase. The values found are comparable with those in Goobar et al. (2014) and Marion et al. (2015) demonstrating that PIRATE is capable of contributing to the ever-growing list of transient events.

- Other transient events observed as part of the Gaia transient verification phase are iptf13ebh, ASASSN-13aw, ASASSN-13ax, ASASSN-13dl and ASASSN-14ae.

Chapter 6

Conclusions and Outlook

This chapter summarises the previous chapters' results and findings. In addition to this, future work and potential improvements to the current systems in place are also described and suggested.

6.1 Summary

6.1.1 SBIG STX-16803 CCD Camera

Through the use of photon transfer curves, the SBIG STX-16803 camera has been characterised in order to check that it meets manufacturer specifications and determine how to minimise noise sources. It uses a Kodak KAF-16803 CCD which has a square 4096 by 4096 pixel array with $9\mu m$ pixels. The manufacturer specifies the read noise and gain of the CCD to be 9 e^- and 1.27 e^-/ADU, respectively. The work performed in Ch. 2 on PIRATE's SBIG STX-16803, showed that the read noise and gain with 1x1 pixel binning are 11.46 $\pm$ 0.15 e^- and 1.25 $\pm$ 0.01 e^-/ADU, respectively, while pixel binnings of 2x2 and 3x3 resulted in read noises of 19.97 $\pm$ 0.78 e^- and 27.85 $\pm$ 1.25 e^-, as well as gains of 1.26 $\pm$ 0.01 e^-/ADU and 1.28 $\pm$ 0.01 e^-/ADU, respectively.

The specified gain value is a close match to the measured gain varying by 1.6%, at most, in binning 1. Conversely, the read noise in binning 1 has a specification difference of 14.6% and unusually the read noise increases with binning. The increase

in read noise with binning was a surprise as it is expected that with on-chip binning the read noise will remain roughly constant (Howell 2011, pg. 50). In order to confirm if the binned read noises were real, the standard deviation of the over-scan were taken and the results compared. Taking an average of the over-scan from the first series for binning 1, 2 and 3 gives read noises of 11.35 $\pm$ 0.15, 19.49 $\pm$ 0.47 and 27.82 $\pm$ 1.18 e^- respectively. The values determined by the two methods for binning 1 and 3 agree within their respective uncertainties while binning 2 is outside of the over-scan uncertainty by 0.01 e^-. Even with the binning 2 discrepancy, all binning states confirm that the increase of read noise with binning is real.

While there is an increase it is noted that there is still a reduction of read noise across all the binned pixels. There is roughly a doubling and tripling of read noise in binnings 2 and 3 respectively suggesting that the A/D converter has been used multiple times during the reading out of each binned pixel. The STX-16803 specification sheet states that the CCD is capable of on-chip binnings of 1x1, 2x2, 3x3, 9x9 and 1xn. Based on this, it is suspected that the 1xn binning method is used for the other on-chip binnings and is then binned into the larger super pixel post conversion either on chip or via software communicating with the SBIG driver.

In addition to these findings, the SBIG STX-16803 is advertised as having a mechanical, evenly illuminated shutter. The results confirmed that the camaera doesn't suffer from any significant shutter lag and hence, the CCD is evenly illuminated when exposed.

The ideal number of flat frames required for calibration of PIRATE data is also investigated and found to be important in the reduction or removal of fixed pattern noise. The overall result indicates that having a large number of frames is ideal in minimizing this noise, although with diminishing returns. It is recommended, based on these results and the practicality of obtaining flats, that PIRATE should aim to collect a minimum of 15 flats, or roughly 581,250 e^- (465,000 ADU).

An issue highlighted during the data gathering of this chapter, is that the CCD may be suffering from a form of residual images. The residual counts are believed to be due

to a form of residual image known as residual bulk image, rather than residual surface image. At wavelengths greater than 700nm (Janesick 2001, pg. 660), photons are able to reach the epitaxial/substrate interface, where the charge is trapped and then leaked into the pixel wells.

6.1.2 PIRATE's Exoplanet Results

The PIRATE exopanet pipeline has undergone several changes from the original version described by Holmes et al. (2011), some minor and some major. The most major in terms of software development has been the switch from the IDL/IRAF pipeline to a converted version making use of Python and pyraf. This overcame limitations imposed by the IDL license.

A flaw has been identified in the calibration methodology used in the IDL/IRAF code that has been fixed in the Python/Pyraf version. Two options for the fix are presented in Sec. 3.2.2.1 with option A being more robust and option B being less computationally expensive. In both cases, the final result should be the same but to allow for flexibility of the pipeline, option A was implemented. In a test case, it was confirmed that the fix resulted in a lower mean count and standard deviation by 1.6 and 0.4 ADU, respectively. These differences are negligible to PIRATE's end results prior to the detection of this error but nonetheless this has removed a small source of error.

A new method for determining the master frame was also implemented into the pipeline and is described in Sec. 3.2.2.2. The previous method used the best frame out of a minimum of 4 frames as the master frame, while the new method relies on a minimum of 20 plate-solved frames in order to median combine the best 5 frames in a more robust master frame. The use of the median value removes any cosmic ray detections and if the science frames have been dithered on acquisition hot pixel false detections can also be minimised. In addition to this, the FWHM of the stars in the new master frame is typically increased compared to that of the old master frame, which should have one of the smallest FWHM measurements. The increase

in FWHM, however, is more representative of the full data set and hence is seen as a positive outcome.

Sec. 3.2.2.3 describes a simple implementation of allowing the pipeline to automatically identify "good" science frames for use in the data reduction. This is solely determined by checking that the science frame is plate solved. The plate solving of a science frame is part of the image acquisition and lack of a plate solution is indicative of a bad frame. Plate solving alone, however, doesn't necessarily constitute a "good" frame as issues such as overhead aircraft, internal reflection, saturated stars and/or poor weather conditions can impact frames. The user is encouraged to double check the suggested "good" frames and more work is needed to ensure that the pipeline is correctly identifying frames that are suitable for reduction.

Sec. 3.6.1 provides a couple of examples of PIRATE's lightcurve performance. These results indicate that PIRATE is capable of searching for exoplanets that produce a $\sim$1% transit around a star of $\sim$11.5 magnitudes or brighter, although it is dependent on the sky conditions. In the event that there aren't any suitable targets that match these criteria, then PIRATE can be used to look for mimics instead.

The remaining sections provide examples of PIRATE's observations of SuperWASP exoplanets, plausible exoplanets and exoplanet mimics. In addition to this, PIRATE's overall contribution to the classification of SuperWASP targets was discussed, with the bulk of PIRATE's observations in the declination range of $\sim$0°to $\sim$60°. The results show that PIRATE's greatest contributions to the SuperWASP project come primarily from the identification of false positives, in particular, blends. PIRATE's higher resolution of 0.63 arcsec/pix (PIRATE Mk 2) and 1.69 arcsec/pix (PIRATE Mk 1.5) as compared to SuperWASP's 13.7 arcsec/pix allows for such blends to be easily separated from the target star.

6.1.3 Exoplanet Roche Lobes

A Roche potential surface mapping code was generated in order to explore the effects that the Roche potential has on exoplanets. The code generated in Ch. 4 has been rigorously tested to be valid and consistent. It was applied to 207 exoplanets and highlighted that WASP-19b, WASP-12b and WASP-103b have significantly filled lobes which leads to strong distortions from a spherical shape. This distortion results in density corrections of 12.7%, 11.8% and 8.9% for these three planets. Additionally, short period Super-Earths 55 Cnc e, CoRoT-7b and Kepler-10b are also examined. All three planets have small density corrections of 1.2%, 0.8% and 0.5% and 55 Cnc e is currently an excellent candidate for some minor distortions to be detected by ellipsoidal variations as it has the largest calculated density correction.

Although the numbers for WASP-19b and WASP-12b differ from those of Burton et al. (2014) the qualitative results are the same; both planets are undergoing severe distortion effects. An issue not examined by Burton et al. (2014) is that of the effects of orbital inclinations differing from precisely edge-on. This work found that the inclination only has a minor impact on distortion results, but should be included in calculations for accuracy. The effects of inclination are more readily seen in planets that heavily fill their Roche lobes along with those that have high inclinations.

The Roche calculations were applied to WASP-12b in Haswell et al. (2012). The transit depths in the NUVA and NUVC spectra regions were up to a factor of three deeper than the optical transit. At these transit depths and given the current fill fraction of WASP-12b's Roche lobe, the opaque material surrounding the planet far overfills its Roche lobe.

Fossati et al. (2012) also demonstrated the application of this work to habitable planets around cool white dwarfs. The Roche geometric distortions for planets orbiting at 0.01 AU from 0.6 $M_{\odot}$ white dwarfs, the CWD habitable zone (Agol 2011), was calculated and presented in Fossati et al. (2012). It was found that planets with masses and radii similar to Earth, CoRoT-7b, Kepler-10b, Kepler-11b and Kepler-11d orbiting

at 0.01 AU from a 0.6 $M_{\odot}$ cool white dwarf were all noticeably distorted from spherical. This resulted in ratios of illuminated areas at maximum and at quadrature of 1.95, 1.95, 1.97, 1.90 and 1.52, respectively. Kepler-11d was also found to overfill its Roche lobe and would be expected to be losing mass. These illuminated area ratios would impact the photometric light curve of such planets introducing a variability which will be synchronised with the orbital phase of the planet.

Finally, look-up contour plots were generated for mass ratios of 10^{-6} through to 10^{-1}. These look-up charts are intended to provide a quick reference volume correction to exoplanets (or any other system of similar mass ratios). WASP-19b was used as an example case with a look-up value of $\sim$12% compared to the calculated value of 11.3%, validating the method.

6.1.4 Gaia Transient Event with PIRATE

The introduction of the ACP Scheduler software has allowed PIRATE to be operated in an autonomous mode, as the software is capable of starting up the facility (starting all relevant software, connecting the equipment and cooling the CCD), acquiring dusk flats, dispatching observations relevant to the observing conditions and then ending the night with dawn flats and calibration frames before finally warming the CCD, disconnecting the equipment and shutting down unused software. ACP Scheduler will then repeat this process night after night until a user intervenes.

The automation of PIRATE has placed it in an ideal position to contribute to high-precision photometry of transient events. SN 2014J has been provided as an example of the capabilities of PIRATE. A peak B apparent magnitude, B_{max} of 11.80 ± 0.14 is observed at a t_{max} of 56690.79 ± 0.01 MJD and provides $\Delta m15 = 0.98 \pm 0.20$. A peak $E(B-V)$ magnitude of 1.24 ± 0.16 is determined which includes extinction due to both the Milky Way and the supernova host galaxy, M82. Removing the extinction due to the Milky Way results in an extinction due to the host galaxy, $E(B-V)_{host}$, of 1.19 $\pm$ 0.16. These values are comparable with those in Goobar et al. (2014) and Marion

et al. (2015) demonstrating that PIRATE is capable of contributing to the ever-growing list of transient events.

In addition to calibrating and normalising PIRATE photometry to other contributors, the Cambridge Photometry Calibration Server also provided an opportunity to compare the PIRATE filters with known catalogues. It was found that for PIRATE Mk 1.5, the filters for VRI are clearly dominated by the APASS/V, APASS/r and APASS/i respectively. The B filter on the other hand is nearly evenly divided with APASS/g just slightly more dominant than APASS/B by 7.9%. For PIRATE Mk 2 the filters RG are constantly resolved as APASS/r and APASS/V catalogue matches respectively while the B filter is once again split between APASS/g and APASS/B although even more dominantly towards APASS/g by 38.4%. The B filters on both PIRATE Mk 1.5 and 2 raise the question as to which filter should be assigned for observations. The recommendation based on this work is to prefer APASS/B as it tends to provide a more consistent RMS scatter across observations. However, in the event that collaborating observers are already supplying and using APASS/g data on the CPCS then it makes sense to use this filter in order to provide a more complete light curve.

6.2 Areas of Improvement and Future Work

6.2.1 CCD Characterisation

In order to improve the results from the photon transfer curve work described in Ch. 2, an evenly illuminated flat surface is required. This will allow for a large sample of pixels to be used which will increase the accuracy of the results. Additionally, the centre of the CCD was the focus of these experiments; other regions can also be investigated to ensure consistency across the CCD.

Due to on-going technical issues at the Mallorca site, there wasn't an opportunity to investigate the CCD's dark current. This can be investigated by taking long-exposure dark frames over a range of temperatures, e.g. from 0 to -20 °C. The exposures need

to be long enough so that the dark current can build up a detectable charge. The dark current at -20°C is expected to be 0.02 electrons per pixel per second with a doubling temperature of 6.3 K. If the value is accurate for PIRATE's SBIG STX-16803 camera, then a 50s exposure is required for a single electron detection at a temperature of -20°C. Ideally, multiple exposures of the same duration and at the same temperatures should be taken in order to average combine the frames and minimise the noise. The combined frames can then be bias corrected and the residual ADU counts divided by the appropriate exposure time and converted from ADU to electron counts to provide a measurement for that temperature. This is a simple process but time consuming in order to collect enough frames with suitable exposure times.

It is also worth noting that Janesick (2007) describes methods for generating Dark Transfer Curves (DTCs) which follow similar principles to the Photon Transfer Curves (PTCs) discussed in Ch. 2. Similar to PTCs, they require a range of frames with varying counts, although in this case the source of the counts is solely from the dark current. Like the flat frames, this can also allow an ideal number of dark frames to be determined. Due to the need to generate a large number of counts this is also a time consuming process that will likely require more time than the previous suggestion. As such, it might be worth attempting during any long periods of downtime caused by poor weather conditions.

One suggested method of dealing with the residual bulk image issue is to build a light source (typically using a long wavelength LED) into the camera itself and flash the CCD, exposing the pixels to signal levels several times the required full well depth of the CCD. The pixels are then flushed and the science image taken. This causes the traps to fill prior to the image exposure and results in a stable and higher quantum efficiency photometric system at the expense of some time resolution. The STX-16803 camera does not have this feature but it is one worth exploring for the future. PIRATE primarily operates in the R filter for exoplanet observations, which Fig. 2.19 shows to overlap with 700nm, and this may be a useful future investment. In the interim, it is recommended to explore the other filters available to PIRATE such as the Baader G

and B and see if the problem persists in these bandwidths.

As the SBIG STX-16803 camera (PIRATE Mk 2) ages, these experiments should be repeated in order to ensure that the CCD is still functioning as expected. These suggestions, as well as the analyses, can also be applied to the SBIG STL-1001E camera (PIRATE Mk 1.5) as well as any future cameras that PIRATE may acquire and make use of. This doesn't just apply to PIRATE, the characterisation of the CCD has shown that some of the values determined through this work differ from the manufacturer specifications. As such, whether professional or amateur, all equipment should be characterised to the best of the observatory's abilities in order to ensure that reductions make use of accurate values and assumptions.

6.2.2 Improving Exoplanet Target Selection

Exoplanet candidates are manually selected from a list of targets expected to show a partial or full transit signal during the observation session. This list is generated by a tool on the SuperWASP hunter pages which then needs to be manually refined to select optimal targets for the night. The number of targets can be quite large and manual selection of targets can result in missing more ideal candidates.

Developing an additional tool that would allow automation of this manual refinement would be more efficient and allow PIRATE to observe targets within its own capabilities. The tool should be able to identify targets that are of suitable brightness and transit depths as well as expected to have a transit without a meridian crossing. Additionally, the tool could generate any necessary files to allow the user to import the observations into ACP Scheduler. Ideally, it would also calculate the limitations on any ephemeris drift and set-up observations to include that window. The ephemeris drift window may span days or weeks so this should be implemented to prioritise targets with ephemeris drifts of a few hours or less. Overall, this would reduce the time required for a user to select and set-up an ideal target observation as well as allow PIRATE to become further automated.

6.2.3 Improving the Exoplanet and Transient Reduction Pipelines

Both of the PIRATE reduction pipelines for exoplanet candidates and transient events can be improved upon. In some cases these improvements apply to both pipelines and in others they are more applicable to one version over the other.

As PIRATE hardware changes and improves over time, maintaining two separate pipelines which run on separate programming languages will be a difficult and tedious endeavour. Unifying both pipelines into a single system will allow common tasks such as data calibration code to only require one set of changes, making it easier to maintain. As such, PIRATE's Gaia transient pipeline would need to be updated from the IDL language to the python language.

A backlog of reductions for both pipelines has frequently occurred and full automation of the pipelines would alleviate this. While maintaining features that allow full user control over the pipeline for manual reductions, having automated options within the pipelines will also allow quick reductions and rapid feedback to the relevant scientific networks.

As part of this the PIRATE exoplanet pipeline has had a basic 'auto' frame selection coded into it which relies on the science frames being plate solved. As stated earlier, plate solving alone doesn't necessarily constitute a "good" frame as issues such as overhead aircraft, internal reflection, saturated stars and/or poor weather conditions can impact frames. Other constraints need to be determined and applied to auto-frame selection to ensure that it is suitable for full automation with minimum human intervention.

User input is currently needed in determining the FWHM of stars in the master frame of the exoplanet pipeline, and all the science frames in the transient pipeline. A simple method for the automation of this would be to take the FWHM included in the FITS header of the science frames. In the first instance, the FWHM is added to the FITS header when the science frame is plate solved to re-align the mount prior to the next exposure. This ensures that the stars remain on the same CCD pixels at

the expense of time resolution. This FITS header FWHM should be suitable for the transient pipeline, although the FWHM in the exoplanet master frame has been shown to increase when the individual science frames are combined. This can then be further improved by using the FITS header FWHM value to identify several unsaturated bright stars in the master frame and measure the average FWHM.

The Gaia transient pipeline also requires the user to input the IVORN number in order to upload the results to the Gaia calibration server. Assuming that the IVORN number is included in the Gaia VOEvent alert, there are two potential solutions to automating this. The simplest solution is to name the science frames with the IVORN number. The second solution would be to have the IVORN number included in the FITS header of the science frames. In either case the pipeline could then be set to read and use this value as it progresses.

With a fully automated pipeline it would then be possible to create a version of the pipeline that will run on PIRATE's control PC. Having a pipeline that produces and frequently updates an ongoing lightcurve of the current target would provide additional information to the operator allowing them to check lightcurve progress and make informed decisions on when to move on to other targets.

Sec. 3.6.1, highlighted that varying weather conditions will impact results. At present, the reduction pipelines have limited diagnostic features with the user expected to dig out any additional information from the various outputs of the pipeline. The inclusion of a diagnostic output with performance charts such as those in Fig. 3.25 should be included in the pipeline. It has already been noted that in these performance charts, stars which have a RMS scatter that is greater than the 3σ value for their magnitude are strong indicators that the star is undergoing detectable variations which may be of scientific interest. This can provide another avenue of scientific discovery for PIRATE to investigate.

In the exoplanet pipeline, stars that don't have a photometric measurement in every remaining science frame (after the frame rejection) are removed from the data. This can result in faint blended stars that are in the SuperWASP aperture being ignored

due to only a single missing measurement as well as bright stars near the saturation limit being rejected if the weather and seeing conditions improve, or if hit by a cosmic ray. Tolerance should be built into the pipeline to allow stars with incompleteitemize photometry to remain in the data set. With the current structure of the pipeline this could be achieved by setting the missing value to a known, and unreal value. This value can then be ignored in calculations and by setting a limit on the number of photometry fails this can be controlled by the user. The lack of complete photometry will mean that these stars should not be used as comparison stars as the lack of data points will interefere with stars with complete photometric measurements.

Both pipelines can be further improved with the inclusion of more than one aperture size. At present the exoplanet pipeline makes use of a single aperture while the transient pipeline makes use of three apertures. The apertures sizes are defined by the FWHM, manually measured and entered into the pipeline, and scaled by a user-defined constant. The number of apertures are hardcoded into the pipelines and allowing a user to define a range of aperture sizes will allow the user or the pipeline to select the best aperture that minimises the noise and resulting lightcurve RMS scatter.

At present, IRAF (and pyraf, which is a python wrapper for IRAF) is a dated tool that no longer receives updates and maintenance. It also doesn't have a version for the Windows operating system, limiting its flexibility. Other calibration and photometry tools should be explored to replace IRAF/pyraf which will allow the pipeline to run on any operating system and offer more flexibility. SExtractor (Bertin & Arnouts 1996) is a source extraction package, and is the recommended method for measuring photometry data for Gaia transients. This package suffers a similar limitation to IRAF in that it isn't designed for use with Windows. Another example tool is Astropy (Astropy Collaboration et al. 2013), an astronomy package for python which is designed to work on Linux, Mac OS X and Windows operating systems. At the time of developing the python/pyraf exoplanet reduction pipeline some simple Astropy functions were implemented into the python pipeline. However, Astropy was still in its infancy as a beta package with limited functionality and subject to change in its coding usage and

language. It is now a stable release and should be investigated further to ascertain the feasibility of replacing any IRAF/pyraf functionality.

Removal or reduction of systematic noise from PIRATE lightcurves should also be investigated further. A brief test at separately applying SYSREM (Tamuz et al. 2005) and SARS (Ofir et al. 2010) algorithms to PIRATE data has been unsuccessfully attempted but not reported in this thesis. These intial attempts showed a general worsening of data sets, burying transit lightcurves in the scatter. Due to the limited time constraints it was decided to abandon this application so the causes for these results are unknown. Possible reasons considered are improper implementation of the algorithms, poor initial conditions and/or a lack of sufficient data. These should be investigated further for feasibility and application to PIRATE data in order to remove more sources of noise.

6.2.4 Exoplanet Roche Lobes

The exoplanet Roche filling code generates a normalised Roche potential for both the Roche lobe and the planetary surface. By taking known exoplanet system values, this can be used to estimate the amount of energy required for a particle at the surface of a planet to reach the Roche lobe and overflow. For planets similar to WASP-12b, which has the presence of an expanded exosphere that over-fills the Roche lobe (Fossati et al. 2010a; Haswell et al. 2012), the Roche code can potentially provide an additional tool to explore the feasibility of various atmospheric escape mechanisms. Examples of atmospheric escape mechanisms are hydrodynamic blow-off (Vidal-Madjar et al. 2003), tidal disruption (Li et al. 2010), coronal entrainment (Vidotto et al. 2010, 2011; Llama et al. 2011), and charge-exchange reactions (Holmström et al. 2008).

Appendix A

Exoplanet Observation List

Table A.1: PIRATE's list of observations. The observation dates with '_' represent a specific data set. The observers and data reduction names are Richard Busuttil (RB), Stefan Holmes (SH), Jakub Bochinski (JJB), Shripathy Hadigal (Shri), Ramasamy Venugopal (ram) and Alistair Bruce (AB). The internal PIRATE classification flags are Plausible/Planet (Pl), Blend (BL), Non-detection (ND), Variable/V-shaped (V), Unknown (U), Not Available/Not Reduced (NA). The SuperWASP classification flags are A priority candidate (A), B priority candidate (B), C priority candidate, a blended star (blend), Eclipsing Binary (EB), Low-mass eclipsing binary (EBLM), Planet (P), Rejected after follow-up (RAF),

SuperWASP ID	Date	Observer	Reduced By	PIRATE LC Flag	Overall Internal Flag	SWASP Hunter Flag
1SWASPJ000521.31+424946.1	20111002_1	SH			Bl	Blend
1SWASPJ000521.31+424946.1	20111003_2	SH			Bl	Blend
1SWASPJ000521.31+424946.1	20111018_1	RB	RB	Bl	Bl	Blend
1SWASPJ000602.54+211529.9	20130822_2	RB	JFJ	Not Reduced		A
1SWASPJ000801.26+360634.3	20111108_1	JJB			V	EB
1SWASPJ001101.75+482200.5	20110917	SH	RB	Pl	Rejected	RAF
1SWASPJ001204.93+394017.6	20131101_1	RB	RB	ND	V	EBLM
1SWASPJ001204.93+394017.6	20131122_1	RB	RB	ND	V	EBLM
1SWASPJ001204.93+394017.6	20131204_2	RB	RB	Not Reduced	V	EBLM
1SWASPJ001204.93+394017.6	20131206_1	RB	RB	ND	V	EBLM
1SWASPJ002328.03-022914.5	20101210_1	SH	SH		V	EB
1SWASPJ002653.14+075717.1	20111014_1	RB	RB	Pl	Rejected	RAF
1SWASPJ003437.56+560154.1	20110919_1	SH	RB	Pl	V	EB
1SWASPJ003437.56+560154.1	20111014_2	RB	RB	V	V	EB
1SWASPJ003750.11+511719.5	20101229_B	SH			Pl	P
1SWASPJ003750.11+511719.5	20101229_R	SH			Pl	P
1SWASPJ003750.11+511719.5	20111031_1	RB	RB	Pl	Pl	P
1SWASPJ003750.11+511719.5	20120722_1	RB	RB	Pl	Pl	P
1SWASPJ003750.11+511719.5	20120909_1	RB	RB	ND	Pl	P
1SWASPJ003750.11+511719.5	20130902_1	RB	RB	Pl	Pl	P
1SWASPJ003750.11+511719.5	20130905_1	RB	JFJ	ND	Pl	P
1SWASPJ003750.11+511719.5	20131016_1	RB	JFJ	Pl	Pl	P
1SWASPJ010443.59+415107.8	20110928_2	SH			V	EB

Continued on next page

Table A.1 – continued from previous page

SuperWASP ID	Date	Observer	Reduced By	PIRATE LC Flag	Overall Internal Flag	SWASP Hunter Flag
1SWASPJ010443.59+415107.8	20111207_1	JB	RB	ND	V	EB
1SWASPJ012720.48+390133.2	20110727_2	SH			Rejected	RAF
1SWASPJ012918.63+415105.3	20110912	SH	JB	ND	Pl	A
1SWASPJ012918.63+415105.3	20111020_2	RB	RB	Pl	Pl	A
1SWASPJ012918.63+415105.3	20130901_2	RB	JFJ	U	Pl	A
1SWASPJ015543.06+362010.1	20120125_1	JJB	JJB	ND	V	EB
1SWASPJ021225.84+335846.9	20110914_1	SH	JJB	Bl	Bl	A
1SWASPJ022036.40+363424.1	20111019_2	RB	RB	Not Reduced	Bl	A
1SWASPJ022036.40+363424.1	20111025_2	JJB	RB	Bl	Bl	A
1SWASPJ022603.68+394458.1	20130901_3	RB	RB	ND	V	EBLM
1SWASPJ022603.68+394458.1	20130903_2	RB	ram	ND	V	EBLM
1SWASPJ022603.68+394458.1	20130906_4	RB	ram	ND	V	EBLM
1SWASPJ022921.00+371700.4	20110920_1	SH	RB	ND	Bl	Blend
1SWASPJ022921.00+371700.4	20111110_3	RB	RB	Not Reduced	Bl	Blend
1SWASPJ022921.00+371700.4	20111206_3	RB	RB	Pl	Bl	Blend
1SWASPJ023112.49+494238.8	20111006_1	SH				A
1SWASPJ023132.81+474134.6	20110920_2	SH	RB	Pl	Pl	B
1SWASPJ023132.81+474134.6	20110925_1	SH			Pl	B
1SWASPJ023132.81+474134.6	20120819_2	RB	RB	Pl	Pl	B
1SWASPJ023140.65+504840.7	20101116	SH	SH	ND	Rejected	RAF
1SWASPJ023441.39+492909.5	20111011_2	SH			V	EB
1SWASPJ023749.84+241848.4	20111119_1	JJB		Not Reduced		A
1SWASPJ024129.64+481911.4	20111001_1	SH	JFJ	Not Reduced	Bl	A
1SWASPJ024129.64+481911.4	20111117_1	RB	JFJ	Not Reduced	Bl	A
1SWASPJ024129.64+481911.4	20131101_2, 20131101_2R	RB	JFJ	Bl	Bl	A
1SWASPJ024129.64+481911.4	20131125_1	RB	JFJ	Not Reduced	Bl	A
1SWASPJ024129.64+481911.4	20131206_2	RB	RB	Bl	Bl	A
1SWASPJ024530.84+305211.4	20111011_1	SH			V	EB
1SWASPJ030032.14+500254.9	20111010_1	SH	RB	ND	Rejected	RAF
1SWASPJ030145.25+280246.5	20110930_2	SH			Bl	Blend

Continued on next page

Table A.1 – continued from previous page

SuperWASP ID	Date	Observer	Reduced By	PIRATE LC Flag	Overall Internal Flag	SWASP Hunter Flag
1SWASPJ030145.25+280246.5	20111021_2	RB	RB	Bl	Bl	Blend
1SWASPJ030556.33+531102.1	20110820	SH	RB	Pl	Rejected	RAF
1SWASPJ030602.24+491538.9	20111015_2	RB	RB	Bl	Pl	A
1SWASPJ030602.24+491538.9	20111217_1	RB	RB	U	Pl	A
1SWASPJ030602.24+491538.9	20131030_1	RB	RB	Bl	Pl	A
1SWASPJ030602.24+491538.9	20131101_3	RB	JFJ	ND	Pl	A
1SWASPJ030602.24+491538.9	20131128_1	RB	RB	ND	Pl	A
1SWASPJ030602.24+491538.9	20131204_2_dupe	RB	RB	Pl	Pl	A
1SWASPJ030602.24+491538.9	20131206_3	RB	RB	Pl	Pl	A
1SWASPJ030647.88+395500.8	20110913_1	SH	RB	V	V	EB
1SWASPJ030745.68+531637.6	20110927_1	SH			V	EBLM
1SWASPJ031533.65+203903.0	20110916_1	SH			Rejected	RAF
1SWASPJ031533.65+203903.0	20110917_2	SH			Rejected	RAF
1SWASPJ031533.65+203903.0	20110921_2	SH	RB	ND	Rejected	RAF
1SWASPJ031917.69+401724.2	20110926_1	SH				C
1SWASPJ031921.42+260658.8	20110914_2	SH	RB	ND	Bl	Blend
1SWASPJ031921.42+260658.8	20120121_1		RB	ND	Bl	Blend
1SWASPJ032259.00+505024.8	20111005_1			Not Reduced	ND	A
1SWASPJ032259.00+505024.8	20120122_1	RB	RB	ND	ND	A
1SWASPJ032346.37+472028.0	20111022_1	SH			Rejected	RAF
1SWASPJ032403.02+360736.5	20110928_1	SH			Bl	Blend
1SWASPJ032403.02+360736.5	20111211_2	JJB			Bl	Blend
1SWASPJ032723.70+060123.3	20101103_2	SH		V	V	B
1SWASPJ032943.36+421342.9	20111212_1		RB	Bl	Bl	Blend
1SWASPJ032943.36+421342.9	20120114_1	JJB	JJB	Bl	Bl	Blend
1SWASPJ032959.14+430956.7	20110921_1	SH	RB	Pl	Rejected	RAF
1SWASPJ032959.14+430956.7	20111016_2	RB	RB	U	Rejected	RAF
1SWASPJ035245.16+331658.4	20111025_1	JJB	RB	Pl	V	EB
1SWASPJ040403.25+372953.2	20091116	SH		Not Reduced	Pl/Bl	A
1SWASPJ040403.25+372953.2	20101111	SH			Pl/Bl	A

Continued on next page

Table A.1 – continued from previous page

SuperWASP ID	Date	Observer	Reduced By	PIRATE LC Flag	Overall Internal Flag	SWASP Hunter Flag
1SWASPJ040403.25+372953.2	20111005_2			Not Reduced	Pl/Bl	A
1SWASPJ040403.25+372953.2	20121031_1	JJB		Not Reduced	Pl/Bl	A
1SWASPJ040403.25+372953.2	20130930_1, 20130930_1R	RB	JFJ	ND	Pl/Bl	A
1SWASPJ040403.25+372953.2	20131010_3	RB	JFJ	Not Reduced	Pl/Bl	A
1SWASPJ040403.25+372953.2	20131101_4	RB	JFJ	ND	Pl/Bl	A
1SWASPJ040403.25+372953.2	20131125_2	RB	JFJ	Not Reduced	Pl/Bl	A
1SWASPJ040403.25+372953.2	20131129_2	RB	JFJ	Pl/Bl	Pl/Bl	A
1SWASPJ040403.25+372953.2	20131206_4	RB	RB	U	Pl/Bl	A
1SWASPJ040543.99+262607.2	20111009_2	SH				B
1SWASPJ040728.00+395735.3	20111101_1	RB	RB	V	Rejected	RAF
1SWASPJ042033.59+412559.0	20111010_2	SH			V	EB
1SWASPJ042033.59+412559.0	20111020_3	RB	RB	Not Reduced	V	EB
1SWASPJ042142.87+513305.6	20110908	SH	RB	Bl	Bl	Blend
1SWASPJ042142.87+513305.6	20110915	SH	RB	ND	Bl	Blend
1SWASPJ042142.87+513305.6	20120822_2	RB	RB	Bl	Bl	Blend
1SWASPJ042142.87+513305.6	20130930_2	RB	ram	U	Bl	Blend
1SWASPJ042142.87+513305.6	20131010_4	RB	JFJ	Not Reduced	Bl	Blend
1SWASPJ043731.38+093121.8	20110929_2	SH			Rejected	RAF
1SWASPJ044102.35+094322.3	20111205_1	RB		Pl	Rejected	RAF
1SWASPJ045315.92+060917.5	20120207_1	JJB		Not Reduced	V	EBLM
1SWASPJ050027.75+235557.8	20120210_1	JJB	JJB	Bl	Bl	Blend
1SWASPJ051330.45+450037.8	20111004_2	OU				B
1SWASPJ051836.56+243555.7	20101217_2			Not Reduced	Bl	Blend
1SWASPJ052512.54+054830.5	20131108_1	RB	JFJ	Not Reduced	ND	B
1SWASPJ052512.54+054830.5	20131110_1	RB	JFJ	Not Reduced	ND	B
1SWASPJ052512.54+054830.5	20131111_1	RB	JFJ	Not Reduced	ND	B
1SWASPJ052512.54+054830.5	20131112_1	RB	JFJ	ND	ND	B
1SWASPJ053050.21+411013.8	20111220_2	JB	RB	U	V	V
1SWASPJ053501.99+441546.3	20111016_1	RB	RB	ND	ND	B
1SWASPJ053501.99+441546.3	20111201_1	RB	RB	Not Reduced	ND	B

Continued on next page

Table A.1 – continued from previous page

SuperWASP ID	Date	Observer	Reduced By	PIRATE LC Flag	Overall Internal Flag	SWASP Hunter Flag
1SWASPJ053512.30+322856.8	20110913_2	SH	RB	Pl	Pl	B
1SWASPJ053512.30+322856.8	20120213_1	RB	RB	ND	Pl	B
1SWASPJ053801.66+371459.0	20111021_1	RB	RB	Pl	Bl	Blend
1SWASPJ053854.30+372657.1	20111212_2		RB	Bl	Bl	Blend
1SWASPJ054526.33+394126.5	20120216_1		RB	V	Rejected	RAF
1SWASPJ055755.70+261102.6	20120224_1	JJB	JJB	Pl/Bl	Bl	Blend
1SWASPJ055755.70+261102.6	20120227_1			Not Reduced	Bl	Blend
1SWASPJ055755.70+261102.6	20120228_1	RB	RB	Pl	Bl	Blend
1SWASPJ055755.70+261102.6	20130130_1	RB	RB	V	Bl	Blend
1SWASPJ055755.70+261102.6	20130131_1	RB	RB	ND	Bl	Blend
1SWASPJ055755.70+261102.6	20130209_1	RB	RB	Pl	Bl	Blend
1SWASPJ055937.07+405625.2	20140215	JFJ	JFJ	Not Reduced	ND	A
1SWASPJ055937.07+405625.2	20140220_1	RB	JFJ	ND	ND	A
1SWASPJ061009.20+395227.8	20111001_2	SH			V	EB
1SWASPJ061332.26+305535.4	20110209	SH	SH	Pl	V	EB
1SWASPJ061555.39+172012.7	20131108_2	RB	JFJ	Not Reduced	Bl	A
1SWASPJ061555.39+172012.7	20131110_2	RB	JFJ	Not Reduced	Bl	A
1SWASPJ061555.39+172012.7	20131111_2	RB	JFJ	Not Reduced	Bl	A
1SWASPJ061555.39+172012.7	20131112_2	RB	RB	Bl	Bl	A
1SWASPJ061555.39+172012.7	20131207_1	RB	RB	ND	Bl	A
1SWASPJ062614.59+304002.9	20111022_2	SH			Bl	Blend
1SWASPJ062614.59+304002.9	20120209_1	JJB	JJB	Bl	Bl	Blend
1SWASPJ063312.09+241643.5	20111002_2			Not Reduced	V	EB
1SWASPJ063608.48+294825.0	20120115_1	JJB	JJB	Bl	Bl	Blend
1SWASPJ063627.06+323542.6	20120124_1	JJB	JJB	Pl	Pl	A
1SWASPJ063739.27+301025.0	20131108_3	RB	JFJ	Not Reduced	ND	A
1SWASPJ063739.27+301025.0	20131111_3	RB	JFJ	Not Reduced	ND	A
1SWASPJ063739.27+301025.0	20131112_3	RB	RB	ND	ND	A
1SWASPJ063815.30+210451.6	20130226_1	RB	RB	V	V	A
1SWASPJ063815.30+210451.6	20131207_2	RB	RB	V	V	A

Continued on next page

Table A.1 – continued from previous page

SuperWASP ID	Date	Observer	Reduced By	PIRATE LC Flag	Overall Internal Flag	SWASP Hunter Flag
1SWASPJ064612.69+351050.4	20120123_1	JJB	JJB	Not Reduced	Rejected	RAF
1SWASPJ065329.01+190612.1	20111006_2	SH	RB	ND	Rejected	RAF
1SWASPJ065329.01+190612.1	20120117_1	RB	RB	Pl	Rejected	RAF
1SWASPJ065617.52+192123.5	20110407_1	SH	SH		Rejected	RAF
1SWASPJ070238.81+321139.5	20110919_2	SH			Rejected	RAF
1SWASPJ070438.74+382125.5	20120120_1	RB	RB	U	U	A
1SWASPJ071058.97+202301.9	20120301_1	RB	RB	ND	ND	A
1SWASPJ072230.10+482503.2	20101123_2	SH		Bl	Rejected	RAF
1SWASPJ073017.41+255244.5	20120113_1	JJB	JJB	Bl	Bl	Blend
1SWASPJ073432.80+324315.8	20120117_2	RB	RB	U	V	EB
1SWASPJ073432.80+324315.8	20120119_1	RB	RB	Not Reduced	V	EB
1SWASPJ075548.69+010837.9	20101210_2			Pl	Rejected	RAF
1SWASPJ075548.69+010837.9	20120229_1	RB	RB	V	Rejected	RAF
1SWASPJ080907.32-044651.7	20111217_2	RB	RB	Not Reduced	Rejected	RAF
1SWASPJ081139.13+394544.1	20140222_1	JFJ	JFJ	ND	ND	A
1SWASPJ081336.95+372340.8	20140414_1	JFJ	JFJ	Not Reduced		A
1SWASPJ084943.30+525745.4	20110406_1	SH		ND	Rejected	RAF
1SWASPJ085317.82+083122.8	20120119_2	RB	RB	Pl	Pl	P
1SWASPJ085317.82+083122.8	20120218_1	RB	RB	Pl	Pl	P
1SWASPJ085317.82+083122.8	20120302_1	RB	RB	ND	Pl	P
1SWASPJ085317.82+083122.8	20120303_1	RB	RB	Pl	Pl	P
1SWASPJ085452.14+265955.5	20120113_2	JJB	JJB	ND	ND	C
1SWASPJ090031.32+425402.8	20140327_3	JFJ	JFJ	U	U	A
1SWASPJ090031.32+425402.8	20140414_2	JFJ	JFJ	Not Reduced	U	A
1SWASPJ091527.10+303807.3	20111108_2	JJB	RB	ND	Pl	A
1SWASPJ091527.10+303807.3	20120118_1	RB	RB	Pl	Pl	A
1SWASPJ091527.10+303807.3	20130212_1	RB	RB	ND	Pl	A
1SWASPJ091527.10+303807.3	20140223_1	RB	JFJ	ND	Pl	A
1SWASPJ092349.39+503821.4	20110208	SH			Rejected	RAF
1SWASPJ092349.39+503821.4	20110407_2	SH		Bl	Rejected	RAF

Continued on next page

Table A.1 – continued from previous page

SuperWASP ID	Date	Observer	Reduced By	PIRATE LC Flag	Overall Internal Flag	SWASP Hunter Flag
1SWASPJ093110.21+231201.7	20111215_2	RB	RB	ND	U	C
1SWASPJ093110.21+231201.7	20120222_1	JJB	JJB	U	U	C
1SWASPJ094045.57+182331.3	20120206_1	JJB		Not Reduced		C
1SWASPJ094405.82+533441.1	20111114_2	RB	RB	ND	Rejected	RAF
1SWASPJ094405.82+533441.1	20120121_2	RB	RB	Pl	Rejected	RAF
1SWASPJ094405.82+533441.1	20120216_2	RB	RB	U	Rejected	RAF
1SWASPJ094405.82+533441.1	20120303_2	OU			Rejected	RAF
1SWASPJ094405.82+533441.1	20120409_1	AB			Rejected	RAF
1SWASPJ094405.82+533441.1	20140222_2, 20140222_2R	JFJ	JFJ	Pl	Rejected	RAF
1SWASPJ094405.82+533441.1	20140327_2	JFJ	JFJ	Pl	Rejected	RAF
1SWASPJ094405.82+533441.1	20140416_2	JFJ	JFJ	Pl	Rejected	RAF
1SWASPJ095527.79+350008.9	20120120_2		RB	Bl	Bl	Blend
1SWASPJ095527.79+350008.9	20120210_2	JJB		Not Reduced	Bl	Blend
1SWASPJ095527.79+350008.9	20120406_1	AB			Bl	Blend
1SWASPJ100632.75+254300.5	20120123_2	JJB	JJB	ND	ND	A
1SWASPJ100632.75+254300.5	20130203_1	RB	RB	ND	ND	A
1SWASPJ101138.55+175929.7	20140416_3	JFJ	JFJ	ND	ND	A
1SWASPJ102815.06+253424.9	20130302_1	RB	RB	ND	Pl	P
1SWASPJ102815.06+253424.9	20140327_1	JFJ	JFJ	V	Pl	P
1SWASPJ102815.06+253424.9	20140416_1	JFJ	JFJ	Not Reduced	Pl	P
1SWASPJ103528.98+404426.2	20120215_1	RB	RB	ND	ND	A
1SWASPJ103528.98+404426.2	20120229_2	RB	RB	ND	ND	A
1SWASPJ112032.03-025353.4	20120115_2	JJB	JJB	Not Reduced	Bl	Blend
1SWASPJ112032.03-025353.4	20120206_3	JJB	JJB	Not Reduced	Bl	Blend
1SWASPJ112925.49+254042.6	20130401_1	RB	RB	ND	ND	A
1SWASPJ112925.49+254042.6	20130402_1	RB	RB	ND	ND	A
1SWASPJ114338.01+063349.4	20130221_1	RB	RB	Not Reduced	Pl	P
1SWASPJ121327.90+230320.2	20111205_2	RB	RB	Pl	Pl	P
1SWASPJ121327.90+230320.2	20111206_2	RB	RB	ND	Pl	P
1SWASPJ123853.66+315659.8	20120122_2		RB	Pl	V	EBLM

Continued on next page

Table A.1 – continued from previous page

SuperWASP ID	Date	Observer	Reduced By	PIRATE LC Flag	Overall Internal Flag	SWASP Hunter Flag
1SWASPJ123853.66+315659.8	20120209_2	JJB	JJB	ND	V	EBLM
1SWASPJ123853.66+315659.8	20120226_1	JJB	RB	Bl	V	EBLM
1SWASPJ125234.11+350344.6	20110404	SH		ND	ND	C
1SWASPJ125234.11+350344.6	20110408_1	SH		ND	ND	C
1SWASPJ132910.73+312407.0	20140404_1	JFJ	JFJ	ND	ND	A
1SWASPJ134149.02-000741.0	20120322_2	JJB	JJB	Pl	Pl	P
1SWASPJ134149.02-000741.0	20120417_1	JJB, AB	JJB	Pl	Pl	P
1SWASPJ134815.27+464811.0	20130615_1	RB	RB	ND	V	EB
1SWASPJ144031.88+370944.9	20120215_2	RB		ND	Rejected	RAF
1SWASPJ145526.85+264408.1	20110720	SH	SH	ND	Bl	Blend
1SWASPJ150735.68+240324.1	20130614_1	RB	ram	ND	Rejected	RAF
1SWASPJ150735.68+240324.1	20130617_1	RB	RB	ND	Rejected	RAF
1SWASPJ150735.68+240324.1	20130620_1	RB	RB	Not Reduced	Rejected	RAF
1SWASPJ150735.68+240324.1	20130623_1	RB	RB	Not Reduced	Rejected	RAF
1SWASPJ150735.68+240324.1	20130630_1	RB	RB	Not Reduced	Rejected	RAF
1SWASPJ150735.68+240324.1	20140404_2	JFJ	JFJ	Not Reduced	Rejected	RAF
1SWASPJ150902.83+215027.5	20120220_2	JJB	JJB	Bl	Bl	Blend
1SWASPJ151147.32+412449.2	20130623_2	RB	RB	Not Reduced		A
1SWASPJ151846.85+234844.0	20130614_2	RB	RB	ND	Rejected	RAF
1SWASPJ151846.85+234844.0	20130623_3	RB	RB	Not Reduced	Rejected	RAF
1SWASPJ152718.81+134115.7	20110614	SH	RB	V	Rejected	RAF
1SWASPJ152718.81+134115.7	20120209_3	JJB	JJB	U	Rejected	RAF
1SWASPJ161034.51+265010.8	20130615_2	RB	RB	Pl	V	EB
1SWASPJ162646.08+510228.2	20120724_1	RB	RB	Pl	Pl	P
1SWASPJ162646.08+510228.2	20120819_1	RB	RB	ND	Pl	P
1SWASPJ164943.85+570727.7	20130628_1	RB	RB	Not Reduced		A
1SWASPJ164943.85+570727.7	20140404_3	JFJ	JFJ	Not Reduced		A
1SWASPJ165052.53+352948.5	20120623_1	RB	RB	ND	Bl	A
1SWASPJ165052.53+352948.5	20130628_2	RB	RB	Not Reduced	Bl	A
1SWASPJ165052.53+352948.5	20130630_2	RB	RB	Bl	Bl	A

Continued on next page

Table A.1 – continued from previous page

SuperWASP ID	Date	Observer	Reduced By	PIRATE LC Flag	Overall Internal Flag	SWASP Hunter Flag
1SWASPJ170219.08+324307.7	20130614_3	RB	ram	ND	ND	A
1SWASPJ171329.50+373037.0	20130628_3	RB	RB	Not Reduced		A
1SWASPJ171804.89+400533.6	20110613_1	SH				A
1SWASPJ172431.36+412230.4	20110405	SH	SH	ND	Bl	Blend
1SWASPJ172917.65+065655.0	20110713	SH			Rejected	RAF
1SWASPJ172917.65+065655.0	20110406_2	SH		Bl	Rejected	RAF
1SWASPJ172940.06+511854.6	20130619_1	RB	RB	ND	V	EB
1SWASPJ173037.88+130443.4	20110801	SH	SH		V	EBLM
1SWASPJ173037.88+130443.4	20120615_1	RB, Shri	RB	ND	V	EBLM
1SWASPJ173213.06+414716.2	20130628_4	RB	RB	Not Reduced		A
1SWASPJ174155.50+214427.1	20110814	SH	SH	ND	ND	A
1SWASPJ174155.50+214427.1	20130615_3	RB	RB	ND	Bl	Blend
1SWASPJ174313.27+093649.6	20110710_1	SH	SH	Bl	Rejected	RAF
1SWASPJ174434.32+103839.2	20110731	SH	SH	ND	Rejected	RAF
1SWASPJ174434.32+103839.2	20120818_1	RB	RB	ND	Rejected	RAF
1SWASPJ174434.32+103839.2	20130616_1	RB	RB	Pl	Rejected	RAF
1SWASPJ174434.32+103839.2	20130619_2	RB	RB	ND	Rejected	RAF
1SWASPJ175033.71+363412.7	20120723_1	RB	RB	Pl	Pl	P
1SWASPJ175856.51+330147.9	20110613_2	SH	RB	Bl	Bl	A
1SWASPJ180509.14+255516.6	20110721	SH	SH	ND	Rejected	RAF
1SWASPJ180509.14+255516.6	20120629_1	RB	RB	ND	Rejected	RAF
1SWASPJ180801.14+364204.1	20130626_1	RB	RB	Not Reduced	ND	A
1SWASPJ180801.14+364204.1	20130820_1	RB	RB	ND	ND	A
1SWASPJ181022.15+172132.3	20101003	SH		Bl	Bl	A
1SWASPJ181022.15+172132.3	20130616_2	RB	RB	ND	Bl	A
1SWASPJ181113.13+141441.9	20110725	SH		Pl	Rejected	RAF
1SWASPJ181602.60+345446.3	20130620_2	RB	RB	Bl	Bl	A
1SWASPJ181848.25+451019.1	20120218_2	RB		Pl	Pl	P
1SWASPJ182429.64+320355.3	20110808	SH	SH	V	V	A
1SWASPJ182553.00+242840.1	20130626_2	RB	RB	ND	V	EB

Continued on next page

Table A.1 – continued from previous page

SuperWASP ID	Date	Observer	Reduced By	PIRATE LC Flag	Overall Internal Flag	SWASP Hunter Flag
1SWASPJ182910.01+480336.0	20130614_4	RB	ram	ND	ND	A
1SWASPJ182910.01+480336.0	20130820_2	RB	RB	ND	ND	A
1SWASPJ182910.01+480336.0	20130901_1	RB	JFJ	Not Reduced	ND	A
1SWASPJ183137.42+402640.8	20130630_3	RB	RB	Bl	Bl	A
1SWASPJ183137.42+402640.8	20130811_1a	RB	RB	Not Reduced	Bl	A
1SWASPJ183137.42+402640.8	20130814_1	RB	RB	ND	Bl	A
1SWASPJ183137.42+402640.8	20140415_1	JFJ	JFJ	Pl	Bl	A
1SWASPJ184336.34+512419.9	20130621_1	RB	RB	Not Reduced		C
1SWASPJ184527.98+604038.6	20110804	SH	SH		Bl	Blend
1SWASPJ184527.98+604038.6	20110811	SH			Bl	Blend
1SWASPJ185240.03+485350.5	20130628_5	RB	RB	Not Reduced	ND	A
1SWASPJ185240.03+485350.5	20130816_1	RB	RB	Not Reduced	ND	A
1SWASPJ185240.03+485350.5	20130831_1	RB	RB	ND	ND	A
1SWASPJ185930.40+513450.3	20120227_2	RB	RB	Pl	V	EB
1SWASPJ185930.40+513450.3	20130617_2	RB	RB	ND	V	EB
1SWASPJ185930.40+513450.3	20130809_1	RB	RB	ND	V	EB
1SWASPJ185930.40+513450.3	20130811_1b	RB	RB	ND	V	EB
1SWASPJ190239.02+451304.2	20120616_1	JJB	Shri	ND	ND	A
1SWASPJ190248.72+483622.8	20140415_2	JFJ	JFJ	ND	ND	A
1SWASPJ190926.21+441743.1	20111020_1	RB	RB	Not Reduced	V	A
1SWASPJ190926.21+441743.1	20120817_1	RB	RB	V	V	A
1SWASPJ191156.10+404411.2	20120626_1	JJB, Shri	Shri	Bl	Bl	A
1SWASPJ191617.77+560341.3	20130811_2a	RB	RB	Not Reduced		A
1SWASPJ193542.37+602705.4	20110727	SH	SH	Bl	Rejected	RAF
1SWASPJ193542.37+602705.4	20110728	SH			Rejected	RAF
1SWASPJ193722.79+600633.5	20140415_3	JFJ	JFJ	ND	ND	A
1SWASPJ194025.44+584522.1	20130809_2	RB	RB	Pl	ND	A
1SWASPJ194025.44+584522.1	20130811_2b	RB	RB	Not Reduced	ND	A
1SWASPJ194025.44+584522.1	20130814_2	RB	RB	ND	ND	A
1SWASPJ194025.44+584522.1	20130815_1	RB	RB	ND	ND	A

Continued on next page

Table A.1 – continued from previous page

SuperWASP ID	Date	Observer	Reduced By	PIRATE LC Flag	Overall Internal Flag	SWASP Hunter Flag
1SWASPJ194025.44+584522.1	20130816_2	RB	RB	Not Reduced	ND	A
1SWASPJ194025.44+584522.1	20130822_1	RB	RB	Not Reduced	ND	A
1SWASPJ194025.44+584522.1	20130823_1	RB	RB	ND	ND	A
1SWASPJ194025.44+584522.1	20130831_2	RB	RB	ND	ND	A
1SWASPJ194025.44+584522.1	20130904_1	RB	JFJ	Not Reduced	ND	A
1SWASPJ194025.44+584522.1	20130906_1	RB	JFJ	ND	ND	A
1SWASPJ194025.44+584522.1	20131010_1	RB	JFJ	Not Reduced	ND	A
1SWASPJ194443.48+500737.0	20110711	SH			Rejected	RAF
1SWASPJ195009.77+581730.4	20110716	SH	SH	V	V	B
1SWASPJ200137.96+553634.3	20130815_2	RB	RB	ND	Bl	A
1SWASPJ200137.96+553634.3	20130823_2	RB	RB	Bl	Bl	A
1SWASPJ201028.76+524040.5	20120922_1	JJB		Not Reduced		A
1SWASPJ201028.76+524040.5	20131020_2	RB	JFJ	Not Reduced		A
1SWASPJ201846.99+511939.9	20120617_1	JJB	Shri	ND	ND	A
1SWASPJ201846.99+511939.9	20130903_1	RB	JFJ	ND	ND	A
1SWASPJ201902.28+541437.7	20130615_4	RB	RB	Bl	Rejected	RAF
1SWASPJ201902.28+541437.7	20130708_1	RB	RB	Bl	Rejected	RAF
1SWASPJ201902.28+541437.7	20130831_3	RB	RB	ND	Rejected	RAF
1SWASPJ202031.24+513942.1	20110809	SH			Bl	A
1SWASPJ202031.24+513942.1	20120822_1	RB	RB	Bl	Bl	A
1SWASPJ202031.24+513942.1	20120826_1	RB	RB	Bl	Bl	A
1SWASPJ202031.24+513942.1	20130616_3	RB	RB	ND	Bl	A
1SWASPJ202031.24+513942.1	20130620_3	RB	RB	ND	Bl	A
1SWASPJ203734.83+160020.6	20121001_1	JJB	RB	Bl	V	EBLM
1SWASPJ203734.83+160020.6	20130629_5	RB	RB	Bl	V	EBLM
1SWASPJ205053.86+183333.9	20101016			Bl	Rejected	RAF
1SWASPJ205053.86+183333.9	20101111	SH			Rejected	RAF
1SWASPJ210006.19-050540.0	20120629_2	RB, Shri	RB	U	Pl	P
1SWASPJ210154.47-132559.7	20121003_1	JJB	RB	ND	Pl	P
1SWASPJ210154.47-132559.7	20121003_2	JJB		Not Reduced	Pl	P

Continued on next page

Table A.1 – continued from previous page

SuperWASP ID	Date	Observer	Reduced By	PIRATE LC Flag	Overall Internal Flag	SWASP Hunter Flag
1SWASPJ210221.17+370850.9	20130629_1	RB	RB	U	Rejected	RAF
1SWASPJ210221.17+370850.9	20130630_4	RB	RB	Pl	Rejected	RAF
1SWASPJ210221.17+370850.9	20130705_1	RB	RB	Pl	Rejected	RAF
1SWASPJ210221.17+370850.9	20130706_1	RB	RB	Bl	Rejected	RAF
1SWASPJ210221.17+370850.9	20130707_1	RB	RB	U	Rejected	RAF
1SWASPJ210221.17+370850.9	20130708_2	RB	RB	V	Rejected	RAF
1SWASPJ210221.17+370850.9	20130714_1	RB	RB	Pl	Rejected	RAF
1SWASPJ210221.17+370850.9	20130715_1	RB	RB	V	Rejected	RAF
1SWASPJ210221.17+370850.9	20130904_2	RB	JFJ	Not Reduced	Rejected	RAF
1SWASPJ210221.17+370850.9	20130906_2	RB	ram	ND	Rejected	RAF
1SWASPJ210310.77+234848.9	20111009_1	SH			V	EB
1SWASPJ210318.01+080117.8	20110815	SH	SH?	Pl	Pl	A
1SWASPJ210432.15+123832.8	20130709_1	RB	RB	Not Reduced	Pl	A
1SWASPJ210448.30+025019.5	20130705_2	RB	RB	Not Reduced	U	A
1SWASPJ210448.30+025019.5	20130706_2	RB	RB	U	U	A
1SWASPJ210448.30+025019.5	20130707_3	RB	RB	U	U	A
1SWASPJ210448.30+025019.5	20130709_4	RB	RB	Not Reduced	U	A
1SWASPJ211916.02+152057.7	20101216_1	SH			Rejected	RAF
1SWASPJ212549.67+333752.8	20130906_3	RB	ram	ND	ND	A
1SWASPJ212707.48+131231.0	20101123_1			Bl	Rejected	RAF
1SWASPJ213236.00+521455.7	20130617_3	RB	RB	ND	ND	A
1SWASPJ213320.84+543037.7	20101005			Bl	Bl	A
1SWASPJ213500.25+201423.2	20130709_2	RB	RB	Not Reduced		A
1SWASPJ213602.95+161602.2	20101103	SH			Bl	A
1SWASPJ213602.95+161602.2	20110806	SH			Bl	A
1SWASPJ213602.95+161602.2	20101103_1			Bl	Bl	A
1SWASPJ213823.77+230708.8	20130714_2	RB	RB	Pl/Bl	Pl	A
1SWASPJ213917.54+535108.4	20111023_1	JJB		Not Reduced	ND	A
1SWASPJ213917.54+535108.4	20111109_1	JJB		Not Reduced	ND	A
1SWASPJ213917.54+535108.4	20130629_3	RB	RB	ND	ND	A

Continued on next page

Table A.1 – continued from previous page

SuperWASP ID	Date	Observer	Reduced By	PIRATE LC Flag	Overall Internal Flag	SWASP Hunter Flag
1SWASPJ213917.54+535108.4	20131001_2	RB	JFJ	Not Reduced	ND	A
1SWASPJ213917.54+535108.4	20131021_1	RB	JFJ	Not Reduced	ND	A
1SWASPJ213942.28+435041.1	20110926_2	SH	JFJ	Not Reduced	Bl	A
1SWASPJ213942.28+435041.1	20120804_1	Shri	Shri		Bl	A
1SWASPJ213942.28+435041.1	20130630_5	RB	RB	Bl	Bl	A
1SWASPJ213942.28+435041.1	20130710_1	RB	RB	Not Reduced	Bl	A
1SWASPJ215011.04+514800.8	20120813_1	RB	RB	Pl	Pl	A
1SWASPJ215011.04+514800.8	20130629_4	RB	RB	ND	Pl	A
1SWASPJ215642.90+333410.9	20100930_1		SH	ND	Bl	Blend
1SWASPJ220524.98+335351.0	20111015_1	RB	RB	Bl	Bl	A
1SWASPJ220524.98+335351.0	20111129_1	RB	RB	Bl	Bl	A
1SWASPJ220524.98+335351.0	20130708_3	RB	RB	ND	Bl	A
1SWASPJ220921.44+332208.9	20130708_4	RB	RB	ND	ND	A
1SWASPJ220921.44+332208.9	20130716_1	RB	RB	ND	ND	A
1SWASPJ220921.44+332208.9	20130716_2	RB	RB	ND	ND	A
1SWASPJ222500.21+403208.0	20111125_1	JJB		Not Reduced	Pl	A
1SWASPJ222500.21+403208.0	20120905_1	RB	RB	ND	Pl	A
1SWASPJ222500.21+403208.0	20130707_2	RB	RB	Pl	Pl	A
1SWASPJ222500.21+403208.0	20130709_3	RB	RB	Not Reduced	Pl	A
1SWASPJ222500.21+403208.0	20130711_1	RB	RB	Not Reduced	Pl	A
1SWASPJ222545.31+374144.2	20110929_1	SH	JFJ	Not Reduced	Pl	A
1SWASPJ222736.63+262658.4	20120908_1	RB	RB	ND	ND	A
1SWASPJ223531.77+395359.0	20101020	SH			Pl	A
1SWASPJ223531.77+395359.0	20101124	SH			Pl	A
1SWASPJ223531.77+395359.0	20101005_2	SH	SH		Pl	A
1SWASPJ223531.77+395359.0	20120827_1	RB	RB	Pl	Pl	A
1SWASPJ223717.77+332801.6	20111003_1			Not Reduced	Bl	Blend
1SWASPJ223717.77+332801.6	20120717_1		RB	Bl	Bl	Blend
1SWASPJ224621.94+304637.1	20111019_1		Shri	V	V	EB
1SWASPJ231622.51+490837.2	20130626_3	RB	RB	Not Reduced	Rejected	RAF

Continued on next page

Table A.1 – continued from previous page

SuperWASP ID	Date	Observer	Reduced By	PIRATE LC Flag	Overall Internal Flag	SWASP Hunter Flag
1SWASPJ231622.51+490837.2	20130705_3	RB	RB	Not Reduced	Rejected	RAF
1SWASPJ231622.51+490837.2	20130710_2	RB	RB	Not Reduced	Rejected	RAF
1SWASPJ231622.51+490837.2	20130715_2	RB	RB	ND	Rejected	RAF
1SWASPJ231829.54+245321.4	20111206_1	RB	RB	U	Pl	P
1SWASPJ231829.54+245321.4	20120823_1	RB	RB	Pl	Pl	P
1SWASPJ232332.12+522539.5	20101026	SH			Rejected	RAF
1SWASPJ232332.12+522539.5	20101102	SH			Rejected	RAF
1SWASPJ232718.73+551928.2	20110810	SH			ND	A
1SWASPJ232718.73+551928.2	20111220_1	JB	RB	ND	ND	A
1SWASPJ232927.22+483524.9	20130706_3	RB		Bl	Bl	A
1SWASPJ232927.22+483524.9	20130717_1	RB		Pl	Bl	A
1SWASPJ233129.75+293952.2	20101018	SH		ND	ND	B
1SWASPJ233129.75+293952.2	20100930_2			ND	ND	B
1SWASPJ234023.79+483905.7	20121002_1	JJB	RB	ND	ND	A
1SWASPJ234049.59+515011.1	20130717_2	RB	RB	Bl	Bl	A
1SWASPJ234257.65+512021.3	20130709_5	RB	JFJ	Not Reduced	Bl	A
1SWASPJ234257.65+512021.3	20130711_2	RB	RB	ND	Bl	A
1SWASPJ234257.65+512021.3	20130714_3	RB	JFJ	Not Reduced	Bl	A
1SWASPJ234257.65+512021.3	20130716_3	RB	JFJ	Bl	Bl	A
1SWASPJ234521.78+480216.8	20110930_1	SH	JFJ	Not Reduced	ND	A
1SWASPJ234521.78+480216.8	20130717_3	RB	JFJ	ND	ND	A
1SWASPJ234639.98+310921.4	20101027	SH			Pl	P
1SWASPJ234639.98+310921.4	20120725_1	Shri	Shri		Pl	P
1SWASPJ234639.98+310921.4	20120824_1	RB	RB	Pl	Pl	P
1SWASPJ234639.98+310921.4	20120906_1	RB	RB	Pl	Pl	P
1SWASPJ235824.05+410745.0	20131026_1	RB	JFJ	Not Reduced		A
1SWASPJ235856.47+353542.3	20130714_4	RB	JFJ	Not Reduced		A
1SWASPJ235856.47+353542.3	20130715_3	RB	JFJ	ND	ND	A

Appendix B

Roche Code

```
/* 22/02/11
  This program is designed to calculate the Roche lobe in the r,theta,phi
*/

#include <iostream>
#include <iomanip>
#include <cmath>
#define M (999999999999999)
using namespace std;


double min(const double x,const double y){ return (x)<(y)?(x):(y);} ;
double max(const double x,const double y){ return (x)>(y)?(x):(y);} ;

double rochesphere(double, double, double, double);
double rochesphere(double, double, double, double, double);
double rochesphere2(double, double, double, double);


int main()
{
  clock_t start = clock();
  double q, qmin, qmax, qstep, Rp, x1, x2, L1min, L1minp, L1minn, L1xp, L2min, L2xp,
    L3min, L3xp, x, y, z, r, thetar, phir, maxr, vol, dv;
  double arstep, adstep, rad, rad3, hillr, nthetad, nphid, pla, Rocheplanet,area,
    area1,area2,radz,rady,A,dA,inc,inc2;
  double thetad,phid, maxy, maxz, maxin, thet, thetr, ph, phr;
  double area3, area4, area5, area6, area7,area8,area9,area10, pla1, pla2, pla3, pla4
    , pla5, pla6,pla7,pla8,pla9,pla10;
  double val,val2,r0,r1,xprime,yprime, zprime;
  cout << fixed << setprecision(15);
//  cout << "Input min mass ratio q=(m2/m1). q = ";
  cin >> q;
//  cout << "Input angle timestep (degrees), adstep = ";
  cin >> adstep;
//  cout << "Input the planet radius, pla = ";
  cin >> pla;
//  cout << "Input the planet inclination (90-i), inc = ";
  cin >> inc;

  L1min = M;
  L2min = M;
  L3min = M;

  x2 = 1.0;
  x1 = 0.0;
  arstep=(adstep/180.0)*M_PI;
```

```
45  inc2=(inc/180.0)*M_PI;
46  val=1.0E-2;
47  r0=0.0;
48  r1=1.0;
49
50  phid=(0.0/adstep);
51  thetad=(90.0/adstep);
52  phir=((phid*adstep)/180.0)*M_PI;
53  thetar=((thetad*adstep)/180.0)*M_PI;
54
55  while (val>=1.0E-15)
56  {
57    for (r= r0; r<=r1; r+=val)
58    {
59      x = r*sin(thetar)*cos(phir);
60      Rp=rochesphere(r,thetar,phir,q);
61      if ((x > x1) && (x < x2))
62      {
63        L1min = min(L1min,Rp);
64        if (L1min==Rp)
65        L1xp = x;
66      }
67    }
68    r0 = L1xp - val;
69    r1 = L1xp + val;
70    val = val/10.0;
71  }
72
73  cout << L1xp << endl << endl;
74
75  area= M_PI*pla*pla;
76
77  maxy=0.0;
78  maxz=0.0;
79  Rocheplanet=rochesphere(pla,0.0,0.0,q);
80  val = 1.0E-2;
81  r = L1xp;
82  x = 0.0;
83  z = 0.0;
84
85  while (val>=1.0E-15)
86  {
87    for (r=r; r>=0.0; r-=val)
88    {
89      Rp=rochesphere2(x,r,z,q);
90      if (Rp>=Rocheplanet)
91      {
92        maxy = max(maxy,r);
93        break;
94      }
95    }
96    r = maxy + val;
97    val = val/10.0;
98  }
99
100 cout << "maxy = " << maxy << endl;
101
102 val = 1.0E-2;
103 r = L1xp;
104 y = 0.0;
105
106 while (val>1.0E-15)
107 {
108   for (r=r; r>=0.0; r-=val)
109   {
110     zprime = r;
111     x = zprime*sin(-inc2);
112     z = zprime*cos(-inc2);
113     Rp=rochesphere2(x,y,z,q);
114     if (Rp>=Rocheplanet)
115     {
116       maxz = max(maxz,r);
```

```
117         break;
118       }
119     }
120     r = maxz + val;
121     val = val/10.0;
122   }
123
124   cout << "maxz = " << maxz << endl;
125
126   maxin = max(maxz,maxy);
127   if (maxin==maxy)
128   {
129     thet = 0.0;
130     ph = 0.0;
131   }
132   else
133   {
134     thet = 90.0;
135     ph = 90.0;
136   }
137
138   thetr = (thet/180.0)*M_PI;
139   phr = (ph/180.0)*M_PI;
140
141   cout << maxin << " " << maxz << " " << maxy << " " << thet << " " << ph << endl <<
      endl;
142   maxin = maxin+(1.0E-2);
143
144 //////////////////////////////////////////////////////////////////////////////
145
146   area1=0.0;
147   pla1=maxin;
148   pla2=maxin;
149
150   double arrthetar[int(180.0/adstep)];  // Initialise array with relevant number of
      steps.
151
152   // Loop to generate a look-up table of sin(thetar)
153   thetad =0.0;
154   while (thetad<=(180.0/adstep))
155   {
156     arrthetar[int(thetad)] = ((thetad*adstep)/180.0)*M_PI;  // Generate array of (sin
      (thetar)*arstep^2)/2.0 values
157     thetad+=1.0;              // Increase thetad by a single step
158   }
159
160   double multiplication = arstep / 2.0;
161   phid=90.0;
162   phir=(phid/180.0)*M_PI;
163   val = 1E-2;
164   while (val>=1E-15)
165   {
166     while (pla1>=0.0)
167     {
168       Rocheplanet=rochesphere(pla1,thetr,phr,q,inc2);
169       area2=area1;
170       area1=0.0;
171       thetad=0.0;
172       while (thetad<(180.0/adstep))
173       {
174         maxr = 0.0;
175         dA = 0.0;
176 //        thetar=((thetad*adstep)/180.0)*M_PI;
177         val2=1E-2;
178
179         while (val2>=1E-15)
180         {
181           for (r=maxin; r>=0.0; r-=val2)
182           {
183 //            Rp=rochesphere(r,thetar,phir,q,inc2);
184             Rp=rochesphere(r,arrthetar[int(thetad)],phir,q,inc2);
185
```

```
186             if (Rp>=Rocheplanet)
187             {
188               maxr = max(maxr,r);
189               break;
190             }
191           }
192           maxin = maxr + val2;
193           if (maxin>=L1xp)
194           {
195             maxin = L1xp;
196           }
197           val2 = val2/10;
198         }
199 //        dA = (maxr*maxr) * arstep / 2.0;
200         dA = (maxr*maxr) * multiplication;
201         area1 += dA;
202         thetad+=1.0;
203       }
204       area1= area1*2.0;
205       cout << area << " " << area1 << " " << pla1 << endl;
206       if (area1 == area || area1 <= area)
207       {
208         break;
209       }
210       pla2=pla1;
211       pla1=pla1-val;
212     }
213     cout << endl << area << " " << area2 << " " << area1 << " " << pla2 << " " <<
      pla1 << endl << endl;
214     pla1=pla1+val;
215     val = val/10;
216   }
217
218 //////////////////
219
220   maxy=0.0;
221   maxz=0.0;
222   Rocheplanet=rochesphere(pla1,0.0,0.0,q);
223   val = 1.0E-2;
224   r = L1xp;
225   x = 0.0;
226   z = 0.0;
227
228   while (val>=1.0E-15)
229   {
230     for (r=r; r>=0.0; r-=val)
231     {
232       Rp=rochesphere2(x,r,z,q);
233       if (Rp>=Rocheplanet)
234       {
235         maxy = max(maxy,r);
236         break;
237       }
238     }
239     r = maxy + val;
240     val = val/10.0;
241   }
242
243   cout << "maxy = " << maxy << endl;
244
245   val = 1.0E-2;
246   r = L1xp;
247   y = 0.0;
248
249   while (val>1.0E-15)
250   {
251     for (r=r; r>=0.0; r-=val)
252     {
253       zprime = r;
254       x = zprime*sin(-inc2);
255       z = zprime*cos(-inc2);
256       Rp=rochesphere2(x,y,z,q);
```

```
257       if (Rp>=Rocheplanet)
258       {
259         maxz = max(maxz,r);
260         break;
261       }
262     }
263     r = maxz + val;
264     val = val/10.0;
265   }
266
267   cout << "maxz = " << maxz << endl;
268 //////////////////////////
269
270
271
272   clock_t end1 = clock();
273   std::cout << "CPU time used: " << 1000.0 * (end1-start) / CLOCKS_PER_SEC << " ms or
        " << (end1-start) / CLOCKS_PER_SEC << "s\n";
274
275   return 0;
276 }
277
278
279
280 double rochesphere(double r, double thetar, double phir, double q)
281 {
282   double x, y, z, r1, r2, q2, t1, t2, t3, Rp;
283
284   x = r*sin(thetar)*cos(phir);
285   y = r*sin(thetar)*sin(phir);
286   z = r*cos(thetar);
287
288   r2 = sqrt((x*x)+(y*y)+(z*z));
289   r1 = sqrt(((x-1.0)*(x-1.0))+(y*y)+(z*z));
290   q2 = 2.0/(1.0+q);
291   t1 = q2*(1.0/r1);
292   t2 = q2*(q/r2);
293   t3 = ((x-(1.0/(1.0+q)))*(x-(1.0/(1.0+q)))+(y*y));
294   Rp = (t1+t2+t3);
295   return Rp;
296 }
297
298 double rochesphere(double r, double thetar, double phir, double q, double inc2)
299 {
300   double x, y, z, r1, r2, q2, t1, t2, t3, Rp, xprime, yprime, zprime;
301
302   xprime = r*sin(thetar)*cos(phir);
303   yprime = r*sin(thetar)*sin(phir);
304   zprime = r*cos(thetar);
305
306   x = xprime*cos(-inc2) + zprime*sin(-inc2);
307   y = yprime;
308   z = zprime*cos(-inc2) - xprime*sin(-inc2);
309
310   r2 = sqrt((x*x)+(y*y)+(z*z));
311   r1 = sqrt(((x-1.0)*(x-1.0))+(y*y)+(z*z));
312   q2 = 2.0/(1.0+q);
313   t1 = q2*(1.0/r1);
314   t2 = q2*(q/r2);
315   t3 = ((x-(1.0/(1.0+q)))*(x-(1.0/(1.0+q)))+(y*y));
316   Rp = (t1+t2+t3);
317   return Rp;
318 }
319
320 double rochesphere2(double x, double y, double z, double q)
321 {
322   double r1, r2, q2, t1, t2, t3, Rp, xprime, yprime, zprime;
323
324   r2 = sqrt((x*x)+(y*y)+(z*z));
325   r1 = sqrt(((x-1.0)*(x-1.0))+(y*y)+(z*z));
326   q2 = 2.0/(1.0+q);
327   t1 = q2*(1.0/r1);
```

```
328     t2 = q2*(q/r2);
329     t3 = ((x-(1.0/(1.0+q)))*(x-(1.0/(1.0+q)))+(y*y));
330     Rp = (t1+t2+t3);
331     return Rp;
332 }
```

Appendix C

Known Exoplanet Roche Density Corrections

Table C.1: Roche lobe filling factor and density change for the 207 exoplanets. q, i and P are the mass ratio, inclination and period, respectively. R_2 is the Roche lobe volume equivalent radius. R_ϕ and $R_{i\phi}$ are the volume equivalent radii of the planet at inclinations of 90°and i. (Note: All distance values are normalised to the orbital separation)

Planet	q	i	P (d)	R_2	R_ϕ	$R_{i\phi}$	Infilling % (90°)	Infilling % (i)	Δ Density (90°)	Δ Density (i)
55Cnce	0.00002763	83.40	0.74	0.014799	0.005768	0.005767	5.92	5.92	1.23	1.20
CoRoT-1b	0.00103089	85.10	1.51	0.048678	0.028505	0.028500	20.08	20.07	4.09	4.04
CoRoT-10b	0.00295411	88.55	13.24	0.068496	0.004396	0.004396	0.03	0.03	0.01	0.00
CoRoT-11b	0.00175227	83.17	2.99	0.057843	0.015533	0.015533	1.94	1.94	0.37	0.36
CoRoT-12b	0.00081135	85.48	2.83	0.045020	0.017209	0.017208	5.59	5.58	1.11	1.09
CoRoT-13b	0.00114733	88.02	4.03	0.050405	0.008285	0.008285	0.44	0.44	0.09	0.09
CoRoT-14b	0.00639282	79.60	1.51	0.087770	0.019371	0.019370	1.07	1.07	0.20	0.19
CoRoT-16b	0.00046590	85.01	5.35	0.037550	0.009059	0.009059	1.40	1.40	0.28	0.27
CoRoT-17b	0.00225683	88.34	3.77	0.062787	0.010149	0.010149	0.42	0.42	0.08	0.08
CoRoT-18b	0.00349651	86.50	1.90	0.072321	0.021223	0.021223	2.53	2.53	0.48	0.48
CoRoT-19b	0.00087344	88.00	3.90	0.046117	0.011948	0.011948	1.74	1.74	0.34	0.34
CoRoT-2b	0.00322113	88.08	1.74	0.070434	0.025016	0.025016	4.48	4.48	0.85	0.85
CoRoT-23b	0.00257600	85.70	3.63	0.065532	0.010384	0.010384	0.40	0.40	0.08	0.08
CoRoT-25b	0.00023194	84.50	4.86	0.029867	0.008947	0.008947	2.69	2.69	0.54	0.53
CoRoT-26b	0.00041922	86.80	4.20	0.036273	0.011500	0.011500	3.19	3.19	0.64	0.63
CoRoT-27b	0.00942775	86.70	3.57	0.099329	0.010317	0.010317	0.11	0.11	0.02	0.02
CoRoT-3b	0.01518773	85.90	4.26	0.115478	0.008413	0.008413	0.04	0.04	0.01	0.01
CoRoT-4b	0.00059033	90.00	9.20	0.040576	0.006299	0.006299	0.37	0.37	0.07	0.07
CoRoT-5b	0.00044032	85.83	4.04	0.036862	0.013409	0.013408	4.81	4.81	0.96	0.95
CoRoT-6b	0.00268465	89.07	8.89	0.066412	0.006525	0.006525	0.09	0.09	0.02	0.02
CoRoT-7b	0.00001597	80.10	0.85	0.012343	0.004176	0.004176	3.87	3.87	0.80	0.76
CoRoT-8b	0.00023428	88.40	6.21	0.029966	0.004299	0.004299	0.30	0.30	0.06	0.06
CoRoT-9b	0.00081332	89.99	95.26	0.045055	0.001233	0.001233	0.00	0.00	0.00	0.00
GJ1214b	0.00012372	90.00	1.58	0.024285	0.007990	0.007990	3.56	3.56	0.72	0.72
GJ3470b	0.00007761	88.12	3.34	0.020822	0.005030	0.005030	1.41	1.41	0.29	0.29
GJ436b	0.00015321	86.36	2.64	0.026057	0.006275	0.006275	1.40	1.40	0.28	0.28

Continued on next page

Table C.1 – continued from previous page

Planet	q	i	P (d)	R_2	R_ϕ	$R_{i\phi}$	Infilling % (90°)	Infilling % (i)	Δ Density (90°)	Δ Density (i)
HAT-P-1b	0.00044746	86.11	4.46	0.037057	0.010745	0.010745	2.44	2.44	0.49	0.48
HAT-P-11b	0.00009723	88.50	4.89	0.022430	0.003840	0.003840	0.50	0.50	0.10	0.10
HAT-P-12b	0.00027559	89.00	3.21	0.031608	0.011988	0.011988	5.46	5.46	1.10	1.10
HAT-P-13b	0.00066612	83.40	2.92	0.042211	0.014378	0.014377	3.95	3.95	0.78	0.77
HAT-P-14b	0.00153000	83.50	4.63	0.055351	0.009069	0.009069	0.44	0.44	0.08	0.08
HAT-P-15b	0.00183862	89.10	10.86	0.058753	0.005311	0.005311	0.07	0.07	0.01	0.01
HAT-P-16b	0.00328755	86.60	2.78	0.070899	0.014916	0.014916	0.93	0.93	0.18	0.18
HAT-P-17b	0.00059042	89.20	10.34	0.040578	0.005472	0.005472	0.25	0.25	0.05	0.05
HAT-P-18b	0.00024440	88.80	5.51	0.030385	0.008512	0.008512	2.20	2.20	0.44	0.44
HAT-P-19b	0.00033116	88.20	4.01	0.033573	0.011632	0.011632	4.16	4.16	0.83	0.83
HAT-P-2b	0.00646268	86.72	5.63	0.088075	0.008143	0.008143	0.08	0.08	0.01	0.01
HAT-P-20b	0.00918919	86.80	2.87	0.098524	0.011461	0.011461	0.16	0.16	0.03	0.03
HAT-P-21b	0.00410573	87.20	4.12	0.076158	0.009890	0.009890	0.22	0.22	0.04	0.04
HAT-P-22b	0.00223852	86.90	3.21	0.062622	0.012472	0.012472	0.79	0.79	0.15	0.15
HAT-P-23b	0.00176405	85.10	1.21	0.057969	0.028402	0.028399	11.76	11.76	2.32	2.29
HAT-P-24b	0.00054950	88.60	3.35	0.039635	0.012794	0.012794	3.36	3.36	0.67	0.67
HAT-P-25b	0.00053554	87.60	3.65	0.039303	0.012234	0.012234	3.02	3.02	0.60	0.60
HAT-P-26b	0.00006858	88.60	4.23	0.019989	0.005650	0.005650	2.26	2.26	0.46	0.46
HAT-P-27b	0.00063820	85.00	3.04	0.041624	0.012224	0.012223	2.53	2.53	0.50	0.49
HAT-P-28b	0.00058430	88.00	3.26	0.040440	0.013389	0.013389	3.63	3.63	0.72	0.72
HAT-P-29b	0.00061525	87.10	5.72	0.041128	0.007938	0.007938	0.72	0.72	0.14	0.14
HAT-P-3b	0.00061201	87.24	2.90	0.041057	0.011081	0.011081	1.97	1.97	0.39	0.39
HAT-P-30b	0.00054308	83.60	2.81	0.039483	0.015343	0.015342	5.87	5.87	1.17	1.15
HAT-P-31b	0.00169763	87.10	5.00	0.057252	0.008359	0.008359	0.31	0.31	0.06	0.06
HAT-P-32b	0.00070876	88.90	2.15	0.043075	0.025297	0.025297	20.25	20.25	4.16	4.16
HAT-P-33b	0.00052921	87.20	3.47	0.039150	0.016215	0.016214	7.10	7.10	1.42	1.42
HAT-P-34b	0.00228321	87.10	5.45	0.063024	0.008446	0.008446	0.24	0.24	0.05	0.05
HAT-P-35b	0.00081322	87.30	3.65	0.045054	0.012810	0.012810	2.30	2.30	0.45	0.45
HAT-P-36b	0.00171357	86.00	1.33	0.057426	0.025503	0.025502	8.76	8.76	1.72	1.70
HAT-P-37b	0.00120407	86.90	2.80	0.051203	0.014868	0.014868	2.45	2.45	0.48	0.48

Continued on next page

Table C.1 – continued from previous page

Planet	q	i	P (d)	R_2	R_ϕ	$R_{i\phi}$	Infilling % (90°)	Infilling % (i)	Δ Density (90°)	Δ Density (i)
HAT-P-38b	0.00028813	88.30	4.64	0.032074	0.007546	0.007546	1.30	1.30	0.26	0.26
HAT-P-39b	0.00040680	87.00	3.54	0.035917	0.014807	0.014807	7.01	7.01	1.41	1.40
HAT-P-4b	0.00051359	89.91	3.06	0.038768	0.013759	0.013759	4.47	4.47	0.89	0.89
HAT-P-40b	0.00039135	88.30	4.46	0.035464	0.013641	0.013641	5.69	5.69	1.14	1.14
HAT-P-41b	0.00053824	87.70	2.69	0.039368	0.019058	0.019058	11.35	11.35	2.30	2.29
HAT-P-49b	0.00106758	86.20	2.69	0.049236	0.015459	0.015459	3.10	3.10	0.61	0.60
HAT-P-5b	0.00086945	86.75	2.79	0.046048	0.014752	0.014752	3.29	3.29	0.65	0.64
HAT-P-6b	0.00078160	85.51	3.85	0.044474	0.012153	0.012153	2.04	2.04	0.40	0.40
HAT-P-7b	0.00113183	83.11	2.20	0.050182	0.017205	0.017203	4.03	4.03	0.79	0.77
HAT-P-8b	0.00096376	87.80	3.08	0.047621	0.015985	0.015985	3.78	3.78	0.74	0.74
HAT-P-9b	0.00057804	86.50	3.92	0.040297	0.012683	0.012683	3.12	3.12	0.62	0.61
HATS-1b	0.00180017	85.60	3.45	0.058352	0.014006	0.014005	1.38	1.38	0.27	0.26
HATS-2b	0.00145831	87.20	1.35	0.054495	0.024432	0.024431	9.01	9.01	1.77	1.77
HD149026b	0.00026543	84.55	2.88	0.031221	0.007253	0.007253	1.25	1.25	0.25	0.25
HD17156b	0.00245151	87.82	21.21	0.064490	0.002987	0.002987	0.01	0.01	0.00	0.00
HD189733b	0.00135050	85.71	2.22	0.053151	0.017589	0.017589	3.62	3.62	0.71	0.70
HD209458b	0.00058106	86.71	3.52	0.040366	0.013787	0.013787	3.98	3.98	0.79	0.79
HD80606b	0.00387604	89.28	111.42	0.074761	0.001099	0.001099	0.00	0.00	0.00	0.00
HD97658b	0.00003158	89.45	9.49	0.015469	0.001253	0.001253	0.05	0.05	0.01	0.01
KELT-2Ab	0.00110935	88.60	4.11	0.049855	0.011189	0.011189	1.13	1.13	0.22	0.22
KELT-3b	0.00108256	84.14	2.70	0.049460	0.015759	0.015758	3.23	3.23	0.63	0.62
KELT-6b	0.00037927	88.81	7.84	0.035101	0.007184	0.007184	0.86	0.86	0.17	0.17
Kepler-10b	0.00001516	84.40	0.84	0.012131	0.003610	0.003609	2.63	2.63	0.54	0.53
Kepler-10c	0.00005772	89.65	45.29	0.018882	0.000418	0.000418	0.00	0.00	0.00	0.00
Kepler-11b	0.00001343	89.64	10.30	0.011653	0.000838	0.000838	0.04	0.04	0.01	0.01
Kepler-11c	0.00004218	89.59	13.02	0.017023	0.001144	0.001144	0.03	0.03	0.01	0.01
Kepler-11d	0.00001906	89.67	22.68	0.013088	0.000859	0.000859	0.03	0.03	0.01	0.01
Kepler-11e	0.00002625	88.89	32.00	0.014550	0.000917	0.000917	0.03	0.03	0.01	0.01
Kepler-11f	0.00000718	89.47	46.68	0.009468	0.000424	0.000424	0.01	0.01	0.00	0.00
Kepler-12b	0.00035352	88.76	4.44	0.034301	0.014637	0.014637	7.77	7.77	1.57	1.57

Continued on next page

Table C.1 – continued from previous page

Planet	q	i	P (d)	R_2	R_ϕ	$R_{i\phi}$	Infilling % (90°)	Infilling % (i)	Δ Density (90°)	Δ Density (i)
Kepler-14b	0.00530685	90.00	6.79	0.082695	0.006729	0.006729	0.05	0.05	0.01	0.01
Kepler-15b	0.00062049	87.44	4.94	0.041243	0.008034	0.008034	0.74	0.74	0.15	0.15
Kepler-16b	0.00046065	89.97	228.65	0.037411	0.000557	0.000557	0.00	0.00	0.00	0.00
Kepler-17b	0.00203779	87.22	1.49	0.060745	0.023818	0.023818	6.03	6.03	1.17	1.16
Kepler-18b	0.00002124	84.92	3.50	0.013564	0.001907	0.001907	0.28	0.28	0.06	0.06
Kepler-18c	0.00005341	87.68	7.64	0.018404	0.003113	0.003113	0.48	0.48	0.10	0.10
Kepler-18d	0.00005064	88.07	14.86	0.018084	0.002541	0.002541	0.28	0.28	0.06	0.06
Kepler-20b	0.00002786	86.50	3.70	0.014839	0.001794	0.001794	0.18	0.18	0.04	0.04
Kepler-20c	0.00005179	88.39	10.85	0.018218	0.001406	0.001406	0.05	0.05	0.01	0.01
Kepler-20d	0.00002479	89.57	77.60	0.014277	0.000339	0.000339	0.00	0.00	0.00	0.00
Kepler-34b	0.00020037	89.64	288.74	0.028464	0.000420	0.000420	0.00	0.00	0.00	0.00
Kepler-35b	0.00013651	89.24	131.41	0.025085	0.000716	0.000716	0.00	0.00	0.00	0.00
Kepler-36b	0.00001251	89.52	13.84	0.011383	0.000548	0.000548	0.01	0.01	0.00	0.00
Kepler-36c	0.00002272	89.76	16.24	0.013870	0.001221	0.001221	0.07	0.07	0.01	0.01
Kepler-37b	0.00001139	88.63	13.37	0.011035	0.000126	0.000126	0.00	0.00	0.00	0.00
Kepler-37c	0.00001282	89.07	21.30	0.011476	0.000226	0.000226	0.00	0.00	0.00	0.00
Kepler-37d	0.00000686	89.33	39.79	0.009328	0.000401	0.000401	0.01	0.01	0.00	0.00
Kepler-39b	0.01577245	88.83	21.08	0.116857	0.003762	0.003762	0.00	0.00	0.00	0.00
Kepler-4b	0.00006027	89.76	3.21	0.019155	0.003746	0.003746	0.75	0.75	0.15	0.15
Kepler-40b	0.00140390	89.70	6.87	0.053826	0.006933	0.006933	0.21	0.21	0.04	0.04
Kepler-41b	0.00050094	88.30	1.86	0.038453	0.013926	0.013926	4.75	4.75	0.95	0.95
Kepler-412b	0.00762925	80.89	1.72	0.092863	0.021364	0.021364	1.22	1.22	0.22	0.21
Kepler-43b	0.00232532	84.35	3.02	0.063397	0.012772	0.012772	0.82	0.82	0.16	0.15
Kepler-44b	0.00081420	83.78	3.25	0.045071	0.013050	0.013050	2.43	2.43	0.48	0.47
Kepler-45b	0.00082637	87.00	2.45	0.045290	0.015394	0.015394	3.93	3.93	0.77	0.77
Kepler-5b	0.00146733	86.30	3.55	0.054604	0.013519	0.013519	1.52	1.52	0.29	0.29
Kepler-6b	0.00052765	86.80	3.23	0.039112	0.013905	0.013905	4.49	4.49	0.90	0.89
Kepler-68b	0.00001663	87.60	5.40	0.012508	0.001593	0.001593	0.21	0.21	0.04	0.04
Kepler-68c	0.00000555	86.93	9.60	0.008691	0.000448	0.000448	0.01	0.01	0.00	0.00
Kepler-7b	0.00030962	86.50	4.88	0.032840	0.011382	0.011382	4.16	4.16	0.84	0.83

Continued on next page

Table C.1 – continued from previous page

Planet	q	i	P (d)	R_2	R_ϕ	$R_{i\phi}$	Infilling % (90°)	Infilling % (i)	Δ Density (90°)	Δ Density (i)
Kepler-74b	0.00045346	85.55	7.34	0.037218	0.007632	0.007632	0.86	0.86	0.17	0.17
Kepler-75b	0.01082878	89.10	8.88	0.103788	0.006097	0.006097	0.02	0.02	0.00	0.00
Kepler-77b	0.00043274	88.00	3.58	0.036652	0.010206	0.010206	2.16	2.16	0.43	0.43
Kepler-8b	0.00045845	84.07	3.52	0.037352	0.014084	0.014083	5.36	5.36	1.07	1.05
Kepler-87b	0.00088621	89.27	114.67	0.046336	0.001212	0.001212	0.00	0.00	0.00	0.00
Kepler-87c	0.00001744	89.59	191.21	0.012708	0.000391	0.000391	0.00	0.00	0.00	0.00
Kepler-9b	0.00023754	88.55	19.24	0.030102	0.002863	0.002863	0.09	0.09	0.02	0.02
Kepler-9c	0.00016091	88.12	38.90	0.026481	0.001750	0.001750	0.03	0.03	0.01	0.01
OGLE-TR-10b	0.00052468	90.00	3.10	0.039040	0.013779	0.013779	4.40	4.40	0.88	0.88
OGLE-TR-111b	0.00061447	88.25	4.02	0.041111	0.010726	0.010726	1.78	1.78	0.35	0.35
OGLE-TR-113b	0.00153784	87.80	1.43	0.055443	0.022922	0.022922	7.07	7.07	1.38	1.38
OGLE-TR-132b	0.00085536	83.40	1.69	0.045803	0.018986	0.018984	7.12	7.12	1.41	1.38
OGLE-TR-182b	0.00085538	85.70	3.98	0.045803	0.010526	0.010526	1.21	1.21	0.24	0.24
OGLE-TR-211b	0.00054071	84.22	3.68	0.039427	0.012703	0.012702	3.34	3.34	0.66	0.65
OGLE-TR-56b	0.00105281	77.60	1.21	0.049013	0.027664	0.027639	17.98	17.93	3.64	3.36
OGLE2-TR-L9b	0.00282717	79.80	2.49	0.067531	0.018644	0.018643	2.10	2.10	0.40	0.38
Qatar-1b	0.00121583	83.47	1.42	0.051365	0.023901	0.023897	10.07	10.07	2.00	1.95
Qatar-2b	0.00320274	88.30	1.34	0.070305	0.025499	0.025499	4.77	4.77	0.91	0.91
TrES-1b	0.00081805	90.00	3.03	0.045141	0.013013	0.013013	2.40	2.40	0.47	0.47
TrES-2b	0.00115857	83.57	2.47	0.050565	0.016481	0.016480	3.46	3.46	0.68	0.66
TrES-3b	0.00195385	81.85	1.31	0.059923	0.028300	0.028293	10.53	10.53	2.06	1.99
TrES-4b	0.00062516	82.81	3.55	0.041344	0.016809	0.016807	6.72	6.72	1.34	1.31
TrES-5b	0.00189190	84.53	1.48	0.059300	0.023667	0.023665	6.36	6.36	1.24	1.22
WASP-1b	0.00065824	88.65	2.52	0.042047	0.018924	0.018924	9.12	9.12	1.83	1.83
WASP-10b	0.00385467	88.49	3.09	0.074628	0.013428	0.013428	0.58	0.58	0.11	0.11
WASP-103b	0.00116168	86.30	0.93	0.050609	0.037823	0.037816	41.74	41.72	8.95	8.89
WASP-11b	0.00064399	89.80	3.72	0.041747	0.009974	0.009974	1.36	1.36	0.27	0.27
WASP-12b	0.00100595	82.50	1.09	0.048291	0.039449	0.039410	54.52	54.35	12.17	11.84
WASP-13b	0.00041365	85.43	4.35	0.036115	0.012557	0.012557	4.20	4.20	0.84	0.83
WASP-14b	0.00557733	84.32	2.24	0.084022	0.016659	0.016659	0.78	0.78	0.14	0.14

Continued on next page

Table C.1 – continued from previous page

Planet	q	i	P (d)	R_2	R_ϕ	$R_{i\phi}$	Infilling % (90°)	Infilling % (i)	Δ Density (90°)	Δ Density (i)
WASP-15b	0.00043798	85.96	3.75	0.036797	0.013238	0.013237	4.66	4.66	0.93	0.92
WASP-16b	0.00080117	85.22	3.12	0.044835	0.011542	0.011542	1.71	1.71	0.34	0.33
WASP-17b	0.00040720	86.63	3.73	0.035929	0.018667	0.018666	14.02	14.02	2.87	2.85
WASP-18b	0.00787355	80.60	0.94	0.093800	0.030128	0.030125	3.31	3.31	0.61	0.58
WASP-19b	0.00114340	79.40	0.79	0.050348	0.042345	0.042254	59.49	59.11	13.43	12.71
WASP-2b	0.00098142	84.73	2.15	0.047904	0.016504	0.016503	4.09	4.09	0.80	0.79
WASP-21b	0.00028371	88.75	4.32	0.031911	0.009833	0.009833	2.93	2.93	0.59	0.59
WASP-22b	0.00048506	89.20	3.53	0.038049	0.011442	0.011442	2.72	2.72	0.54	0.54
WASP-23b	0.00106694	88.39	2.94	0.049226	0.012432	0.012432	1.61	1.61	0.31	0.31
WASP-24b	0.00087412	83.64	2.34	0.046128	0.017072	0.017071	5.07	5.07	1.00	0.98
WASP-25b	0.00055181	88.00	3.76	0.039690	0.012333	0.012333	3.00	3.00	0.60	0.59
WASP-26b	0.00085970	82.50	2.76	0.045879	0.015827	0.015826	4.11	4.10	0.81	0.79
WASP-29b	0.00028107	88.80	3.92	0.031813	0.008300	0.008300	1.78	1.78	0.36	0.36
WASP-3b	0.00156818	85.06	1.85	0.055796	0.019631	0.019631	4.36	4.36	0.85	0.84
WASP-31b	0.00039094	84.54	3.41	0.035452	0.015851	0.015849	8.94	8.94	1.81	1.78
WASP-32b	0.00306957	85.10	2.72	0.069348	0.013476	0.013476	0.73	0.73	0.14	0.14
WASP-34b	0.00054937	85.20	4.32	0.039632	0.011214	0.011214	2.27	2.27	0.45	0.44
WASP-35b	0.00063929	87.96	3.16	0.041647	0.014670	0.014670	4.37	4.37	0.87	0.87
WASP-36b	0.00211054	83.65	1.54	0.061439	0.023176	0.023174	5.37	5.37	1.04	1.02
WASP-37b	0.00185043	88.82	3.58	0.058875	0.012430	0.012430	0.94	0.94	0.18	0.18
WASP-38b	0.00210216	89.50	6.87	0.061360	0.006869	0.006869	0.14	0.14	0.03	0.03
WASP-39b	0.00029162	87.83	4.05	0.032201	0.012543	0.012543	5.91	5.91	1.19	1.19
WASP-4b	0.00128287	89.47	1.34	0.052270	0.028103	0.028103	15.54	15.54	3.12	3.11
WASP-41b	0.00093616	87.70	3.05	0.047172	0.014188	0.014188	2.72	2.72	0.53	0.53
WASP-42b	0.00053819	88.30	4.98	0.039366	0.009290	0.009290	1.31	1.31	0.26	0.26
WASP-43b	0.00289856	82.60	0.81	0.068077	0.031419	0.031414	9.83	9.83	1.90	1.85
WASP-44b	0.00089096	86.02	2.42	0.046416	0.015725	0.015725	3.89	3.89	0.77	0.76
WASP-45b	0.00105203	84.47	3.13	0.049001	0.013693	0.013693	2.18	2.18	0.43	0.42
WASP-46b	0.00208168	82.63	1.43	0.061166	0.025686	0.025682	7.41	7.40	1.44	1.40
WASP-47b	0.00100060	89.20	4.16	0.048207	0.010575	0.010575	1.06	1.06	0.21	0.21

Continued on next page

Table C.1 – continued from previous page

Planet	q	i	P (d)	R_2	R_ϕ	$R_{i\phi}$	Infilling % (90°)	Infilling % (i)	Δ Density (90°)	Δ Density (i)
WASP-48b	0.00077768	80.09	2.14	0.044401	0.023369	0.023358	14.58	14.56	2.95	2.80
WASP-49b	0.00038336	84.89	2.78	0.035225	0.014123	0.014122	6.44	6.44	1.30	1.28
WASP-5b	0.00153143	86.10	1.63	0.055368	0.020099	0.020099	4.78	4.78	0.93	0.92
WASP-50b	0.00156699	84.00	1.95	0.055783	0.018744	0.018744	3.79	3.79	0.74	0.72
WASP-52b	0.00049992	85.35	1.75	0.038427	0.022684	0.022680	20.57	20.56	4.26	4.21
WASP-54b	0.00049597	84.97	3.69	0.038327	0.015914	0.015913	7.16	7.16	1.44	1.42
WASP-55b	0.00053978	89.60	4.47	0.039404	0.011687	0.011687	2.61	2.61	0.52	0.52
WASP-56b	0.00052181	88.50	4.62	0.038970	0.009304	0.009304	1.36	1.36	0.27	0.27
WASP-57b	0.00067583	88.00	2.84	0.042411	0.011346	0.011346	1.91	1.91	0.38	0.38
WASP-58b	0.00090420	87.40	5.02	0.046640	0.011662	0.011662	1.56	1.56	0.31	0.31
WASP-59b	0.00114039	89.27	7.92	0.050305	0.005316	0.005316	0.12	0.12	0.02	0.02
WASP-6b	0.00053490	88.47	3.36	0.039287	0.013684	0.013684	4.23	4.23	0.84	0.84
WASP-61b	0.00160761	89.35	3.86	0.056248	0.011526	0.011526	0.86	0.86	0.17	0.17
WASP-62b	0.00042916	88.30	4.41	0.036553	0.011739	0.011739	3.31	3.31	0.66	0.66
WASP-63b	0.00027320	87.80	4.38	0.031518	0.011938	0.011938	5.43	5.43	1.10	1.09
WASP-64b	0.00120653	86.57	1.57	0.051237	0.023043	0.023042	9.10	9.10	1.80	1.79
WASP-66b	0.00169427	85.90	4.09	0.057215	0.012170	0.012170	0.96	0.96	0.19	0.18
WASP-67b	0.00045880	85.80	4.61	0.037362	0.012955	0.012955	4.17	4.17	0.83	0.82
WASP-7b	0.00073119	89.60	4.95	0.043516	0.007236	0.007236	0.46	0.46	0.09	0.09
WASP-71b	0.00136347	84.20	2.90	0.053317	0.015497	0.015496	2.46	2.46	0.48	0.47
WASP-72b	0.00101098	86.80	2.22	0.048369	0.013216	0.013216	2.04	2.04	0.40	0.40
WASP-75b	0.00088950	82.00	2.48	0.046391	0.016227	0.016226	4.28	4.28	0.84	0.82
WASP-77Ab	0.00167573	89.40	1.36	0.057011	0.024162	0.024162	7.61	7.61	1.49	1.49
WASP-78b	0.00062996	83.20	2.17	0.041447	0.022732	0.022727	16.50	16.49	3.37	3.29
WASP-79b	0.00055553	85.40	3.66	0.039777	0.015251	0.015251	5.64	5.64	1.13	1.11
WASP-8b	0.00198062	88.55	8.16	0.060187	0.006190	0.006190	0.11	0.11	0.02	0.02
WASP-80b	0.00090803	89.92	3.07	0.046705	0.013220	0.013220	2.27	2.27	0.45	0.45
XO-1b	0.00085344	88.81	3.94	0.045769	0.011709	0.011709	1.67	1.67	0.33	0.33
XO-2b	0.00055510	88.90	2.62	0.039767	0.012782	0.012782	3.32	3.32	0.66	0.66
XO-3b	0.00883740	79.32	3.19	0.097310	0.012193	0.012193	0.20	0.20	0.04	0.03

Continued on next page

Table C.1 – continued from previous page

Planet	q	i	P (d)	R_2	R_ϕ	$R_{i\phi}$	Infilling % (90°)	Infilling % (i)	Δ Density (90°)	Δ Density (i)
XO-5b	0.00109846	86.90	4.19	0.049695	0.009683	0.009683	0.74	0.74	0.14	0.14

Bibliography

Agol, E. (2011). Transit Surveys for Earths in the Habitable Zones of White Dwarfs. ApJ, 731, L31.

Akeson, R. L., Chen, X., Ciardi, D., Crane, M., Good, J., Harbut, M., Jackson, E., Kane, S. R., Laity, A. C., Leifer, S., Lynn, M., McElroy, D. L., Papin, M., Plavchan, P., Ramírez, S. V., Rey, R., von Braun, K., Wittman, M., Abajian, M., Ali, B., Beichman, C., Beekley, A., Berriman, G. B., Berukoff, S., Bryden, G., Chan, B., Groom, S., Lau, C., Payne, A. N., Regelson, M., Saucedo, M., Schmitz, M., Stauffer, J., Wyatt, P., & Zhang, A. (2013). The NASA Exoplanet Archive: Data and Tools for Exoplanet Research. PASP, 125, 989–999.

Alsubai, K. A., Parley, N. R., Bramich, D. M., Horne, K., Collier Cameron, A., West, R. G., Sorensen, P. M., Pollacco, D., Smith, J. C., & Fors, O. (2013). The Qatar Exoplanet Survey. Acta Astron., 63, 465–480.

Anderson, D. R., Collier Cameron, A., Delrez, L., Doyle, A. P., Faedi, F., Fumel, A., Gillon, M., Gómez Maqueo Chew, Y., Hellier, C., Jehin, E., Lendl, M., Maxted, P. F. L., Pepe, F., Pollacco, D., Queloz, D., Ségransan, D., Skillen, I., Smalley, B., Smith, A. M. S., Southworth, J., Triaud, A. H. M. J., Turner, O. D., Udry, S., & West, R. G. (2014). Three newly discovered sub-Jupiter-mass planets: WASP-69b and WASP-84b transit active K dwarfs and WASP-70Ab transits the evolved primary of a G4+K3 binary. MNRAS, 445, 1114–1129.

Astropy Collaboration, Robitaille, T. P., Tollerud, E. J., Greenfield, P., Droettboom, M., Bray, E., Aldcroft, T., Davis, M., Ginsburg, A., Price-Whelan, A. M., Kerzendorf, W. E., Conley, A., Crighton, N., Barbary, K., Muna, D., Ferguson, H., Grollier, F., Parikh, M. M., Nair, P. H., Unther, H. M., Deil, C., Woillez, J., Conseil, S., Kramer, R., Turner, J. E. H., Singer, L., Fox, R., Weaver, B. A., Zabalza, V., Edwards, Z. I., Azalee Bostroem, K., Burke, D. J., Casey, A. R., Crawford, S. M., Dencheva, N., Ely, J., Jenness, T., Labrie, K., Lim, P. L., Pierfederici, F., Pontzen, A., Ptak, A., Refsdal, B., Servillat, M., & Streicher, O. (2013). Astropy: A community Python package for astronomy. A&A, 558, A33.

Batalha, N. M., Borucki, W. J., Bryson, S. T., Buchhave, L. A., Caldwell, D. A., Christensen-Dalsgaard, J., Ciardi, D., Dunham, E. W., Fressin, F., Gautier, III, T. N., Gilliland, R. L., Haas, M. R., Howell, S. B., Jenkins, J. M., Kjeldsen, H., Koch, D. G., Latham, D. W., Lissauer, J. J., Marcy, G. W., Rowe, J. F., Sasselov, D. D., Seager, S., Steffen, J. H., Torres, G., Basri, G. S., Brown, T. M., Charbonneau, D., Christiansen, J., Clarke, B., Cochran, W. D., Dupree, A., Fabrycky, D. C., Fischer, D., Ford, E. B., Fortney, J., Girouard, F. R., Holman, M. J., Johnson, J., Isaacson,

H., Klaus, T. C., Machalek, P., Moorehead, A. V., Morehead, R. C., Ragozzine, D., Tenenbaum, P., Twicken, J., Quinn, S., VanCleve, J., Walkowicz, L. M., Welsh, W. F., Devore, E., & Gould, A. (2011). Kepler's First Rocky Planet: Kepler-10b. ApJ, 729, 27.

Beaulieu, J.-P., Bennett, D. P., Fouqué, P., Williams, A., Dominik, M., Jørgensen, U. G., Kubas, D., Cassan, A., Coutures, C., Greenhill, J., Hill, K., Menzies, J., Sackett, P. D., Albrow, M., Brillant, S., Caldwell, J. A. R., Calitz, J. J., Cook, K. H., Corrales, E., Desort, M., Dieters, S., Dominis, D., Donatowicz, J., Hoffman, M., Kane, S., Marquette, J.-B., Martin, R., Meintjes, P., Pollard, K., Sahu, K., Vinter, C., Wambsganss, J., Woller, K., Horne, K., Steele, I., Bramich, D. M., Burgdorf, M., Snodgrass, C., Bode, M., Udalski, A., Szymański, M. K., Kubiak, M., Więckowski, T., Pietrzyński, G., Soszyński, I., Szewczyk, O., Wyrzykowski, Ł., Paczyński, B., Abe, F., Bond, I. A., Britton, T. R., Gilmore, A. C., Hearnshaw, J. B., Itow, Y., Kamiya, K., Kilmartin, P. M., Korpela, A. V., Masuda, K., Matsubara, Y., Motomura, M., Muraki, Y., Nakamura, S., Okada, C., Ohnishi, K., Rattenbury, N. J., Sako, T., Sato, S., Sasaki, M., Sekiguchi, T., Sullivan, D. J., Tristram, P. J., Yock, P. C. M., & Yoshioka, T. (2006). Discovery of a cool planet of 5.5 Earth masses through gravitational microlensing. Nature, 439, 437–440.

Bertin, E. & Arnouts, S. (1996). SExtractor: Software for source extraction. A&AS, 117, 393–404.

Bloom, J. S., Kasen, D., Shen, K. J., Nugent, P. E., Butler, N. R., Graham, M. L., Howell, D. A., Kolb, U., Holmes, S., Haswell, C. A., Burwitz, V., Rodriguez, J., & Sullivan, M. (2012). A Compact Degenerate Primary-star Progenitor of SN 2011fe. ApJ, 744, L17.

Boisse, I., Bouchy, F., Hébrard, G., Bonfils, X., Santos, N., & Vauclair, S. (2011). Disentangling between stellar activity and planetary signals. A&A, 528, A4.

Brothwell, R. D., Watson, C. A., Hébrard, G., Triaud, A. H. M. J., Cegla, H. M., Santerne, A., Hébrard, E., Anderson, D. R., Pollacco, D., Simpson, E. K., Bouchy, F., Brown, D. J. A., Chew, Y. G. M., Cameron, A. C., Armstrong, D. J., Barros, S. C. C., Bento, J., Bochinski, J., Burwitz, V., Busuttil, R., Delrez, L., Doyle, A. P., Faedi, F., Fumel, A., Gillon, M., Haswell, C. A., Hellier, C., Jehin, E., Kolb, U., Lendl, M., Liebig, C., Maxted, P. F. L., McCormac, J., Miller, G. R. M., Norton, A. J., Pepe, F., Queloz, D., Rodríguez, J., Ségransan, D., Skillen, I., Smalley, B., Stassun, K. G., Udry, S., West, R. G., & Wheatley, P. J. (2014). A window on exoplanet dynamical histories: Rossiter-McLaughlin observations of WASP-13b and WASP-32b. MNRAS, 440, 3392–3401.

Burke, C. J., Gaudi, B. S., DePoy, D. L., & Pogge, R. W. (2006). Survey for Transiting Extrasolar Planets in Stellar Systems. III. A Limit on the Fraction of Stars with Planets in the Open Cluster NGC 1245. AJ, 132, 210–230.

Burton, J. R., Watson, C. A., Fitzsimmons, A., Pollacco, D., Moulds, V., Littlefair, S. P., & Wheatley, P. J. (2014). Tidally Distorted Exoplanets: Density Corrections for Short-period Hot-Jupiters Based Solely on Observable Parameters. ApJ, 789, 113.

Burwitz, V., Pietsch, W., Henze, M., Rodriguez, J., Haswell, C. A., Holmes, S., Kolb, U., & Lucas, R. (2010a). Apparent Nova in M31: M31N 2010-06c. *Central Bureau Electronic Telegrams*, 2343, 1.

Burwitz, V., Pietsch, W., Henze, M., Updike, A., Milne, P., Williams, G., Hartmann, D. H., Rodriguez, J., Holmes, S., Kolb, U., & Lucas, R. (2010b). Apparent Nova in M31: M31N 2010-01a. *Central Bureau Electronic Telegrams*, 2124, 1.

Burwitz, V., Rodriguez, J., Holmes, S., Kolb, U., & Lucas, R. (2009). Apparent Nova in M31: M31N 2009-11a. *Central Bureau Electronic Telegrams*, 2003, 2.

Campbell, H. C., Marsh, T. R., Fraser, M., Hodgkin, S. T., de Miguel, E., Gänsicke, B. T., Steeghs, D., Hourihane, A., Breedt, E., Littlefair, S. P., Koposov, S. E., Wyrzykowski, Ł., Altavilla, G., Blagorodnova, N., Clementini, G., Daml-janovic, G., Delgado, A., Dennefeld, M., Drake, A. J., Fernández-Hernández, J., Gilmore, G., Gualandi, R., Hamanowicz, A., Handzlik, B., Hardy, L. K., Harrison, D. L., Iłkiewicz, K., Jonker, P. G., Kochanek, C. S., Kołaczkowski, Z., Kostrzewa-Rutkowska, Z., Kotak, R., van Leeuwen, G., Leto, G., Ochner, P., Pawlak, M., Palaversa, L., Rixon, G., Rybicki, K., Shappee, B. J., Smartt, S. J., Torres, M. A. P., Tomasella, L., Turatto, M., Ulaczyk, K., van Velzen, S., Vince, O., Walton, N. A., Wielgórski, P., Wevers, T., Whitelock, P., Yoldas, A., De Angeli, F., Burgess, P., Busso, G., Busuttil, R., Butterley, T., Chambers, K. C., Copperwheat, C., Danilet, A. B., Dhillon, V. S., Evans, D. W., Eyer, L., Froebrich, D., Gomboc, A., Holland, G., Holoien, T. W.-S., Jarvis, J. F., Kaiser, N., Kann, D. A., Koester, D., Kolb, U., Komossa, S., Magnier, E. A., Mahabal, A., Polshaw, J., Prieto, J. L., Prusti, T., Riello, M., Scholz, A., Simonian, G., Stanek, K. Z., Szabados, L., Waters, C., & Wilson, R. W. (2015). Total eclipse of the heart: the AM CVn Gaia14aae/ASSASN-14cn. MNRAS, 452, 1060–1067.

Campo, C. J., Harrington, J., Hardy, R. A., Stevenson, K. B., Nymeyer, S., Ragozzine, D., Lust, N. B., Anderson, D. R., Collier-Cameron, A., Blecic, J., Britt, C. B. T., Bowman, W. C., Wheatley, P. J., Loredo, T. J., Deming, D., Hebb, L., Hellier, C., Maxted, P. F. L., Pollaco, D., & West, R. G. (2011). On the Orbit of Exoplanet WASP-12b. ApJ, 727, 125.

Carrol, B. W. & Ostlie, D. A. (2007). *An Introduction to Modern Astrophysics*. Pearson/Addison-Wesley, Second edition.

Collier Cameron, A., Wilson, D. M., West, R. G., Hebb, L., Wang, X.-B., Aigrain, S., Bouchy, F., Christian, D. J., Clarkson, W. I., Enoch, B., Esposito, M., Guenther, E., Haswell, C. A., Hébrard, G., Hellier, C., Horne, K., Irwin, J., Kane, S. R., Loeillet, B., Lister, T. A., Maxted, P., Mayor, M., Moutou, C., Parley, N., Pollacco, D., Pont, F., Queloz, D., Ryans, R., Skillen, I., Street, R. A., Udry, S., & Wheatley, P. J. (2007). Efficient identification of exoplanetary transit candidates from SuperWASP light curves. MNRAS, 380, 1230–1244.

Contardo, G. (2001). *Analysis of Light Curves of Type Ia Supernovae*. Dissertation, Technische UniversitÃd't MÃijnchen, MÃijnchen.

Contardo, G., Leibundgut, B., & Vacca, W. D. (2000). Epochs of maximum light and bolometric light curves of type Ia supernovae. A&A, 359, 876–886.

Copperwheat, C. M., Bersier, D. F., Shappee, B. J., Kochanek, C. S., Stanek, K. Z., Jencson, J., Basu, U., Beacom, J. F., Prieto, J. L., Szczygiel, D., Pojmanski, G., Dubberley, M., Elphick, M., Foale, S., Hawkins, E., Mullens, D., Rosing, W., Ross, R., Walker, Z., & Brimacombe, J. (2013). Spectrum of Bright Transient ASASSN-13ax: Hydrogen-Rich Dwarf Nova in Outburst. *The Astronomer's Telegram*, 5195, 1.

da Silva, L. A. L. (1993). The classification of supernovae. Ap&SS, 202, 215–236.

Denny, R. B. (2004). Dispatch Scheduling of Automated Telescopes. *Society for Astronomical Sciences Annual Symposium*, 23, 35.

Eggleton, P. P. (1983). Approximations to the radii of Roche lobes. ApJ, 268, 368–+.

Enoch, B., Collier Cameron, A., Parley, N. R., & Hebb, L. (2010). An improved method for estimating the masses of stars with transiting planets. A&A, 516, A33.

Faedi, F., Gómez Maqueo Chew, Y., Pollacco, D., Brown, D. J. A., Hébrard, G., Smalley, B., Lam, K. W. F., Veras, D., Anderson, D., Doyle, A. P., Gillon, M., Goad, M. R., Lendl, M., Mancini, L., McCormac, J., Plauchu-Frayn, I., Prieto-Arranz, J., Scholz, A., Street, R., Triaud, A. H. M., West, R., Wheatley, P. J., Armstrong, D. J., Barros, S. C. C., Boisse, I., Bouchy, F., Boumis, P., Collier Cameron, A., Haswell, C. A., Hay, K. L., Hellier, C., Kolb, U., Maxted, P. F. L., Norton, A. J., Osborn, H. P., Palle, E., Pepe, F., Queloz, D., Ségransan, D., Udry, S., & Wilson, P. A. (2016). WASP-86b and WASP-102b: super-dense versus bloated planets. *ArXiv e-prints*.

Faedi, F., Pollacco, D., Barros, S. C. C., Brown, D., Collier Cameron, A., Doyle, A. P., Enoch, R., Gillon, M., Gómez Maqueo Chew, Y., Hébrard, G., Lendl, M., Liebig, C., Smalley, B., Triaud, A. H. M. J., West, R. G., Wheatley, P. J., Alsubai, K. A., Anderson, D. R., Armstrong, D., Bento, J., Bochinski, J., Bouchy, F., Busuttil, R., Fossati, L., Fumel, A., Haswell, C. A., Hellier, C., Holmes, S., Jehin, E., Kolb, U., McCormac, J., Miller, G. R. M., Moutou, C., Norton, A. J., Parley, N., Queloz, D., Santerne, A., Skillen, I., Smith, A. M. S., Udry, S., & Watson, C. (2013). WASP-54b, WASP-56b, and WASP-57b: Three new sub-Jupiter mass planets from SuperWASP. A&A, 551, A73.

Ferraz-Mello, S., Tadeu Dos Santos, M., Beaugé, C., Michtchenko, T. A., & Rodríguez, A. (2011). On the mass determination of super-Earths orbiting active stars: the CoRoT-7 system. A&A, 531, A161.

Filippenko, A. V. (1988). Taxonomy of supernovae. *Proceedings of the Astronomical Society of Australia*, 7, 540–547.

Fossati, L., Haswell, C. A., Froning, C. S., Hebb, L., Holmes, S., Kolb, U., Helling, C., Carter, A., Wheatley, P., Collier Cameron, A., Loeillet, B., Pollacco, D., Street, R., Stempels, H. C., Simpson, E., Udry, S., Joshi, Y. C., West, R. G., Skillen, I.,

& Wilson, D. (2010a). Metals in the Exosphere of the Highly Irradiated Planet WASP-12b. ApJ, 714, L222–L227.

Fossati, L., Bagnulo, S., Elmasli, A., Haswell, C. A., Holmes, S., Kochukhov, O., Shkolnik, E. L., Shulyak, D. V., Bohlender, D., Albayrak, B., Froning, C., & Hebb, L. (2010b). A Detailed Spectropolarimetric Analysis of the Planet-hosting Star WASP-12. ApJ, 720, 872–886.

Fossati, L., Bagnulo, S., Haswell, C. A., Patel, M. R., Busuttil, R., Kowalski, P. M., Shulyak, D. V., & Sterzik, M. F. (2012). The Habitability and Detection of Earth-like Planets Orbiting Cool White Dwarfs. ApJ, 757, L15.

Fossey, J., Cooke, B., Pollack, G., Wilde, M., & Wright, T. (2014). Supernova 2014J in M82 = Psn J09554214+6940260. *Central Bureau Electronic Telegrams*, 3792, 1.

Gómez Maqueo Chew, Y., Faedi, F., Pollacco, D., Brown, D. J. A., Doyle, A. P., Collier Cameron, A., Gillon, M., Lendl, M., Smalley, B., Triaud, A. H. M. J., West, R. G., Wheatley, P. J., Busuttil, R., Liebig, C., Anderson, D. R., Armstrong, D. J., Barros, S. C. C., Bento, J., Bochinski, J., Burwitz, V., Delrez, L., Enoch, B., Fumel, A., Haswell, C. A., Hébrard, G., Hellier, C., Holmes, S., Jehin, E., Kolb, U., Maxted, P. F. L., McCormac, J., Miller, G. R. M., Norton, A. J., Pepe, F., Queloz, D., Rodríguez, J., Ségransan, D., Skillen, I., Stassun, K. G., Udry, S., & Watson, C. (2013). Discovery of WASP-65b and WASP-75b: Two hot Jupiters without highly inflated radii. A&A, 559, A36.

Goobar, A., Johansson, J., Amanullah, R., Cao, Y., Perley, D. A., Kasliwal, M. M., Ferretti, R., Nugent, P. E., Harris, C., Gal-Yam, A., Ofek, E. O., Tendulkar, S. P., Dennefeld, M., Valenti, S., Arcavi, I., Banerjee, D. P. K., Venkataraman, V., Joshi, V., Ashok, N. M., Cenko, S. B., Diaz, R. F., Fremling, C., Horesh, A., Howell, D. A., Kulkarni, S. R., Papadogiannakis, S., Petrushevska, T., Sand, D., Sollerman, J., Stanishev, V., Bloom, J. S., Surace, J., Dupuy, T. J., & Liu, M. C. (2014). The Rise of SN 2014J in the Nearby Galaxy M82. ApJ, 784, L12.

Greiner, J., Mazzali, P. A., Kann, D. A., Krühler, T., Pian, E., Prentice, S., Olivares E., F., Rossi, A., Klose, S., Taubenberger, S., Knust, F., Afonso, P. M. J., Ashall, C., Bolmer, J., Delvaux, C., Diehl, R., Elliott, J., Filgas, R., Fynbo, J. P. U., Graham, J. F., Guelbenzu, A. N., Kobayashi, S., Leloudas, G., Savaglio, S., Schady, P., Schmidl, S., Schweyer, T., Sudilovsky, V., Tanga, M., Updike, A. C., van Eerten, H., & Varela, K. (2015). A very luminous magnetar-powered supernova associated with an ultra-long γ-ray burst. Nature, 523, 189–192.

Guy, J., Astier, P., Baumont, S., Hardin, D., Pain, R., Regnault, N., Basa, S., Carlberg, R. G., Conley, A., Fabbro, S., Fouchez, D., Hook, I. M., Howell, D. A., Perrett, K., Pritchet, C. J., Rich, J., Sullivan, M., Antilogus, P., Aubourg, E., Bazin, G., Bronder, J., Filiol, M., Palanque-Delabrouille, N., Ripoche, P., & Ruhlmann-Kleider, V. (2007). SALT2: using distant supernovae to improve the use of type Ia supernovae as distance indicators. A&A, 466, 11–21.

Haswell, C. A. (2010). *Transiting Exoplanets*. New York, United States of America: Cambridge University Press.

Haswell, C. A., Fossati, L., Ayres, T., France, K., Froning, C. S., Holmes, S., Kolb, U. C., Busuttil, R., Street, R. A., Hebb, L., Collier Cameron, A., Enoch, B., Burwitz, V., Rodriguez, J., West, R. G., Pollacco, D., Wheatley, P. J., & Carter, A. (2012). Near-ultraviolet Absorption, Chromospheric Activity, and Star-Planet Interactions in the WASP-12 system. ApJ, 760, 79.

Hatzes, A. P., Dvorak, R., Wuchterl, G., Guterman, P., Hartmann, M., Fridlund, M., Gandolfi, D., Guenther, E., & Pätzold, M. (2010). An investigation into the radial velocity variations of CoRoT-7. A&A, 520, A93.

Hatzes, A. P., Fridlund, M., Nachmani, G., Mazeh, T., Valencia, D., Hébrard, G., Carone, L., Pätzold, M., Udry, S., Bouchy, F., Deleuil, M., Moutou, C., Barge, P., Bordé, P., Deeg, H., Tingley, B., Dvorak, R., Gandolfi, D., Ferraz-Mello, S., Wuchterl, G., Guenther, E., Guillot, T., Rauer, H., Erikson, A., Cabrera, J., Csizmadia, S., Léger, A., Lammer, H., Weingrill, J., Queloz, D., Alonso, R., Rouan, D., & Schneider, J. (2011). The Mass of CoRoT-7b. ApJ, 743, 75.

Hay, K. L., Collier-Cameron, A., Doyle, A. P., Hébrard, G., Skillen, I., Anderson, D. R., Barros, S. C. C., Brown, D. J. A., Bouchy, F., Busuttil, R., Delorme, P., Delrez, L., Demangeon, O., Díaz, R. F., Gillon, M., Gómez Maqueo Chew, Y., Gonzàlez, E., Hellier, C., Holmes, S., Jarvis, J. F., Jehin, E., Joshi, Y. C., Kolb, U., Lendl, M., Maxted, P. F. L., McCormac, J., Miller, G. R. M., Mortier, A., Pallé, E., Pollacco, D., Prieto-Arranz, J., Queloz, D., Ségransan, D., Simpson, E. K., Smalley, B., Southworth, J., Triaud, A. H. M. J., Turner, O. D., Udry, S., Vanhuysse, M., West, R. G., & Wilson, P. A. (2016). WASP-92b, WASP-93b and WASP-118b: three new transiting close-in giant planets. MNRAS, 463, 3276–3289.

Hebb, L., Collier-Cameron, A., Loeillet, B., Pollacco, D., Hébrard, G., Street, R. A., Bouchy, F., Stempels, H. C., Moutou, C., Simpson, E., Udry, S., Joshi, Y. C., West, R. G., Skillen, I., Wilson, D. M., McDonald, I., Gibson, N. P., Aigrain, S., Anderson, D. R., Benn, C. R., Christian, D. J., Enoch, B., Haswell, C. A., Hellier, C., Horne, K., Irwin, J., Lister, T. A., Maxted, P., Mayor, M., Norton, A. J., Parley, N., Pont, F., Queloz, D., Smalley, B., & Wheatley, P. J. (2009). WASP-12b: The Hottest Transiting Extrasolar Planet Yet Discovered. ApJ, 693, 1920–1928.

Hébrard, G., Collier Cameron, A., Brown, D. J. A., Díaz, R. F., Faedi, F., Smalley, B., Anderson, D. R., Armstrong, D., Barros, S. C. C., Bento, J., Bouchy, F., Doyle, A. P., Enoch, B., Gómez Maqueo Chew, Y., Hébrard, É. M., Hellier, C., Lendl, M., Lister, T. A., Maxted, P. F. L., McCormac, J., Moutou, C., Pollacco, D., Queloz, D., Santerne, A., Skillen, I., Southworth, J., Tregloan-Reed, J., Triaud, A. H. M. J., Udry, S., Vanhuysse, M., Watson, C. A., West, R. G., & Wheatley, P. J. (2013). WASP-52b, WASP-58b, WASP-59b, and WASP-60b: Four new transiting close-in giant planets. A&A, 549, A134.

Hellier, C., Anderson, D. R., Collier-Cameron, A., Miller, G. R. M., Queloz, D., Smalley, B., Southworth, J., & Triaud, A. H. M. J. (2011). On the Orbit of the Short-period Exoplanet WASP-19b. ApJ, 730, L31.

Henze, M., Pietsch, W., Burwitz, V., Rodriguez, J., Bochinski, J., Busuttil, R., Haswell, C. A., Holmes, S., & Kolb, U. (2012). New disk nova candidate in M 31. *The Astronomer's Telegram*, 3932, 1.

Holmes, S., Kolb, U., Haswell, C. A., Burwitz, V., Lucas, R. J., Rodriguez, J., Rolfe, S. M., Rostron, J., & Barker, J. (2011). PIRATE: A Remotely Operable Telescope Facility for Research and Education. PASP, 123, 1177–1187.

Holmström, M., Ekenbäck, A., Selsis, F., Penz, T., Lammer, H., & Wurz, P. (2008). Energetic neutral atoms as the explanation for the high-velocity hydrogen around HD 209458b. Nature, 451, 970–972.

Holoien, T. W.-S., Prieto, J. L., Bersier, D., Kochanek, C. S., Stanek, K. Z., Shappee, B. J., Grupe, D., Basu, U., Beacom, J. F., Brimacombe, J., Brown, J. S., Davis, A. B., Jencson, J., Pojmanski, G., & Szczygieł, D. M. (2014). ASASSN-14ae: a tidal disruption event at 200 Mpc. MNRAS, 445, 3263–3277.

Howell, S. B. (2011). *Handbook of CCD Astronomy*. New York, United States of America: Cambridge University Press.

Husnoo, N., Pont, F., Hébrard, G., Simpson, E., Mazeh, T., Bouchy, F., Moutou, C., Arnold, L., Boisse, I., Díaz, R. F., Eggenberger, A., & Shporer, A. (2011). Orbital eccentricity of WASP-12 and WASP-14 from new radial velocity monitoring with SOPHIE. MNRAS, 413, 2500–2508.

Janesick, J. R. (2001). *Scientific charge-coupled devices*.

Janesick, J. R. (2007). *Photon Transfer DN* $\rightarrow \lambda$. SPIE.

Jehin, E., Gillon, M., Queloz, D., Magain, P., Manfroid, J., Chantry, V., Lendl, M., Hutsemékers, D., & Udry, S. (2011). TRAPPIST: TRAnsiting Planets and Planetes-Imals Small Telescope. *The Messenger*, 145, 2–6.

Kahan, W. (1965). Pracniques: Further remarks on reducing truncation errors. *Commun. ACM*, 8(1), 40–.

Kato, T., Hambsch, F.-J., Maehara, H., Masi, G., Nocentini, F., Dubovsky, P. A., Kudzej, I., Imamura, K., Ogi, M., Tanabe, K., Akazawa, H., Krajci, T., Miller, I., de Miguel, E., Henden, A., Noguchi, R., Ishibashi, T., Ono, R., Kawabata, M., Kobayashi, H., Sakai, D., Nishino, H., Furukawa, H., Masumoto, K., Matsumoto, K., Littlefield, C., Ohshima, T., Nakata, C., Honda, S., Kinugasa, K., Hashimoto, O., Stein, W., Pickard, R. D., Kiyota, S., Pavlenko, E. P., Antonyuk, O. I., Baklanov, A. V., Antonyuk, K., Samsonov, D., Pit, N., Sosnovskij, A., Oksanen, A., Harlingten, C., Tyyskä, J., Monard, B., Shugarov, S. Y., Chochol, D., Kasai, K., Maeda, Y., Hirosawa, K., Itoh, H., Sabo, R., Ulowetz, J., Morelle, E., Michel, R., Suárez, G., James, N., Dvorak, S., Voloshina, I. B., Richmond, M., Staels, B., Boyd, D., Andreev, M. V., Parakhin, N., Katysheva, N., Miyashita, A., Nakajima, K., Bolt, G., Padovan, S., Nelson, P., Starkey, D. R., Buczynski, D., Starr, P., Goff, W. N., Denisenko, D., Kochanek, C. S., Shappee, B., Stanek, K. Z., Prieto, J. L., Itagaki, K.-i., Kaneko, S., Stubbings, R., Muyllaert, E., Shears, J., Schmeer, P., Poyner, G.,

& Rodríguez-Marco, M. (2014). Survey of period variations of superhumps in SU UMa-type dwarf novae. V. The fifth year (2012-2013). PASJ, 66, 30.

Li, S., Miller, N., Lin, D. N. C., & Fortney, J. J. (2010). WASP-12b as a prolate, inflated and disrupting planet from tidal dissipation. Nature, 463, 1054–1056.

Llama, J., Wood, K., Jardine, M., Vidotto, A. A., Helling, C., Fossati, L., & Haswell, C. A. (2011). The shocking transit of WASP-12b: modelling the observed early ingress in the near-ultraviolet. MNRAS, 416, L41–L44.

Lohr, M. E., Norton, A. J., Gillen, E., Busuttil, R., Kolb, U. C., Aigrain, S., McQuillan, A., Hodgkin, S. T., & González, E. (2015). The doubly eclipsing quintuple low-mass star system 1SWASP J093010.78+533859.5. A&A, 578, A103.

Madhusudhan, N., Lee, K. K. M., & Mousis, O. (2012). A Possible Carbon-rich Interior in Super-Earth 55 Cancri e. ApJ, 759, L40.

Marion, G. H., Sand, D. J., Hsiao, E. Y., Banerjee, D. P. K., Valenti, S., Stritzinger, M. D., Vinkó, J., Joshi, V., Venkataraman, V., Ashok, N. M., Amanullah, R., Binzel, R. P., Bochanski, J. J., Bryngelson, G. L., Burns, C. R., Drozdov, D., Fieber-Beyer, S. K., Graham, M. L., Howell, D. A., Johansson, J., Kirshner, R. P., Milne, P. A., Parrent, J., Silverman, J. M., Vervack, Jr., R. J., & Wheeler, J. C. (2015). Early Observations and Analysis of the Type Ia SN 2014J in M82. ApJ, 798, 39.

Marois, C., Lafrenière, D., Doyon, R., Macintosh, B., & Nadeau, D. (2006). Angular Differential Imaging: A Powerful High-Contrast Imaging Technique. ApJ, 641, 556–564.

Maxted, P. F. L., Bloemen, S., Heber, U., Geier, S., Wheatley, P. J., Marsh, T. R., Breedt, E., Sebastian, D., Faillace, G., Owen, C., Pulley, D., Smith, D., Kolb, U., Haswell, C. A., Southworth, J., Anderson, D. R., Smalley, B., Collier Cameron, A., Hebb, L., Simpson, E. K., West, R. G., Bochinski, J., Busuttil, R., & Hadigal, S. (2014). EL CVn-type binaries - discovery of 17 helium white dwarf precursors in bright eclipsing binary star systems. MNRAS, 437, 1681–1697.

Mayor, M. & Queloz, D. (1995). A Jupiter-mass companion to a solar-type star. Nature, 378, 355–359.

Mazzali, P. A., Röpke, F. K., Benetti, S., & Hillebrandt, W. (2007). A Common Explosion Mechanism for Type Ia Supernovae. *Science*, 315, 825.

Nagasawa, M., Ida, S., & Bessho, T. (2008). Formation of Hot Planets by a Combination of Planet Scattering, Tidal Circularization, and the Kozai Mechanism. ApJ, 678, 498–508.

Nugent, P. E., Sullivan, M., Cenko, S. B., Thomas, R. C., Kasen, D., Howell, D. A., Bersier, D., Bloom, J. S., Kulkarni, S. R., Kandrashoff, M. T., Filippenko, A. V., Silverman, J. M., Marcy, G. W., Howard, A. W., Isaacson, H. T., Maguire, K., Suzuki, N., Tarlton, J. E., Pan, Y.-C., Bildsten, L., Fulton, B. J., Parrent, J. T., Sand, D., Podsiadlowski, P., Bianco, F. B., Dilday, B., Graham, M. L., Lyman, J., James, P., Kasliwal, M. M., Law, N. M., Quimby, R. M., Hook, I. M., Walker, E. S., Mazzali,

P., Pian, E., Ofek, E. O., Gal-Yam, A., & Poznanski, D. (2011). Supernova SN 2011fe from an exploding carbon-oxygen white dwarf star. Nature, 480, 344–347.

Ofir, A., Alonso, R., Bonomo, A. S., Carone, L., Carpano, S., Samuel, B., Weingrill, J., Aigrain, S., Auvergne, M., Baglin, A., Barge, P., Borde, P., Bouchy, F., Deeg, H. J., Deleuil, M., Dvorak, R., Erikson, A., Mello, S. F., Fridlund, M., Gillon, M., Guillot, T., Hatzes, A., Jorda, L., Lammer, H., Leger, A., Llebaria, A., Moutou, C., Ollivier, M., Päetzold, M., Queloz, D., Rauer, H., Rouan, D., Schneider, J., & Wuchterl, G. (2010). The SARS algorithm: detrending CoRoT light curves with Sysrem using simultaneous external parameters. MNRAS, 404, L99–L103.

Pastorello, A. (2012). Supernova Taxonomy - New Types. *Memorie della Societa Astronomica Italiana Supplementi*, 19, 24.

Perryman, M. (2011). *The Exoplanet Handbook*. New York, United States of America: Cambridge University Press.

Phillips, M. M., Lira, P., Suntzeff, N. B., Schommer, R. A., Hamuy, M., & Maza, J. (1999). The Reddening-Free Decline Rate Versus Luminosity Relationship for Type IA Supernovae. AJ, 118, 1766–1776.

Pollacco, D., Skillen, I., Collier Cameron, A., Loeillet, B., Stempels, H. C., Bouchy, F., Gibson, N. P., Hebb, L., Hébrard, G., Joshi, Y. C., McDonald, I., Smalley, B., Smith, A. M. S., Street, R. A., Udry, S., West, R. G., Wilson, D. M., Wheatley, P. J., Aigrain, S., Alsubai, K., Benn, C. R., Bruce, V. A., Christian, D. J., Clarkson, W. I., Enoch, B., Evans, A., Fitzsimmons, A., Haswell, C. A., Hellier, C., Hickey, S., Hodgkin, S. T., Horne, K., Hrudková, M., Irwin, J., Kane, S. R., Keenan, F. P., Lister, T. A., Maxted, P., Mayor, M., Moutou, C., Norton, A. J., Osborne, J. P., Parley, N., Pont, F., Queloz, D., Ryans, R., & Simpson, E. (2008). WASP-3b: a strongly irradiated transiting gas-giant planet. MNRAS, 385, 1576–1584.

Pollacco, D. L., Skillen, I., Collier Cameron, A., Christian, D. J., Hellier, C., Irwin, J., Lister, T. A., Street, R. A., West, R. G., Anderson, D., Clarkson, W. I., Deeg, H., Enoch, B., Evans, A., Fitzsimmons, A., Haswell, C. A., Hodgkin, S., Horne, K., Kane, S. R., Keenan, F. P., Maxted, P. F. L., Norton, A. J., Osborne, J., Parley, N. R., Ryans, R. S. I., Smalley, B., Wheatley, P. J., & Wilson, D. M. (2006). The WASP Project and the SuperWASP Cameras. PASP, 118, 1407–1418.

Pont, F., Aigrain, S., & Zucker, S. (2011). Reassessing the radial-velocity evidence for planets around CoRoT-7. MNRAS, 411, 1953–1962.

Prieto, J. L., Sheffield, A., Wagner, R. M., Woodward, C. E., Starrfield, S. G., & Hounsell, R. A. (2013). Spectroscopic Classification of ASASSN-13dl. *The Astronomer's Telegram*, 5508, 1.

Queloz, D., Bouchy, F., Moutou, C., Hatzes, A., Hébrard, G., Alonso, R., Auvergne, M., Baglin, A., Barbieri, M., Barge, P., Benz, W., Bordé, P., Deeg, H. J., Deleuil, M., Dvorak, R., Erikson, A., Ferraz Mello, S., Fridlund, M., Gandolfi, D., Gillon, M., Guenther, E., Guillot, T., Jorda, L., Hartmann, M., Lammer, H., Léger, A., Llebaria, A., Lovis, C., Magain, P., Mayor, M., Mazeh, T., Ollivier, M., Pätzold, M., Pepe, F.,

Rauer, H., Rouan, D., Schneider, J., Segransan, D., Udry, S., & Wuchterl, G. (2009). The CoRoT-7 planetary system: two orbiting super-Earths. A&A, 506, 303–319.

Ragozzine, D. & Wolf, A. S. (2009). Probing the Interiors of very Hot Jupiters Using Transit Light Curves. ApJ, 698, 1778–1794.

Rixon, G., Fraser, M., Koposov, S., Blagorodnova, N., Campbell, H., Hodgkin, S. T., van Leeuwen, G., Walton, N., Wyrzykowski, L., Wevers, T., Jonker, P., van Velzen, S., Benetti, S., Breedt, E., Busso, G., Busuttil, R., Davis, C., De Angeli, F., Dennefeld, M., Elias-Rosa, N., Evans, D. W., Froebrich, D., Gaensicke, B., Gilmore, G., Gomboc, A., Hamanowicz, A., Handzlik, B., Hardy, L., Ilkiewicz, K., Irwin, M., Jarvis, J. F., Kann, D. A., Kolb, U., Komossa, S., Kostrzewa-Rutkowska, Z., Littlefair, S., Mahabal, A., O'Brien, P., Ochner, P., Riello, M., Pawlak, M., Pigulski, A., Pretorius, R., Rybicki, K., Scholz, A., Sitek, M., Steeghs, D., Tomasella, L., Turatto, M., Ulaczyk, K., Van Leeuwen, F., & Prusti, T. (2014). Gaia Alerts classified at the William Herschel Telescope. *The Astronomer's Telegram*, 6593.

Salaris, M., Cassisi, S., Pietrinferni, A., Kowalski, P. M., & Isern, J. (2010). A Large Stellar Evolution Database for Population Synthesis Studies. VI. White Dwarf Cooling Sequences. ApJ, 716, 1241–1251.

Seager, S. (2010). *Exoplanets*. University of Arizona Press.

Seaman, R., Williams, R., Allan, A., Barthelmy, S., Bloom, J., Brewer, J., Denny, R., Fitzpatrick, M., Graham, M., Gray, N., Hessman, F., Marka, S., Rots, A., Vestrand, T., & Wozniak, P. (2011). Sky Event Reporting Metadata Version 2.0. IVOA Recommendation 11 July 2011.

Smith, A. M. S. & WASP Consortium (2014). The SuperWASP exoplanet transit survey. *Contributions of the Astronomical Observatory Skalnate Pleso*, 43, 500–512.

Staab, D., Haswell, C. A., Smith, G. D., Fossati, L., Barnes, J. R., Busuttil, R., & Jenkins, J. S. (2017). SALT observations of the chromospheric activity of transiting planet hosts: mass-loss and star-planet interactions. MNRAS, 466, 738–748.

Struve, O. (1952). Proposal for a project of high-precision stellar radial velocity work. *The Observatory*, 72, 199–200.

Sumi, T., Kamiya, K., Bennett, D. P., Bond, I. A., Abe, F., Botzler, C. S., Fukui, A., Furusawa, K., Hearnshaw, J. B., Itow, Y., Kilmartin, P. M., Korpela, A., Lin, W., Ling, C. H., Masuda, K., Matsubara, Y., Miyake, N., Motomura, M., Muraki, Y., Nagaya, M., Nakamura, S., Ohnishi, K., Okumura, T., Perrott, Y. C., Rattenbury, N., Saito, T., Sako, T., Sullivan, D. J., Sweatman, W. L., Tristram, P. J., Udalski, A., Szymański, M. K., Kubiak, M., Pietrzyński, G., Poleski, R., Soszyński, I., Wyrzykowski, Ł., Ulaczyk, K., & Microlensing Observations in Astrophysics (MOA) Collaboration (2011). Unbound or distant planetary mass population detected by gravitational microlensing. Nature, 473, 349–352.

Tamuz, O., Mazeh, T., & Zucker, S. (2005). Correcting systematic effects in a large set of photometric light curves. MNRAS, 356, 1466–1470.

Torres, G., Winn, J. N., & Holman, M. J. (2008). Improved Parameters for Extrasolar Transiting Planets. ApJ, 677, 1324–1342.

Vidal-Madjar, A., Lecavelier des Etangs, A., Désert, J.-M., Ballester, G. E., Ferlet, R., Hébrard, G., & Mayor, M. (2003). An extended upper atmosphere around the extrasolar planet HD209458b. Nature, 422, 143–146.

Vidotto, A. A., Jardine, M., & Helling, C. (2010). Early UV Ingress in WASP-12b: Measuring Planetary Magnetic Fields. ApJ, 722, L168–L172.

Vidotto, A. A., Jardine, M., & Helling, C. (2011). Prospects for detection of exoplanet magnetic fields through bow-shock observations during transits. MNRAS, 411, L46–L50.

von Essen, C., Schröter, S., Agol, E., & Schmitt, J. H. M. M. (2013). Qatar-1: indications for possible transit timing variations. A&A, 555, A92.

Wheatley, P. J., Mauche, C. W., & Mattei, J. A. (2003). The X-ray and extreme-ultraviolet flux evolution of SS Cygni throughout outburst. MNRAS, 345, 49–61.

Wheatley, P. J., Pollacco, D. L., Queloz, D., Rauer, H., Watson, C. A., West, R. G., Chazelas, B., Louden, T. M., Walker, S., Bannister, N., Bento, J., Burleigh, M., Cabrera, J., Eigmüller, P., Erikson, A., Genolet, L., Goad, M., Grange, A., Jordán, A., Lawrie, K., McCormac, J., & Neveu, M. (2013). The Next Generation Transit Survey (NGTS). In *European Physical Journal Web of Conferences*, volume 47 of *European Physical Journal Web of Conferences* (pp. 13002).

Winn, J. N., Matthews, J. M., Dawson, R. I., Fabrycky, D., Holman, M. J., Kallinger, T., Kuschnig, R., Sasselov, D., Dragomir, D., Guenther, D. B., Moffat, A. F. J., Rowe, J. F., Rucinski, S., & Weiss, W. W. (2011). A Super-Earth Transiting a Naked-eye Star. ApJ, 737, L18.

Wolszczan, A. & Frail, D. A. (1992). A planetary system around the millisecond pulsar PSR1257 + 12. Nature, 355, 145–147.

Wright, J. T., Fakhouri, O., Marcy, G. W., Han, E., Feng, Y., Johnson, J. A., Howard, A. W., Fischer, D. A., Valenti, J. A., Anderson, J., & Piskunov, N. (2011). The Exoplanet Orbit Database. PASP, 123, 412–422.

Wyrzykowski, L., Campbell, H. C., Koposov, S., Pawlak, M., Ulaczyk, K., Rynkiewicz, A., Wielgorski, P., Ilkiewicz, K., Handzlik, B., Rybicki, K., Obuchowicz, W., Khamitov, I. M., Esenoglu, H., Bikmaev, I. F., Zhuchkov, R. Y., Busuttil, R., Kolb, U., Burwitz, V., Rodriguez, J., Zeilinger, W., Leonini, S., Conti, M., Guerrini, G., Rosi, P., Ramirez, L. M. T., Damljanovic, G., Vince, O., Pavlovic, R., Cvetkovic, Z., & Stojanovic, M. (2014). Multiband photometric follow-up of supernova iPTF13ebh. *The Astronomer's Telegram*, 5926, 1.

Wyrzykowski, L., Campbell, H. C., Koposov, S., Ulaczyk, K., Damljanovic, G., Vince, O., Pavlovic, R., Cvetkovic, Z., Stojanovic, M., Kolb, U., Bochinski, J., Burwitz, V., Haswell, C., Rodriguez, J., Harding, J., & Busuttil, R. (2013). Multiband photometric follow-up of ASASSN-13aw (SN 2013dr). *The Astronomer's Telegram*, 5245, 1.

Wyrzykowski, L., Hodgkin, S., Blogorodnova, N., Koposov, S., & Burgon, R. (2012). Photometric Science Alerts from Gaia. *ArXiv e-prints*.

Zheng, W., Shen, R. F., Sakamoto, T., Beardmore, A. P., De Pasquale, M., Wu, X. F., Gorosabel, J., Urata, Y., Sugita, S., Zhang, B., Pozanenko, A., Nissinen, M., Sahu, D. K., Im, M., Ukwatta, T. N., Andreev, M., Klunko, E., Volnova, A., Akerlof, C. W., Anto, P., Barthelmy, S. D., Breeveld, A., Carsenty, U., Castillo-Carrión, S., Castro-Tirado, A. J., Chester, M. M., Chuang, C. J., Cunniffe, R., De Ugarte Postigo, A., Duffard, R., Flewelling, H., Gehrels, N., Güver, T., Guziy, S., Hentunen, V. P., Huang, K. Y., Jelínek, M., Koch, T. S., Kubánek, P., Kuin, P., McKay, T. A., Mottola, S., Oates, S. R., O'Brien, P., Ohno, M., Page, M. J., Pandey, S. B., Pérez del Pulgar, C., Rujopakarn, W., Rykoff, E., Salmi, T., Sánchez-Ramírez, R., Schaefer, B. E., Sergeev, A., Sonbas, E., Sota, A., Tello, J. C., Yamaoka, K., Yost, S. A., & Yuan, F. (2012). Panchromatic Observations of the Textbook GRB 110205A: Constraining Physical Mechanisms of Prompt Emission and Afterglow. ApJ, 751, 90.

Zheng, W., Silverman, J. M., Filippenko, A. V., Kasen, D., Nugent, P. E., Graham, M., Wang, X., Valenti, S., Ciabattari, F., Kelly, P. L., Fox, O. D., Shivvers, I., Clubb, K. I., Cenko, S. B., Balam, D., Howell, D. A., Hsiao, E., Li, W., Marion, G. H., Sand, D., Vinko, J., Wheeler, J. C., & Zhang, J. (2013). The Very Young Type Ia Supernova 2013dy: Discovery, and Strong Carbon Absorption in Early-time Spectra. ApJ, 778, L15.

Zissell, R. E. (2000). Shutter Mapping Correction for Short CCD Exposures. *Journal of the American Association of Variable Star Observers (JAAVSO)*, 28, 149–156.